EXTRACTION OF SPATIAL INFORMATION FROM STEREOSCOPIC SAR IMAGES

By

Pu-Huai Chen

A Thesis Submitted for the Degree of

Doctor of Philosophy

of the University of London

Department of Geomatic Engineering

University College London

May 2000

Abstract

Synthetic Aperture Radar (SAR) is now widely used for generating Digital Elevation Models (DEMs) and has advantages over optical data in terms of availability as it allows all-day and all-weather operations. The stereoscopic SAR method, which allows direct extraction of spatial information in three-dimensional space, has been established for decades. However, the traditional stereoscopic methods developed for SAR data depend on many human operations and need ground control points (GCPs), to set up geometric models. The aims of the thesis are not only to propose a refined rigorous stereoscopic SAR method and a new error model to predict theoretic errors, but also to achieve a higher level of automation and accuracy. By using a weighting matrix, which is derived by considering different observations in the space intersection algorithm, the minimal number of the GCPs required for the refined algorithm is only two. To achieve a high degree of automation, an optimized strategy of parameter selection for the pyramidal image correlation scheme employing a region-growing technique has been proposed. This avoids a trial-and-error approach to produce digital parallax data from the same-side SAR image pairs. A new method to derive GCPs automatically has been developed using a SAR image simulation technique, under the condition that a known DEM chip is available, to minimize human interventions and operator error. The proposed method for providing GCPs and the DEMs generated from space intersection have been incorporated into the procedures for geocoding SAR images to validate the proposed algorithms. The results derived show that the stereoscopic SAR data can be applied to geometric rectification in flat-to-moderate areas, and other applications of extraction of spatial information are promising.

To Hsiu-Lan

Contents

List of Tables

List of Figures

Acknowledgements

The name list of acknowledgements followed is definitely incomplete, and I apologize if any people or organization has been missed on the list. Firstly, I am grateful to the following individuals and organizations that help me directly to the production of the thesis:

Prof. Ian Dowman for supervising this Ph.D. project,

Prof. Jan-Peter Muller for providing papers,

Dr. Jonathan Iliffe for giving advice on the weighting matrix,

Ms. Leoni Blank for giving an introduction to the workstation-based ERDAS® system,

Mr. Mark Upton for arranging the co-ordinate transformation routines,

Mr. José Gonçalves for the interpretation of RADARSAT image header data, and

RADARSAT International (RSI) for providing RADARSAT SAR images under the Application Development and Research Opportunity (ADRO) programme (No.136).

Secondly, my thanks also go to Chung Cheng Institute of Technology for the recommendation of the fellowship and for the logistic support required, and the Government of the Republic of China for the grant of the fellowship for overseas Ph.D. study.

Finally, I am in debt to my wife, Hsiu-Lan, and my parents. Without their encouragement, the Ph.D. study and thesis would not have been possible to complete. Particularly, my wife is the main supporter behind this thesis. She spent 15 months in London giving me great help when the Ph.D. work was at the peak load.

Chapter 1
Introduction

"Modern man knows where he stands.
His map tells him."

-Quoted from *The Economist* [1999]

1.1 Overview

"Where are we?" or "Where is it?" is one of the basic and complicated questions for human beings, which can be answered by maps. Making maps can be carried out using the techniques of photogrammetry and remote sensing, and is one of the reasons for extracting spatial information from remotely sensed data. The spatial information required includes, not only the locations, but also the distributions and the relationships, of objects of interest in space that can be represented in various forms, for instance, object co-ordinates, linear, area and even volume measures, such as Digital Elevation Models (DEMs). The means and systems used for extracting spatial information must be accurate, efficient and robust to environments. Photogrammetry, the science of measuring the size and shape of objects or terrain surfaces from images (photographs), has been regarded as the most accurate, fast and efficient way for doing it in the past decades.

Extraction of spatial information from space-borne remotely sensed data using photogrammetry has been established for a long time. There are many practical remote sensing systems available for space cartography, such as the American Landsat series, French SPOT (*Satellite Pour l'Observation de la Terre*) series, German MOMS-02 (Modular Opto-electronic Multispectral Scanner) and numerous other commercialized high-resolution photographic systems. All of the systems in operation can be classified into two categories, a large number of the sensors operating in or near the visible wavelength and a small number of radar systems. A major problem with the optical systems is the difficulties of mapping under cloud cover and of collecting spatial data

without having a passive energy source. It means that the photogrammetric method is relatively sensitive to the environment and to the availability of the reflected energy.

Radar systems provide an alternative way to extract spatial information. Radar (acronym for *ra*dio *d*etection *a*nd *r*anging) is the use of radio waves to locate the illuminated objects and to determine their angular position and range, or the system for doing so. Traditional radar systems have been in use for over sixty years at various frequencies for different fields of application. For instance, the over-the-horizon (OTH) radar for air traffic control may be operated at frequency as low as 4 or 5 MHz and the laser radar operated at even higher frequencies in infrared and visible regions, [Skolnik, 1981], [Kingsley and Quegan, 1992]. Among various radar systems, the Synthetic Aperture Radar (SAR), operated at microwave frequencies, achieves high resolution in the along-track (azimuth) and the range direction by taking advantage of the motion of the platform carrying the radar to synthesize the effect of a large antenna aperture. Thanks to the robustness of extracting spatial information to varied environments, SAR systems are recognized as important mapping tools and are now widely used in the mapping and remote sensing community.

1.2 Overview of Radargrammetry

Radargrammetry, as a branch of photogrammetry, is the science and technology of extracting spatial information from radar data, in particular for terrain mapping using SAR images. Air-borne SAR systems have been developed for decades and achieved some results for terrain mapping, particularly in tropical areas under cloud-cover [Leberl, 1990]. Most of the methods developed are specialized and based on a local Cartesian co-ordinate system. A number of Ground Control Points (GCPs), or the reference points with known ground co-ordinates giving connection for co-ordinate transformations of other ground points, are always essential. The advantage of airborne SAR systems is their mobility for specific mapping missions. But, it may be not applicable when frequent thematic mapping and global monitoring is requested. In terms of availability for frequent mapping and global monitoring, satellite SAR systems are preferred.

Several Space-borne SAR systems have been in regular use, for example, the American Shuttle Imaging Radar (SIR-A/-B/-C), European Remote Sensing satellite (ERS-1/-2) SAR, Japanese Earth Resource Satellite (J-ERS-1) and Canadian RADARSAT SAR. The space-borne SAR systems have transmitted abundant data and

make the applications for global mapping and monitoring possible. Particularly, the RADARSAT SAR system can provide images with a variety of bases and look angles and so for the first time DEMs can be generated using stereoscopic principles from space-borne SAR image pairs on a routine basis.

Among the applications of SAR data, terrain mapping using SAR images has been proposed and studied by various authors in the photogrammetry and remote sensing community. Leberl [1990] gives a comprehensive review on this broad topic. Most of the early mapping work relates to SAR image interpretation, geocoding or image-map production, [Guindon, 1986], [Domik *et al.*, 1986], [Dowman *et al.*, 1993], [Schreier *et al.*, 1993]. Geocoding is to geometrically rectify a remotely sensed image according to a specific map projection system and a DEM to eliminate terrain induced image distortion (see Section 2.6 and Chapter 7). The key factor to produce geocoded images is the use of DEMs and GCPs. However, DEMs are not always available and may be difficult to produce, e.g. in cloud-covered areas where optical data is not available or in underdeveloped areas where collecting GCPs is difficult. Two distinctive and practical methods have been developed for generating a DEM from SAR data: interferometric SAR (IfSAR) and stereoscopic SAR.

IfSAR is based on the measurement of the phase difference (0 to 2π) between the back-scattered electromagnetic wave fronts received by two spatially separated antennas from a common target point. Terrain elevation mapping with the IfSAR approach can be carried out deriving relative elevation data from phase difference and registering to a map projection system. The IfSAR approach has achieved reasonable results on the order of a few metres using a single-pass (two-antenna) airborne IfSAR system, according to Mercer [1995]. Recently, the Shuttle Radar Topography Mission (SRTM) has been launched in early 2000. That uses a single-pass IfSAR system and is designed to carry out terrain elevation mapping of 80% of the Earth's land. It is expected to fully demonstrate the ability of the IfSAR method for generating DEMs, [JPL, 2000].

In terms of frequent mapping and global monitoring, however, experiments of the repeat-pass space-borne IfSAR system show that the method often gives poor results due to poor coherence and to different atmospheric and physical conditions, [Hartl *et al.*, 1995]. Some results can be obtained under special circumstances and conditions, [Ferretti *et al.*, 1999]. Compared with the IfSAR approach, the stereoscopic SAR method, based on measuring the co-ordinate difference of a common ground point from an image pair

and converting it to spatial data according to an appropriate radargrammetric model (or simply called 'geometric model' in this thesis), does not require such tight conditions. Another advantage of the stereoscopic SAR method is the ability of direct provision of the spatial information of any image point and of linear/area measures. It means that the stereo SAR method is relatively flexible. In theory, there also remain other conditions for stereo SAR, such as a reasonable intersection angle between each image for collecting distinctive parallaxes, allowing them to be transformed into height data. This condition is less significant, since multiple options of incidence angle of space-borne SAR data are available nowadays, [CSA, 1995].

Early work on SIR-B data and ERS-1 data at UCL suggests that the stereoscopic radargrammetric approach is a promising tool for extracting elevation data from space-borne SAR images, [Clark, 1991], [Dowman, 1992]. For instance, Chen and Dowman [1996] proposed an analytic approach to carry out space intersection using a least squares adjustment for ERS-1 data and reported results without using any GCPs, if good quality orbit data of the order of metres is available (see Section 2.3).

There are some other results reported using radar data for terrain mapping, such as Mercer [1995] and Sowter [1998], however, the detailed algorithms used have not been illustrated completely. Other stereo methods need many human operations and GCPs for model set-up, such as Sylvander *et al.* [1998] and Toutin [1999]. Most of the current methods do not give a complete radargrammetric error model for predicting theoretical errors due to observation errors (or simply called 'error model' in this thesis) hence the limitations of the geometric model used cannot be fully understood. A rigorous geometric algorithm for generating spatial information with an error model to be validated is necessary to understand the full potential and limitations of extracting spatial information from stereoscopic SAR data. Also, the requirements of human operations and GCPs have to be reduced. Further consideration and refinement for the geometric model to be applied to the SAR data with inferior quality orbit data, such as RADARSAT SAR imagery, is essential.

Automation is to use computers to carry out the tasks that human operators find inconvenient to do, such as repeat stereoscopic measurements, and is the kernel task of digital radargrammetry. Digital image correlation is one of the key steps from analytic to digital radargrammetry. Pyramidal correlation strategy (see Section 2.4) using a least-squares correlation method, [Gruen, 1985], with a region-growing approach, [Otto and Chau, 1989], has been proved useful to generate a parallax file from SIR-B SAR data,

[Denos, 1992], and a DEM can be generated from ERS-1 images, [Twu, 1996]. However, a trial-and-error method for giving the pyramidal structure is required, [Twu, 1996].

Providing ground control is another problem in digital radargrammetry. Traditionally, the provision of GCPs for radargrammetry is carried out manually, such as, Leberl, *et al.* [1986], Raggam and Gutjahr [1998] and Singh *et al.* [1998]. Manual operations for collecting GCPs from radar images and maps are usually limited by visual image-map correlation, and are not always stable hence the GCP quality cannot be assured (see Section 2.5). Thus, automatic provision of ground control is one of the main concerns in the radargrammetric process, which needs to be developed to reduce human interventions and errors in collecting GCPs.

In general, digital radargrammetry has been developing progressively, but more improvements are still needed in terms of rigidity and robustness of the geometric model. Also, there is plenty of room for upgrading automation in many aspects of radargrammetry, including image correlation, provision of ground control, and feature extraction *etc.* Under the RADARSAT Application Development and Research Opportunity (ADRO) Programme, SAR images have been provided by RADARSAT International (RSI) and used for testing the possibility of producing DEMs and of other applications such as geocoding. This gives the author a chance to carry out the main task of the thesis, based on previous work on SIR-B and ERS-1 data, such as Clark [1991], Denos [1992], Chen and Dowman [1996] and Twu [1996]. The aims of the PhD work are set out in the next section and a brief introduction to the structure of the thesis follows.

1.3 Aims of the Ph.D. Project

Radargrammetry is not only able to deal with the production of a DEM, but also to extract spatial information, such as ground point co-ordinates and linear or surface measures. That is a relatively broad topic. In order to make a solid foundation for developing digital radargrammetry, this thesis firstly has been focused on developing the space intersection algorithm for extracting spatial information from stereo SAR data, which is represented by the generation of DEMs. Secondly, automation of the relevant procedures in radargrammetry including image correlation and provision of ground control is included in the thesis. Digital radargrammetry needs to be improved in many aspects. Other topics of automatic extraction of object co-ordinates or linear features are also important, but these are beyond the scope of this thesis.

The entire Ph.D. project does not intend to achieve a full automation of radargrammetry. However, the development of digital radargrammetry is indeed the direction of the Ph.D. project. In general, the aims of the Ph.D. project include:

(1) To refine the rigorous stereo intersection algorithm using a least squares adjustment allowing spatial data to be extracted from a pair of images with the minimal requirement of human operations and GCPs, and with the minimal error propagation from image co-ordinate measurements. Particularly, the geometric model has to be robust when good quality orbit data is not available.
(2) To develop an error model to predict the errors of the results derived from space intersection caused by the image pixel measuring errors, including the range pixel and azimuth line observations. The error model has to be able to predict theoretical errors accurately in respect to the space intersection algorithm and be compared with the actual errors generated.
(3) To improve the level of automation of image correlation, i.e., to initiate the pyramidal correlation scheme using an optimized strategy, instead of a trial-and-error approach. A satisfactory DEM, representing the spatial information extracted from a SAR image pair, has to be generated to verify the geometric algorithm as well as the automatic procedures of image correlation.
(4) To develop an automatic way of providing ground control for radargrammetry in order to get rid of the errors from manual operations of collecting GCPs. A SAR image simulator is considered, to provide GCPs using a known DEM chip. The quality of the GCPs provided has to be proved better than that of the manually collected ones.
(5) To refine and to improve the DEM derived using suitable procedures, such as interpolation techniques and DEM filtering methods. The generated DEM and the automatically derived GCPs will be used for SAR image geocoding for verification of the proposed algorithms in the thesis. An adequate geocoding algorithm has to be considered to avoid any possibility of the positional accuracy degradation of the geocoded image, in respect to the presentation of the generated DEM.

All of the results derived using the proposed algorithms in this project have to be validated by any means, such as individual check points, statistical analysis and image presentation, whenever necessary. It is expected that the performance and the limitations of the proposed algorithms, in terms of extraction of spatial information from SAR data,

can be understood, and the work carried out in the thesis may contribute knowledge to the science and technology of photogrammetry and remote sensing.

1.4 Outline of the Thesis

An introduction to mapping using SAR data and a literature review are made in Chapter 2 to show the advantages and the shortcomings of the currently available methods for radargrammetry. Radargrammetry covers knowledge of wide scope, and there seems to be an endless reference list. Hence it is not possible to include every aspect of radargrammetry in this thesis. The methods of relevance of other authors, in respect to the thesis, will be reviewed concisely and briefly. The literature review in Chapter 2 follows the order of the contents of the other main chapters.

Chapter 3 gives the foundation of the extraction of spatial information from a SAR image pair, i.e., the formulation of the refined space intersection algorithm and of the error model. Independent check points are used to verify the results derived, and the predicted errors of observations are compared with the actually derived errors.

In Chapter 4, the optimized pyramidal structure is established and provides a reliable way to control the least squares correlation routines with a region-growing approach. The DEM results derived using the parallax data generated from image correlation of different combinations of parameters employed in the pyramidal correlation scheme, and the algorithm in Chapter 3, are compared with a reference DEM to validate the proposed strategy.

A SAR image simulator is proposed in Chapter 5 to produce simulated images using a known DEM chip. The corner elements of the DEM are assigned as GCPs. A normalized cross-correlation measure is introduced to carry out SAR real-simulated image correlation to make the provision of ground control possible. The automatically generated GCPs will be validated by means of giving control to the DEM derived in Chapter 4 so the systematic shifts remaining in the DEM can be reduced.

Chapter 6 illustrates the refinement and improvement being made to the DEM derived and corrected by the automatically generated GCPs in Chapter 5. A step-by-step approach of the DEM refinement and verification, including DEM data fusion, interpolation and filtering, is carried out to guarantee that the improvement of the quality of the DEM derived is made before proceeding to next step.

In Chapter 7, geocoded real SAR images are used as the application examples of the DEM extracted in Chapter 6. An algorithm of geocoding to keep the quality of the generated DEM from any possible degradation in the geocoding process has been developed. The geocoded images derived using the reference DEM and those using the DEM refined and generated are validated by independent check points. This chapter shows the use of the derived and refined DEM as well as the automatically generated GCPs.

Finally, the Ph.D. project is concluded in Chapter 8 to give a general review of the results derived in the thesis. The performance and limitations of the proposed algorithms are analyzed to provide a rough guide for future study in digital radargrammetry. A list of software used in this thesis is shown in Appendix A highlighting their contributors. Appendix B gives the software developed by the author together with brief descriptions of usage. Appendix C illustrates the source of check points. Appendix D shows the test images and the reference DEM. Appendix E and F give the DEM generated and the geocoded images derived at a larger scale, respectively.

Chapter 2

Mapping Using SAR Data

2.1 Introduction

Synthetic Aperture Radar (SAR) imagery is now widely used for generating Digital Elevation Models (DEMs) and has advantages over optical data in terms of availability as SAR systems allow all-day and all-weather operations. The methodology employed for extracting spatial information from SAR data, such as a DEM, is the science and technology called radargrammetry. Radargrammetry is established connecting radar image and object space, which utilizes radar (SAR) images to carry out spatial measurements and terrain mapping applications with a reliable geometric model. On the one hand, an overlapping SAR image pair can be used to model spatial characteristics of terrain surface, such as a DEM, which is one of the most interesting objectives in the photogrammetry and remote sensing community. That is an image-to-object connection. On the other hand, a SAR image can be geometrically rectified using a known DEM to produce an image-map. That is an object-to-image connection. Radargrammetry is based on the geometric models employed for the image-object connection in both directions. In the digital era, automation in many aspects of radargrammetry is progressing slowly. It will be shown that more research on (digital) radargrammetry is necessary.

It is not possible to cover every aspect of radargrammetry in this thesis. A review of radargrammetry of wide scope can be seen in Leberl [1990]. This chapter can only briefly review the radargrammetric developments with concentrations on stereo SAR data, including the geometric model for retrieving spatial information, automation for SAR image correlation, SAR image simulation using a known DEM for providing control and geometric rectification of SAR images. In respect to the limitations of the current methods employed, it will be shown that there is plenty of room for improvement in terms of the geometric model and of automation leading to the main topics of this thesis. The

following sections give a brief review of the work being done by other authors, and indicate the direction of research in this thesis, as mentioned in Section 1.3. The literature review is carried out section by section to reflect the corresponding topics conveyed by the chapters, which follow.

In Section 2.2 of this chapter, an introduction is given to the space-borne SAR data and systems available to general users, in particular those of the free-flying satellites, such as RADARSAT. The characteristics of SAR data are also reviewed. Different approaches for terrain mapping using SAR data are surveyed in Section 2.3, including the interferometric SAR (IfSAR) methods and the stereo approaches. The disadvantages of the current approaches will be identified leading to the proposal of the refined geometric model. Algorithms dealing with image correlation are evaluated in Section 2.4 to identify the one suitable for SAR image pairs. Section 2.5 gives the ideas of providing ground control in radragrammetry. Human operations are still needed for the currently available methods, and these must be replaced by automatic techniques to achieve a higher level of automation for digital radargrammetry. The simulated SAR image, based on an existing DEM, used to provide ground control is particularly discussed. Methods of geocoding, that allow a SAR image to be rectified geometrically with respect to a specific map projection or a local co-ordinate system, are reviewed and evaluated in Section 2.6. SAR geocoding will be used as an application example to show the use of the automatically generated DEM and of the automatically provided Ground Control Points (GCPs) to verify the algorithms proposed in the thesis.

2.2 Overview of SAR Systems and Data

The basic concept of radar systems is covered in radar textbooks, for instance, Skolnik [1981] and Kingsley and Quegan [1992]. While most of the radar systems inherited the initial ideas designed for finding specific moving objects or for navigation, SAR systems are commonly recognized as being useful as a mapping tool. In brief, SAR images are formed by an active microwave instrument transmitting electromagnetic waves towards the ground and receiving back that part of the radar signal that is scattered back towards the sensor/receiver. The azimuth position is computed in a SAR image from a large number of reflected pulses recorded and correlated as the radar beam passes by the ground point. The azimuth direction of a SAR image is approximately represented by the flying direction of the sensor's platform. A range timing value is associated with each

ground point recorded that is related to the back-scattered signal from that point and give the distance between the sensor position and the ground point. Generally, an image is made up of pixels recording the scattered signal of the ground point, the position of the point being defined by range value and azimuth time, [Chen and Dowman, 1996]. Let a SAR image be given in a rectangular co-ordinate system, which is composed of two orthogonal components: the range and azimuth direction and gives the relative position of a SAR image pixel. The azimuth line of a SAR image is given by ordinate parallel to the flying direction of the sensor and the range is given by abscissa or the orthogonal component with respect to the azimuth line (see Section 2.2.2 and in Chapter 3). More illustrations for the basic digital SAR processing theory can be found in the review article by Barber [1985] or in textbooks of remote sensing and radargrammetry, such as Elachi [1988] and Leberl [1990]. Even more sophisticated description for SAR processing algorithms and systems of wide scope can be found in SAR textbooks, such as Curlander and McDonough [1991].

A SAR system has to be mounted onboard a fast moving platform, such as an aircraft, a Space Shuttle or a satellite, to form a synthetic aperture, instead of a physically fixed aperture as in a Real Aperture Radar (RAR) or a brute force radar. The physical distance from a sensor to an object is not critical in deciding the resolution of a SAR sensor. Every object is assumed relatively stationary within the sensed area, otherwise, the object will become defocused or displaced in respect to the ground. In general, SAR systems are used for terrain mapping, long-term global monitoring and planetary mapping, instead of for real-time navigation and fast-response surveillance. Terrestrial mapping applications of SAR data are the most important subject in this thesis. The methods of extra-terrestrial mapping are also important, but this is beyond the scope of the thesis. A review for planetary (for instance, Venus) mapping and radar systems can be seen in Leberl [1990], Curlander and McDonough [1991] and Jet Propulsion Laboratory (JPL) [2000] for the most recent development in this realm.

2.2.1 Space-borne SAR Systems for Terrestrial Mapping

Initially, SAR systems were mounted onboard airplanes to carry out terrain elevation mapping of cloud-covered areas. In terms of frequent mapping and global monitoring, the air-borne SAR systems are not always accessible to general users hence the following text will focus on the space-borne SAR systems only. Thanks to the launch

of the American SEASAT in 1978, the space-borne SAR data provided an alternative way to see the planet Earth that inspired research for SEASAT SAR image geocoding, for example, Curlander [1982], Naraghi *et al.* [1983], Kowk *et al.* [1987] and Wivell *et al.* [1992].

After the unfortunate termination of SEASAT, the USA initiated Shuttle Imaging Radar (SIR-A/-B) in the early 1980s which contributes more developments for stereoscopy as well as geocoding, for example, Leberl *et al.* [1986], Domik *et al.* [1986], Clark [1991] and Dowman *et al.* [1992]. The SIR missions were followed by two SIR-C/X-SAR missions in 1994 to carry out a series of SAR experiments in particular for the repeat-pass Interferometric SAR (IfSAR) applications, [Moreira *et al.*, 1995]. The most recent development of SIR system is the single-pass Shuttle Radar Topography Mission (SRTM) which has been launched in February 2000, more details see web site at http://www.jpl.nasa.gov/srtm. The mission uses C-/X-band IfSARs to acquire topographic data of the Earth land (discussions see Section 2.3.4). Some key parameters for these Space Shuttle SAR missions are shown in Table 2.1. Since the Space Shuttle can only fly for a short period, it is not ideal for frequent monitoring and thematic mapping.

Space Shuttle Mission	SIR-A	SIR-B	SIR-C / X-SAR	SRTM
Country	USA	USA	USA / Germany + Italy	USA + Germany + Italy
Launch Date	1981	1984	1994 (flew twice)	2000
Altitude (km)	259	225	225	233
Frequency (GHz)	L(1.28)	L(1.28)	L(1.25),C(5.3) / X (9.6)	C(5.3) / X (9.6)
Polarization	HH	HH	HH, HV, VH, VV / VV	HH, VV / VV
Incidence Angle (°)	50	15~60	20~55 / 15~60	-
Antenna Size (m×m)	9.4×2.2	10.7×2.2	12×2.9,12×0.7 / 12×0.4	-
Swath Width (km)	50	15-50	15~90 / 15~60	225 (total) / -
Azi./R. Resolution (m)	4.7/33	5.4/14.4	6.1/8.7	-

Table 2.1 Key parameters of the Shuttle Imaging Radar SAR systems (compiled from Curlander and McDonough [1991] and JPL [2000]).

Although the life-span of the SEASAT was merely several months, it encouraged the development of the successive space-borne SAR systems, such as the Russian ALMAZ-1, the Japanese Earth Resource Satellite (J-ERS-1) and the European Remote Sensing satellite (ERS-1/-2) in the early 1990s. The latest development of the ERS radar systems will be onboard the new ENVISAT satellite to be launched in 2001. More details for the ERS and ENVISAT SAR systems see web site at http://earth1.esrin.esa.it/ERS/. Some key parameters for these satellite SAR systems are shown as in Table 2.2.

There are only relatively few reports available and are limited to general descriptive analysis and geocoding for the Russian ALMAZ-1 SAR data, [Marek and Schmidt, 1994]. Thanks to the orbit data with accuracy of the order of metres provided by ERS, [Massmann *et al.*, 1993], radargrammetric results of geocoding, stereo radargrammetry and IfSAR, have been obtained, such as, Dowman *et al.* [1993], Zebker *et al.* [1994], Guindon [1995], Toutin [1996], Chen and Dowman [1996] and Twu [1996]. However, the incidence angle of ERS SAR imagery is fixed to 23° for the regular product Precision Image (PRI), except a short period of Roll-Tilt Mode (RTM) campaign in early 1992 using an incidence angle of 37°. This makes routine stereoscopic applications difficult.

Satellite	Seasat	Almaz	ERS-1/-2	J-ERS-1	Radarsat	Envisat
Country	USA	Russia	EU	Japan	Canada	EU
Launch Date	1978	1991	1991/1995	1992	1995	(2001)
Approx. Altitude (km)	800	280	785	570	790	800
Frequency Band (GHz)	L (1.3)	S (3.0)	C (5.3)	L (1.2)	C (5.3)	C (5.3)
Polarization	HH	HH	VV	HH	HH	HH~VV
Incidence Angle (°)	23	30~60	23	35	10~59	14~45
Antenna Size (m×m)	10.7×2.2	15×1.5	10×1.0	1.2×2.2	15×1.6	-
Swath Width (km)	100	25~50	100	75	49~520	58~400
Azimuth Resolution (m)	23	15	25	30	8~100	30
Looks	4	2	3	4	1~14	-

Table 2.2 Key parameters of the satellite SAR systems (compiled from Curlander and McDonough [1991] and ESA [2000]).

Comparing to earlier SAR systems, the RADARSAT SAR data provides a wide variety of different types of images with versatile options of incidence angle and resolution for the first time. The RADARSAT data allows the stereoscopic application for terrain mapping on a routine basis. Some of the operating modes and beam angles available for users are given in Table 2.3 and 2.4, respectively.

Beam Mode		Angle Options	Incidence Angle(°)	Swath Width(km)	Resolution Ra.(m)/Azi.(m)	Looks
Standard		7	20~49	105	24/26	4
Fine		5	37~48	49	9/8	1
Extended Coverage	Low	1	10~23	170	43/26	4
	High	6	49~59	75	19/26	4
ScanSAR	2-Beam	1	20~39	310	35/30 100/100	1 14
	4-Beam	1	20~49	520	34/52 100/100	1 8

Table 2.3 Summary of the RADARSAT SAR beam modes (after Luscombe *et al.* [1993]).

Due to the inferior quality of orbit information available, RADARSAT SAR data can hardly be used for IfSAR applications. Many projects regarding radargrammetry using RADARSAT data have been carried out under the Application Development and Research Opportunity (ADRO) programme (No.136), [Dowman and Chen, 1998], [Singh *et al.*, 1998] and [Toutin, 1999]. The RADARSAT SAR images provided by RADARSAT International (RSI) under the ADRO programme No.136 were used in the thesis. More details for the RADARSAT SAR systems see web site at http://radarsat.space.gc.ca/.

Beam Mode		Beam Number	Incidence Angle (°) Near	Far
Standard		S1	20.0	27.4
		S2	24.2	31.2
		S3	30.4	36.9
		S4	33.6	39.6
		S5	36.5	42.2
		S6	41.4	46.5
		S7	44.9	49.4
Fine		F1	36.9	40.1
		F2	39.3	42.3
		F3	41.6	44.2
		F4	43.5	46.0
		F5	45.3	47.8
ScanSAR	2-Beam	-	20.0	39.5
	4-Beam	-	20.0	49.4

Table 2.4 Incidence angles of each beam number of RADARSAT SAR data (after Luscombe *et al.* [1993]).

2.2.2 SAR Image Products for Users

According to different levels of post-processing, various SAR products derived from raw data are available for users as summarized in Table 2.5. The SAR primary products convey the original imaging geometry together with the header and ephemeris data that allows the rigorous transformations between the SAR image and object space. Further processing can be performed for the generation of variable secondary products. The SAR single-look complex images and multi-look intensity images fall into the category of the SAR primary products.

A SAR single-look complex image, for instance, the ERS SLC product, is composed of the magnitude (amplitude) and the phase part of the scattered signal. The magnitude simply represents the scattered power. On the other hand, the phase, that is

extremely sensitive to range, contains the information of roughness of the surface within a fraction of the wavelength. This kind of information contained in the complex image is not ready to use for general users. To make full use of the phase data, such as IfSAR, some problems have to be solved subject to various limitations and conditions (see Section 2.3.4).

The outcome of IfSAR is generally a relative elevation data set that has to be related to a designated ellipsoid to form a DEM. For measuring the shape of spatial features on the Earth land, the IfSAR-generated DEM must be derived firstly and then employed for geocoding intensity images to carry out the feature measures. The complex image co-ordinate system is given as the azimuth direction (line) and slant range (pixel). The azimuth direction is nominally similar to that of the platform velocity vector. The slant range is simply the measure of the distance (time) between the sensor and the illuminated target.

Level	SAR Product	Reference Frame	Examples	Applications
Primary	Single-look complex image	Satellite track Slant-range	ERS.SLC RADARSAT SLC	IfSAR DEM Differential IfSAR
	Multi-look processed intensity image	Satellite track Ground-range	ERS.PRI/RTM RADARSAT SGF	DEM, Line-map Feature extraction Hazard map Stereo-interpretation Iceberg tracking
Secondary	Ellipsoid corrected geocoded image	Map projection	ERS.GEC RADARSAT SSG	Quick delivery Offshore applications Index image
	Terrain corrected geocoded image	Map projection +DEM+GCPs	ERS.GTC RADARSAT SPG	Geological analysis GIS, Thematic map Image map

Table 2.5 Summary of SAR image products.

A multi-look intensity SAR image is produced using different sections of the full length of the synthetic aperture to carry out the radar image formation. Speckle, caused by randomly constructive or destructive interference of scatter from terrain and objects, is quite common which can make image interpretation and extraction of spatial information difficult. A common practice to suppress the inherited speckle from image formation is to use the so-called multi-look processing for generating the intensity image. This is done dividing the full synthetic aperture into several sections in which the full-scene SAR image is processed independently. Then, the homologous pixels of the SAR images generated from individual looks are averaged to reduce the effect of speckle, [Curlander

and McDonough, 1991]. The multi-look intensity image is processed and interpolated giving an image co-ordinate system defined by the azimuth direction (line) and ground range (pixel). In general, the ground range images transformed from the slant range ones are recognized as the standard images of the space-borne SAR systems that are the subjects being studied in the thesis.

The ground range representation of a SAR intensity image, known as the geo-referenced image, gives the relationships between spatial features somewhat similar to its optical counterpart, which is familiar to human eyes. The above-mentioned ERS PRI/RTM products and the RADARSAT SAR Geo-referenced Full resolution (SGF) products are typical multi-look intensity images. Most of the SAR products and applications are dealing with the magnitude part of the back-scattered energy, because the intensity images show the shape of features of interest and are much easier to be related to the real world than the single-look complex images. The intensity images may be employed for stereo interpretation, for the generation of DEMs and cartographic line-maps, and for analysis of artificial/natural features, such as flood monitoring and iceberg location, allowing the generation of various products as shown in Table 2.5.

Geocoding is to geometrically rectify a space-borne remotely sensed image, particularly the SAR imagery, in respect to a specific map projection and to eliminate terrain induced image distortions. A terrain corrected geocoded image is one of the secondary SAR products that is similar to, but not identical to, the orthogonal projection rectified image of optical data using photogrammetry (called ortho-rectification) that is derived from the original image of a perspective projection. Terrain effects in SAR images must be corrected and registered according to a map projection system before importing to a Geographic Information System (GIS). This can be done using the slant range SAR intensity data, the real orbit information provided and a known DEM (see Section 2.6). In general, two kinds of geocoded products can be derived according to the availability of DEMs. The ERS Geocoded Ellipsoid Corrected (GEC) products, or the RADARSAT SAR System Geocoded (SSG) products, generated using only the ellipsoid parameters, the SAR orbit data and imaging geometry, do not consider detailed terrain relief. These products suitable for offshore applications cannot be considered for rigorous land applications due to the relatively poor positioning accuracy given.

An external DEM of the area of interest is essential for the ERS Geocoded Terrain Corrected (GTC) products, or the RADARSAT SAR Precision Geocoded (SSG) products, which require precise transformation between the object and image space. In

order to guarantee satisfactory location accuracy for these geometrically rectified products obtained, ground control of some form must be used to compensate the errors of range and azimuth timing data. Ground Control Points (GCPs) are defined as the reference points with known ground co-ordinates giving connection in co-ordinate transformations for other ground points. Re-sampling is an interpolation procedure for deciding the density number of the corresponding pixels of an original image in the transformed image, according to the geometric transformations applied to the original image, such as rotation. Re-sampling is required at the final stage of geocoding to generate the equivalent density number for each pixel corresponding to the local terrain slope of each element of the DEM. This kind of geocoded image is regarded as the standard geocoded product that will be used to verify the results derived in the thesis.

2.2.3 Automatic Extraction of Spatial Information from SAR data

There are many aspects that distinguish a radar image from an optical one, and most of the classical photogrammetric concepts are not applicable for terrain mapping using SAR image pairs. For instance, a SAR image can be directly related to the object space with no regard to any interior orientation of image space. Since there is no perspective geometry in a SAR image, the co-planarity condition does not apply to any pair of SAR images. Each pixel of a SAR image is defined by the range and azimuth time. Thus, the azimuth lines of a SAR image have individual origins for counting distance from the sensor position to any ground point that can be related by a discrete series of timing data corresponding to the sensor velocity and position. The so-called 'range-projection', instead of perspective projection, is being used to describe such an unusual type of imagery. That leads to a different term, so-called 'radargrammetry', being used to describe the methodology of derivation of three-dimensional data from radar imagery, [Leberl, 1990].

A review of radargrammetry given in Section 2.3 will show the limitations of the currently available methods in terms of robustness and automation for the extraction of spatial information from SAR images. Improvements have to be made in the radargrammetric methodology leading to the proposal of the revised rigorous method and a new error model for stereo intersection as described in Chapter 3. Another key factor in producing a DEM from an image pair is the use of an automatic correlation method. Image correlation is dealing with the problem of searching for a defined part of one image

on the conjugate one. Based upon the automatic correlation results human operations can be minimized. Both the least-squares correlation method and the normalized cross-correlation measure are well known examples for doing this (see Section 2.4). A revision for the current method is proposed and described in Chapter 4.

Providing control for extracting spatial information has been a problem due to the unfamiliarity of SAR images to human eyes. SAR simulation methods allow the reconstruction of image features from available elevation data, such as a known DEM chip, that can be related with the real SAR image (see Section 2.5). An image correlator is then essential to relate the simulated-real image pair. Based on the ground control provided, accurate spatial information can be extracted. An automatic method proposed to provide control for radargrammetry is illustrated in Chapter 5. The development of the SAR simulation technique also helps with providing control for geocoding (see Section 2.6 and Chapter 7).

2.3 Radargrammetry

Since classical photogrammetric algorithms do not fit with the physical reality of SAR data, different ideas have been developed to carry out terrain mapping, such as mono-image mapping, stereo radargrammetry and IfSAR methods. Some other methods, e.g., shape-from-shading approach have also been proposed, [Wildey, 1986] and [Goller *et al.*, 1999]. However, it is strongly dependent upon uniform thematic value for all of the terrain in a scene that may not be applicable because of speckle as well as the complexity of terrestrial surfaces affected by artificial features and vegetation cover. Shape-from-shading will not be discussed further. The review of radargrammetric methods in the following will be focused on space-borne SAR data.

2.3.1 Mono-image Mapping

Curlander [1982] proposed a mono-image approach for positioning a ground point from SEASAT data using the simultaneous solution of a range equation, a Doppler equation and a designed earth model that is an exact solution for the location of a ground point on the terrain surface without redundant observations. This method shows that the ground location of an arbitrary pixel of a SAR image may be derived, independent of any reference or tie points, and it is suggested that this method can be used for terrain

mapping of planets. However, the theoretical accuracy of this approach is not only dependent upon the accuracy of the ephemeris data and range, but also on the validity of the fit of the designated ellipsoid to the local mapping site. Consequently, the derived accuracy is reported on the order of 200m.

2.3.2 Stereo Radargrammetry

The main concern of stereo radargrammetry is to use parallaxes of an image pair to derive spatial information, or to use the range and Doppler equations for the extraction of three-dimensional spatial information. In general, the stereo methods can be classified into two categories. The first approach has a rigorous solution of the range and Doppler equations defined as the computation of intersections of two range spheres and two Doppler cones. The second method, approximate stereo-radargrammetry, is to convert the parallax differences measured into height differences based on radar projection arcs or its tangent in a local Cartesian co-ordinate system, [Leberl, 1990].

The approximate approach is dependent upon the assumptions of the known incidence angles of each image and of a flat earth, as shown in Figure 2.1. A great number of well-distributed GCPs are essential for converting the relative height data set to a DEM. Also, the look-angle measured from a sensor to a ground point (the nominal incidence angles provided with header information) may not equal the actual incidence angle at the intersecting point on the surface of a given ellipsoid.

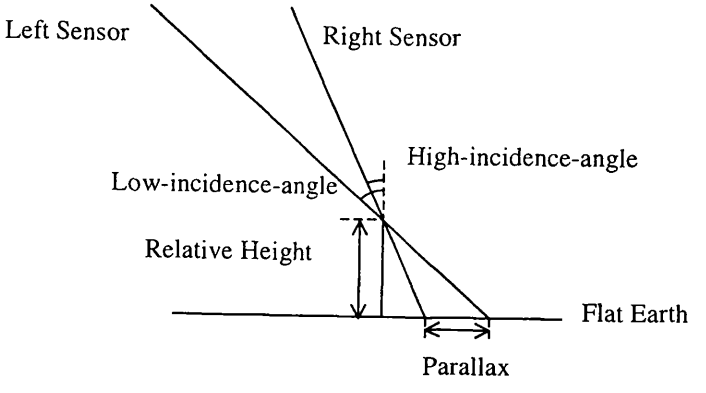

Figure 2.1 Approximate stereo radargrammetric model.

The incidence angle is liable to change non-linearly according to the earth curvature. Since it is not possible to record incidence angle for each range pixel, there are

only a few samples of nominal incidence angles provided by SAR image header information and the deviations due to incorrect incidence angles cannot be underestimated. Therefore, the approximate stereo approach is only suitable for a relatively small area to fulfill the assumption of a flat earth, [Dowman *et al.*, 1997].

Leberl *et al.* [1986] carried out the rigorous solution of stereo intersection and established an approximate error model of range pixel observations for SIR-B data. The image co-ordinates of the GCPs calculated and observed form the basis of the least squares adjustment to improve the assumed approximations of orbit positions. All entities including orbit data and near-range value are considered as observed with variable weights in the computation to differentiate between different quality of parameters, but there is no weighting matrix described. According to the algorithm published, neither the velocity vector of a ground point or the speed of the Earth rotation has been considered in the rigorous solution. In addition, Leberl *et al.* [1986] reported that the experimental results do not conform well to the predictions from error models. In a survey for stereo radargrammetry, Leberl [1990] summarized that the accuracy of different test results from stereo models differs from one (in a flat area) to five times the range resolution.

Stereo radargrammetry for ERS-1 PRI/RTM data carried out by Mercer [1995] produced elevation accuracy of 10-15m in moderate relief areas. In more rugged topography, the results were less accurate. There is no detailed description published for the algorithm being used. Toutin [1996] reported work on stereo mapping over rolling topography (slope less than 10%) for opposite-side ERS-1 SAR data. Twelve (12) ground points were identified manually and were used to set up stereo models. The results derived from independent check points show accuracy as two times the pixel size with a significant bias of one pixel size caused by the human operator. The same algorithm has been used for RADARSAT SAR data showing an accuracy in elevation of the same order in a moderate-relief area using a standard image pair, [Toutin, 1999]. The proposed radargrammetric process demands many GCPs and an operator to set up stereo models.

Sowter [1998] reported the automatic extraction of DEMs from stereo RADARSAT data and an error model for the range observation. The DEM was derived with no GCPs at all, but the orbit correction may be necessary when good quality orbit information supplied by the RADARSAT data is not available. The detailed algorithm used is not clear. A quantitative analysis of the DEM quality is not given owing to the coarseness of the ground truth (1:100,000 scale maps) of the tropical areas being compared. Another test in rugged topography for RADARSAT data, according to Singh

et al. [1998], shows that the non-weighted least squares adjustment with GCPs for radargrammetric analysis generates an RMS error in 3D of GCPs as 48m and that of arbitrary points as 90m in 3D. The space triangulation method employed for deriving DEM from RADARSAT data, proposed by Sylvander *et al.* [1998], requires at least four GCPs to fix the absolute position of each image and a number of tie points to register individual images to form a block of images. It is reported that 12~48 GCPs have been used to achieve stability within the image block. This algorithm depends on many human operations and there is no error model available.

An ideal geometric model for generating spatial information is expected to minimize the need of GCPs and human operations, to obtain high quality results and to be verified by an error model. The previous tests on RADARSAT data indicate that the figures of accuracy in height achieved approach one to two pixels (12.5 ~ 25m) of a standard image, however, most of those results can only be derived when many GCPs/tie points are available and human operations are required. In terms of deriving good quality result, predicting errors of azimuth line and range pixel observations, there is plenty of room for the stereo radargrammteric algorithm and the error model to be improved. Also, there is a need to reduce the number of GCPs required in the geometric model used. Further analysis and comment on stereo radargrammetry will be given after the description of the development of radargrammetry at University College London (UCL) and of the interferometric SAR techniques in the following sections.

2.3.3 Recent Development of Stereo Radargrammetry at UCL

In order to carry out terrain mapping for space-borne SAR data, Clark [1991] revised the rigorous stereo approach by incorporating the velocity of a ground point and applied this to SIR-B data to derive the three-dimensional locations of ground points. It was predicted that a rigorous approach could be used to terrain mapping using stereo ERS-1 SAR data for same-side and opposite-side configurations, [Dowman, 1992], [Dowman *et al.*, 1993]. After revision with a least squares adjustment, a space intersection algorithm has been applied to ERS-1 SAR images of the same-side pairs and the opposite-side ones without GCPs or with only two GCPs. This will be referred to as the Chen-Dowman geometric model, for deriving position vectors of ground points, [Chen and Dowman, 1996]. GCPs are not essential in the Chen-Dowman model. Chen and Dowman [1996] has proposed an error model to predict the theoretical errors. The

results derived from a varied land-use area with terrain relief ranging from 1m to 623m above mean sea level show accuracy from one to two times the range resolution with two GCPs and four to five times the range pixel without any GCPs.

It is possible to derive spatial information from ERS-1 data without using any GCPs, because the ERS-1 SAR imagery provides orbit data with accuracy of the order of metres and also has well-defined geometric relationships between azimuth lines and range pixels. The Chen-Dowman model is sensitive to a same-side configuration (such as parallel orbits, and this is liable to magnify radargrammetric errors due to observation errors referred to as 'critical parallelism'). The Chen-Dowman model is applicable when the orbit data quality is of the order of metres.

Twu and Dowman [1996] adopted the Chen-Dowman geometric model to generate a DEM from a same-side ERS-1 image pair using a geometric constraint condition for checking blunders. According to Twu [1996], the geometric constraint condition is based on the analysis of the differences between the derived range values from image co-ordinate observations and the ones calculated from stereo intersection. An uncorrected DEM derived by this method has achieved accuracy of only 148m in height. The poor accuracy is probably due to a small convergent angle of orbit tracks (2°) between the images. The application of the geometric constraint condition in object space, provided that the orbit data with accuracy of the order of metres is available, and a coarse DEM of a 1km grid is incorporated to remove the errors, generated a DEM with accuracy of 20m in height. Since RADARSAT SAR data do not provide orbit data with accuracy of the order of metres, the geometric constraint condition, proposed by Twu [1996], is not applicable. Hence a revision of the Chen-Dowman model for space intersection to allow these possible errors in the use of RADARSAT data for terrain mapping is essential, as presented in Chapter 3.

2.3.4 Interferometric SAR

IfSAR is based upon the measurement of the phase difference (0 to 2π) between the back-scattered wave fronts received by two spatially separated antennas from a common target point. Key parameters, including the baseline of antenna, its orientation with respect to nadir and the altitude of the sensor, are essential. If the phase difference is measured in conjunction with the above data, the relative height data can be derived, provided that an absolute phase ambiguity is resolved using ground control and a 'phase

unwrapping' technique, [Mercer, 1995], or other means, [Ghiglia and Pritt, 1998] and [Ferretti *et al.*, 1999].

Initially, the IfSAR approach was proposed to replace the role of the stereoscopic SAR technique and it was expected that IfSAR would be able to produce a DEM of accuracy within centimetres, for a single-pass system, according to Zebker and Goldstein [1986]. Tests for terrain elevation mapping using a single-pass air borne IfSAR system can achieve relative precision varying from 3m to 10m and absolute accuracy from 3m to 22m, as reported by Zebker and Goldstein [1986]. Mercer [1995] reported that elevation mapping using a single-pass air borne IfSAR system has achieved accuracy in height of 5m. It is presumed that the accuracy of terrain elevation mapping using a real baseline interferometric SAR can be sustainable when precise attitude of the aircraft and some GCPs are available, [Zebker and Goldstein, 1986], [Mercer, 1995]. In order to concentrate on space-borne SAR data, air borne IfSAR will not be discussed further.

A routine space-borne single-pass IfSAR system onboard satellite, which provides the applications of frequent monitoring and measurement, is still not available at this stage. Alternatively, the method of repeat-pass IfSAR, i.e., a pair of images derived separately at different locations by the same antenna or different ones, has been proposed to generate a DEM. But, in repeat-pass IfSAR it is difficult to maintain numerous rigorous geometric and physical conditions. For instance, the base length must lie within defined limits without losing phase coherence and the repeat period must be very short to avoid temporal de-correlation due to change of environment, [Zebker *et al.*,1994], [Hartl *et al.*, 1995], [Moreira *et al.*,1995].

Honikel [1998] has shown that the IfSAR-generated DEM using a pair of ERS-1 SAR images in hilly areas with data fusion from other elevation data sources improves the DEM quality from 76m to 42m. In flat areas, the IfSAR-generated DEM using ERS tandem data, with 24 hours time difference between image acquisitions, achieves quality of ±30m for 90% of the DEM data, provided that at least 10 location and 30 phase tie points for every scene are available, [Roth *et al.*, 1998]. The most recent results using IfSAR technique for producing DEMs with ERS-1/-2 data show that the height accuracy may achieve 5m when using multi-baseline and multi-pair data for IfSAR method employing the wavelet approach, [Ferretti *et al.*, 1999]. The results were derived from a number of generated raw DEMs by means of a weighted average based on the assumption that multiple inteferograms are available.

In February 2000, the single-pass IfSAR systems of the Shuttle Radar Topography Mission (SRTM), containing a fixed baseline of 60m long (the Mast) connecting the Main Antenna and the Outboard Antenna, have been launched to carry out terrain elevation mapping. It is used to generate a digital terrain elevation map of 80% of Earth's land surface at 30m grid spacing. The absolute horizontal and vertical accuracy of a DEM point is expected to be 20m and 16m, respectively. More details of the relevant references for IfSAR methods and applications can be found at the web site http://www.jpl.nasa.gov/srtm (file: interfbiblio.html).

The IfSAR approach is an active research area, for instance, each phase-unwrapping algorithm developed can only solve a specific problem, but it probably fails on others, [Ghiglia and Pritt, 1998]. The phase difference is critical for the IfSAR method, which can be affected by different factors, such as the baseline distortions, antenna misalignment effects and other phase noise (speckle or layover) *etc*, [JPL, 2000]. In repeat-pass IfSAR it is sensitive to the geometric configuration and many physical conditions, such as the base length (for keeping phase coherence) and the repeat period (to avoid temporal de-correlation due to change of environment, such as atmospheric effects).

When a DEM is generated successfully from the IfSAR method, the corresponding intensity image has to be geocoded in respect to a map projection system allowing for further terrain mapping and feature extraction applications. Extraction of spatial information can be difficult for the IfSAR approach, if the requested DEM cannot be generated successfully. Regarding direct extraction of spatial information in three-dimensional space, IfSAR is still not able to completely replace the role of stereo SAR method, such as the applications of iceberg detection, ship tracking and cartography in the areas where the phase ambiguity (layover) or phase noise (speckle) problems cannot be solved.

2.3.5 Comments on the Current Radargrammetric Methods

The IfSAR method can give good positioning accuracy in theory, but it is not always applicable for a repeat-pass IfSAR system. Besides the physical and geometric restrictions as mentioned before, the IfSAR method cannot directly extract three-dimensional spatial information from SAR data, say a point location or a linear feature, as mentioned in Section 2.3.4. That shows the stereo approach as being important as an

alternative tool for terrain mapping. The main disadvantage of the current stereo methods are that the parameters in the stereo model must be determined using GCPs, or there is a need of a number of GCPs for setting up stereo models. The predictions made from the corresponding error models do not cover the errors from all observations. The current methods have not completely explored the potential of stereo radargrammetry.

Previous work on SIR-B data and ERS-1 data at University College London (UCL) suggests that the stereo approach is a promising tool for providing spatial data from space-borne SAR data with/without GCPs. However, the rigorous algorithm faces difficulties when good quality orbit data are not available. In order to overcome such problems, a revision of the initial algorithm can be achieved using a weighting matrix in the least squares adjustment of space intersection. That leads to the development of new error models, which predict the theoretical errors of observations as described in Chapter 3. As the revised algorithm and the error models demonstrate the potential and robustness of the rigorous stereo intersection algorithm for terrain mapping using space-borne SAR data, an automatic way to derive conjugate image points, say image correlation, for extracting spatial information, such as a DEM, must be considered.

2.4 Image Correlation

In order to generate a DEM from an image pair with satisfactory coverage and density, it is necessary to use a proper image correlation strategy for automatic derivation of parallaxes from the image space that can be converted into object space using an adequate geometric model. The methods of automatic correlation for an image pair have been developed from the early electronic approaches in 1950s to the digital approaches in 1970s, [Dowman, 1981]. Following the development of digital computers during the last two decades, image correlation techniques are maturing and play a critical role in digital photogrammetric mapping, [Gruen, 1996]. Since digital radargrammetry is at a relatively primitive stage, the image correlation methods used in digital photogrammetry can be reasonable candidates to be employed for SAR imagery. However, SAR imagery exhibits speckle and severe spatial distortion compared with optical imagery, so general image correlation algorithms must be refined and optimized before using them for SAR image correlation.

2.4.1 Optical Image Correlation

The object to be correlated can be a point, a one-dimensional line, an edge, a two-dimensional curve or an enclosed region. An edge-based or feature-based correlation method may be used to derive some other specific information efficiently, such as edge-detection, [Marr and Hildreth, 1980], but, the outcome of this method cannot give enough samples to represent an undulating surface. In order to provide a dense coverage of parallax data for generation of a DEM, an area-based method of image correlation is preferred. It gives an extensive measurement for most of the conjugate points of an image pair and provides abundant points to represent a DEM, so an area-based method of image correlation is always adopted for digital elevation mapping applications. Most of the image correlation methods developed so far in photogrammetry and other areas have been focused on optical imagery. Some prior knowledge of the optical images can be employed to increase the reliability of image correlation, [Gruen, 1996].

For instance, Ho [1984] utilized the well-known normalized cross-correlation measure (see equation (5.23)) to carry out image correlation by searching for conjugate points along epi-polar lines in close-range mapping using a solid-state digital camera. The experiment achieved accuracy of 0.4 pixel, but some problems are unsolved, such as the selection of the optimal array dimension and the specification of rejection limits for image correlation, according to Wong and Ho [1986]. This approach might help with searching for the target of interest in terms of one-dimensional signal correlation or two-dimensional area correlation, but it lacks the flexibility for an image pair of perspective projection with geometric distortions. Particularly, it is obviously not suitable for radar data without intrinsic epi-polar geometry.

Ackermann [1984] proposed a least squares correlation method for local image correlation of high precision taking into account that the two conjugate image areas to be correlated differ both in geometry (different relief displacement) and in radiometry (image taken in different conditions). This method allows rectification for such differences by applying geometric and radiometric transformation in the process of window correlation which employs an iterative least squares solution for deriving the affine transformation and other additional parameters. The algorithm was developed specifically for the high-resolution aerial photographs and was implemented in an analytical plotter. It is reported that the positioning accuracy obtained on the order of 0.1~0.2 pixel is achievable. However, this method demands detectable textures to achieve

successful correlation results and assumes an initial location available. It also lacks flexibility for SAR imagery when speckle effect needs to be considered.

Gruen [1985] proposed a similar, but 'adaptive', least squares correlation technique to carry out the optimum correlation for the conjugate images. This approach not only considers the image distortions in radiometric and geometric aspects, but also suggests automatic variation of the image chip to grab a signal that is close but was ignored initially. The analysis of a covariance matrix is then critical to the updating process. This approach is suggested to be applied to air photographs as well as other remotely sensed images.

Otto and Chau [1989] developed a least squares correlation method, based on Gruen [1985], with a region-growing technique to automatically generate a dense coverage of parallax data from a SPOT image pair. The essence of the region-growing algorithm is to start with an approximate correlation between a pair of conjugate points. These points are called seed points. Firstly, the least squares correlation method is used to derive a more accurate match and the (geometric and radiometric) distortion parameters, and use the parameters derived to predict approximate matches for points in the neighbourhood of the first match. Then, the least squares correlation method is used to refine these matches again, and so on, [Otto and Chau, 1989]. This allows a progressive and robust way to carry out image correlation for the entire image pair of interest. Without any prior knowledge of the imaging model of the sensor or epi-polar geometry, this approach has produced good quality DEMs, [Day and Muller, 1989].

All of these various methods of least squares correlation demand a very good initial approximation to start the correlation or some constraint conditions available from the imagery with a perspective geometry, [Gruen, 1996]. It seems that there is no perfect and universal algorithm of image correlation available for various kinds of images.

2.4.2 Image Pyramid Data Structure

An image pyramid is among the simplest hierarchical data structures that have been widely adopted in image processing, [Sonka *et al*, 1993], as well as in digital photogrammetry, [Ackermann and Hahn, 1991]. For example, Marr and Poggio [1979] proposed a hierarchical approach where the edges in images are correlated in decreasingly filtered images of the original one for studying human stereo vision. In general, an image pyramid can be generated by averaging the surrounding pixels of a kernel pixel of the

original image to generate image tiers of reduced number of pixels by a factor, say two, from tier to tier. Each image tier is then correlated with its conjugate image to derive the best disparity estimates sequentially to guarantee good correlation of the major features by smoothing out the noise in the reduction process.

In order to propagate the correlation results efficiently, Quam [1984] suggested the use of an image pyramid for the area-based correlation operator employing a coarse-to-fine hierarchical control structure for estimating disparity to derive a DEM from optical data. The Hierarchical Warp Stereo (HWS) correlation is based on a cross-correlation measure for the reduced conjugate images (aerial photographs) and particularly used a one-dimensional distortion function to warp one of the images to derive disparity subsequently. Some problems have also been found, for instance, that manual selection of the size of cross-correlation window is inevitable, as demonstrated similarly by Wong and Ho [1986]. The range of disparities to compute at each level of the hierarchy is also determined manually. It has been noticed that some of the parameters, such as the range of disparities to be computed at each tier, affect the hierarchical correlation system. The depth of the hierarchical correlation system is defined by estimating the maximal disparity to be able to detect parallax within the range of (+2: -2) at the top level, [Quam, 1984]. The definition of the depth of image levels is not flexible for detecting other useful parallaxes, besides the maximal one, hence a global comparison of the best correlation within the reduced image is difficult that could be critical for a SAR image corrupted by speckle.

Hsia and Newton [1999] proposed a method for the automated production of digital terrain models using a combination of feature points, grid points, and filling back points with a hierarchical approach. The procedure starts from three matched points measured manually. The feature points are located approximately by a normalized cross-correlation measure and then decided precisely using a least squares correlation method. Grid points can be decided by the corresponding feature points of the appropriate triangle within a triangular irregular network (TIN), which connects the existing matched feature points. The mismatched grid point is filled back with aids from the nearest feature points and the neighbouring matched grid points. This method can fill back one mismatched point each time when the surrounding image features are acute and reliable.

2.4.3 Considerations for SAR Image Correlation

The characteristics of SAR imagery have to be considered before selecting an appropriate automatic image correlation method. Compared with optical imagery, the characteristics of SAR data show some fundamental differences from the former, such as:

(1) The imaging geometry of a SAR image is defined by the range and azimuth timing data (see details described in Chapter 3), i.e., there is neither intrinsic co-planarity condition in any overlapping image pair nor co-linearity condition for constructing image-object relationship, as used in optical photographs, [Albertz and Kreiling, 1980].
(2) A relatively big difference of radiometric reflection between the homologous points in a SAR image pair is always evident due to the change of illumination for the same object and to the sensitivity of the physical condition of the surface sensed, in case of a slight difference of orbital directions or viewing aspects, [Skolnik, 1981];
(3) The textures and features in SAR images are distorted by speckle caused by constructive or destructive interference from the SAR imaging procedures. A SAR image can be defocused occasionally by moving objects, such as vehicles, in the mapping area, [Curlander and McDonough, 1991].

As reported by Leberl *et al.* [1994], SAR data is strongly affected by speckle and therefore edge- or feature-based correlation cannot be considered in terms of generation of a DEM. Since the application of a pyramidal correlation scheme may help to propagate results of image correlation from the top tier to the bottom level to reduce speckle effect, the next step is to find a good image correlation method to guarantee that correct correlation results can be derived.

The development of digital photogrammetry has been more advanced than radargrammetry; several authors adopted the available techniques that were originally developed for optical data to carry out image correlation for radar data. Ramapriyan *et al.* [1986] followed the pyramidal approach proposed by Quam [1984] to test SIR-B data for generating a DEM using the Massively Parallel Processor (MPP) based on a cross-correlation measure. However, no accuracy assessment is available for the generated DEM. Welch and Papacharalampo [1990] also used a similar correlation method for SIR-B image correlation on a PC-based workstation.

Leberl *et al.* [1994] carried out automated image matching experiments for Magellan radar data and found that using the normalized cross-correlation measure can achieve a best accuracy of ±2 pixel compared with a human operator. A test of RADARSAT data using the same measure by Singh *et al.* [1998] demonstrates that the resultant error magnitude of arbitrary points is about 90m (42m in height) showing that the results can be affected by the correlation method as well as the geometric model. The correlation errors may be owing to the use of a normalized cross-correlation measure that does not take into account the geometric distortions between two radar images. Paillou and Gelautz [1999] proposed an "Optimal Gradient" Matching method (OGM) based on the assumption that the SAR image features represent the terrain relief only and on the normalized cross-correlation measure with a hierarchical approach. The proposed gradient operator may not work properly when the SAR image conveys many artificial features and vegetation cover that affect radar illumination strongly.

2.4.4 Recent Development of Image Correlation at UCL

At UCL, a least squares correlation method, based on Gruen [1985], with a region growing technique has been developed by Otto and Chau [1989] to automatically generate a dense coverage of parallax data from a SPOT image pair, as mentioned in Section 2.4.1. Without any prior knowledge of the imaging model of a sensor or epi-polar geometry, this approach has produced good quality DEMs, [Day and Muller, 1989]. But, there are still some disadvantages including the need of manually selected seed points and significant texture within the image, for example, discontinuities of image textures may stop the region growing process. Nonetheless, this correlation method considers radiometric and geometric differences between the conjugate images without regard to specific imaging geometry hence it can be useful for SAR image correlation.

The remaining question is to know the way to automatically generate enough seed points used for initiating the region-growing harness. Feature detectors have been suggested to produce the seed points required, but features are always not well defined in a SAR image pair. This is due to speckle and difference in radar illumination as mentioned before. It is suggested that the seed points can be generated automatically in a dense grid form or in a random distribution together with a hierarchical structure for image correlation that can be robust to speckle at the reduced image tiers, [Denos, 1992]. Due to the uncertainty of random distribution, a grid form that will be easy to be

controlled is preferred. Thus, a better way to carry out SAR image correlation seems to be a pyramidal correlation scheme employing the least-squares method with a region-growing harness, [Dowman *et al.*, 1992]. The structure of an image pyramid and the way to generate seed points of the top image tier are determined by some parameters, such as the number of image tiers, the number of seeding grids and the uncertainty radius for predicting the locations of the generated seed points. The pyramidal correlation harness has been used to carry out stereo correlation for SIR-B SAR image pairs, but the parameters for the configurations of an image pyramid are determined according to experience, [Denos, 1992].

In order to generate a DEM from ERS-1 SAR data, Twu [1996] tested some of the parameters used in the pyramidal correlation scheme which can affect the results, such as the number of tiers and that of seeding grids. These parameters were selected based upon a trial-and-error method. There is no definite relationship established between the parallaxes in SAR images and the number of tiers used, as demonstrated by Quam [1984]. The results derived from image correlation particularly show that unpredictable blunders are liable to occur using arbitrarily selected parameters. It is probably because there is no rigid rule established to determine the best combination of parameters for pyramidal correlation scheme so that a healthy parallax data set cannot be obtained.

2.4.5 Comments on the Current SAR Image Correlation Methods

An area-based image correlation method may provide an abundance of successfully correlated samples from an image pair, which allows a DEM to be generated. The normalized cross-correlation measure is less suitable for radar data, since it does not take into account the geometric distortions between two images. The least squares correlation method that considers both geometric and radiometric differences in conjunction with a hierarchical structure seems the better choice for radar image correlation. A hierarchical image structure helps with suppressing noise signals in the reduced image hence SAR image correlation can be robust to speckle.

There remain other questions that how many tiers in an image pyramid will be appropriate and how many seed points will be enough for initiating the SAR image correlation scheme. It means that the consideration of the pyramid geometry is essential to give adequate parameters, which can be employed for the pyramidal correlation scheme. The rule for selecting the optimized parameters has to be developed, and the

connection between different parameters needs to be established. It is essential to preserve major terrain features in the parallax data set and allows the parallaxes to be converted into a good quality DEM with minimal blunders from false correlation. The optimized strategy required for selecting parameter in the pyramidal correlation scheme is proposed in Chapter 4. This is based on the analysis of the pyramid geometry and of the relationship between the parallaxes of an image pair and the reduced image tiers leading to the generation of a good quality DEM.

An appropriate SAR image correlation method helps with creating DEMs automatically, but providing ground control is also an important factor in digital radargrammetry. Automation is necessary to minimize the dependence on human operations, because the quality of measurement made by human operators from maps or images may not be stable. Also, the radar illumination of the same object in different images of a pair can be quite different, and the shape of the object in images can also be dissimilar to its counterpart observed on maps. Thus, an automatic way of finding GCPs for radargrammetry is considered, as presented in Chapter 5.

2.5 Providing Ground Control

If header/orbit data of relatively good quality is available, such as ERS-1/-2 data, the SAR image geometry can be determined independent of GCPs, [Chen and Dowman, 1996]. When accurate orbit data is not available, providing control is the only way to relate the results derived from the radar image to object space. Thus, the quality of ground control is one of the key factors affecting the resultant accuracy of the spatial information derived in radargrammetry. The traditional method for providing control is by means of measuring image and map co-ordinates manually. However, the performance of human operations is not always stable hence the quality of the derived GCPs may vary. On the other hand, the visual SAR image-map correlation can be difficult due to the characteristics of radar illumination and speckle in SAR images, as mentioned in Section 2.4.3. This leads to other methods, such as image simulation for providing control, being developed to cope with this problem. The following sections will give estimations of the precision of the manually selected GCPs according to different map scales and review the development of SAR image simulation methods.

2.5.1 Manually Collected GCPs

In general, a linear feature presented on a map is not always clearly shown in the corresponding SAR image due to speckle and varying radar illumination. The SAR image resolution is another important factor, which also contributes difficulties in finding good quality GCPs. For example, a good quality GCP collected using field surveying, such as Global Positioning System (GPS), may be not always identifiable in a SAR image. Using a corner reflector would be the most accurate way to provide control, but many human operations are required. Experiences from collecting GCPs show that the accuracy of the manually measured GCPs is not only limited by the resolution of a SAR image and the illumination of individual features appearing in that SAR image, but also dependent upon the scale of the map used.

For example, a 1:25,000 scale map produced by the French *Institut Geographique National* (IGN), [IGN, 1989], provides a set of GCPs with accuracy about 25m in plan and 10m in height, due to errors from measurements. The figures quoted are the resultant errors of observations made for collecting GCPs, instead of the original mapping accuracy. It is assumed that the measuring error of a selected GCP on the map sheet is about 0.5mm accuracy in plan that equals ±12.5m on the ground, excluding the errors from procedures of surveying/photogrammetry, cartographic generalization, lithography and map sheet distortion (stretch and shrinkage) *etc.* One ground-range pixel size of a standard space-borne SAR image is given nominally as 12.5m, [CSA, 1995], which is estimated as the location uncertainty of ground objects identified in SAR images. Both errors caused by measuring the map and image co-ordinates contribute independently to the subtotal of the measuring error in plan as ±18m.

The vertical deviation of a measured GCP (or a ground object) is estimated as one contour interval, or ±5m, [IGN, 1989]. The unknown height of the measured object is assumed as ±5m (a building or road/rail junction can be above the measured ground, but river/lake bank is probably below the measured surface). Then the subtotal of the measuring error in elevation is estimated as ±7m. This leads to a resultant error magnitude of 26m in 3D, as shown in Table 2.6. Those errors calculated from different mapping scales, such as 1:50000 scale maps, [IGN, 1992], and 1:100000 scale maps, [IGN, 1993], are also listed in Table 2.6. The measuring error of GCPs does not necessarily reflect the mapping accuracy, since it comes from the visual map-image correlation error made by a human operator as well as from the limitation of the image

resolution. Notice that the precision of measurement for GCPs is also not certainly leading to the positional accuracy of the same order using a radargrammetric model (see Section 2.3 and Chapter 3 and 5). Due to the difficulties of the traditional method of providing control, an alternative method has to be considered.

IGN Map Scale	1: 100,000	1: 50,000	1: 25,000
Measuring error on Map ΔM (m)	50	25	12.5
SAR image pixel size ΔI (m)	12.5		
Error in plan (m): ΔE, or $\Delta N = \sqrt[2]{(\Delta M^2 + \Delta I^2)}$	52	28	18
Contour interval Δh (m)	40	20	5
Measured object height deviation Δi (m)	(5)		
Error in height (m): $\Delta H = \sqrt[2]{(\Delta h^2 + \Delta i^2)}$	40	21	7
Total error (m): $\sqrt[2]{(\Delta E^2 + \Delta N^2 + \Delta H^2)}$	84	45	26

Table 2.6 Resultant error magnitude of the GCPs (the measured objects) estimated.

If there is a known DEM chip available, it can be useful to see the distortion of spatial (elevation) data in the image resulting from simulation using that radar imaging geometry. Information available from the simulated image will be the similar features (layover pattern) in the real SAR image corresponding to that DEM chip. If the features in the real and simulated image chips are distinctive compared with the surrounding area, then real-simulated image correlation may be possible. This approach can help with providing control. However, the terrain relief within the DEM chip selected for simulation must be significant, so that the spatial features in the simulated SAR image can be used for correlation.

2.5.2 SAR Simulation

Radar image simulation can be used to improve interpretation of radar images and to extract valuable information, such as the determination of the optimal stereoscopic configuration and the identification of the surface scattering due to different incidence angles. Thus, SAR simulation techniques not only provide useful knowledge for system design, but also for interdisciplinary studies. Smith *et al.* [1984] summarized SAR simulation methods as two categories including SAR system simulation and SAR product simulation. The former simulator attracts the attention of SAR system designers and microwave/electronic engineers for testing performance of different parameters and the algorithm used in a SAR system. The SAR system simulator can be very complicated and

will not be discussed further. The latter is dealing with the final intensity image product using a DEM to generate an accurate likeness of a SAR image, while preserving the image geometry that is interesting to the remote sensing and mapping community. The SAR image product simulator is relatively simple compared with the SAR system simulator.

In general, a SAR image simulator requires a SAR geometric model, a reflectivity model of the sensed area and a DEM. A SAR geometric model is used to describe the relationship between the sensor and the illuminated terrain (represented by a DEM) giving the incidence angles required by a SAR product simulator. The state vectors of the platform, including the velocity and position vectors in respect to the corresponding azimuth time series, are the basic parameters for a space-borne SAR geometric model. The state vectors of the platform give the orbit description and the geometric relationship between the sensor and the sensed area in a geocentric Cartesian co-ordinate system (see Chapter 5). Various simplified SAR geometric models can be derived either assuming a flat earth surface, or giving a simple orbit description, such as a line segment or a circular curve.

The reflectivity model of the sensed area is used to indicate the radar cross-section (RCS) parameter for each element of the sensed area with respect to the interaction between the transmitted electromagnetic energy and the illuminated DEM element, [Holtzman *et al.*, 1978]. The measure of RCS is strongly dependent on the aspect (incidence angle) of radar illumination, the material of the ground surface and the moisture or atmospheric conditions which can be quite complicated as a result, [Skolnik, 1981]. In order to make the SAR image product simulation convenient, the reflectivity model can be simplified and the assumption made that the terrain slope is the only factor deciding the magnitude of the reflected energy. Thus, the reflectivity model can only present the geometric characteristic of the sensed ground with no regard to other factors. In this sense, this simulation approach cannot be applied to a flat area where the terrain relief is not significant. The sensed DEM provides terrain slope between DEM elements that can be used to calculate the relative reflected energy based on the angle calculated between the range direction (or the nominal incidence-angle) and the normal of that local terrain slope. The cosine angle (in radian) measured with respect to the range direction is always used as the simplified reflectivity model as shown in Figure 2.2, more details see equation (5.17) in Chapter 5.

The SAR product simulation was initiated in the 1970s. Holtzman *et al.* [1978] proposed the Point Scattering Model to simulate the analogue processes of an air-borne imaging radar system. The key components used in this model include the operating parameters of the radar, a digital terrain model and a reflectivity model of the sensed DEM. This model is initially designed for studying the interaction between the scattered surface and the air borne radar system. Kaupp *et al.* [1982] then utilized a similar methodology to carry out SAR image simulation for the analogue imaging radar model and for analysis of effects from different incidence angles. This early work dealt with the general aspects of SAR simulation, but not with providing control in radargrammetry.

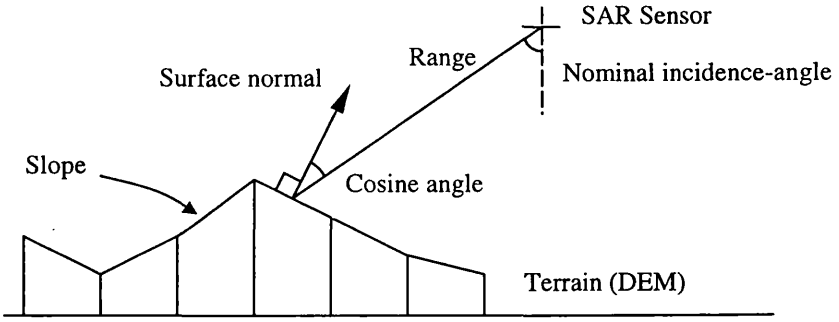

Figure 2.2 A simplified reflectivity model

2.5.3 SAR Image Simulation for Providing Control

The considerations of the simulation techniques used for terrain mapping primarily focus on the provision of ground control for geocoding. For instance, a simulation method proposed by Naraghi *et al.* [1983] has been employed to aid the interpretation and the derivation of tie points for SEASAT SAR image geocoding (see Section 2.6.1). The simulation algorithm has not been explained clearly, but manual identification of tie points for the real-simulated image pair is utilized. Another simplified imaging model was employed for SIR-B SAR image simulation based on a DEM, as presented by Domik *et al.* [1986]. The proposed simulation approach uses a DEM to predict the geometry and radiometry of a radar image based on terrain slope, assuming uniform back scattering from the surface cover. An approximate geometric model is used to relate the sensor and ground points. The simulated SAR image must be correlated manually with the real one to derive common features that are used as ground control for geometric rectification. These early methods depend on human operators to identify image features, instead of automatic correlation for the real-simulated image pair.

Another radar image simulation technique described by Kwok *et al.* [1990] has been used for registering a patch of simulated image to the corresponding real image to provide control for mosaicking SEASAT SAR images. Image correlation between the real image and the simulated counterpart is carried out automatically using the normalized cross-correlation measure. The simulated SAR image was produced using the imaging geometry of the sensor, a DEM and a simplified back-scattering model. The way to establish the relationship between every DEM cell and each pixel in the simulated image has not been clearly explained. The simulation method has not been evaluated specifically for positional accuracy, but the registration errors due to correlation technique ranges from two to four pixels. If the geocoding error is considered, the overall accuracy may degrade, according to Kwok *et al.* [1990].

The approximate method proposed by Arai [1991] for simulation of a SAR image and for the acquisition of GCPs is applicable within a small area under the assumption of knowing the fixed heading angle of a SAR sensor and the local difference of the neighboring elevation data points. Wivell *et al.* [1992] assumed a circular orbit for the SEASAT satellite to simulate a sub-image using a terrain model for providing control in SAR image geocoding. The misalignment in range and azimuth between the simulated and real images are determined through a cross-correlation measure and are used to locate each cell of the geocoded image. The incidence angle is referred to a simplified flat Earth. There is no report about the accuracy of the simulated image. The main concern of the work is to evaluate different terrain models for geocoding and terrain correction of SAR images. Geometric verifications of the geocoded SAR images show that the positioning error can be four times the resolution of SAR imagery at mountain peaks.

A PC-based SAR data acquisition planning tool (SARPLAN) developed by Guindon [1993] is based on a simulation method. A spherical Earth and a constant heading velocity and altitude of the SAR sensor are assumed in the simulation process. The incidence angle from the sensor to the ground points must be calculated in advance. The simulated image error is estimated to be 56.1m in range direction. Based on this simulator, Guindon [1995] then employed the Spearman rank correlation coefficient to match the real-simulated image pair and to provide ground control for ERS-1 image geocoding that demands manual refinement and editing operations. An affine transformation is also required to compensate the minor rotational errors of the simulated images due to 'ephemeris uncertainty'. More discussions of real-simulated image correlation are given in Chapter 5.

Recently, an object-space algorithm proposed by Gelautz *et al.* [1998] to produce simulated SAR images uses an iterative solution for transformation of DEM points to the corresponding co-ordinates of the simulated image, assuming that a start point for the simulated image is available. This approach employs a parametric mapping model using the range/Doppler equations and requires a DEM, a sensor flight path and manually derived parameters including the range and azimuth timing offsets for simulation. The simulation accuracy for check points is reported as less than 25m, if sufficiently accurate sensor parameters are available and manual refinement of SAR processing parameters is used. There are no results reported for the applications of the simulator using real-simulated SAR image correlation for automatic provision of ground control.

2.5.4 Comments on the Current Methods of Providing Control

The accuracy of the automatically provided ground control relies on the quality of the simulator as well as on the outcome derived from the real-simulated SAR image correlation. A poor quality simulated image may certainly lead to poor results of real-simulated image correlation. Previous work shows that most of the current SAR image simulators still require many human interventions. A good quality simulated image, in terms of geometric accuracy, with a higher level of automation is preferred for providing control. Also, the real-simulated SAR image correlation can only provide ground control by means of the offsets in terms of the image co-ordinates (lines and pixels) measured, instead of the exact location of a GCP. However, the accurate co-ordinates of a GCP are essential for systematic corrections of the results derived using space intersection for a SAR image pair.

The need to overcome the above problems inspired the development of a SAR image simulation technique in conjunction with the cross-correlation measure, as described in Chapter 5. The simulator is designed to provide GCPs by detecting four corner elements of a known DEM chip, according to the relationship between the DEM sensed and a SAR image geometry. The proposed method for providing GCPs gets rid of the errors from the manually selected GCPs leading to further refinements of the results derived from space intersection. The applications of the automatic provision of GCPs should not be confined to the DEM generated. After eliminating the systematic shifts and reducing the DEM 'noises' as described in Chapter 6, the generated DEM and the automatically derived GCPs can then be used for geocoding (see Chapter 7).

2.6 SAR Image Geocoding

Geocoding is the method of geometric rectification for a space-borne remotely sensed image, particularly the SAR imagery, according to a specific map projection in order that the terrain induced image distortions of the images can be eliminated. The geocoded SAR images provide further applications for various fields, such as image mosaic, geological analysis and multi-sensor data integration *etc.* In general, the geocoding operation needs a DEM in a map co-ordinate system to carry out the map-to-image transformation. Namely, each map pixel co-ordinate within the defined extent of the map grid is being transformed into image co-ordinates, calculating an intensity value for the image co-ordinates, and assigning it to the map pixel, [Laycock *et al.*, 1992]. Since the map pixels will not necessarily correspond to integer image sample co-ordinates, re-sampling is required to estimate intensity values at the requested positions.

The map-to-image transformation consists of a series of steps of co-ordinate transformation. The intermediate co-ordinates of each step include geographic co-ordinates (latitude and longitude), local Cartesian co-ordinates (local datum), global Cartesian co-ordinates (global datum) and specific geocentric (inertial) co-ordinates for the SAR data. In the course of the map-to-image transformation, tie points (GCPs) are required to compensate the inaccurate orbit data and range origin. Different methods have been proposed for geocoding process as briefly reviewed in the following section. An example of the geocoded image is shown in Figure 2.3 (right) together with the original RADARSAT SAR Standard Beam-1 ground-range intensity image (left).

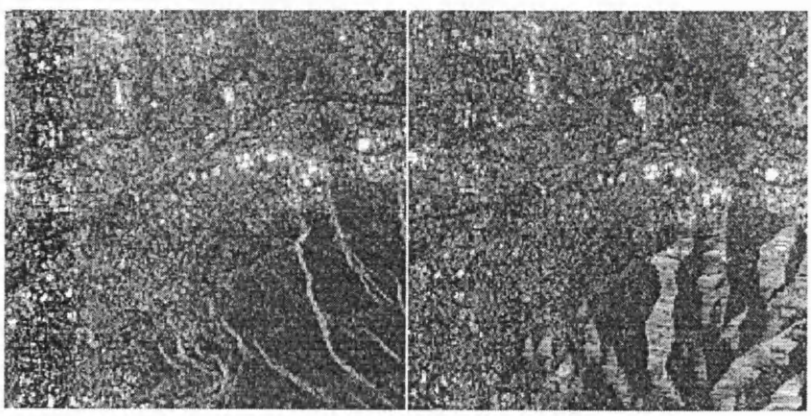

Figure 2.3 A sub-scene of RADARSAT SAR image (left) and the corresponding geocoded image (right). Size: 400 × 400 pixels or 5km × 5km.

The orientation and structure of the geocoded image has been changed from the original ground range image to French Lambert Conformal Conic Zone III projection system in conjunction with a DEM (see Figure 4.9). The distortions caused by terrain relief have been 'rectified', but information loss in the distorted area cannot be recovered. More details are given in Chapter 6 and 7.

2.6.1 Overview of SAR Geocoding

The early development of SAR geocoding algorithms is based on a polynomial approximation to relate ground and image points or on a simplified imaging model together with a DEM to remove distortions caused by terrain induced effects. For instance, Naraghi *et al.* [1983] utilized a DEM to rectify SEASAT SAR images employing a two-step process to perform rotation, scaling and de-skew removing distortions row-by-row. The basic scene geometry is assumed as a simple trigonometric identity relating the range, the horizontal distance from the nominal sensor nadir point to a terrain sample and the sensor height. A number of manually selected control points are required to carry out the transformation from slant range to SAR image co-ordinates. Similar work has been carried out for SIR-B data employing a polynomial fit function, as described by Domik *et al.* [1986].

An alternative approach proposed by Curlander *et al.* [1987] employs the Earth model, the Doppler and range equations in conjunction with orbit information for geo-coding SEASAT and SIR-B data. The three-pass algorithm, including along-track rectification, cross-track rectification and horizontal image shear transformation can be performed independently without operator interaction or using tie-points to provide control, if accurate range timing data and reliable state vectors of the platform available. Since there is no DEM being incorporated to the geo-coding procedures, the SAR image is resampled according to a specified map projection system hence the derived product is not a standard geocoded image.

Kwok *et al.* [1987] reported that geocoding a SAR image can be carried out efficiently using orbit information and a DEM without using simulation methods to provide control. The approach is modified from the previous three-pass algorithm developed by Curlander *et al.* [1987] and requires two or three tie points to compensate the errors from the platform state vectors. The positional accuracy of the geocoded image

is about several pixels of the SEASAT SAR imagery. Kwok *et al.*, [1990] adopted a simulation technique to provide control, instead of the manually selected tie points, for SAR image geocoding and for producing image mosaics. Registration errors are expected to be about two to four pixels. The product derived is a standard geocoded image.

Dowman *et al.* [1993] employed a map-to-image transformation based on the range/Doppler equations and the zero-Doppler assumption for the ERS-1 SAR image geocoding. The details of the range/Doppler equations are given in Chapter 3. A super-grid structure, which is a set of equal size three-dimensional orthogonal blocks partitioning the map space and spanning the terrain height extent, is used to improve the computation efficiency through a polynomial fit to perform the map-to-image transformation. Manually selected tie points are employed to check the fit of the image to the tie points and to apply the correction required. The residuals of the tie points, in terms of standard deviation, are reported as 1.3 pixels in range and 1.5 pixels in azimuth direction, [Laycock *et al.*, 1992].

Another algorithm for geocoding is the backward transformation as adopted by German SAR Processing and Archiving Facility (G-PAF) for producing ERS-1 SAR geocoded products, [Schreier *et al.*, 1993] and [Meier *et al.*, 1993]. Each back-scattered element has to be converted from map co-ordinates into slant-range image co-ordinates corresponding to the satellite datum using the range-Doppler approach. The range-Doppler approach can be performed only for an anchor point grid constructed by regularly spaced DEM elements to reduce the computational load. All of the other DEM elements are then transformed into image co-ordinates by an efficient bilinear interpolation according to the previously derived anchor point grid. Automatic derivation of tie points using a simulation method can also be employed, [Linder and Meuser, 1993], however, there is no detailed algorithm and evaluation given.

Rantakokko and Rosenholm [1999] proposed an algorithm for rectification of the slant range imagery through a direct image-to-ground relationship. This theoretical model formulates the SAR image-to-ground relationship based on a set of simplified orbital parameters, such as the orbit inclination, the right ascension of the ascending node, the time at the ascending node and the orbital radius. The use of GCPs, in terms of latitude, longitude and height, and of a least squares solution for the direct approach is essential. The methodology proposed has not been implemented and evaluated.

2.6.2 Geocoding Using the Generated DEM

The accuracy of a geocoded SAR image will be affected by the quality (resolution) of the generated DEM, [Wivell *et al.*, 1992] and [Saundercock, 1995], the performance of the geocoding algorithm employed and the ground control provided. Previous work on geocoding employs a map-to-image approach that saves computational time. But, it needs interpolation at the last stage to fill gaps between grid points that may risk degrading the geometric accuracy. Since traditional methods use the resultant co-ordinate offsets between the simulated and real images as ground control, a number of image chips may be required to increase redundant observations. The accuracy of the ground control provided tends to be limited by the resolution cell of the SAR image (about 25m for a standard SAR ground range image) that does not make full use of SAR simulation techniques.

It is proposed in Chapter 7 that a DEM generated from a stereo SAR image pair can be used in geocoding, hence the performance of the geocoding algorithm must be considered in the first place. The proposed simulator in the thesis detects the corner points of a known DEM chip, and guarantees that the accuracy of the derived GCPs is at sub-pixel level. In order to make full use of the automatically derived GCPs, as described in Chapter 5, and to achieve high quality results, a geocoding algorithm compatible with the automatically derived GCPs has been developed. Hence the outcome of geocoding using the generated DEM, as described in Chapter 6, can be evaluated correctly as presented in Chapter 7. The accuracy evaluation of the geocoded images derived may verify the proposals of the algorithms described in the thesis.

2.7 Summary

SAR data can be an important alternative tool to optical data for extracting spatial information. However, the algorithms employed must be robust to external conditions, such as physical and geometric limitations, and be stable when the errors of observations are significant. The rigorous stereo method must be revised to be adaptive when inferior orbit data is used. The geometric model has to be verified by an appropriate error analysis. Automatic image correlation for SAR data must consider the use of a hierarchical structure and of the least squares correlation method with a region-growing approach. The image pyramid can be defined using the parameters predicted by an

optimized strategy to avoid a trial-and-error approach. Further steps of automation for terrain mapping are possible by using a simulation technique for provision of ground control when a known DEM chip is available. The SAR image simulator must fit the physical reality of the imaging geometry and be able to provide accurate ground control for terrain mapping with minimal human intervention. The geocoded images produced will be used to show the applications of the stereo SAR generated DEMs and of the automatically derived GCPs to verify the proposals in the thesis.

Chapter 3

A Rigorous Solution for Space Intersection

3.1 Introduction

An ideal geometric model for extracting spatial information from a Synthetic Aperture Radar (SAR) image pair is expected to obtain high quality results, to require a minimal number of Ground Control Points (GCPs) and human interventions, and to be justified by an error model. To obtain good quality results, the geometric model has to meet the physical reality connecting SAR image and object space and to use appropriate ground control for accurate positioning. An appropriate error model is essential to predict the errors of the outcome and to show the robustness of the algorithm employed that reflects the precision the algorithm can achieve. Since it can be difficult to identify tie points or GCPs from images and maps, as explained in Section 2.5, the reduction of the number of GCPs/tie points required in radargrammetry is considered in this chapter.

This proposal is opposed to the currently available methods, such as Leberl *et al.* [1986], Raggam and Gutjahr [1998] and Singh *et al.* [1998]. These previously developed methods employ GCPs for determining the radargrammetric model. The proposed method described in this chapter will show that it avoids many human interventions required by other algorithms, such as Sylvander *et al.* [1998] and Toutin [1999]. The error model of image pixel observations developed in this chapter, as shown later, will help with understanding the observation errors in stereo radargrammetry.

A rigorous approach for carrying out space intersection using a least squares adjustment is described in Section 3.2. The approach primarily utilizes two Doppler equations and two range equations to calculate the position of a ground point with equal weights assigned to each observation based on the zero-Doppler assumption. However, accurate orbit information is not always provided by space-borne SAR data and there may exist range/azimuth timing errors in the orbit data. Therefore, a weighting matrix is proposed in Section 3.3 to improve the least squares solution based on the considerations of different effects coming from the range/azimuth timing errors. A new error model is

then proposed based on the weighting concept according to the revised geometric model, as presented in Section 3.4. In Section 3.5, the practical implementation of the proposed geometric model is outlined. The test results for RADARSAT data and the relevant analysis of the proposed algorithms are demonstrated in Section 3.6 to validate the proposal in this chapter.

3.2 Rigorous Stereo Intersection

The azimuth lines and range pixels form the orthogonal co-ordinate system of a SAR image. The azimuth time data provided by image header file gives the state vectors of a sensor for that azimuth line, and the slant range time or the equivalent parameters define the distance between the sensor and a ground point. Thus, two basic equations for each orbit can be treated as the observation equations in radargrammetry, according to Clark [1991] and Dowman [1992]:

Doppler equation
$$f_{DC} = \frac{2(\mathbf{V_S} - \mathbf{V_P}) \bullet (\mathbf{S} - \mathbf{P})}{\lambda |\mathbf{S} - \mathbf{P}|} \tag{3.1}$$

Range equation
$$|\mathbf{R}| = |\mathbf{S} - \mathbf{P}|. \tag{3.2}$$

f_{DC} is the Doppler central frequency observed; λ the given wavelength; $\mathbf{V_S}$ and $\mathbf{V_P}$ the velocity vector of a sensor and a ground point, respectively; $\mathbf{S}$ and $\mathbf{P}$ the position vector of the sensor and the ground point, respectively; and $|\mathbf{R}|$ the given range between the sensor and the ground point. Generally, header information provides data for $\mathbf{V_S}$ and $\mathbf{S}$, according to the azimuth line observed. Also, a range pixel observation gives a range value $|\mathbf{R}|$ according to the header data provided, [CSA, 1995]. These two equations give a Doppler cone in space with a range circle in respect to the centre corresponding to the sensor in space as will be shown later in Figure 3.1. Equation (3.1) then gives

$$f_{DC} = \left(\frac{2|\mathbf{V_S} - \mathbf{V_P}|}{\lambda} \right) \cdot \left(\frac{(\mathbf{V_S} - \mathbf{V_P}) \bullet (\mathbf{S} - \mathbf{P})}{|\mathbf{V_S} - \mathbf{V_P}| \cdot |\mathbf{S} - \mathbf{P}|} \right) = \left(\frac{2|\mathbf{V_S} - \mathbf{V_P}|}{\lambda} \right) \cdot \sin\tau. \tag{3.3}$$

τ is the deflected angle between the surface of a Doppler cone and the normal plane, which is perpendicular to the velocity vector as shown later in Figure 3.1. When a zero-

Doppler image is obtained or there is no azimuth time error, $\tau = 0$ and the resultant velocity vector ($\mathbf{V_S} - \mathbf{V_P}$) is exactly perpendicular to the resultant range vector ($\mathbf{S} - \mathbf{P}$), or $f_{DC} = 0$.

According to a least squares adjustment of indirect observations, the problem of space intersection can be solved for an unknown ground point $\mathbf{P}(x, y, z)$ from the azimuth line and range pixel observations using equation (3.1) and (3.2) derived from two same-side orbits which give four non-linear observation equations. These four equations used to solve an unknown ground point (three unknown parameters of a ground position vector) leads to the need of a least-squares adjustment. The four non-linear equations have to be linearized following the procedures of a least squares adjustment to give a normal equation as

$$F_1 = \frac{2(\mathbf{V_{S1}} - \mathbf{V_P}) \bullet (\mathbf{S_1} - \mathbf{P})}{\lambda |\mathbf{S_1} - \mathbf{P}|} - f_{DC} \equiv 0 \tag{3.4a}$$

$$F_2 = |\mathbf{S_1} - \mathbf{P}| - R_1 \equiv 0 \tag{3.4b}$$

$$F_3 = \frac{2(\mathbf{V_{S2}} - \mathbf{V_P}) \bullet (\mathbf{S_2} - \mathbf{P})}{\lambda |\mathbf{S_2} - \mathbf{P}|} - f_{DC} \equiv 0 \tag{3.5a}$$

$$F_4 = |\mathbf{S_2} - \mathbf{P}| - R_2 \equiv 0 \tag{3.5b}$$

$$\begin{aligned} &\Rightarrow \underset{4\times1}{[\mathbf{v}]} + \underset{4\times3}{[\mathbf{A}]}\underset{3\times1}{[\Delta\mathbf{X}]} = \underset{4\times1}{[\mathbf{B}]}; \qquad \sum_{i=1}^{4} \upsilon_i^2 w_{ii} \rightarrow \min; \\ &\Rightarrow \underset{3\times4}{[\mathbf{A}]^{\mathrm{T}}}\underset{4\times4}{[\mathbf{W}]}\underset{4\times3}{[\mathbf{A}]}\underset{3\times1}{[\Delta\mathbf{X}]} = \underset{3\times4}{[\mathbf{A}]^{\mathrm{T}}}\underset{4\times4}{[\mathbf{W}]}\underset{4\times1}{[\mathbf{B}]}; \\ &\Rightarrow \underset{3\times1}{[\mathbf{X}]} = \underset{3\times1}{[\Delta\mathbf{X}]} + \underset{3\times1}{[\mathbf{X_o}]} \end{aligned} \tag{3.6}$$

$$\underset{4\times3}{[\mathbf{A}]} = \begin{bmatrix} \frac{\partial F_1}{\partial x} & \frac{\partial F_1}{\partial y} & \frac{\partial F_1}{\partial z} \\ \frac{\partial F_2}{\partial x} & \frac{\partial F_2}{\partial y} & \frac{\partial F_2}{\partial z} \\ \frac{\partial F_3}{\partial x} & \frac{\partial F_3}{\partial y} & \frac{\partial F_3}{\partial z} \\ \frac{\partial F_4}{\partial x} & \frac{\partial F_4}{\partial y} & \frac{\partial F_4}{\partial z} \end{bmatrix}; \underset{4\times1}{[\mathbf{B}]} = \begin{bmatrix} F_1^0 \\ F_2^0 \\ F_3^0 \\ F_4^0 \end{bmatrix}; \underset{4\times4}{[\mathbf{W}]} = \begin{bmatrix} w_{1,1} & 0 & 0 & 0 \\ 0 & w_{2,2} & 0 & 0 \\ 0 & 0 & w_{3,3} & 0 \\ 0 & 0 & 0 & w_{4,4} \end{bmatrix}.$$

$\mathbf{V_P}$ the velocity vector of a ground point $\mathbf{P}$ (or Earth rotation) can be calculated according to the provisional location of the unknown $\mathbf{P}$ as given in Clark [1991]. The other parameters, except $\mathbf{P}$, can be collected from header information, [CSA, 1995]. Equation

(3.4a) ~ (3.5b) are four observation equations and $[\mathbf{v}]=[v_1, v_2, v_3, v_4]^T$ is the residual matrix of the linearized observation equations in equation (3.6). Matrix **[A]** denotes the coefficient matrix of the partial derivatives of the linearized observation equations with respect to the three unknowns of the ground point **P**, or $[\mathbf{X}]=[X, Y, Z]^T$. The increment matrix $[\Delta\mathbf{X}]=[\Delta X, \Delta Y, \Delta Z]^T$ is used to update the unknown **[X]** after each iterative solution, until it meets the criterion of the assigned convergent threshold, say 1×10^{-8}. Matrix $[\mathbf{X}_o] = [X_o, Y_o, Z_o]^T$ gives the initial location of the ground point, which can be given by the SAR scene centre for the first ground point to be solved, and the solved point will be treated as the initial location for the next point and so on. Matrix **[B]** denotes the provisional function values of F_1, F_2, F_3 and F_4 in equation (3.4a) ~ (3.5b) derived using the provisional value of unknown **[X]**. Matrix **[W]** denotes a weighting matrix, which is given as an identity matrix for a non-weighted least squares adjustment, and w_{ii} (i = 1, 2, 3 and 4) denotes the diagonal elements of **[W]**. Each element of the matrix **[A]** and **[B]** is given in Clark [1991]. Following the standard procedures of the least squares adjustment, the position vector of a ground point can be derived based on a non-weighted least squares solution, [Chen and Dowman, 1996].

If a SAR image and the header information give a definite geometry for range pixels as well as azimuth lines, then the relationships between the image lines or between the range pixels are relatively stationary. It means that the azimuth time of any azimuth line or the range value of any range pixel of that image can be retrieved precisely, or the image geometry can be restored simply using header information. This reduces the need of GCPs dramatically. Experience with ERS-1 data indicates that space intersection without using GCPs can be carried out, provided that the ephemeris data given is accurate, and the azimuth time errors are tolerable, [Chen and Dowman, 1996].

Any attempts to refine the relationship between image lines and between pixels needs a great number of GCPs with a dense and appropriate spatial distribution that is generally impractical. In addition, the quality of the provided GCPs is not always reliable due to speckle and poor illumination of features in SAR images, the limitations of mapping accuracy and human observation errors, as described in Section 2.5.1. Therefore, it seems that using poor quality GCPs to set up a geometric model causes more problems than if no GCPs are used in that geometric model. An attempt has been made here to avoid any involvement of GCPs in the proposed geometric model and to use the minimal number of GCPs for final correction of systematic shifts only. In doing so, the GCPs have

to be treated as unknown points and to be solved without using any other GCPs or tie points. The co-ordinates of GCPs derived are compared with the real co-ordinates to obtain the overall shifts in 3-D space giving ground control, provided that the image geometry is well defined and the resultant range vector (**S** - **P**) is perpendicular to the resultant velocity vector ($\mathbf{V_S} - \mathbf{V_P}$). It is opposed to the traditional methods that employ GCPs to reconstruct the image geometry, [Leberl *et al.*, 1986] and [Singh *et al.*, 1998].

The relative geometric distortion of RADARSAT SAR data in terms of the positional error of an image pixel is expected approximately as 30m [Denyer *et al.*, 1993]. Also, the Processed Data Record in RADARSAT image header file gives the zero-Doppler time of each image azimuth line with precision of 0.001sec and the Detailed Processing Parameters Record defines the ground-range-to-slant-range transformation parameters with precision of the order of metres. It gives a relatively definite description of the SAR image geometry hence using a least squares solution without GCPs may be possible. But, according to CSA [1995], the nominal along-track orbit position error provided by RADARSAT image header data (Data Quality Summary Record) is given as 600m and the across-track error 40m. Without accurate orbit information the perpendicular relationship between the resultant velocity vector ($\mathbf{V_S} - \mathbf{V_P}$) and the resultant range vector (**S** - **P**) remains uncertain, or $f_{DC} \neq 0$. A problem arises that the along-track orbit error is a significant 'systematic error', which has to be eliminated before using a least squares adjustment for solving ground points, but, the quality of GCPs is not necessarily good enough for doing so.

According to Gauss [1823], the distinction between the random error and the systematic (constant) error is to some extent relative and depends on how broadly the notion of observations of the same class is being taken. Gauss [1823] indicates:

> *"For example, consider irregularities in the graduations of an instrument for measuring angles. If we need to measure a given angle again and again, then the irregularities produce constant errors, since the same defective graduation is used repeatedly. On the other hand, the same errors can be regarded as random when one is measuring unknown angles of arbitrary magnitude, since there is no table of errors in the individual graduations."*

Stereoscopic space intersection needs observations of a pair of homologous points whose azimuth time and range are observed only once for each image point. In analogy to the example illustrated by Gauss [1823], the azimuth lines and range pixels of individual points (comparing to angle observations) have not been observed repeatedly. There is no

table of the azimuth timing errors in the individual azimuth lines (comparing to the graduation irregularities of an instrument for measuring angle). Also, when the observation errors have a constant part, that constant can be approximated by the arithmetic mean of the errors, according to Gauss [1823]. Therefore, the errors of the azimuth timing observations (including timing 'shifts') of individual azimuth lines are firstly treated as random errors, and the constant errors will be corrected after space intersection. So, a different consideration for the least squares solution is proposed in next section in order to make the least squares solution without using any GCPs possible.

3.3 Formation of a Weighting Matrix

If the resultant velocity vector is not perpendicular to the resultant range vector, and since the axes of the azimuth and range components in the SAR image co-ordinate system remain orthogonal, then the deflected range vector does not correspond to the nominal range vector (azimuth line) of that image. This is clearly shown in Figure 3.1(a). The range direction deflected by an azimuth time error ΔS (converted to distance) produces a deviation ΔP in along-track direction of the ground position in respect to the image co-ordinate system, as demonstrated in Figure 3.1 (b) and gives

$$\begin{aligned}
&\textbf{if } \Delta S << R \textbf{ and } R \approx R', \textbf{ then } \Delta S \approx |\mathbf{R}'| \cdot \sin(\tau) \approx \Delta P; \\
&\Delta S \approx R \cdot \frac{\lambda \cdot f_{DC}}{2|\mathbf{V_S} - \mathbf{V_P}|} \quad \Rightarrow f_{DC} \approx \frac{2|\mathbf{V_S} - \mathbf{V_P}| \cdot \Delta S}{\lambda \cdot R} \\
&\sigma_f = f_{DC} - f_{DC}^{(0)} = f_{DC} \approx \frac{2|\mathbf{V_S} - \mathbf{V_P}| \cdot \Delta S}{\lambda \cdot R}, \quad \textbf{if } f_{DC}^{(0)} = 0
\end{aligned} \tag{3.7}$$

Recall equation (3.3). σ_f is the precision of prior estimation for f_{DC} observation. $f^{(0)}_{DC}$ is the nominal zero Doppler frequency given by image header data (for a RADARSAT SAR Standard image). R' is the deflected range magnitude, which is approximately the same as R when it is relatively large, say 880,000m for a RADARSAT SAR image, compared with ΔS, say 600m, the nominal along-track orbit error, according to CSA [1995].

Consider equation (3.3) and the difference between the range and the Doppler equations. Let the magnitude of the resultant velocity vector ($\mathbf{V_S} - \mathbf{V_P}$) be 8000m/s and the wavelength 0.05656m (C band), and assume only one unit of non-zero f_{DC} (sec^{-1}) error, equation (3.3) gives the angle $\tau = 3.594 \times 10^{-6}$ (in radian) or 0.73″. Equation (3.7)

gives 3.3m error of ΔS corresponding to one unit of f_{DC} (sec^{-1}) error. Apparently, ΔS increases in proportion to the magnitude of f_{DC}. But, the f_{DC} error is set as zero in the least squares resolution, under the zero-Doppler assumption, which causes a relatively large residual for the Doppler equation. If the same weights were given to the Doppler and range equations in the least squares adjustment, a small error of angle τ could be magnified to produce a significant residual in (3.4a) and (3.5a), under the circumstances of a relatively large range magnitude of space-borne SAR images. A suitable weighting matrix is then considered to suppress such possible effects in the least-squares adjustment.

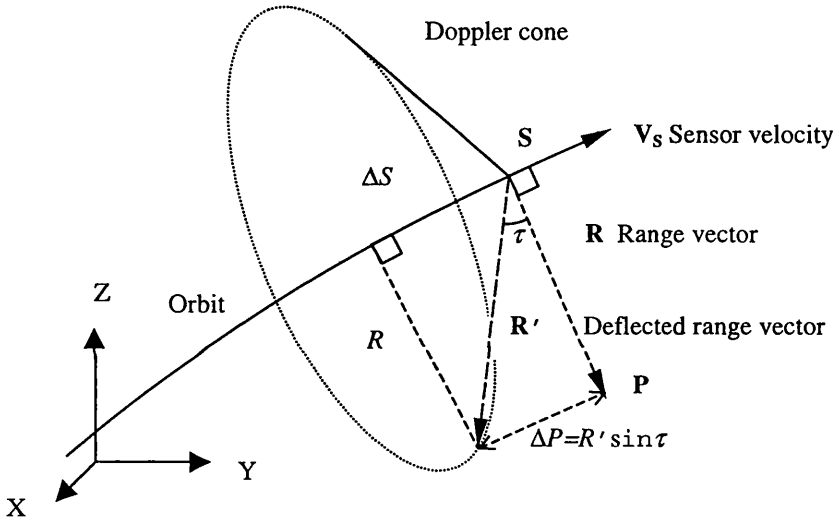

Figure 3.1 (a) A Doppler cone and the deflected angle τ.

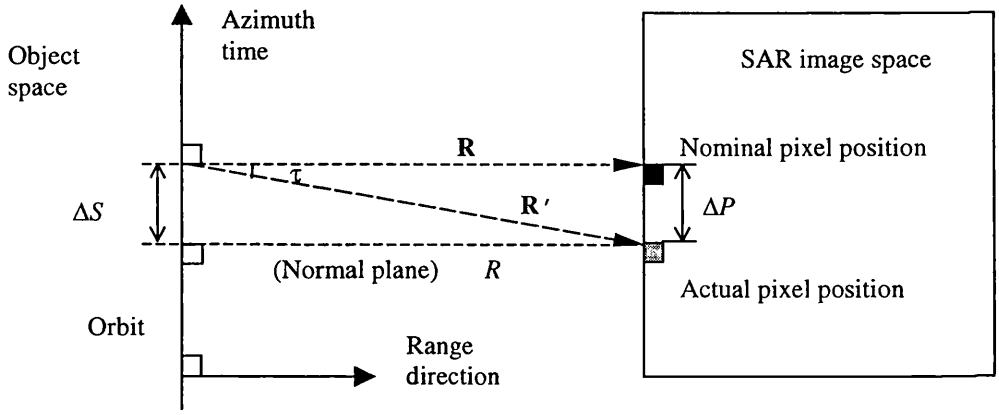

Figure 3.1 (b) A 2-D view of SAR image geometry.

The condition is that the effects from azimuth time error are expected to be minimal, since observations are made in respect to an orthogonal SAR image co-ordinate system. If the along-track orbit error is given as ΔS = 600m, [CSA, 1995], the velocity magnitude 7460m/s, R_1 = 880km for a high-incidence-angle (left) image and λ = 0.05656m, then, the precision of prior estimation for the f_{DC} observation of the left image σ_{f1} can be determined as 180sec^{-1}, according to equation (3.7). If R_2 is given as 1100km for a low-incidence-angle (right) image, σ_{f2}, the precision of prior estimation for the f_{DC} observation of the right image, is given as 144sec^{-1}. According to Gauss [1823], Mikhail [1976], Cooper and Robson [1996], the weights are taken to be quantities proportional to the reciprocals of the square of precision (or the reciprocals of variance). Then, the weights for the Doppler equations can be given, according to the precision derived above, as

$$w_{1,1} = \sigma_{f1}^{-2} = 3.1\times10^{-5}; \qquad w_{3,3} = \sigma_{f2}^{-2} = 4.8\times10^{-5} \tag{3.8}$$

$w_{1,1}$ is the weight of the Doppler equation of a low-incidence-angle image, and $w_{3,3}$ that of a high-incidence-angle image. The difference between $w_{1,1}$ and $w_{3,3}$ is relatively insignificant. Let the precision of the slant range observation of each orbit be approximately the same as σ_r. For example, if σ_r is given as 5m, the weights of both range equations can be given as

$$w_{2,2} = \sigma_r^{-2} = 4.0\times10^{-2} \approx w_{4,4} \tag{3.9}$$

The other elements of the weight matrix are all zero since linearly independent observations are assumed. Hence the weighting matrix [W] of the normal equation in equation (3.6) is derived as

$$[\mathbf{W}]_{4\times4} = \begin{bmatrix} \sigma_{f1}^{-2} & 0 & 0 & 0 \\ 0 & \sigma_r^{-2} & 0 & 0 \\ 0 & 0 & \sigma_{f2}^{-2} & 0 \\ 0 & 0 & 0 & \sigma_r^{-2} \end{bmatrix} = \begin{bmatrix} 3\times10^{-5} & 0 & 0 & 0 \\ 0 & 0.04 & 0 & 0 \\ 0 & 0 & 5\times10^{-5} & 0 \\ 0 & 0 & 0 & 0.04 \end{bmatrix} \tag{3.10}$$

The location of a ground point decides the magnitude of the resultant velocity vector ($\mathbf{V_S} - \mathbf{V_P}$). The velocity magnitude of a ground point $\mathbf{V_P}$ is identical to that of the Earth rotation that changes according to the latitude of that ground point and gives

$$\begin{aligned} &|\mathbf{V_S}|-|\mathbf{V_P}| \le |\mathbf{V_S}-\mathbf{V_P}| \le |\mathbf{V_S}|+|\mathbf{V_P}| \\ &\Rightarrow \frac{1}{|\mathbf{V_S}|-|\mathbf{V_P}|} \ge \frac{1}{|\mathbf{V_S}-\mathbf{V_P}|} \ge \frac{1}{|\mathbf{V_S}|+|\mathbf{V_P}|} \\ &\Rightarrow \frac{0.5\lambda}{|\mathbf{V_S}|-|\mathbf{V_P}|} \ge \frac{0.5\lambda}{|\mathbf{V_S}-\mathbf{V_P}|} \ge \frac{0.5\lambda}{|\mathbf{V_S}|+|\mathbf{V_P}|} \end{aligned} \tag{3.11}$$

For example, if the resultant vector between sensor and ground velocity has achieved a maximal magnitude at low latitude, the elements of the weighting matrix are given as

$$\underset{4\times4}{[\mathbf{W}]} = \sigma_r^{-2}\begin{bmatrix} \left(\dfrac{0.5\lambda R_1\sigma_r}{(|\mathbf{V_{S1}}|+|\mathbf{V_P}|)\Delta S}\right)^2 & 0 & 0 & 0 \\ 0 & 1 & 0 & 0 \\ 0 & 0 & \left(\dfrac{0.5\lambda R_2\sigma_r}{(|\mathbf{V_{S2}}|+|\mathbf{V_P}|)\Delta S}\right)^2 & 0 \\ 0 & 0 & 0 & 1 \end{bmatrix} \tag{3.12}$$

Numerically, let $\lambda = 0.05656$m, $\sigma_r \approx 5$m (one slant range pixel of the RADARSAT SAR Standard image), the same sensor speed assumed for both orbits 7460m/sec and the Earth rotation speed at low latitude 400m/sec and the along-track error as 600m, the weighting matrix is derived and normalized as

$$\underset{4\times4}{[\mathbf{W}]} \approx \begin{bmatrix} 7\times10^{-4} & 0 & 0 & 0 \\ 0 & 1 & 0 & 0 \\ 0 & 0 & 1.1\times10^{-3} & 0 \\ 0 & 0 & 0 & 1 \end{bmatrix} \approx \begin{bmatrix} 1\times10^{-3} & 0 & 0 & 0 \\ 0 & 1 & 0 & 0 \\ 0 & 0 & 1\times10^{-3} & 0 \\ 0 & 0 & 0 & 1 \end{bmatrix}$$

Similarly, the magnitude of possible weights can be derived using equation (3.10) or (3.12) under different circumstances, according to sensor speed, latitude of test area and slant range pixel size, as summarized in Table 3.1. In practice, remote sensing satellites are always operating on nearly circular orbits and the journey of a space-borne

sensor within a SAR standard image scene is less than 15 seconds. To change the location of test site or the speed of the sensor on different orbits makes insignificant effects on the weights. Using the weighting matrix in the least squares solution for the geometric model generates errors in a different way and leads to the proposal of new error models.

Ground Latitude	Low	High	Middle	Middle	Middle
Along-track Orbit Error (m)	600	600	600	200	600
Earth Rotation (m/sec)	400	0	300	300	300
Left Sensor Speed (m/sec)	7560	7560	7500	7560	7560
Left Range (m)	880,000	880,000	880,000	880,000	880,000
Right Sensor Speed (m/sec)	7460	7460	7500	7460	7460
Right Range (m)	1,100,000	1,100,000	1,110,000	1,100,000	1,100,000
Slant Range Precision (m)	5	5	5	5	9
Weight $w_{1,1}$	6.8×10^{-4}	7.5×10^{-4}	7.1×10^{-4}	6.3×10^{-3}	2.3×10^{-3}
Weight $w_{2,2}\approx w_{4,4}$	1	1	1	1	1
Weight $w_{3,3}$	1.1×10^{-3}	1.2×10^{-3}	1.1×10^{-3}	1×10^{-2}	3.6×10^{-3}

Wavelength=0.05656m

Table 3.1 Weights derived under various conditions.

3.4 Error Models

In terms of terrain mapping, the observation errors of the image co-ordinates (automatic or manual correlation) may introduce random errors into the geometric model causing uncertainties in the radargrammetric results. Also, poor radargrammetric configurations may be sensitive to the observation errors. It is then useful to investigate the theoretical errors generated by the proposed rigorous algorithm that can show its robustness to observation errors under different circumstances. The rigorous stereo radargrammetric algorithm requires the co-ordinate observations of a SAR image pair, including range pixels and azimuth lines, which may behave differently. The following sub-sections deal with the error models in respect to the observations of range pixels and azimuth lines, independently, based on the assumption that linearly independent observations on each component (range, azimuth) of the SAR image co-ordinate system are made. After derivation of the error model, the resultant error magnitude will be calculated to evaluate the performance of the proposed geometric algorithm. The theoretical errors derived will be compared with the actual errors generated by real observations, as presented in Section 3.6.

3.4.1 Observation Errors from Range Pixels

As derived in Section 3.3, the weight of range observation is relatively large compared with that of Doppler observation as shown in equation (3.10), therefore, the range magnitude is nearly 'fixed'. It means that any error introduced to one range observation can hardly be shared (adjusted) by another range beam in the weighted least squares solution, because a relatively large weight has been given to each range observation. In the case when a non-weighted (equal-weighted) least squares adjustment is applied, the range observation can then be changed, according to Chen and Dowman [1996]. In this section, only the weighted least squares adjustment for the same side stereo radargrammetry will be considered.

The same-side stereo radargrammetric configuration is given in Figure 3.2. Assuming that one of the range beams is fixed, by introducing a certain range pixel measuring error, $|d\mathbf{R}|$, into the other range data from the expected intersecting point **P** to $\mathbf{P}_1$, an error vector ($\mathbf{E}_r = \mathbf{P}_2 - \mathbf{P}$) from **P** to $\mathbf{P}_2$ will be generated. The ground point $\mathbf{P}_2$ is the new intersecting point.

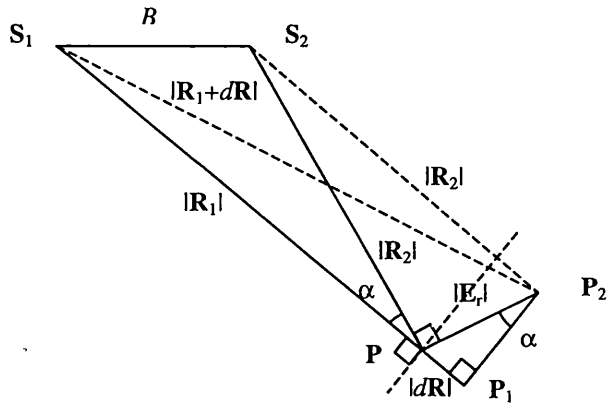

Figure 3.2 Range pixel observation error of two range beams of large weight.

If the intersection angle between two range beams is α, then the error vector length caused by the range observation error of a single range beam is approximately given by

$$|\mathbf{E}_r| = |\mathbf{P}_2 - \mathbf{P}| \approx \frac{dR}{\sin\alpha}; \qquad \alpha = \cos^{-1}\left(\frac{R_1^2 + R_2^2 - B^2}{2R_1R_2}\right) \tag{3.13}$$

if $dR << R_1$ **and** $dR << R_2$.

$\mathbf{E}_r$ is the error vector generated in 3-D space, R_1 and R_2 the actual range from each sensor to a ground point and B the base length between two sensors. The intersection angle α is calculated by applying the cosine rule. In practice, the measuring error of the range pixel dR has to be converted to physical distance. The error magnitude $|\mathbf{E}_r|$ of each range pixel observation is decided by the intersecting angle α of two range vectors based on the condition of 'fixed' range observations of each image, and given that a relatively large weight is assigned to range.

Consider the effects from the intersection angle due to various geometric configurations of space intersection, the scale factor ($1 / \sin\alpha$) of the range observation error increases with decreasing intersection angle, as shown in Figure 3.3. For example, with α=24° and the nominal resolution of a slant range pixel of a low-incidence-angle SAR image as 9.1m, $|\mathbf{E}_r|$ is approximately 22.4m. If the nominal resolution of a slant range pixel of a high-incidence-angle SAR image as 4.9m, $|\mathbf{E}_r|$ is approximately 12m. Obviously, the intersection angle has significant effects on the final results in particular a narrow intersection angle (say, less than 10°), which can magnify (6 times of) the range observation errors.

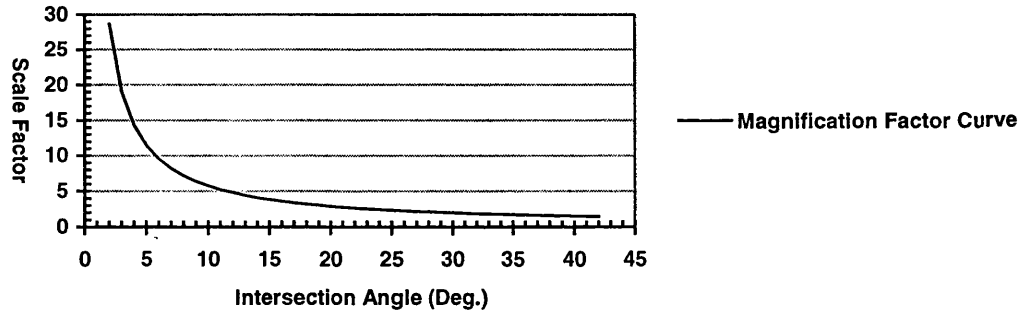

Figure 3.3 Magnification curve of the error caused by range pixel observations.

3.4.2 Observation Errors from Azimuth Lines

Space intersection for a ground point from a pair of SAR images is achieved by solving the intersecting point of the range circles of two distinctive orbits. A convergent angle θ is then formed by two intersecting range planes or each orbit as shown in Figure 3.4 and is determined by two velocity vectors of each range plane as

$$\cos\theta = \frac{\mathbf{V}_{S1} \bullet \mathbf{V}_{S2}}{|\mathbf{V}_{S1}| \cdot |\mathbf{V}_{S2}|} \tag{3.14}$$

Because the weight of range is relatively large, as shown in Equation (3.12), the ground point is solved mainly using the range observations. The greatest concern in space intersection is to find an intersecting point to satisfy a balance of range shifts between $\mathbf{R}_1$ and $\mathbf{R}_2$, the range vector from the right and left sensor, respectively, to the ground point, as shown in Figure 3.4.

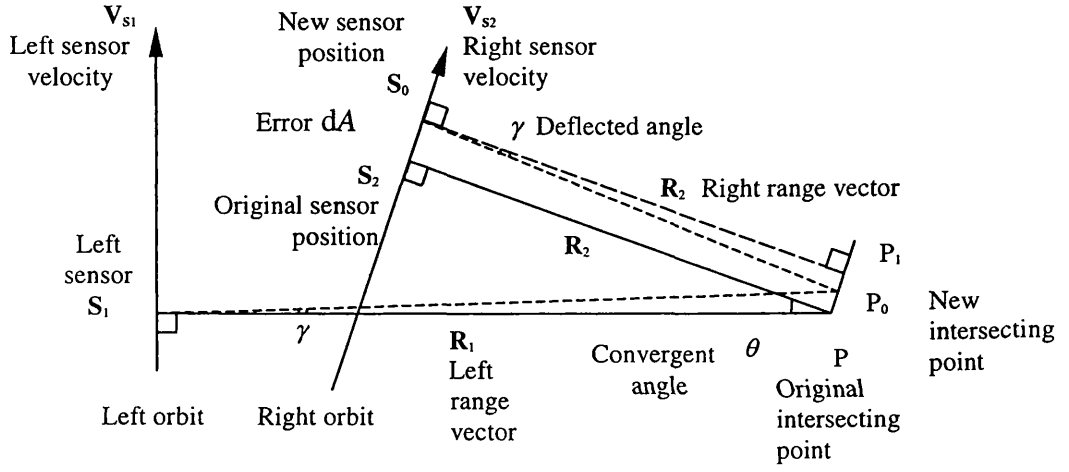

Figure 3.4 Swings of range beams in space intersection achieving a balance (top view of the two orbits).

Assume that similar weight is assigned to the Doppler observation of each orbit, the deviation of range distance caused by the deflected angle for each orbit tends to be the same value in the least squares adjustment. An intersecting point solved from space intersection must satisfy two conditions, i.e., a similar but relatively large weight for each range observation and a similar but relatively small weight for each Doppler observation. The range beam of each orbit can swing from one side to the other and intersect at the point where the range and the deflected angle of the range beam achieve a balance. Let a line from P to P_3 intersecting the range direction of $\mathbf{R}_2$ at P_3 and in parallel with the velocity vector $\mathbf{V}_{S1}$ in the case that a small observation error of azimuth line dA is incorporated, as shown in Figure 3.5.

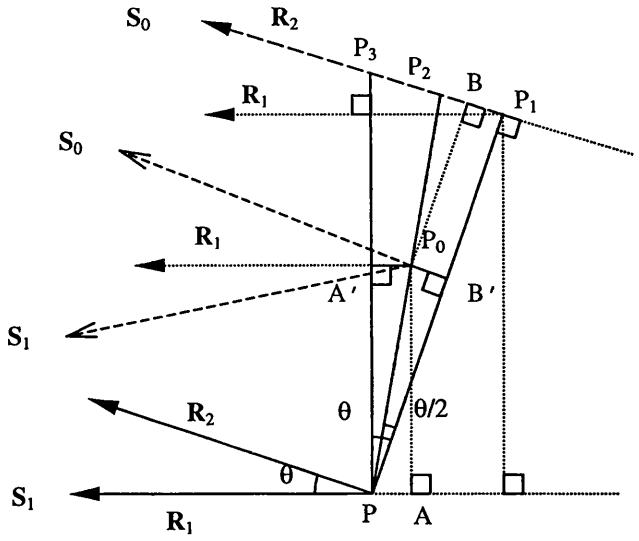

Figure 3.5 Azimuth line observation error in the weighted space intersection (an enlargement of the right part in Figure 3.4).

Change of $\mathbf{R}_2$ causes a shift in $\mathbf{R}_1$ from P to A and that of $\mathbf{R}_2$ from P_1 to B., i.e.,

$$dA = \overline{PP_1} \quad , \quad \textbf{if} \quad dA << R_1 \quad \textbf{and} \quad dA << R_2$$

Let P_0 be the intersecting point, the deviation in $\mathbf{R}_1$ from P to A, or A′ to P_0 must equal to that of $\mathbf{R}_2$ from P_1 to B, or B′ to P_0, under the two conditions. Then,

$$\overline{PP_2} = \overline{PP_0} + \overline{P_0P_2} = \frac{\overline{PP_1}}{\cos(0.5\theta)} = \frac{dA}{\cos(0.5\theta)} \tag{3.15}$$

There are an infinite number of points satisfying the criterion forming the track of the line from P to P_2. Obviously, such a line is a bisector of the convergent angle θ of two orbit tracks as in Figure 3.5. There is only one intersecting point that makes a balance between two Doppler equations, i.e., the deflected angle γ tends to be the same for each range direction as

$$\gamma = \angle P_1 \mathbf{S}_0 P_0 = \angle P_0 \mathbf{S}_1 P$$

$$\tan\gamma \approx \frac{\overline{P_0 A}}{R_1} = \frac{\overline{P_0 P} \cdot \cos(0.5\theta)}{R_1}; \quad \tan\gamma \approx \frac{\overline{P_0 B}}{R_2} = \frac{\overline{P_0 P_2} \cdot \cos(0.5\theta)}{R_2}$$

$$\overline{P_0 P} = \overline{P_0 P_2} \cdot \frac{R_1}{R_2} = \left(\overline{PP_2} - \overline{P_0 P}\right) \cdot \frac{R_1}{R_2} = \left(\frac{dA}{\cos(0.5\theta)} - \overline{P_0 P}\right) \cdot \frac{R_1}{R_2} \tag{3.16}$$

$$\overline{P_0 P} = \left(\frac{R_1}{R_1 + R_2}\right) \cdot \left(\frac{dA}{\cos(0.5\theta)}\right) = |\mathbf{E}_{az}|$$

R_1 and R_2 the magnitude of $\mathbf{R}_1$ and $\mathbf{R}_2$, respectively, and $\mathbf{E}_{az}$ the error vector of the azimuth line observation. Consider the factor of the convergent angle in equation (3.16) which is given as $(1/\cos(0.5\theta))$. For instance, let two range distance values R_1 = 1100km and R_2 = 880km, respectively, the nominal resolution of the azimuth line of a geo-referenced SAR image 14m and the orbital convergence angle about 9°, then, Equation (3.16) gives the error vector length approximately as 7.8m. Apparently, the orbit convergent angle has no significant effects on the azimuth observation errors, as shown in Figure 3.6, in the case of the weighted solution of space intersection.

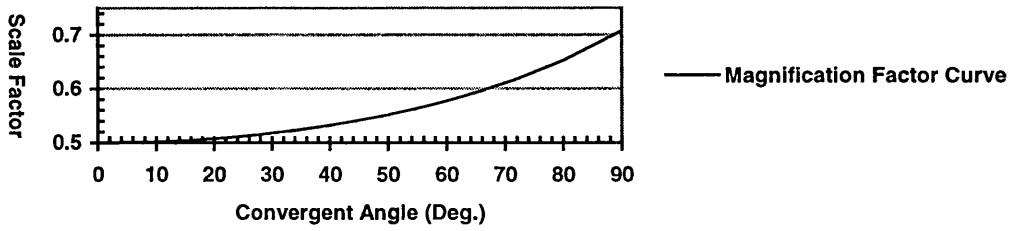

Figure 3.6 Magnification curve of the error caused by the azimuth line observation.

3.4.3 Resultant Observation Errors

The errors of observations made on each component in the SAR image geometry have been derived independently, but the actual influence of both errors on solving the ground point location cannot be understood without consideration of their resultant effects. The range pixel observation error occurs in the range plane, which is perpendicular to the azimuth direction as shown in Figure 3.2, and the azimuth line observation error is approximately parallel to the azimuth direction as in Figure 3.5. In general, both vectors $\mathbf{E}_{az}$ and $\mathbf{E}_r$ are approximately perpendicular to each other, according to the SAR image geometry, therefore, the resultant error vector $\mathbf{E}_0$ can be given as

$$\mathbf{E}_0 = \mathbf{E}_{az} + \mathbf{E}_r \quad \Rightarrow |\mathbf{E}_0| \approx \sqrt{|\mathbf{E}_{az}|^2 + |\mathbf{E}_r|^2} \tag{3.17}$$

$|\mathbf{E}_0|$ the magnitude of the resultant observation error vector in three-dimensional space. For instance, if $|\mathbf{E}_r|$=22.4m and $|\mathbf{E}_{az}|$=7.8m according to previous examples, equation (3.17) gives a theoretical error $|\mathbf{E}_0|$ in 3-D space about 23.7m for a low-incidence-angle SAR image. In case of a RADARSAT SAR image pair containing a high and a low incidence-angle image, the resultant error magnitude would be 28m, according to the error propagation from both images as in Table 3.2.

SAR Images	Left	Right
Incidence Angle (°)	21	45
Nominal Slant Range Resolution *dR* (m)	4.9	9.1
Nominal Azimuth Line Resolution *dA* (m)	14.1	14.0
Intersection Angle α(°)	24	
Range Observation Error $\mathbf{E}_r$ (m)	12	22.4
Orbit Convergent Angle θ(°)	9	
Azimuth Line Observation Error $\mathbf{E}_{az}$ (m)	7.8	7.8
Observation Error from an Image $\mathbf{E}_o$ (m)	14.3	23.7
Resultant Observation Error from a Pair	28	

Table 3.2 Resultant observation errors derived under various circumstances.

3.5 Procedures of Space Intersection

The practical procedures shown in Figure 3.7 explain how the rigorous algorithm works. The kernel software used in the procedures will be described in Section 3.6. The procedures start from a parallax file that is a data set of successfully matched points, either manually measured on a computer screen or automatically derived using an image correlator (see Chapter 4). The parallaxes generated have to be transformed from a sub-scene image (or the screen system, if applicable) into a full-scene image co-ordinate system defined by the image header file according to the orientation of that SAR image.

RADARSAT SAR images provide header files including Platform Position Data Record, Data Set Summary Record, Detailed Processing Parameters Record and Processed Data Record, according to CSA [1995]. Each image header file required by the space intersection process includes ephemeris data, scene center time and location, earth model parameters, image size, wavelength, ground-range-to-slant-range transformation

parameters and azimuth timing data *etc.* The required parameters can be collected from SAR image header files as shown in Section 3.6 for more details. The precision of the individual parameters required will also be given in Section 3.6.

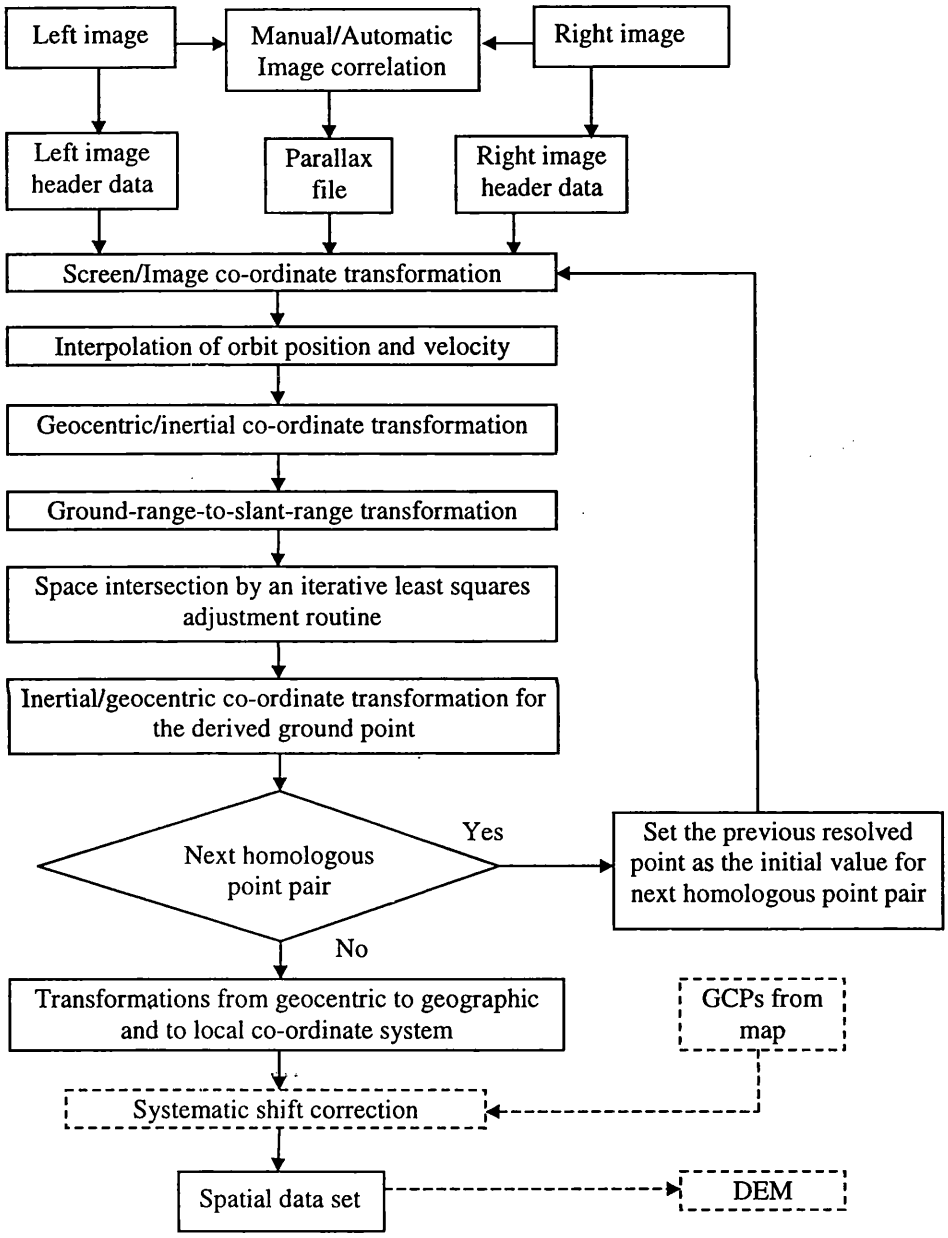

Figure 3.7 Space intersection procedures for SAR data

The intermediate transformations between the geocentric/inertial systems, the geocentric/geographic systems and the geographic/local map systems use the standard map projection procedures, [Green, 1985], [Clark, 1991] and [Laycock *et al.*, 1992].

More details of the auxiliary routines used in the thesis are described in Appendix A. The initial location of the first ground point corresponding to the first homologous point pair of the parallax file required in the iterative least-squares solution is given by the scene centre of each SAR image. The first point derived is then treated as the initial point for solving the next ground point corresponding to the next homologous point pair in the parallax file, and so on.

As mentioned before, there is no need to incorporate GCPs into the space intersection algorithm. GCPs are treated as unknown ground points to be solved from the image co-ordinates independently and to be compared with the corresponding map co-ordinates to derive a difference. This can be used to correct systematic shifts for the other unknown ground points calculated. Using only one GCP to do correction is theoretically possible. However, the quality of the manually selected GCPs is not stable hence using two GCPs with one redundant observation is the minimal requirement. In the case of more than three GCPs available, a three-dimensional similarity transformation can be employed to correct the systematic shifts, [Albertz and Kreiling, 1980].

3.6 Test Results of Space Intersection

The proposed rigorous algorithm is coded as programme `rsatsar1` in FORTRAN by the author and implemented in a SUN SPARC4/50 workstation under the Sun-OS UNIX operating system within a local area network at UCL. A brief description of this programme is given in Appendix B. Programme `rsatsar1` reads in two files of specific parameters from two orbits, `rsat.1` and `rsat.2`, and a parallax file, `rsat.ddm`. The formats for both kinds of files are shown as in Table 3.3 (a) and (b).

The parameter files contain parameters provided by header data files of SAR images, including RADARSAT SAR Platform Position Data Record, Data Set Summary Record, Detailed Processing Parameters Record and Processed Data Record as described in Table 3.3 (a). The precision of each parameter required in the programme is recommended as the last digit of the real numbers shown in the first column of Table 3.3 (a). For instance, the precision of individual components of the position and velocity vectors of the sensor is given as 0.01m and 0.01mm/s, respectively. The parallax file contains the parallaxes of the homologous point pairs in SAR image co-ordinate system derived manually or automatically.

Contents	Unit	Descriptions	Source
1997 8 22 5 54 50.76	date/time	Given time of the first data point	Platform Position Data Record
6	-	Number of the given data points	
4.0	s	Sampling interval of the data points	
1878434.23 4878054.87 4901508.03 3220956.05 4118837.03 -5319652.26	m mm/s	Sensor position of the first point Sensor velocity of the first point	
... ...	m mm/s	Repeat the state vectors for other points until the full-scene covered	
1997 8 22 5 54 59.960	date/time	Scene centre time	Data Set Summary Record
43.432 5.832	degree	Scene centre latitude and longitude	
6378140.0 6356755.0	m	Earth semi-major/-minor axes	
3951.0 4537.5	pixel	Scene centre line and pixel number	
0.05656	m	Wavelength	
6	-	No. of the polynomial coefficient for the ground-range-to-slant-range (GRSR) transformation	Detailed Processing Parameters Record
8.3931088E+05	m	Constant of the GRSR polynomial	
3.3013824E-01	m	Coefficient of the 1st power term	
...	m	Repeat until the 5th power term	
12.5	m	Range pixel spacing	
21292550.0 21307360.0	ms	Azimuth time of the 1st and the last line counted from the start of the day	Processed Data Record

Table 3.3 (a) Format of the parameter files `rsat.1` and `rsat.2`

Contents	Unit	Descriptions
3529.0 192.0 3948.0 7591.0	pixel/line/pixel/line (left) (right)	Image co-ordinates of the correlated point of the left image and right one
...	pixel/line/pixel/line	Repeat until the last correlated point

Table 3.3 (b) Format of the parallax file `rsat.ddm`

3.6.1 Test Images and Test Site

The RADARSAT SAR test images, provided by RADARSAT International (RSI) under the Application Development and Research Opportunity (ADRO) programme, are located on the Aix-Marseilles test site in south France as in Figure 3.8. In general, terrain relief of the test area varies from moderate to hilly and ranges from 0m to 1147m above mean sea level. Varied land utilization, seasonal vegetation cover and complicated landscape including urban areas, forests, mountains, seashores, lakes and rivers, are evident in this area. Table 3.4 gives some specific characteristics for the test images. Each Descending Standard beam-7 (DS7a or DS7b) SAR image is taken together with the Descending Standard beam-1 (DS1) image to form two stereoscopic pairs as Case (1) and (2). Notice that the difference of acquisition time of the images in Case (1) is 13 days and that of Case (2) is more than six months!

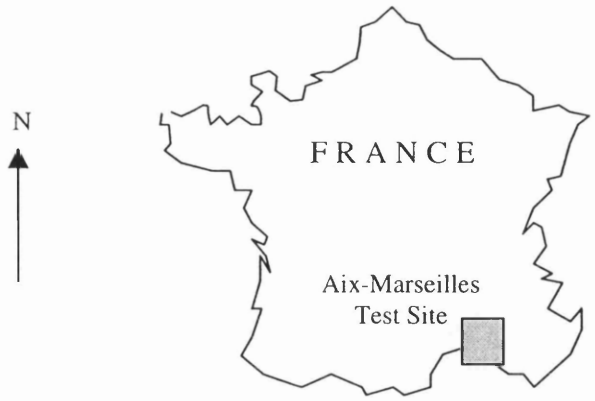

Figure 3.8 Location of the test site in south France (not to scale)

SAR sensor Orbit Direction	RADARSAT Beam Mode	Year-Month-Date	Full-scene Size (row/column)	Alias Name
Descending	Standard-1	1997-08-22	7901 / 9075	DS1
	Standard-7	1997-08-09	5739 / 8942	DS7a
	Standard-7	1998-03-13	7875 / 8937	DS7b

Table 3.4 Characteristics of the test images for space intersection.

An example of the SAR image of full-scene (DS1) is shown in Figure 3.9 (a). A sketch map of the geography for the full-scene image DS1, as demonstrated in Figure 3.9 (b), shows the main features appearing in the test area.

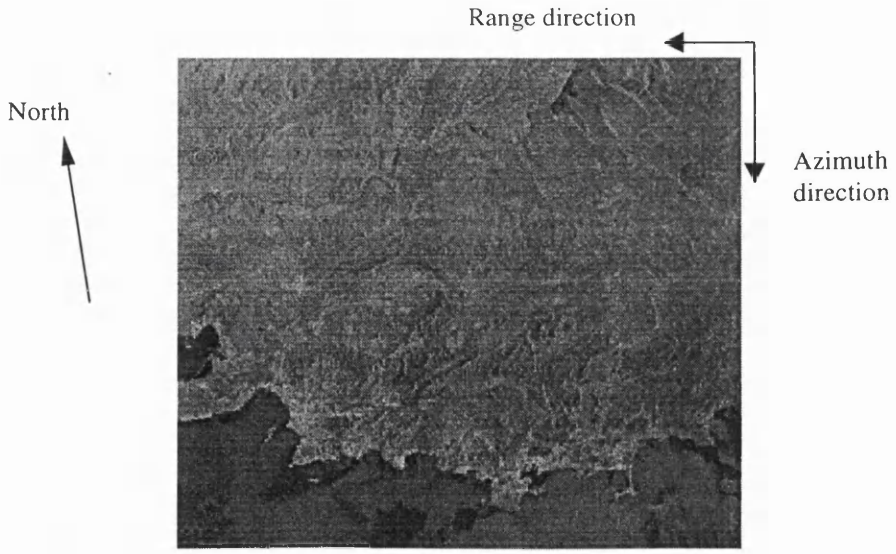

Figure 3.9 (a) A full-scene descending SAR image (DS1) at the test site

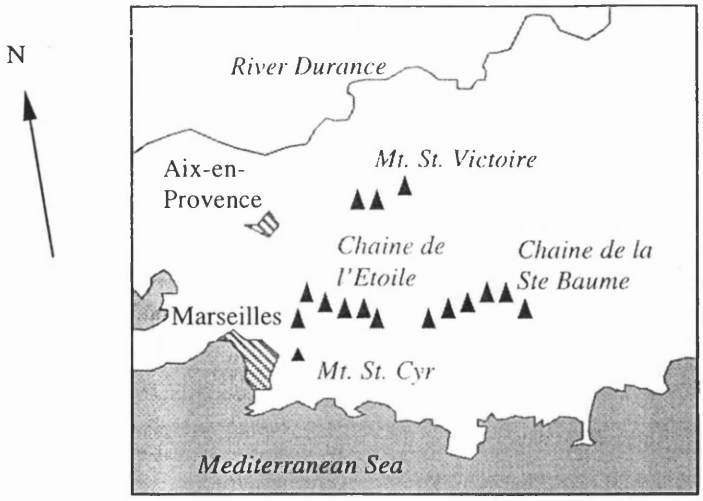

Figure 3.9 (b) A sketch map of the geography of SAR image DS1 (not to scale).

3.6.2 Space Intersection for Check Points

To evaluate the performance of the algorithm for space intersection, 34 ground points have been selected manually from the three images of descending passes. These ground points were selected as evenly as possible over the common area of each scene. The man-made objects/features being measured include the corner of buildings, bridge, the junction of road/railway/canal, the end point of a runway, embankment, pier and beacon. The identifiable natural features have been adopted carefully, such as a cliff on hilltop, shoreline of lake/pond/river and rocky coastline, when the man-made features are not available. The detailed descriptions for the characteristic of the selected ground points are listed in Table 3.5 together with the corresponding French IGN map sheets where the ground points locate, [IGN, 1989] and [IGN, 1992]. The map sheet number is given by IGN, for instance, '3143E' (3143*est*) or '3143W' (3143*ouest*) as a 1:25000-scale map and '3345' as a 1:50000-scale map, as shown by the map-index in Appendix C with the check points numbered.

Two ground points were selected as candidate GCPs and others as check points. Both GCPs are man-made objects, a building and a pier, respectively, which have good contrast against the surrounding areas. It will be shown later that the revised radargrammetric model is insensitive to the relative locations of the GCPs. The elevation of check points ranges from 0m to 600m above mean see level as shown in Figure 3.10. Figure 3.11 gives the spatial distribution in plan of the check points and candidate GCPs in the French local co-ordinate system (Lambert Conformal Conic Zone III). The image

co-ordinates of each pair of manually identified and matched check points were used as input for space intersection following the rigorous approach proposed in Figure 3.7. The co-ordinates of the check points calculated using the proposed algorithms were compared with the co-ordinates measured from the IGN maps of a 1:25,000 or 1:50,000 scale.

IGN Map-sheet Point No.	Attribute of Each Ground Point						
	Bridge	Building	Runway	Cliff	Road/Canal Junction	Lake/River Coastline	Embankment /Pier/Beacon
3143E-1	√						
3143E-2	√						
3143E-3		√					
3243W-1						√	
3243W-2	√						
3243W-4					√		
3243E-1	√						
3243E-2	√						
3243E-3	√						
3144E-1						√	
3144E-2						√	
3244W-1	√						
3244W-2						√	
3244W-3		√					
3244E-1					√		
3344-01					√		
3344-02	√						
3145E-1*							√
3145E-2*		√					
3145E-3						√	
3145E-4							√
3145E-6		√					
3145E-7				√			
3145E-8						√	
3145E-9							√
3145E10						√	
3245E-1		√					
3245E-3		√					
3245E-4						√	
3245E-5							√
3345-01			√				
3345-02						√	
3345E-1						√	
3345E-3	√						

*Ground Control Points

Table 3.5 Characteristic of the selected ground points for space intersection.

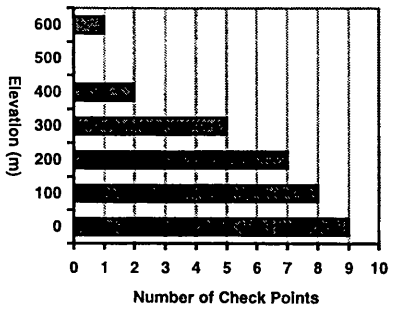

Figure 3.10 Distribution of check points in elevation.

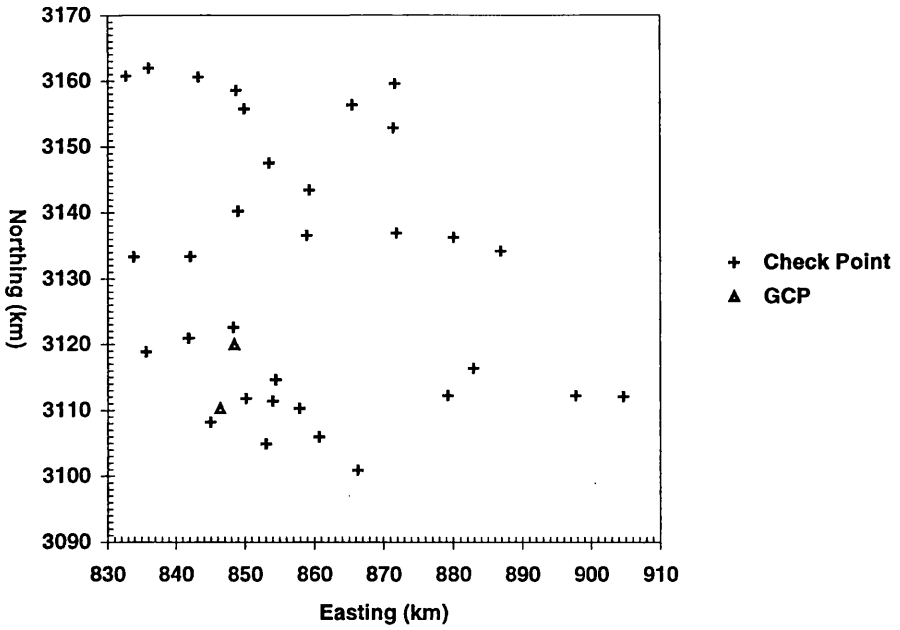

Figure 3.11 Spatial distribution of check points in plan (French Lambert Zone III).

The measuring error for the map co-ordinates is estimated as 18m in plan and 7m in height giving an error vector with a magnitude of 26m in 3D, as derived in Table 2.6 (see Section 2.5.1). The errors resulting from the cartographic procedures and distortions of map sheets are not taken into account in the calculation of the error magnitude in collecting GCPs. It is obvious that the quality of manually selected GCPs may not be consistent from one to another, due to the difficulties of the exact identification of GCPs on maps and SAR images for human operators. The tests were carried out for two cases including Case (1): DS1 (left) and DS7a (right), Case (2): DS1 (left) and DS7b (right). The statistics from 34 ground points (including two candidate GCPs) calculated using the weighted space intersection without GCPs for each case are shown in Table 3.6 in respect to easting (E), northing (N) and height (H) components.

Configuration	Component	Mean (m)	Min.(m)	Max.(m)
Case (1): DS1(left)+ DS7a(right)	E	**143.9**	70	277
	N	**153.8**	24	219
	H	**53.2**	20	70
Case (2): DS1(left)+ DS7b(right)	E	**-249.8**	-304	-189
	N	**-48.8**	-102	23
	H	**215.8**	178	247

Table 3.6 Statistics from 34 check points derived from the weighted solution without using any GCPs.

The weights of Doppler observations are given approximately as 1.0×10^{-3} and those of range observations as 1.0 in the case of the weighted space intersection based on the prior knowledge of the orbit data quality, CSA [1995], as derived in Section 3.3. Obviously, the results derived without using any GCPs exhibit significant systematic shifts that can be greater than two hundred metres hence GCPs are needed for systematic corrections. Two check points selected were used as GCPs to correct the systematic shifts. The precision of the GCPs derived using the non-weighted solution and that of the weighted solution are shown in Table 3.7 for both cases showing the improvements made in northing, approximately the azimuth direction. Note that the quality of the manually selected GCPs and check points, which can strongly affect the resultant accuracy, is similar to the predicted accuracy of the proposed geometric model.

Configuration		RMSE-GCPs Non-Weighted (m)	RMSE-GCPs Weighted (m)
Case (1): DS1(left)+ DS7a(right)	E	6.8	6.6
	N	**23.5**	**20.9**
	H	0.3	0.6
	3D	**24.5**	**21.9**
Case (2): DS1(left)+ DS7b(right)	E	16.8	17.2
	N	**25.0**	**18.6**
	H	11.9	11.5
	3D	**32.4**	**27.8**

Table 3.7 Precision of the two GCPs using the non-weighted solution and the weighted solution.

For comparison and contrast, the other 32 check points have been tested with the non-weighted least squares solution for both cases as demonstrated in Table 3.8. The results derived using the weighted space intersection for the same 32 check points in both cases, as shown in Table 3.8, demonstrate that the systematic shifts can be eliminated dramatically using a very small number of GCPs. The magnitude of the error calculated from the overall RMS errors of the check points is about 38.8m in Case (1) and 36.3 in Case (2). These errors are comparable with the resultant error calculated from two sources: the measuring error of GCPs 26m (see the estimated precision of the manual measurements described in Table 2.6) and the predicted error of space intersection 28m (see the error model described in Table 3.2), or 38m ($=\sqrt{(26^2+28^2)}$).

Comparing the results derived using the weighted solution and the non-weighted solution as shown in Table 3.8, the weighting matrix improves the precision of the results in northing, in terms of the absolute error extent between positive and negative errors,

24m and 47m for both cases, respectively. This is due to a relatively greater weight given to the range observation hence the azimuth line (time) measuring error may not affect the positioning precision as explained in the mentioned error model (recall Section 3.4). Although, the overall accuracy cannot be improved enormously using the weighted least-squares solution, the deviation extent in easting and northing of the calculated co-ordinates has shown a reasonable balance.

Configuration		R.M.S.E. (m)	Mean (m)	Min.(m)	Max.(m)	Error Range (m)
Case (1): DS1(left)+ DS7a(right)	E	27.3	+8.3	-62	+55	117
	N	23.0	-3.1	**-69**	**+57**	**126**
	H	11.3	-0.2	-34	+24	58
	3D	37.4	**Non-weighted solution**			
Case (2): DS1(left)+ DS7b(right)	E	25.3	+10.2	-43	+71	114
	N	20.0	+0.6	**-53**	**+72**	**125**
	H	19.7	-4.7	-43	+26	69
	3D	37.8	**Non-weighted solution**			
Configuration		R.M.S.E. (m)	Mean (m)	Min.(m)	Max.(m)	Error Range(m)
Case (1): DS1(left)+ DS7a(right)	E	27.2	+8.2	-62	+54	116
	N	25.3	-5.7	**-60**	**+42**	**102**
	H	11.3	-1.0	-34	+24	58
	3D	38.8	**Weighted solution**			
Case (2): DS1(left)+ DS7b(right)	E	25.6	+10.6	-45	+71	116
	N	17.0	+5.7	**-42**	**+36**	**78**
	H	19.4	-4.3	-43	+25	68
	3D	36.3	**Weighted solution**			

Table 3.8 Statistics of 32 check points derived using the non-weighted solution (above) and the weighted solution (below) with two GCPs.

In addition, the results derived from the non-weighted space intersection suggest that the zero-Doppler assumption does not cause serious deviation in this case. It shows that the range and azimuth components of the SAR image co-ordinate system remain reasonably orthogonal, and confirm that the image distortion is tolerable, as reported by Denyer *et al.* [1993]. Figure 3.12 gives the histograms of the deviations of the results derived using the non-weighted solution and the weighted solution for Case (1) and (2), respectively, showing that most of the errors in each component distribute within ±40m and exhibit peaks around zero error. The statistics shown here can only give the overall concept of the positioning errors, the more detailed analysis is given in next section to demonstrate the error behaviour of individual check points in terms of errors in plan and those in height.

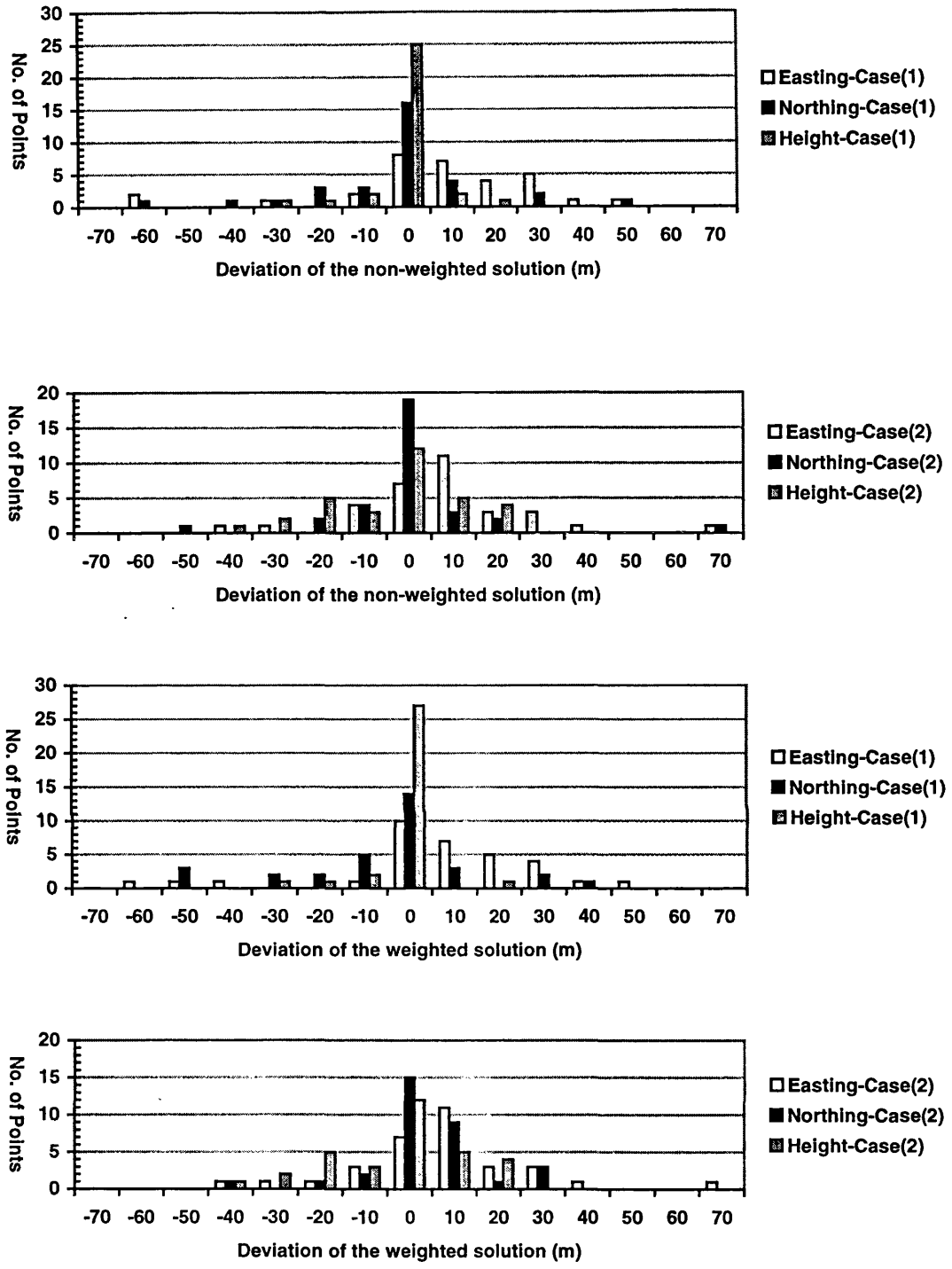

Figure 3.12 Histograms of deviations of the check points derived using the non-weighted solution and the weighted solution in Case (1) and (2).

3.6.3 Analysis of the Results Derived from Space Intersection

The errors of the co-ordinates of check points calculated using the non-weighted solution and the weighted solution with two GCPs for both cases can be seen from the

deviations (error vectors) in plan as shown in Figure 3.13 (a) and (b), respectively, for both cases. The expected position (the map co-ordinates measured) of each check point is represented by a square dot (the head) with an error vector pointing to the co-ordinates derived (the tail) using the non-weighted (weighted) solution. Geometrically, the error vectors of the check points in plan do not point to any specific direction, and there is no particular bias in respect to any specific trend. Although, there are only two GCPs used for systematic corrections, the overall remaining systematic shifts are not significant. Figure 3.13 (a) and (b) demonstrate that the measuring errors of azimuth lines are relatively insignificant and do not cause problems in solving the positions of ground points. In the case of the non-weighted solution without using GCPs in the geometric model, the results derived in terms of deviations in plan are reasonable.

In the case of using the weighted solution, the precision in terms of the extent of the deviations, approximately in the azimuth direction, has been improved in northing direction, but there is no improvement made in the easting direction (range direction). This coincides with the concept of the weighting matrix, since it is assumed that the along-track orbit error distorts the imaging geometry and needs to be adjusted. The absolute accuracy cannot be improved significantly, because the weighting matrix can only deal with the stochastic problems of observations (errors) of different classes, (recall Gauss [1823]).

Also, the positioning errors on each component in plan of 32 check points are arranged according to the range direction and azimuth direction with respect to the left image co-ordinates for both cases to detect any systematic effects. Figure 3.14 and 3.15 demonstrate the deviations of check points in easting (E) and in northing (N) using the non-weighted solution and the weighted solution, respectively, for both cases. Obviously, most of the deviations of check points in plan (E or N) range within ±40m and there is no significant systematic bias exhibited.

Figure 3.16 (a) and (b) shows the deviations in height of the check points derived using the non-weighted solution and the weighted solution, respectively, with two GCPs in both cases. The expected position (the map co-ordinates and elevation measured) of each check point is again represented by a square dot (the head) with an error vector pointing up (positive error) or down (negative error) to show the deviations in height of the check points derived using the non-weighted (weighted) solution.

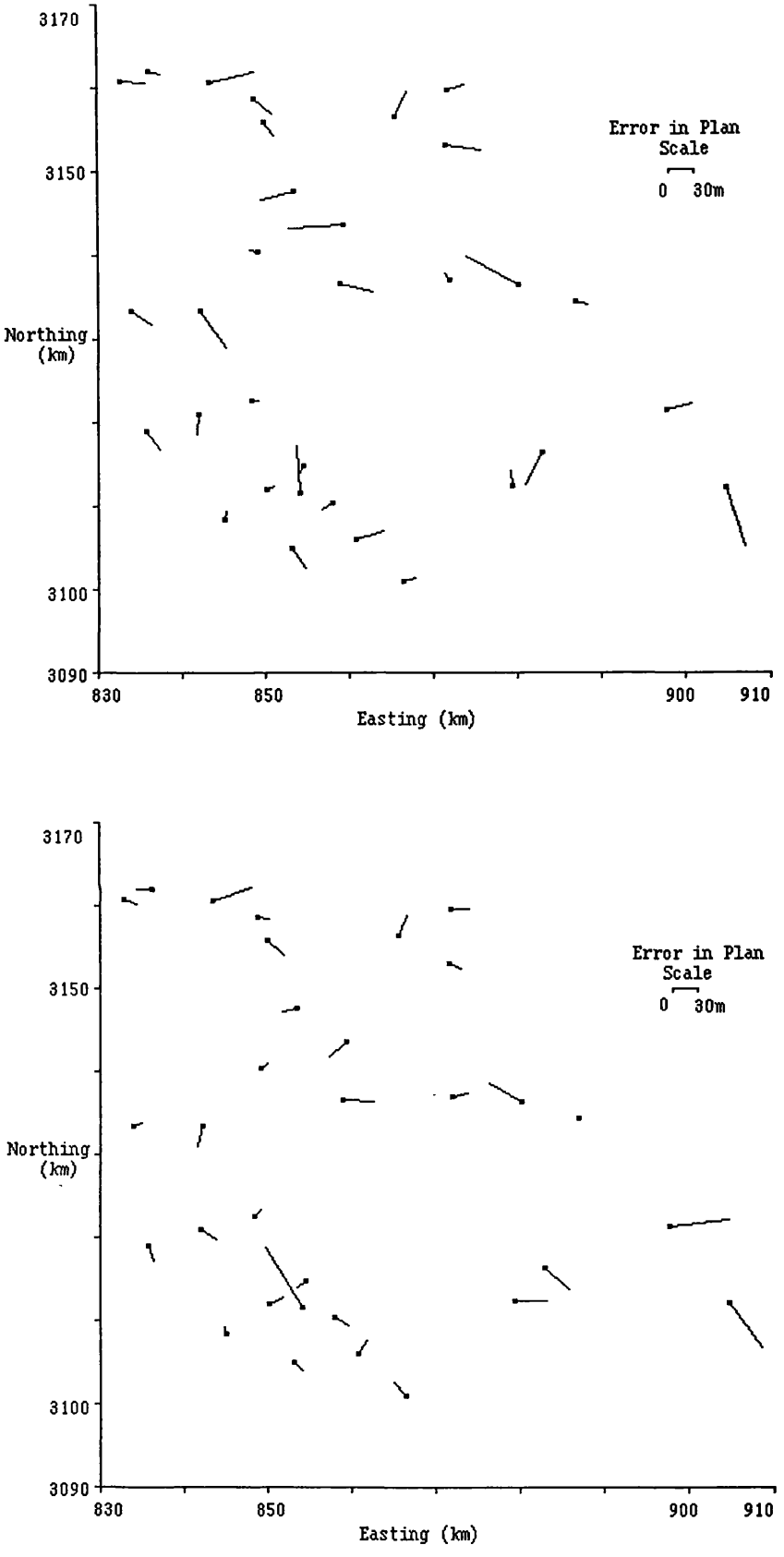

Figure 3.13 (a) Error vectors in plan of check points calculated using the non-weighted space intersection with two GCPs in Case (1) (above) and Case (2) (below).

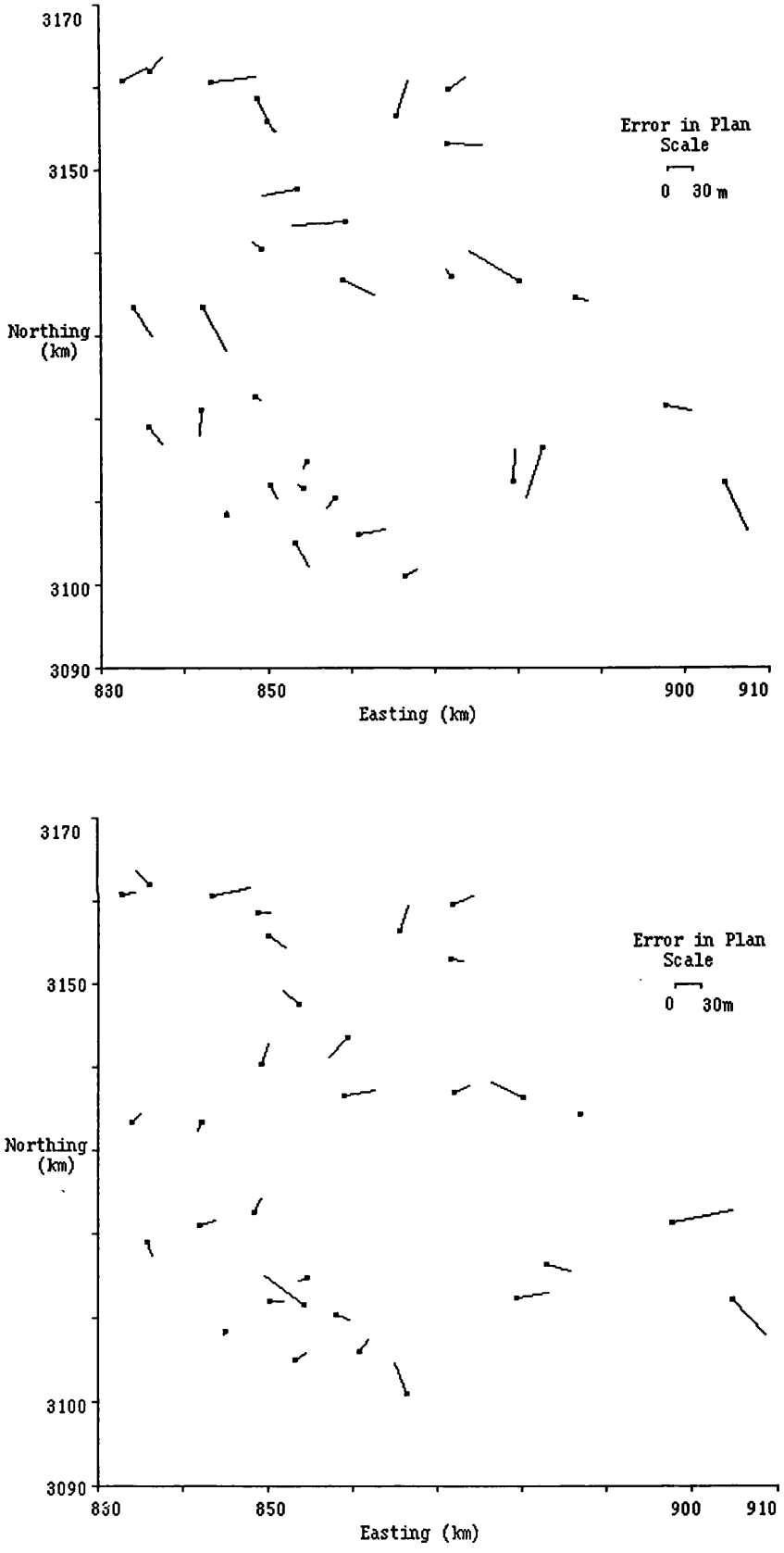

Figure 3.13 (b) Error vectors in plan of check points calculated using the weighted space intersection with two GCPs in Case (1) (above) and Case (2) (below).

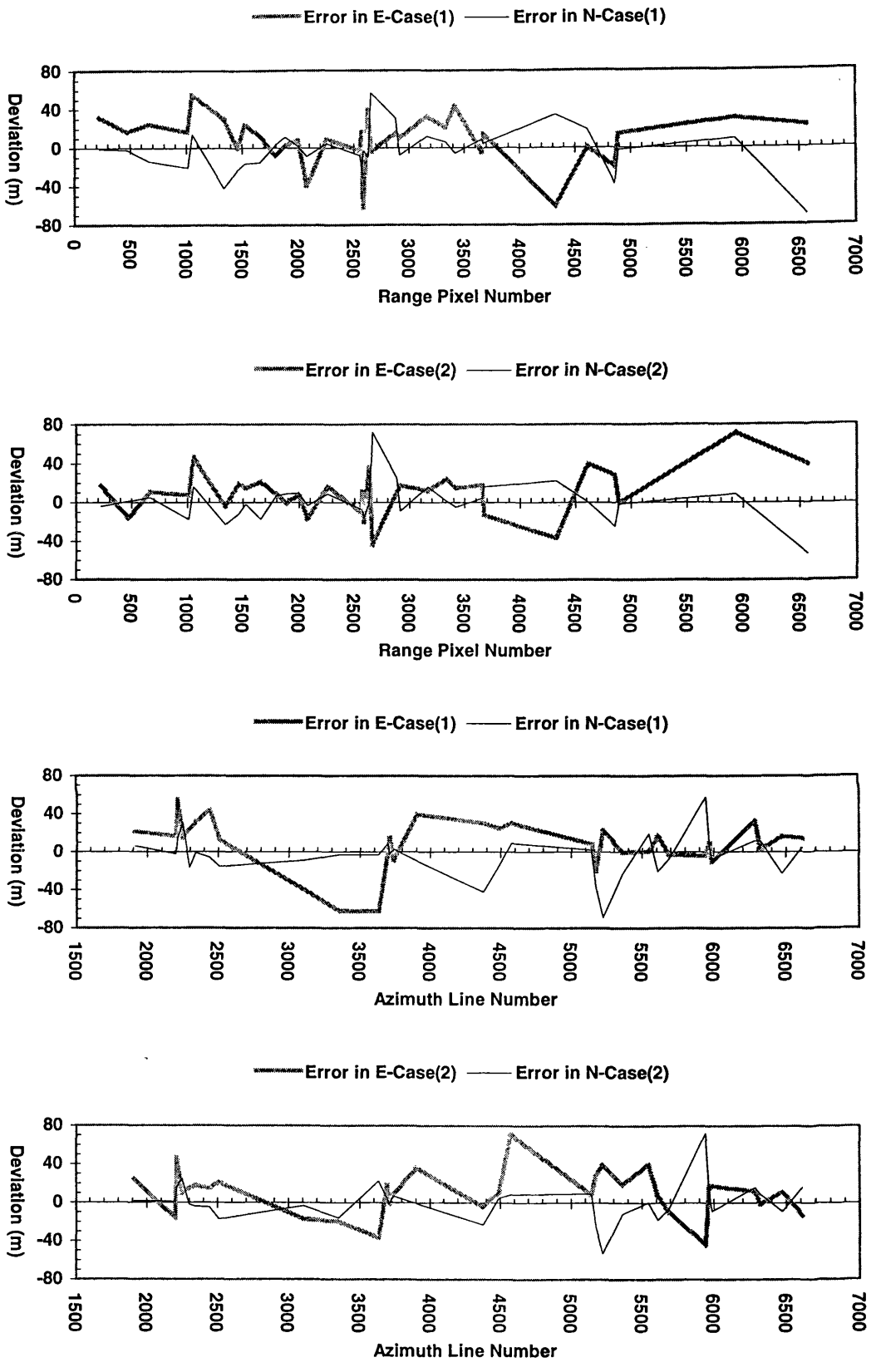

Figure 3.14 Deviations of check points in easting and in northing derived using the non-weighted solution in Case (1) and (2).

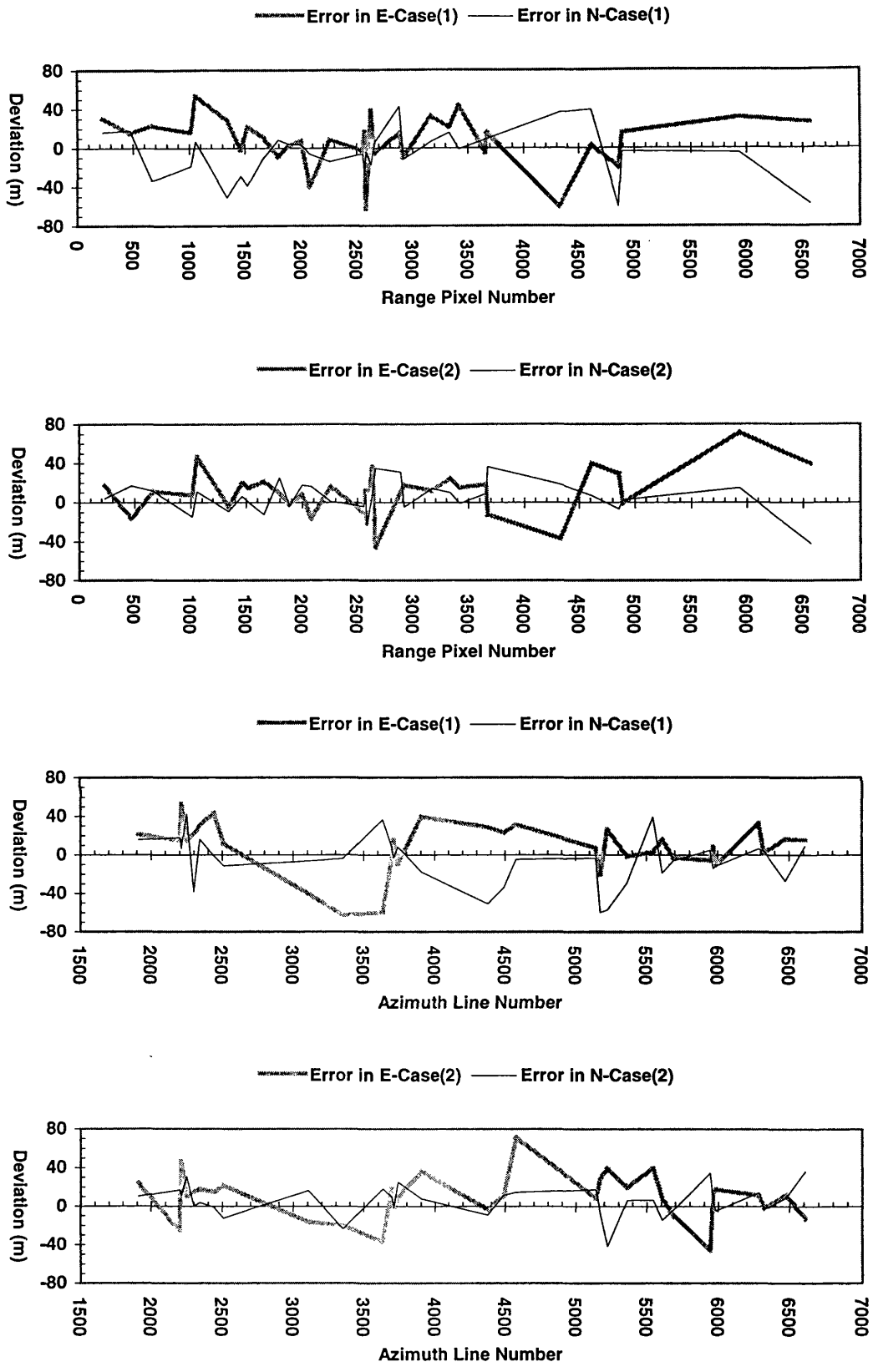

Figure 3.15 Deviations of check points in easting and in northing derived using the weighted solution in Case (1) and (2).

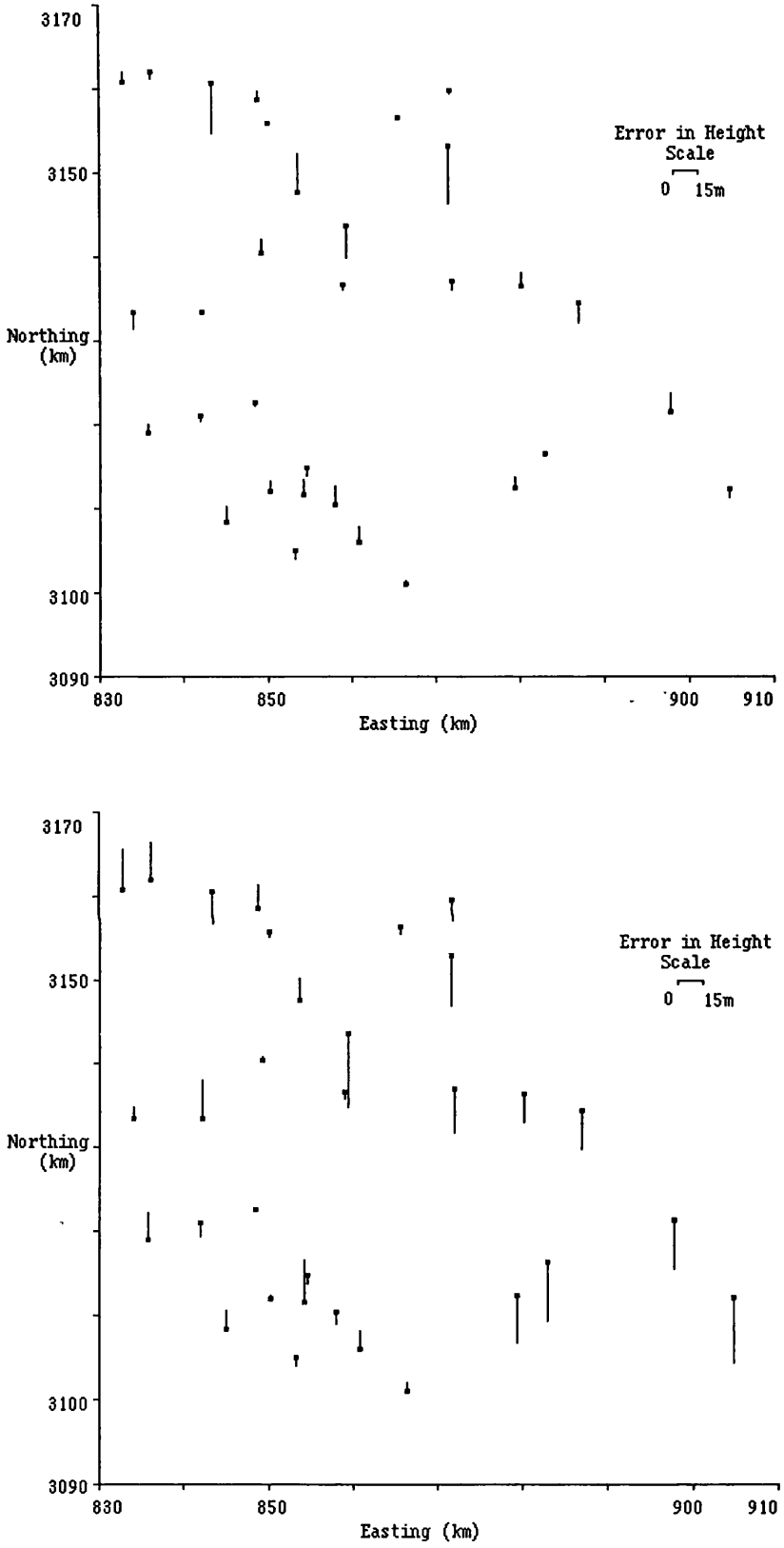

Figure 3.16 (a) Error vectors in height of the check points derived using the non-weighted solution in Case (1) (above) and Case (2) (below).

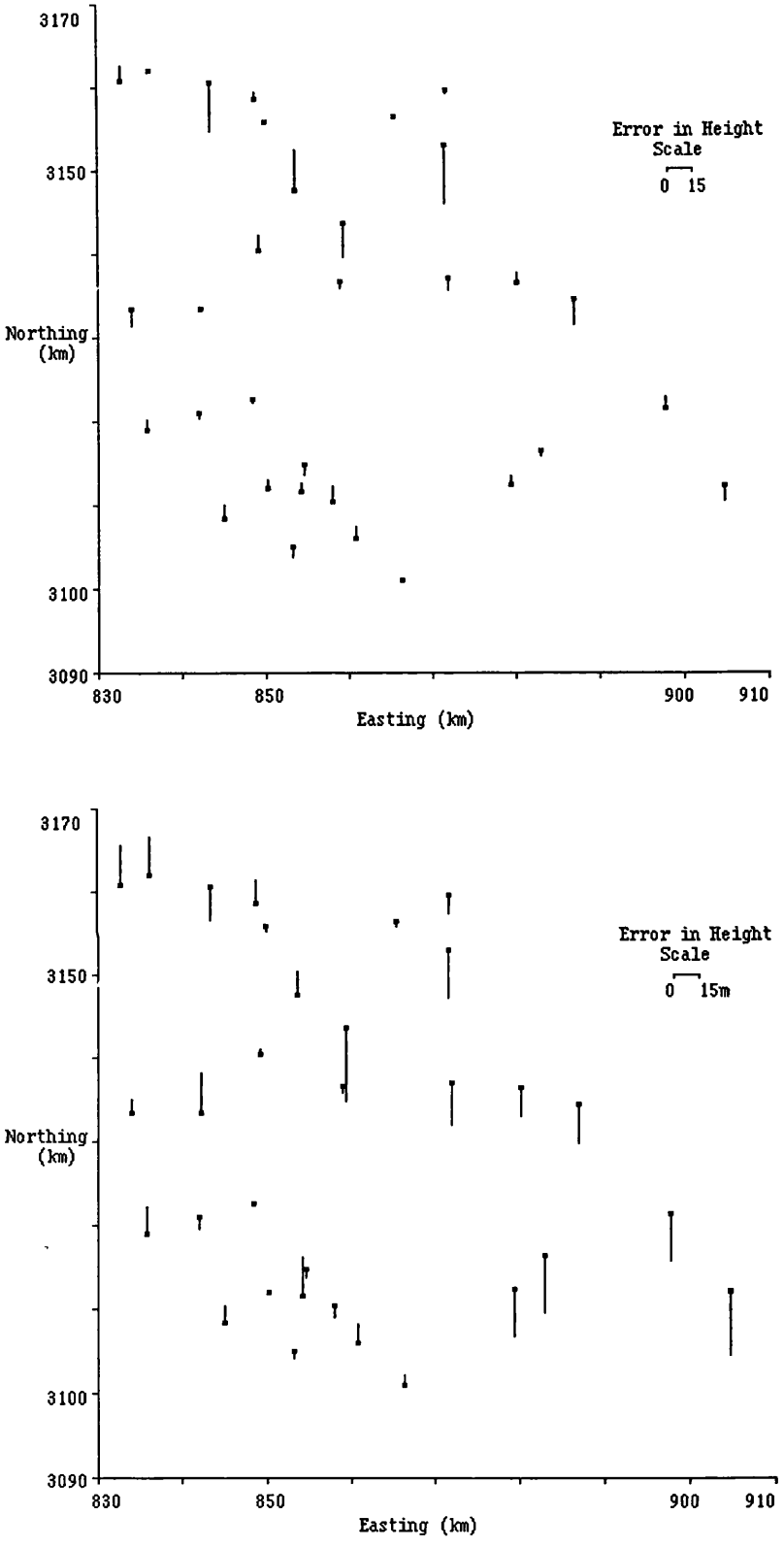

Figure 3.16 (b) Error vectors in height of the check points derived using the weighted solution in Case (1) (above) and Case (2) (below).

In terms of deviations in height, there is no significant difference between the results derived using the weighted solution and the non-weighted solution, as shown in. Figure 3.16 (a) and (b). Figure 3.17 indicates the deviations in height of the check points derived using the weighted solution, respectively, arranged according to the range pixel number and to the azimuth line number for both cases.

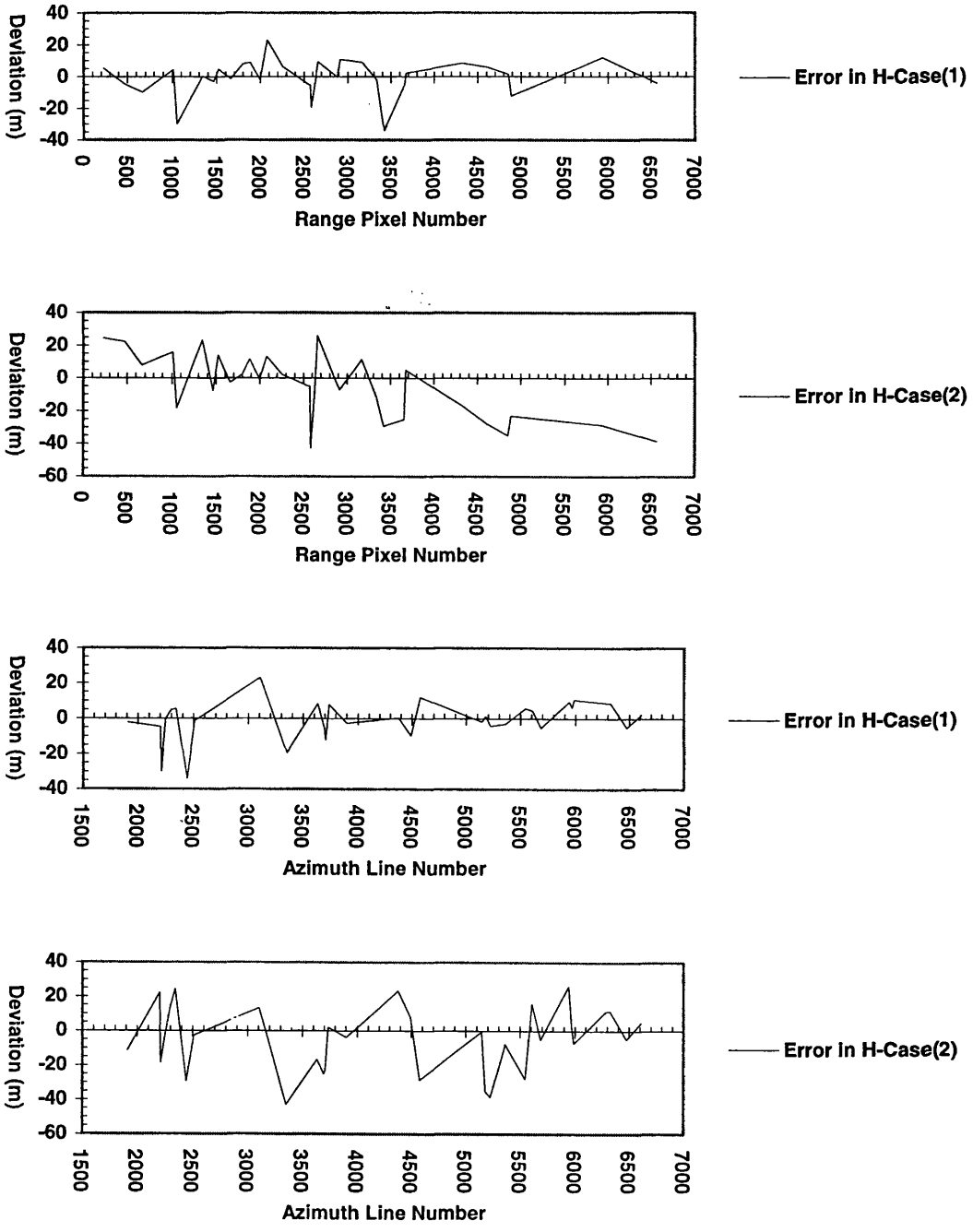

Figure 3.17 Deviations in height of check points using the weighted solution in Case (1) and (2)

Geometrically, the error vectors of the check points in height do not show an enormous bias or a constant trend. The deviations in height of the six check points at the eastern part in the test area in Case (2) show a local 'shift' of 17~43m, approximately. It is probably due to poor image quality in one of the images in Case (2). However, most of the deviations of the check points in height (H) are distributed within ±30m and there is no significant systematic bias in Case (1). In general, the deviations of the check points are relatively smaller in height (H) than those in plan (E or N). Figure 3.18 illustrates the relationship between the deviation in height calculated and the actual elevation of individual check points, which shows no systematic trend in both cases. That demonstrates the space intersection algorithm is robust and independent of the terrain relief variation.

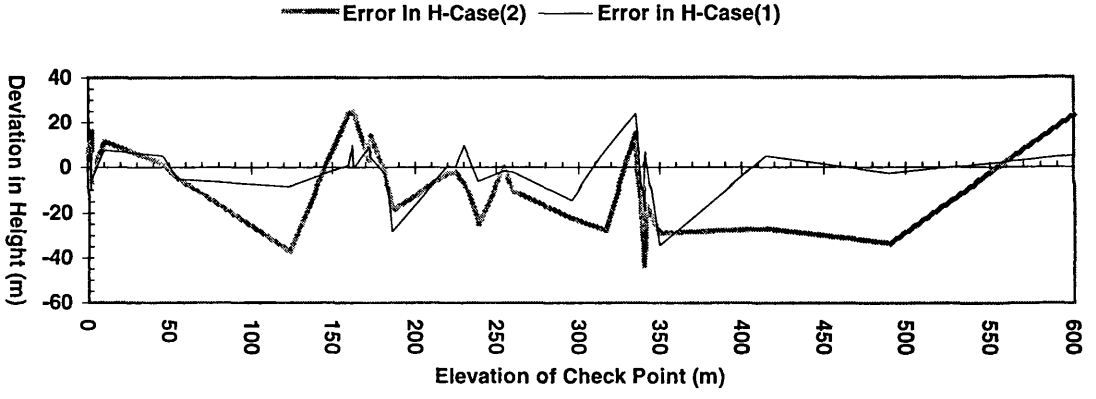

Figure 3.18 Deviation in height of each check point against its elevation in both cases.

3.6.4 Discussion

The weighting matrix proposed for the two kinds of SAR image co-ordinate observations is based on the prior knowledge of the accuracy of the orbit information reported, [CSA, 1995]. It has been shown that improvement for the stereo radargrammetry can be made in terms of precision. The predicted errors calculated using the proposed error model are comparable with the experimental results. Comparing the errors of the three components derived from both cases, there is no significant periodic systematic effect or constant bias remaining in the results. Obviously, both cases show that the algorithm is still able to carry out space intersection under the condition of a big temporal difference, provided that the conjugate points can be identified in an image pair.

In general, the residual errors of the check points are comparable with the estimated measuring errors of check points on maps. There are two main factors contributing to the residual errors: the observation errors of map/image co-ordinates and the precision of the GCPs measured. The observation errors can be predicted using the proposed error model, but the measuring errors on maps can only be minimized by using large-scale maps or field surveying techniques, such as Global Positioning System (GPS). However, such a large-scale map is not always available and this is still one of the major problems for providing control in radargrammetry.

The risk of using a medium- or small-scale map for providing poor GCPs is that the SAR image geometry can be distorted, if the GCPs are being used to 'refine' the image geometry. Compared with the proposed algorithm, other methods that need GCPs to refine a image geometry, for example, Singh *et al.* [1998], can generate less favourable results from RADARSAT data as quoted in Table 3.9.

Other Least-Squares Approach ([Singh *et.al.*, 1998])	Component	RMSE-GCPs (m)	RMSE-Arbitrary Points (m)
RADARSAT Stereo Configuration S2+S7	E	36.5	75.5
	N	25.0	27.0
	H	15.8	42.5
	Error in 3D	**47.0**	**90.8**

Table 3.9 Precision of GCPs and accuracy of the results derived using a traditional least-squares method that needs GCPs in the algorithm.

The GCPs were collected from 1:20,000-scale maps. The precision of the GCPs calculated is quoted as 47m in terms of error magnitude in 3D space and the algorithm generates error magnitude of 90m in 3D space for arbitrary points, [Singh *et al.*, 1998]. Although the number of GCPs employed has not been shown, the map employed for collecting GCPs has a larger scale (1:20,000) than those used in this thesis (1:25,000 and 1:50,000). The misusage of GCPs in the algorithm has been demonstrated by the precision of GCPs derived and the relatively poor quality results of the ground points calculated. The method proposed in this thesis is validated from the comparisons between Table 3.7/3.8 and 3.9. The radargrammetric results reported by other authors, such as Raggam and Gutjahr [1998], Sylvander *et al.* [1998] and Toutin [1999] that demand many GCPs and human interventions for model set-up or determining parameters, do not explicitly show the evaluation of the proposed geometric algorithm in respect to

independent check points. Compared with the results derived by other authors, it can be concluded that the method proposed in this chapter, which does not use GCPs to carry out model set-up or to derive relevant parameters to change the SAR image geometry, gives robust solutions and relatively better quality results.

The proposed algorithm provides only a geometric model, which is used to reconstruct the terrain surface from an image pair. But, this is not enough for automatic derivation of spatial data, such as a DEM. Further study about automatic image correlation is illustrated in Chapter 4 to show how to generate a parallax file in order to produce a DEM. Also, the uncertainty of manually selected GCPs can affect the accuracy of the results calculated from space intersection leading to a systematic shift of the spatial data derived. This will be solved later with the proposal of a new method for providing GCPs automatically based on a simulation method, as described in Chapter 5.

3.7 Summary

Space intersection for stereoscopic SAR imagery can be achieved using the weighted least squares adjustment for the range equation and the Doppler equation of each image of two orbits. The proposed weighting matrix is based on the general consideration of the different properties and influences from angle and distance observations hence reducing the effects from inferior orbit data and achieving a reasonable balance between two kinds of observation errors. The algorithm is independent of the need of GCPs, which are used only for systematic corrections. A new error model is proposed to predict theoretical errors from the revised algorithm. The test results of the check points selected from RADARSAT data meet the prediction made by the error model. The results derived using the non-weighted space intersection and the weighted solution suggest that the zero-Doppler assumption does not cause problems for solving unknown ground points in this case.

Chapter 4

SAR Image Correlation

4.1 Introduction

Image correlation is one of the key steps in generating a DEM automatically from a SAR image pair, which deals with the problem of searching for a defined part of one image within the conjugate one. In comparison with optical data, there is neither epipolar geometry nor any good texture in SAR imagery suitable for image correlation, and SAR data are particularly affected by speckle. The least squares correlation method, mentioned in Chapter 2, considers the geometric and radiometric differences between images without regard to imaging geometry and is then suitable for SAR image correlation. Using a hierarchical approach, the main features of a SAR image can be preserved and the speckle can be smoothed out after adequate reduction from the original image tier, hence the propagation of control in the top-down direction is possible. Therefore, the best way to carry out SAR image correlation seems to be a pyramidal correlation scheme employing the least squares method with a region-growing approach, [Otto and Chau, 1989] and [Dowman *et al.*, 1992]. The detailed illustrations for the pyramidal correlation routines are referred to Denos [1992] and Twu [1996]. A full explanation of the least-squares correlation algorithm can be found in Gruen [1996].

The main concern here is to know the way to automatically generate enough seed points to initiate the pyramidal correlation harness. The seed points are the conjugate points of an image pair used as the initial approximations for the least squares image correlation routine employing a region-growing approach, as mentioned in Section 2.4.4. It is suggested that the seed points can be generated automatically in a grid form, according to Denos [1992]. This leads to other questions: how many tiers of an image pyramid are suitable, how many seed points will be enough for image correlation of a SAR image pair and what is the adequate uncertainty radius for predicting the seed points. These parameters were determined by a trial-and-error method as given by Denos

[1992] and Twu [1996] that is time-consuming and has no definite rules established. As opposed to the trial-and-error approach of other authors, an optimized parameter decision strategy is proposed in this chapter to achieve a higher level of automation for the image correlation scheme. This method is based upon a pyramidal geometry analysis and the greatest parallax of an image pair giving a solution for the optimal number of tiers in an image pyramid, as described in Section 4.2. Further considerations about generating seed points at the top tier are given in Section 4.3 which leads to a solution for the optimal number of seeding grid cells and the uncertainty radius for predicting seed points. Section 4.4 gives the test results of the automatically generated DEMs from a RADARSAT SAR image pair using different combinations of parameters: the number of image tiers, the number of seeding grid cells and the uncertainty radius for predicting seed points. The results were evaluated in terms of the accuracy of the DEM derived and the percentage of correlated points achieved.

This chapter focuses on the comparisons of the DEMs generated using different combinations of parameters for commanding the pyramidal image correlation scheme. The more detailed analysis and refinement of the generated DEMs will be given in Chapter 6, after revision of the method of providing control in Chapter 5. It will be shown that the proposed strategy is not only able to construct the relationship between different parameters of an image pyramid to minimize the possibility of false image correlation, but also to reduce manual intervention to reach a higher level of automation for producing a DEM.

4.2 Image Pyramid

The pyramidal image correlation approach is primarily controlled by the key parameters of a hierarchical structure including the reduction factor between image tiers and the total number of image tiers. This section gives an analysis of the pyramidal geometry and the greatest parallax of the reduced images, in order to establish a definite rule for initiating image correlation routines and to get rid of the trial-and-error method. Having derived the size of the top image tier, the seed points, which are needed to initiate the least squares correlation (see Section 2.4.1), can be generated as described in the following section.

4.2.1 Reduction Factor

An image pyramid data structure is given by the reduction factor and the number of image tiers in which the upper tier is reduced from an image at the lower tier according to the reduction factor. The factor of reduction between image tiers is defined as the square root of the quotient derived from the result of dividing the number of pixels of the lower (original) image tier by that of the upper (reduced) image tier. Generally, a factor of two is adopted to construct an image pyramid because of its efficiency, i.e., a pixel at the upper level is simply averaged from the corresponding four pixels at the lower tier in the direction of bottom-up as shown in Figure 4.1. Given a reduction factor as two, the ambiguity of the exact location of the seed points is two pixels in range or azimuth direction. In terms of automatically predicting seed points, the possibility of successful correlation for the seed point pair is derived as one in four pixels (25%), or the inverse of the square of 2, provided that one image overlaps 100% with another. In such a case, the hierarchical structure is equivalent to a quad-tree structure.

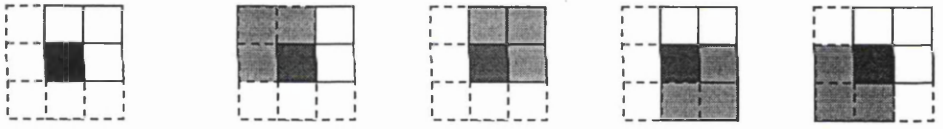

Figure 4.1 A seed point located at the reduced image tier (a);
(b)~(e) four possible locations of the original pixel at the lower image tier.

On the one hand, a larger reduction factor than 2 may increase the speed of reaching the bottom tier from the top in the image pyramid, but it carries the risk of a greater ambiguity than that of two pixel hence undermining the quality of control in the top-down direction. If the reduction factor is given as 3, it may decrease the possibility of successful prediction for seed points down to 11% (the inverse of the square of 3), as shown in Figure 4.2, which leads to a smaller number of seed points available for initiating the image correlation routines.

On the other hand, a reduction factor smaller than two takes a longer time to reach the bottom tier and particularly needs more complicated sub-sampling operations to derive a reduced image which does not help too much when speckle degrades image

features. Hence the reduction factor as the first key parameter for the image pyramid is assigned as two in the following study.

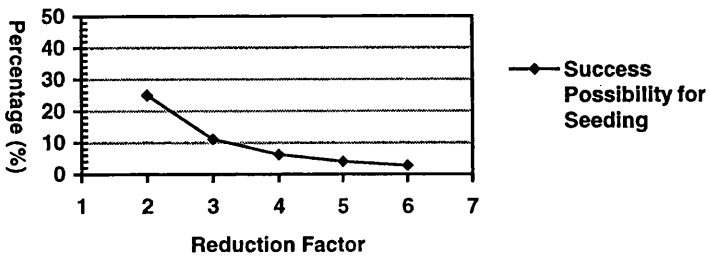

Figure 4.2 Possibility of success for seeding using different reduction factors.

4.2.2 Number of Image Tiers

It is not reasonable to reduce any image down to one pixel for selecting seed points hence the second key parameter for an image pyramid is then to decide what is the appropriate number of tiers or the size of the top image tier. Consider an original image of $M \times M$ pixels being reduced by a factor of two to construct an image pyramid as shown in Figure 4.3. The size of the top tier varies from $A \times A$ pixels down to 1 pixel depending on the number of tiers given.

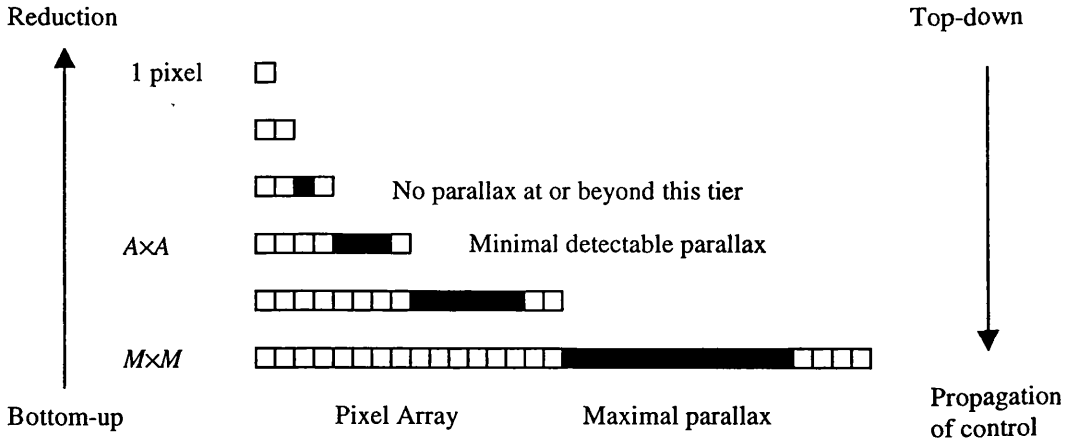

Figure 4.3 Image pyramid derived using the reduction factor of 2.

In case of a SAR image of $M \times M$ pixels reducing to n tiers by a factor of 2, the size of top tier is given as $A \times A$ pixels, or

$$\begin{aligned} & A = M \cdot 2^{1-n}; \quad M \geq A \geq 1; \quad n \in \mathbf{N} \\ \log_2 A &= \log_2 \left(M \cdot 2^{1-n}\right) = \log_2 M + \log_2 2^{1-n} . \\ & n = \log_2 M - \log_2 (A) + 1 \end{aligned} \tag{4.1}$$

n is a natural number. Similarly, an original parallax p, a natural number, at the bottom (original) image tier will be reduced and given as p_i at the i^{th} tier, i.e.,

$$p_i = p \cdot 2^{1-n}; \; p \in \mathbf{N} \tag{4.2}$$

Assuming that a sub-scene image pair for correlation are extracted manually from the original full-scene image at the same location. Thus, if M = 1024 pixels and n = 5 tiers, then A = 64 pixels. If p = 45 pixels, then $p_i = 2.8 \approx 3$ pixels. Before reaching the very top tier with size of one pixel, the parallaxes or the image features of an image pair will be reduced tier after tier in the reduction procedures. If there is no parallax or feature in a reduced image pair, it tends to cause ambiguities in image correlation. There is a need to preserve the parallaxes/features detectable at certain level of the image pyramid.

Although sub-pixel measurement is a common practice in image correlation routines, the gray value (density number) within a pixel after sub-sampling in the reduced image is certainly the same. In fact, there is no difference between parallaxes of 1.6 pixels and 1.9 pixels in a reduced image. A parallax of two pixels guarantees that it is detectable. The largest detectable parallax, however, should not be smaller than two pixels within the i^{th} tier with the size $A \times A$ pixels. Thus, equation (4.2) is valid only if

$$p \cdot 2^{1-n} > 2 \quad \Rightarrow 1 \leq n \leq \text{int}[\log_2 p] \leq \log_2 p \tag{4.3}$$

int[] denotes the integer part of a real number and p is the largest parallax among all pairs of homologous points. For example, if p = 45 pixels, inequality (4.3) gives the number of tiers as

$$1 \leq n \leq \text{int}[\log_2 45] = \text{int}[5.49] = 5$$

According to the region-growing procedures, the results derived from image correlation of each upper tier must be used as the seed points for the lower image tier to propagate control down to the bottom image. The smaller the number of tiers, the more the homologous points will be detected. On the other hand, the lower the image tier, the more the image suffers from speckle. There must be a compromise between two extremes. In addition, it is not practical to carry out image correlation directly at the very bottom image tier to derive a sub-pixel accuracy, due to ambiguities of features in a SAR image pair. Hence the minimal number of tiers must be larger than 2, because the upper tier will be treated as the source of seed points. Thus, inequality (4.3) can be revised as

$$2 < n < \text{int}[\log_2 p] + 1 \tag{4.4}$$

For example, if the largest parallax is measured as p = 45 pixels, then inequality (4.4) gives the number of tiers as $2 < n < 6$. The first choice of the number of tiers is 5 that will give a good start and then n can be decreased to 4 or even to 3, if necessary. This consideration is based on the assumption of parallel orbits of an image pair, i.e., the heading angle difference (azimuth offset) of two images is less than the largest parallax.

4.3 Generation of Seed Points

Seed points are the approximation of the correlated points in an image pair for initiating the least squares correlation process, [Otto and Chau, 1989]. The seed points of each tier are generated automatically using a seeding grid for the left image and searching for their homologous points within the defined uncertainty radius around the predicted location of the right one, [Denos, 1992]. A seeding grid is the definition of the spatial location of seed points used for the least squares correlation in respect to a two-dimensional grid structure. The greater the number of seeding grid cells, the more candidate seed points will be generated. The distance between the neighbouring seed points is called the seeding grid size, or the grid spacing. The larger the grid spacing, the less the number of seed points will be derived. Since there is no definite way established to give the seeding grid spacing or the number of the seeding grid cells, nor that of uncertainty radius, in previous studies of Denos [1992] and Twu [1996], this section develops a method to give these parameters.

4.3.1 Seeding Grid at the Top Tier

In order to guarantee as many seed points as possible derived for region-growing procedures, the top image tier should not only preserve the maximal parallax, but it must also allow the majority of other small parallaxes to be detected. Assuming that the distribution of seed points in a grid form is adopted for the reason of efficiency, and the number of seeding grid cells in a row/column is given as S_g employed to generate seed points. Then, the nominal grid spacing G_s can be calculated as

$$G_s = \frac{A}{S_g} = \frac{M \cdot 2^{1-n}}{S_g} \tag{4.5}$$

Notice that the largest number of seeding grid cells is then decided by the size of the top tier in the image pyramid. Obviously, it is definitely not possible to generate more seed points than the total amount of pixels at the top tier, and it is not reasonable to use every pixel at the top tier as seed points. In addition, as shown in Figure 4.4, a small seeding grid spacing is liable to lose candidate seed points in hilly areas.

On the one hand, if $G_s \rightarrow A$, the grid spacing, or the distance between the neighbouring seed points, approaches the top image size and will be too large to achieve a satisfactory number of seed points. For example, if $G_s = A$, it means that there is only one seed point available, and this is not reasonable. On the other hand, it doesn't make sense to generate redundant seed points within a pixel at the top tier in case of $G_s \rightarrow 1$, i.e.,

$$\begin{aligned} & 1 << G_s << A \quad \Rightarrow 1 << \frac{A}{S_g} << A \\ & \Rightarrow 1 << S_g << A = M \cdot 2^{1-n} \end{aligned} \tag{4.6}$$

Hence the number of seeding grid cells S_g in a row/column can be selected within the range (1: A). The size of the top tier A and the number of tier n is given by equation (4.1) and inequality (4.4), respectively. For example, let the size of the original image be 1024 $\times$ 1024 pixels and the number of tiers 3, then inequality (4.6) gives a number of seeding grid cells in a row/column as $1 << S_g << 256$.

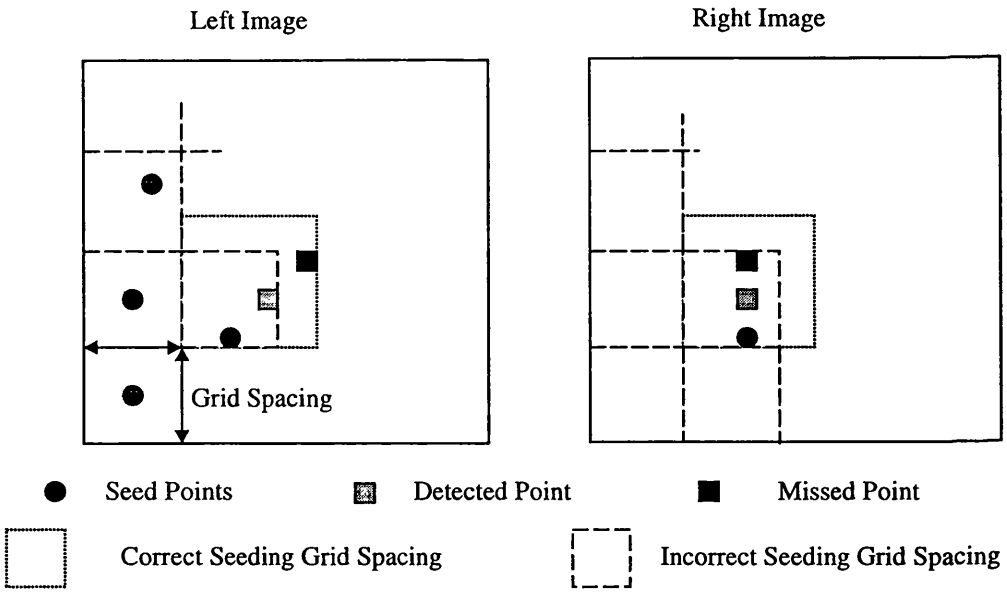

Figure 4.4 A small seeding grid misses points of large parallax.

However, the optimal value still remains unknown in inequality (4.4), it is considered to use the largest parallax to achieve a balance between left and right ends. According to equation (4.2), the reduced parallax at the top tier is given as p_i. Then, equation (4.5) is revised as

$$\begin{aligned} & G_s \approx p_i \qquad \Rightarrow G_s = \frac{A}{S_g} \approx p_i = p \cdot 2^{1-n} \\ & \Rightarrow S_g \approx \frac{A}{p \cdot 2^{1-n}} = \frac{M}{p} \end{aligned} \tag{4.7}$$

For instance, let the original image size be 1024×1024 pixels, the largest parallax 45 pixels. The optimal number of seeding grid cells in a row/column S_g is given as 23 pixels. Let S_g be specified by a natural number to the second power that is suitable for the image pyramid with reduction factor of 2 on the right hand side of inequality (4.6). Then, the number of seeding grid cells in a row/column is given as

$$M \cdot 2^{1-n} >> S_g \approx \frac{M}{p} = 2^{\log_2\left(\frac{M}{P}\right)} \geq 2^{\text{int}\left[\log_2\left(\frac{M}{P}\right)\right]} \tag{4.8}$$

On the right hand side, inequality (4.6) gives

$$1 << S_g \approx \frac{M}{p} = 2^{\log_2\left(\frac{M}{P}\right)} \leq 2^{\text{int}\left[\log_2\left(\frac{M}{P}\right)\right]+1} \tag{4.9}$$

For example, if the size of original image $M \times M$ or 1024×1024 pixels, $p = 45$ pixels and $n = 3$, then inequality (4.8) gives a number of seeding grid cells in a row/column as $16 \approx S_g << 256$, while inequality (4.9) gives $1 << S_g \approx 32$. Both numbers of seeding grid cells in a row/column are expected to work well in providing enough seed points for initiating the least-squares correlation.

4.3.2 Uncertainty Radius of the Generated Seed Point

Given the seeding grid spacing, or the number of seeding grid cells, the candidate seed points in the conjugate image can be generated automatically and randomly within a range in two dimensions by multiplying a scale factor, or the so-called uncertainty radius. Due to random characteristics of terrain relief, a trial-and-error method for giving the uncertainty radius without considering the differences between parallaxes can only generate a limited number of seed points qualified for image correlation, because most of them are liable to be located at distances exceeding the extent of seeding grid spacing.

Consider an uncertainty radius for predicting seed points, the seeding grid size has to be taken into account. Having the number of seeding grid cells in a row/column S_g given by inequality (4.8) or (4.9), the seeding grid spacing G_s of equation (4.5) can be calculated. In order to make full use of each seeding grid cell without interfering with each other, the uncertainty radius U_r is given as the maximal value of one half of the size of a seeding grid cell. It can be easily understood as shown in Figure 4.5 and gives

$$1 \leq U_r \leq \frac{G_s}{2} \tag{4.10}$$

For example, if $M = 1024$, $p = 45$ and $n = 3$, inequality (4.9) gives a number of seeding grid cells in a row/column as 32. Then, the seeding grid spacing can be given by equation (4.5) as $G_s = 256/32 = 8$ and inequality (4.10) gives uncertainty as $1 \leq U_r \leq 4$. If the terrain relief varies, a better value of U_r can be selected from the right limit of inequality (4.10) providing a larger uncertainty radius. Incidentally, if the uncertainty radius of a generated

seed point is much less than $0.5G_s$, it tends to generate a small number of seed points in areas having small parallaxes, due to failures of correlation of the larger parallaxes. Generally, it is not a critical problem provided that the region-growing harness can work by starting correlation from flat areas where enough seed points remain and the terrain relief is always moderate and continuous through the entire area.

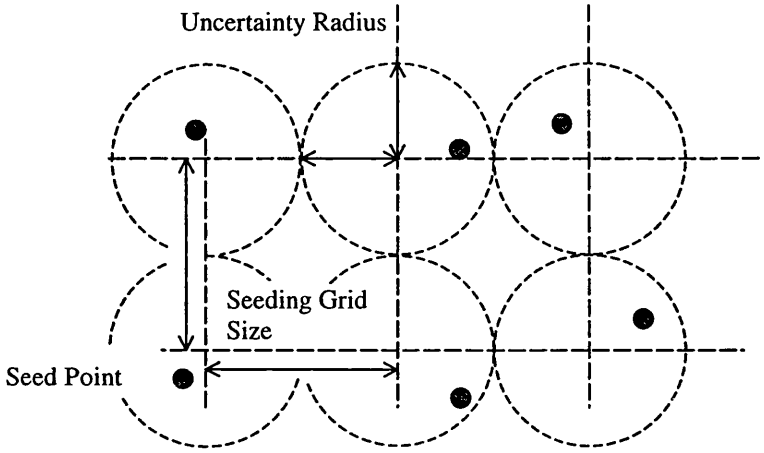

Figure 4.5 Uncertainty radius of a candidate seed point.

4.3.3 Optimized Parameters for an Image Pyramid

The performance of the pyramidal image correlation scheme varies with different parameters, such as the number of image tiers and that of seeding grid cells for generating seed points as stated before. Firstly, the largest parallax should be decided manually, or calculated by any coarse DEM available using the approximate parallax formula as described in Leberl [1990]. The next step is setting the number of tiers. It is expected to have a good start for image correlation by setting up the number of tiers according to the right limit of inequality (4.4), and then reduce the number of tiers gradually to the left limit, if necessary. The seed points of the top tier can be generated evenly in a grid form to ensure the success of the region growing approach. Subsequently, the number of seed points is given using equation (4.5) and inequality (4.8) or (4.9). The uncertainty radius for predicting the seed points can be decided by one half of seeding grid spacing to guarantee that seed points may fall within the expected extent and then provide enough good seed points. Finally, inequality (4.10) gives the uncertainty radius of seed points to be detected.

These parameters are related with the largest parallax and particularly the number of image tiers. Notice that parameters selected near two extremes of inequality (4.6) may lead to risks of failure in image correlation. Thus, all of the parameters for controlling an image pyramid in the correlation scheme can be decided without a laborious trial-and-error approach. The largest parallax is the only input for optimizing the decision strategy. A flow chart for optimizing the selection strategy of parameters in pyramidal matching scheme is shown in Figure 4.6.

The procedure starts from the maximal number of tiers to carry out image correlation procedures for the first run. A full explanation of the pyramid least squares correlation routines employed in this thesis can be found in Denos [1992] and Twu [1996]. Further illustrations of the region-growing approach for image correlation refer to [Otto and Chau, 1989]. The software used in this chapter is given in Appendix A.

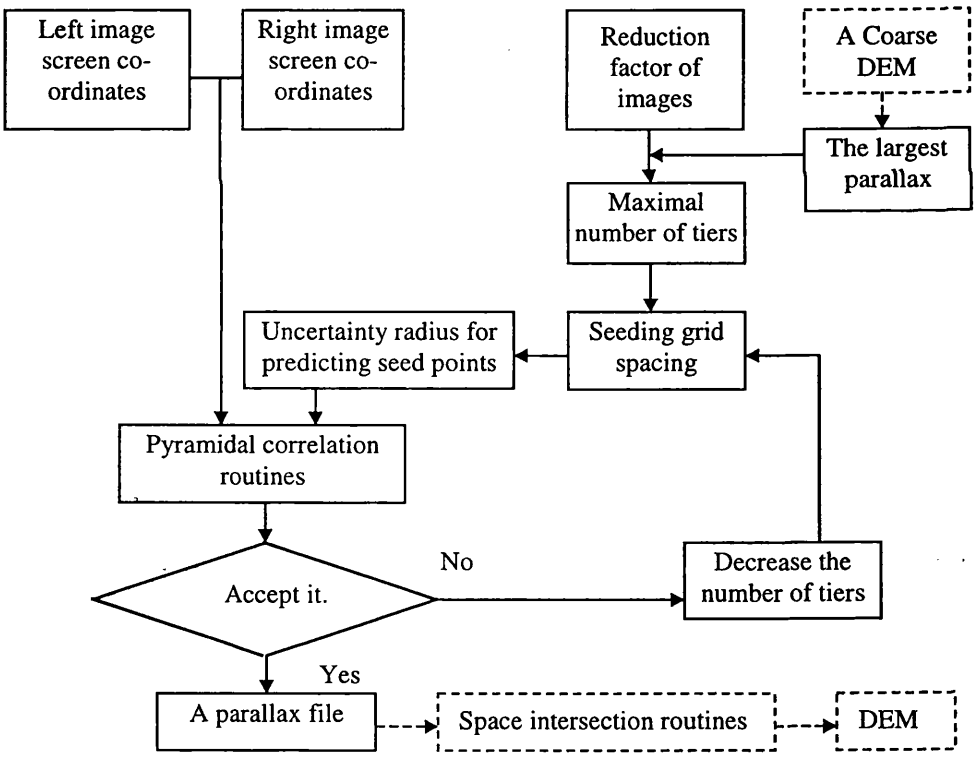

Figure 4.6 An optimized strategy for pyramidal image correlation scheme.

If the results are not accepted, another run of image correlation of a smaller number of tiers is followed to seek a better result. The result of these procedures is a parallax file providing all of the image co-ordinates of the successfully matched points that can be imported into the space intersection routines together with other header information to generate a DEM as described in Chapter 3.

4.4 Test Results

4.4.1 Test Images and the Reference DEM

Two RADARSAT SAR sub-scene images of the descending orbit DS1 and DS7b, provided under the ADRO programme as in Table 3.4, have been tested to validate the above inference. Both images are located on the Aix-Marseilles test area in south France. A sub image of 1024 × 1024 pixels was extracted from each full-scene SAR image as shown by an example in Figure 4.7 for image DS1 (see Appendix D.1 for the full-scene DS1 at a larger scale). The descending images of the sub-scene extracted from DS1 and DS7b is shown in Figure 4.8 (see Appendix D.2 for the sub-scene DS1 at a larger scale).

The test area for image correlation covers the urban area of Marseilles, the southern part of Chaine de l'Etoile, Mountain St. Cyr and a small portion of the Mediterranean Sea. The terrain relief within the sub-scene image varies from 0 m to 646 m above mean sea level at Mountain St. Cyr. The central and eastern part of the test image is occupied by hilly mountain where serious layover effects are evident.

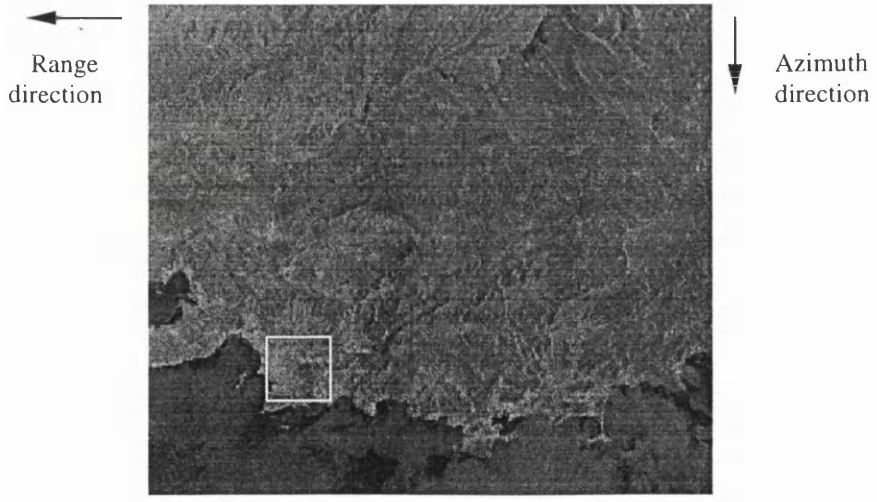

Figure 4.7 Location of the extracted image in the full-scene SAR image DS1.

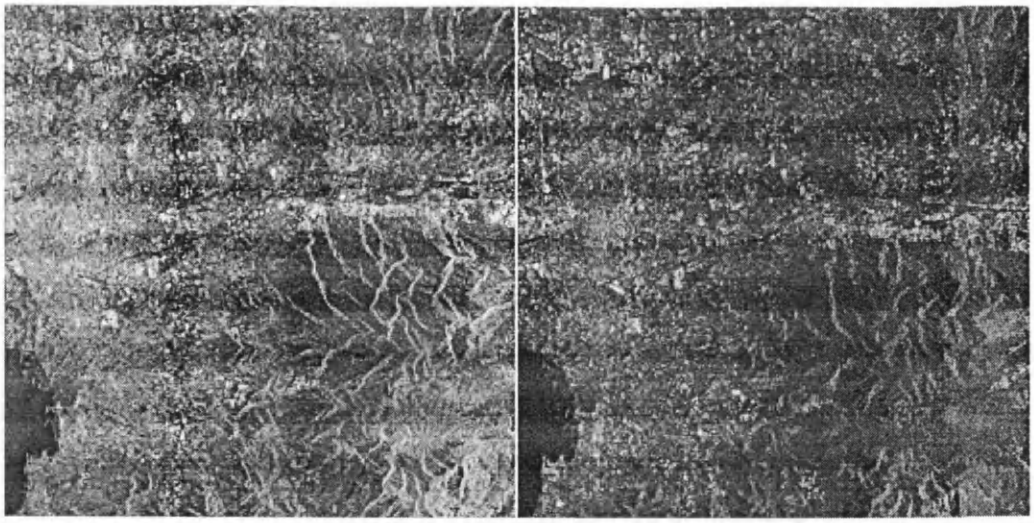

Figure 4.8 Sub-scene image pair for stereo-image correlation. (Left: DS1 image; Right: DS7b image. Size: 1024 × 1024 pixels)

A corresponding reference DEM of the test site extracted from an IGN (*Institut Geographique National*) DEM at French Lambert Conformal Conic Zone III projection system, as shown in Figure 4.9, which covers a 13.5km × 13.5km area with original resolution of a 50m grid, will be compared with the DEM generated. Appendix D.3 and D.4 show the original IGN reference DEM in a 50m grid and the extracted DEM at a larger scale, respectively.

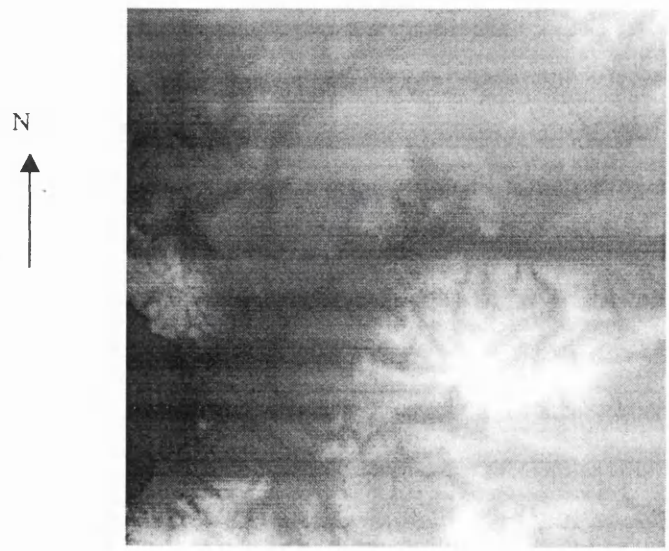

Figure 4.9 Extracted reference DEM for comparison (Size: 13.5km × 13.5 km in a 50m grid).

The height accuracy quoted as ±5m refers to each reference DEM grid point only, according to the specifications of the DEM data given by IGN, [Alias, 1994, private communication]. This is reasonable for evaluation of the DEMs derived from SAR image pair whose theoretical accuracy is expected to be of the order of 10m as stated in Chapter 3. However, it can be expected that the accuracy in height derived for an arbitrarily interpolated point in the reference DEM may be more or less inferior to that quoted figure as ±5m. The following sections show comparisons between the interpolated reference DEM and the corresponding DEM elements derived using the pyramidal image correlation and the weighted space intersection routines. The resultant DEMs derived using different kinds of combinations of parameter will be summarized and analyzed to validate the proposed strategy for parameter selection.

4.4.2 Evaluation of the Automatically Generated DEMs

Regarding the generation of the DEMs that are the final product of pyramidal correlation procedures, there are two GCPs selected manually to correct the systematic shift caused by the inferior orbit information provided by RADARSAT SAR data as stated in Chapter 3. Initially, the results derived from space intersection and a series of co-ordinate transformation are random points with irregular distribution through the test-site. In order to make comparisons between the reference DEM and the generated ones, the corresponding elevation of any point in the reference DEM has to be interpolated according to the position of the derived elevation point. The DEMs derived from image correlation as shown in the following section will be discussed again in Chapter 5 and 6. More details will be given together with discussion and other topics, such as the impacts from automatically generated GCPs. A typical generated DEM is shown in Figure 4.10.

There are two criteria specified for comparing the results derived from image correlation: the percentage of the successfully correlated points of image C_p and the conventional accuracy statistics of the generated DEMs. The former shows the quantity and density of the results derived from image correlation, the latter indicates the quality of the final results as used traditionally. The first quality measure is given by

$$C_p = \frac{T_s}{T_p} \tag{4.11}$$

T_s is the total number of the successfully correlated samples and T_p the total population of candidate pixels to be correlated within the overlapping area of an image pair. It is assumed that the image size $M \times M$ pixels is the same for the left and right ones with the shape of a square and the image pair is selected manually from the same location, according to the requirements of a least squares correlation algorithm, [Ackermann, 1984], [Gruen, 1985]. A typical overlapping image pair shows the configuration as in Figure 4.11.

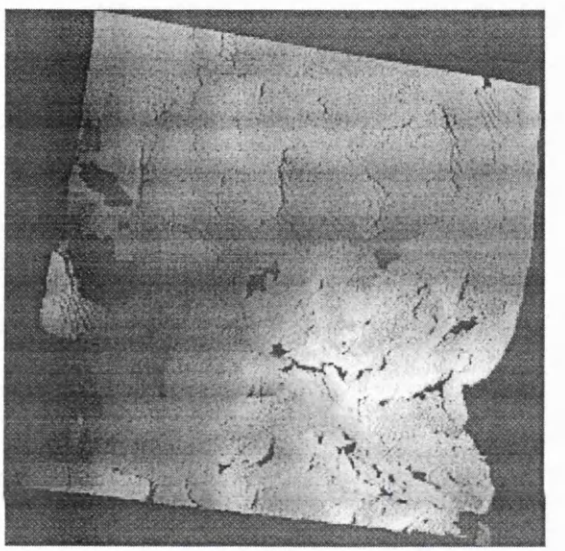

Figure 4.10 A DEM generated from the descending RADARSAT SAR image pair (using three tiers, the number of seeding grids 32×32 and uncertainty radius 3 pixels). Size: 13.5×13.5 km with a 25 m grid, approximately.

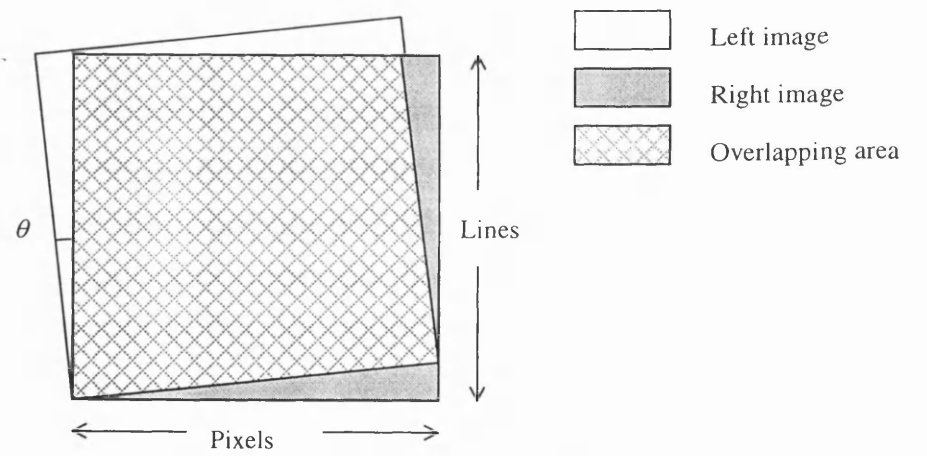

Figure 4.11 A sketch of an overlapping SAR image pair.

Because each image of a pair is not always perfectly parallel to each other, the configuration of the same-side stereoscopic radargrammetry determines the percentage of the overlapping area of an image pair, according to the convergent angle θ between the two heading angles of the images. Also, it is not possible to carry out image correlation around the fringe of the overlapping area. The total number of pixels of the fringe area (H) where image correlation is not effective depends on the size of the image correlation window ($Q \times Q$ pixels) employed and the original image size ($M \times M$ pixels), or $H=2W \times M-4W^2$ pixels. For example, let Q=40 pixels and M=1024 pixels, then, H=75,520 pixels, which is equivalent to 7.2% of the number of pixels of the image for correlation.

Therefore, the total population of image pixels to be correlated is definitely less than that of the overlapping area and even less than that of the entire left or the right image. It is also not easy to calculate the exact population of pixels to be correlated before correlation, since the parallax of each conjugate point pairs varies. For the sake of convenience of comparison, the total population of image pixels to be correlated within the overlapping area of an image pair will be referred to the number derived from the product of range pixels multiplied by azimuth lines. This is a relatively conservative estimation for the percentage of the successfully correlated points. Nevertheless, it meets the need of comparison based on the same total population without exaggeration of the results and is not misleading in evaluation of the results of image correlation.

4.4.3 Evaluation of the Optimized Parameters

In this section, attention will be focused on the performance of the pyramidal correlation scheme directed by the optimized parameters to see the impact on the resultant DEMs from different parameter combinations. According to the procedures described before, the image correlation scheme is initiated by setting the parameters for the configuration of the image pyramid and for the generation of seed points. Firstly, the largest parallax is measured manually as 47 pixels approximately. Inequality (4.4) gives the number of tiers as $2<n<6$. Let n = 3, the number of seeding grid cells in a row/column is given as $16<S_g<<256$, according to inequality (4.9). Then, the uncertainty radius is derived using inequality (4.10) giving $1 \leq U_r \leq 4$. Notice that there is no fixed value for each parameter, since the terrain relief can vary from one end to the other for any image. These optimized parameters are given within an extent that minimize trial-and-error operations hence the pyramidal correlation scheme can then be carried out smoothly.

In order to clarify the influence from a specific parameter for the pyramidal correlation scheme, there is a need to isolate only one kind of parameter each time, while the others remaining the same. Firstly, for example, let the uncertainty radius for predicting seed points be 3 and then change the other parameters, such as the number of seeding grid cells and of tiers. Secondly, fix the number of seeding grid cells and give different numbers of tier, case by case, to see the consequences, and so on. Therefore, there are many combinations of parameters available for pyramidal image correlation scheme. Finally, the results from the pyramidal correlation scheme as a parallax file must be imported into the space intersection routines to solve the ground points as shown in Chapter 3.

The results derived are then transformed back into the French Lambert Conformal Conic Zone III co-ordinate system where a reference DEM can be compared. Table 4.1 shows the accuracy of the DEMs derived and the percentage of the correlated points. Those cases that failed to carry out image correlation are labeled as 'N/A' in the corresponding column.

The uncertainty radius was set as 3 pixels with different numbers of seeding grids in a row/column (8, 16, 32, 64 and 128) and different numbers of image tiers (3, 4, 5, 6, 7 and 8) for the pyramidal image correlation scheme. Since the other numbers of seeding grids in a row/column, such as 2, 4 or 256 failed to generate enough seed points at the top tier to proceed image correlation procedures, there is no result available to be shown in Table 4.1. Figure 4.12 and 4.13 demonstrate the comparisons of the coverage and accuracy of the generated DEMs between different numbers of seeding grids while using 3 and 4 tiers, respectively. In terms of the accuracy and coverage of the DEM generated, there is no significant difference between the results derived from various combinations of parameters in Table 4.1, also shown in Figure 4.14.

In order to see the effects from different sizes of uncertainty radius for predicting seed points, the initial uncertainty radius 3 pixels was replaced by 1 pixel to repeat all of the possible combinations for image correlation. The DEMs derived using the uncertainty radius as 1 are listed according to different parameter combinations as shown in Table 4.2. Obviously, Table 4.2 shows similar results to those presented in Table 4.1. For instance, Figure 4.15 indicates that different numbers of seeding grid cells do not cause significant change of the accuracy and coverage of the DEM derived.

Uncertainty Radius	Number of seeding grid cells in a row/column	Total number of tiers	DEM coverage (%)	Accuracy of DEM (m)
3	1/2/4	3~8	N/A	
	8	3~4	N/A	
		5	78.4	21.4
		6	77.6	21.2
		7	78.1	21.8
		8	N/A	
	16	3	82.8	23.8
		4	79.3	22.9
		5	78.3	21.6
		6	77.2	21.2
		7~8	N/A	
	32	3	83.6	22.8
		4	78.8	23.6
		5	78.0	21.2
		6~8	N/A	
	64	3	82.3	26.1
		4	78.0	22.3
		5~8	N/A	
	128	3	78.2	25.0
		4~8	N/A	
	256	3~8	N/A	

Table 4.1 DEM results using different numbers of tiers and those of seeding grid cells, while fixing the uncertainty radius as 3 pixels at the top tier.

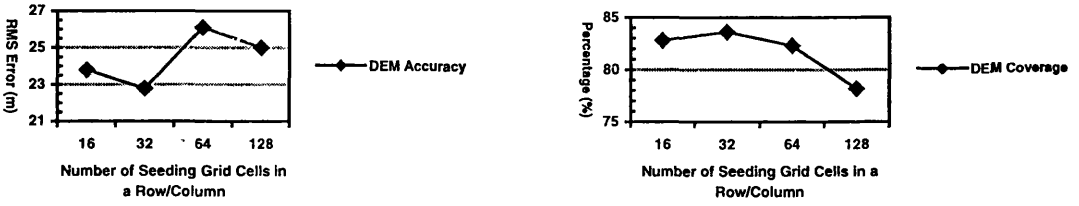

Figure 4.12 Accuracy (left) and coverage (right) of the generated DEMs, given 3 image tiers and uncertainty radius 3 pixels.

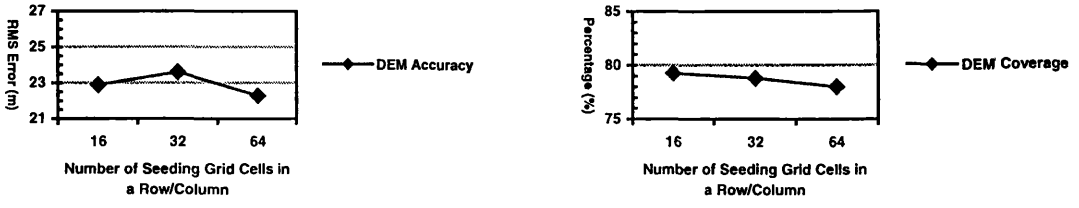

Figure 4.13 Accuracy (left) and coverage (right) of the generated DEMs, given 4 image tiers and uncertainty radius 3 pixels.

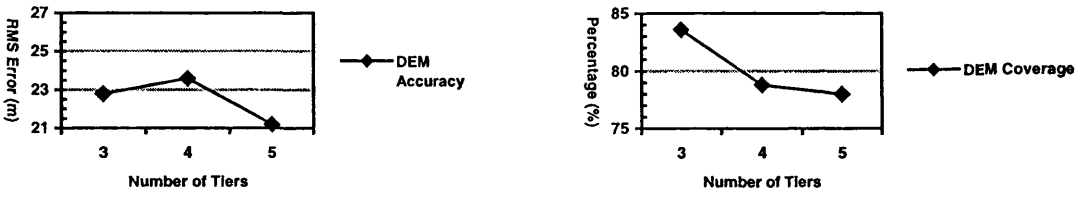

Figure 4.14 Accuracy (left) and coverage (right) of the generated DEMs, given a number of seeding grid cells 32 by 32 and uncertainty radius 3 pixels.

Uncertainty Radius	Number of seeding grid cells in a Row/Column	Total number of tiers	DEM Coverage (%)	Accuracy of DEM (m)
1	1/2/4	3~8	N/A	
	8	3~4	N/A	
		5	77.9	20.7
		6	77.5	21.8
		7~8	N/A	
	16	3	N/A	
		4	79.4	22.1
		5	78.2	21.4
		6	77.8	22.0
		7	78.0	21.4
		8	N/A	
	32	3	83.5	22.1
		4	78.4	22.7
		5	77.8	21.0
		6~8	N/A	
	64	3	82.1	24.4
		4	78.3	23.7
		5~8	N/A	
	128	3	77.8	24.9
		4~8	N/A	
	256	3~8	N/A	

Table 4.2 DEM results using different numbers of tiers and those of seeding grid cells, while fixing the uncertainty radius as 1 pixel at the top tier.

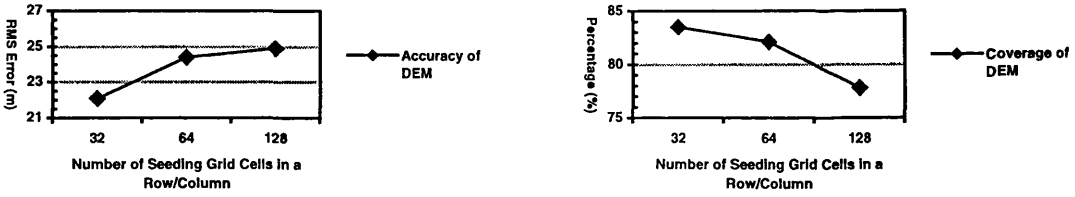

Figure 4.15 Accuracy (left) and coverage (right) of the generated DEMs, given 3 image tiers and uncertainty radius 1 pixel.

In the case of using the uncertainty radius as 5 pixels and repeating all of the experiments carried out in Table 4.1 and 4.2, similar results are derived again as in Table 4.3 and Figure 4.16. Comparing the results of image correlation derived as in Table 4.1, 4.2 and 4.3, the uncertainty radius, ranging from 1 to 5 pixels for predicting seed points, is not a critical parameter for the final outcome, in terms of the DEM coverage and accuracy derived. Apparently, when the parameters, such as the number of seed points and that of image tiers, are given properly according to the proposed decision strategy, the results derived from the pyramidal image correlation procedures show similar results, otherwise, it simply fails to proceed.

Uncertainty Radius	Number of seeding grid cells in a Row/Column	Total number of tiers	DEM Coverage (%)	Accuracy of DEM (m)
5	1/2/4	3~8	N/A	
	8	3~4	N/A	
		5	78.3	21.6
		6	78.0	21.6
		7~8	N/A	
	16	3	77.7	24.1
		4	79.3	21.9
		5	78.0	22.1
		6	78.0	22.2
		7~8	N/A	
	32	3	82.7	22.3
		4	78.7	21.6
		5	77.9	21.7
		6	77.9	22.0
		7	77.9	21.7
		8	N/A	
	64	3	82.0	23.3
		4	78.0	21.7
		5~8	N/A	
	128	3	78.3	25.1
		4~8	N/A	
	256	3~8	N/A	

Table 4.3 DEM results using different numbers of tiers and those of seeding grid cells, while fixing the uncertainty radius as 5 pixels at the top tier.

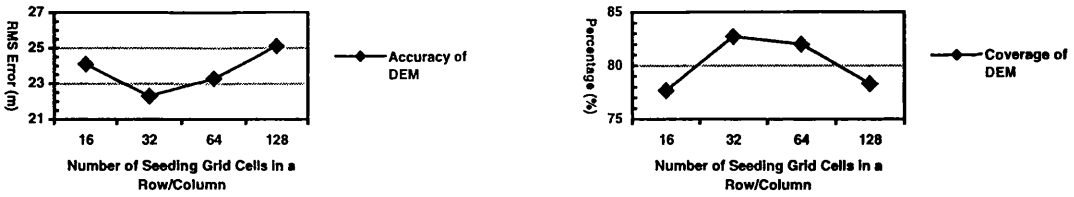

Figure 4.16 Accuracy (left) and coverage (right) of the generated DEMs, given 3 image tiers and uncertainty radius 5 pixels.

4.4.4 Discussion

Previous work carried out by Twu [1996] for ERS-1 SAR image correlation shows that the quality of the DEMs derived is relatively inferior to that derived in this chapter. In addition, the extent of terrain relief variation of the test area selected by Twu [1996] is 210m, but that of the test area used in this thesis is about 640m. It seems that a relatively poor stereo intersection geometry of ERS data affects the results derived by Twu [1996]. On the contrary, a good intersection configuration of SAR image pair is available from RADARSAT SAR data used in the thesis. The strategy of selecting parameters used to command the pyramidal geometry and of generating seed points may be of relevance. Twu [1996] and Denos [1992] employ a trial-and-error approach to decide the parameters that are required to construct the pyramidal geometry. Generally, Twu [1996] utilizes a relatively greater number of image tiers (8 tiers) that is liable to lose image feature in the very top image tier and to decrease the number of seed points available. Hence propagating control from top to down (the bottom image tier) can be difficult and blunder errors are liable to occur.

The pyramidal image correlation may perform well in terms of the DEM coverage and accuracy derived, provided that the parameters are given following the rule suggested in this thesis. The number of image tiers is related to other parameters. Particularly, a smaller number of tiers is better than a larger one, because a larger number of tiers leads to a smaller size top tier that allows only a relatively small number of seed points. The results derived meet the prediction made before. It can be seen when the number of seeding grids in a row/column is given smaller than 16, say 8, the number of seed points will not be enough to initiate the region-growing correlation procedures. On the other hand, it is also not good to let the number of seeding grids in a row/column approach or greater than 256, as the correlation routines cannot proceed further in such a case that

validates the inference of inequality (4.8) and (4.9). According to the above experimental results, the uncertainty radius for predicting seed points is not critical to the outcome.

Regarding the accuracy of the DEM derived in this chapter, there is no specific trend showing that changing various parameters may improve or degrade the results derived significantly. The results derived show that the pyramidal correlation method may lead to reasonable results, or it just fails to proceed, depending on the pyramid being defined and the parameters given. The comparisons of the results derived prove the stability of the least-squares correlation with a region-growing approach when the pyramidal structure has been defined reasonably.

In terms of the generation of DEMs using stereo RADARSAT data, the results derived in this chapter are comparable with those results obtained by other authors, as shown in Table 4.4. The relief extent and actual complexity of terrain surface differ from case to case, and the difference of the acquisition time of the image pair employed varies. For instance, the acquisition time of the images used in this chapter differs more than six months! The image DS1 employed in this thesis has evident layover effects hence information loss can be serious (see Chapter 6 for more detailed discussion). Also, the actual performance of other geometric models proposed are not known, since there are no RMS errors of independent check points reported (recall Chapter 3). Therefore, it is not convenient to evaluate the results of image correlation derived by different authors.

Author(s)	The Author	Raggam and Gutjahr [1998]	Sylvander *et al.* [1998]	Toutin [1999]
RADATSAT Image Mode	Standard (S1+S7)	Fine (F5+F1)	Fine/Standard	Fine/Standard
DEM Accuracy (m)	**21~26**	**35**	**9~51/21~42**	**25~34/14~45**
Test Site	South France (Aix-Marseilles)	Austria (Northern Styria)	South France (Salon de Provence)	Canada (Sherbrooke)
Terrain Relief (Extent in m.)	**Moderate-to-hilly** (640)	**Hilly** (400~1900)	**Flat-to-moderate** (less than 400m)	**Flat-to-moderate** (450)
Correlation Algorithm (Source)	Pyramidal least squares correlation	Normalized cross-correlation measure	DAUPHIN Image correlator (IGN)	Multi-scale cross-correlation measure (PCI®)
Geometric Model **(Requirement of GCPs)**	Rigorous space intersection **(No GCPs)**	Parametric model **(Parameters determined by GCPs)**	Image block triangulation **(GCPs/tie points required)**	Parametric model set-up manually **(GCPs required)**

Table 4.4 Comparison of the DEMs derived using image correlation by different authors.

Further efforts for automation of generating a DEM should consider the method of the provision of ground control that is currently carried out using a manual method. Automatically generated GCPs will be investigated in Chapter 5 to improve the overall quality of the DEM generated. More detailed study will be carried out in Chapter 6 to give a close look at the DEM generated together with further refinement and analysis.

4.5 Summary

This chapter describes the pyramidal image correlation scheme that can achieve a higher level of automation for producing a parallax file from same-side image pairs. The strategy is mainly based on the analysis of the greatest parallax in an image pair and a pyramidal geometry. The image pyramid is described using the number of tiers and the reduction factor between each tier. The number of image tiers is related to the maximal magnitude of parallax. The generation of seed points is controlled by the seeding grid spacing and the uncertainty radius to predict the location of seed points that is also related to the size of the maximal parallax of an image pair and the number of image tiers. The optimized strategy of selecting parameters for the pyramidal matching scheme avoids a trial-and-error approach and reduces the manual operations at the first stage of image correlation. The greatest parallax of an image pair is the only input required. The pyramid geometry and the relationship between various parameters in the generation of seed points have been clarified and applied to the generation of DEMs from stereoscopic RADARSAT data.

Chapter 5

Automation for Providing Control

5.1 Introduction

The demand for Ground Control Points (GCPs) in radargrammetry is usually provided by measuring co-ordinates from maps and images manually. Uncertainty is liable to arise in such a manual method for collecting GCPs hence the quality of the radargrammetric results generated cannot be assured, as mentioned in Section 2.5. Synthetic Aperture Radar (SAR) image product simulation techniques have been used to provide control for geocoding by using an existing Digital Elevation Model (DEM). Most of the currently available methods are based on simplified image-object models that ignore the physical reality of a SAR image, such as Naraghi *et al.* [1983], Domik *et al.* [1986], Arai [1991], Wivell *et al.* [1992] and Guindon [1993]. Many human interventions are required for the simplified simulation methods.

In terms of a more rigorous approach for SAR image simulation, the provision of ground control is always given as the pixel offsets of the simulated image in respect to the real image co-ordinate system, according to Kwok *et al.* [1990]. This does not fulfill the need of a rigorous stereo intersection algorithm that requires the exact position vectors of GCPs, as described in Chapter 3. Other simulation methods demand extra parameters that require extra human interventions, such as incidence angles, range and azimuth time offsets, to carry out image simulation, for instance, Gelautz *et al.* [1998]. Hence the level of automation for providing control can be degraded. In general, there is no equivalent approach being proposed to provide control for the results derived from SAR stereo intersection.

This chapter describes a new method of automatic provision of control for radargrammetry using a simulation method to reduce manual operations, and then to improve and to stabilize the quality of GCPs. The requirement is that a small patch of DEM, say 1km × 1km area, with varied terrain surface is available. Section 5.2 describes the details of the proposed simulator that is based on a simple reflectivity model, the

assumption of the perpendicular relationship between the resultant range and velocity vectors in SAR imagery, a known DEM chip and the header/orbit data of a real SAR image. Four corner points of the known DEM are treated as GCPs whose ground co-ordinates are already known, but the real image co-ordinates of the GCPs have to be derived using a real-simulated image correlation technique. The simulator also gives the simulated range and azimuth time data for the GCPs based on the imaging geometry that can be compared with those observations derived from the real image.

The real-simulated image correlation routine used for registering the simulated image chip onto the real image co-ordinate system is illustrated in Section 5.3. This gives the observations of the range and azimuth time data of the GCPs required, hence the range and azimuth time corrections can be made. The examples of the applications of providing control for the radargrammetric results using the proposed simulation method based on a known DEM chip are shown in Section 5.4. Two data sets of different orbit passes, including ascending and descending orbits, have been tested to validate the algorithms for generating GCPs to correct the systematic shifts of the DEMs derived using the stereoscopic RADARSAT SAR images. If the systematic shift of the DEM derived is eliminated reasonably, further analysis and refinement for the stereo-generated DEM can be carried out as discussed in Chapter 6. Further applications of the automatically generated GCPs will be applied to geocoding as presented in Chapter 7.

5.2 The Proposed Simulator

The basic requirements of the proposed SAR image simulator include the header information of a real SAR image, the corresponding orbit data and a small DEM chip containing non-flat topography. The header information of a real SAR image gives the image structure for simulation, such as ellipsoid parameters, scene centre heading angle, range sampling rate, azimuth line and range pixel spacing of a real SAR image, CSA [1995]. The orbit data provided with a SAR image include state vectors, such as the position and velocity vectors of the sensor, and the corresponding azimuth time of each data point hence connecting individual azimuth lines as an entire SAR image. The DEM with reasonably varied terrain surface may generate significant foreshortening or layover effects as image features that make the simulated-real SAR image correlation possible with no regard to other ground truth data.

The SAR image simulator is considered according to two aspects: the geometric structure and radiometric characteristic of a simulated image. Since the main concern of the proposed simulator is the provision of ground control with a higher level of automation, the following assumptions are made:

(1) Geometrically, the velocity vector of the sensor is perpendicular to that of the range vector. In the case of space-borne SAR data, the velocity of a ground point or the Earth rotation must be considered. Also, it is assumed that the structure of a real SAR image is well defined by the header/orbit information allowing automatic detection of the extent of the simulated area without human intervention.
(2) In terms of radiometric considerations, a simple reflectivity model is applied to the entire simulated area without regard to speckle or different ground cover, as mentioned in Section 2.5. This is because the detailed ground truth data of an arbitrary real image, which affects the reflectance of a radar wave, is not always available.

The geometric considerations for a SAR image simulator include the simulation of the image structure of a real image with no manually defined parameters required, such as the range and azimuth time offsets and incidence angles which are demanded by other methods. In addition, radiometric considerations lead to a method for deciding the normal of a DEM cell, and give the density number (*DN*) of an image pixel according to a relatively simple reflectivity model (see Section 2.5.2 and 5.2.3).

5.2.1 Geometric Considerations

The track of a sensor in 3-D space is a smooth curve that is continuous and differentiable. There always exists a tangent passing through a point on the orbit, say **S**, and a normal plane perpendicular to the tangent at point **S** as shown in Figure 5.1. Physically, the position vector of a SAR sensor **S** (S_x, S_y, S_z) is changing along its orbit corresponding to its azimuth time, and the tangent at the point **S** coincides with the sensor velocity vector $\mathbf{V_S}$ (V_{Sx}, V_{Sy}, V_{Sz}). The normal plane, the x-z plane in Figure 5.1, passing through the point **S** represents a zero-Doppler plane with an equal range circle from the sensor to ground points.

Thus, the azimuth lines and range pixels of a SAR image are represented by elements on y-axis and x-axis, respectively, and form the co-ordinate system of the SAR

imagery. Following the azimuth time sequence, the position vector and the velocity vector of the sensor is changing and holding a normal plane that scans the sensed area and detects each DEM point to build a simulated image. A plane in space is given as

$$\begin{aligned} & c_1 \cdot X + c_2 \cdot Y + c_3 \cdot Z = c_0 \\ & (V_{Sx} - V_{Px}) \cdot X + (V_{Sy} - V_{Py}) \cdot Y + (V_{Sz} - V_{Pz}) \cdot Z \\ & = (V_{Sx} - V_{Px}) \cdot S_x + (V_{Sy} - V_{Py}) \cdot S_y + (V_{Sz} - V_{Pz}) \cdot S_z \end{aligned} \tag{5.1}$$

c_1, c_2 and c_3 are the direction cosines of the normal to the plane, directed from the origin in a geocentric co-ordinate system to the plane; c_0 the length from the origin to the plane; (X, Y, Z) the co-ordinates of any point **P** in the plane. The velocity vector of the sensor is corrected by the Earth rotation $\mathbf{V_P}$ (V_{Px}, V_{Py}, V_{Pz}).

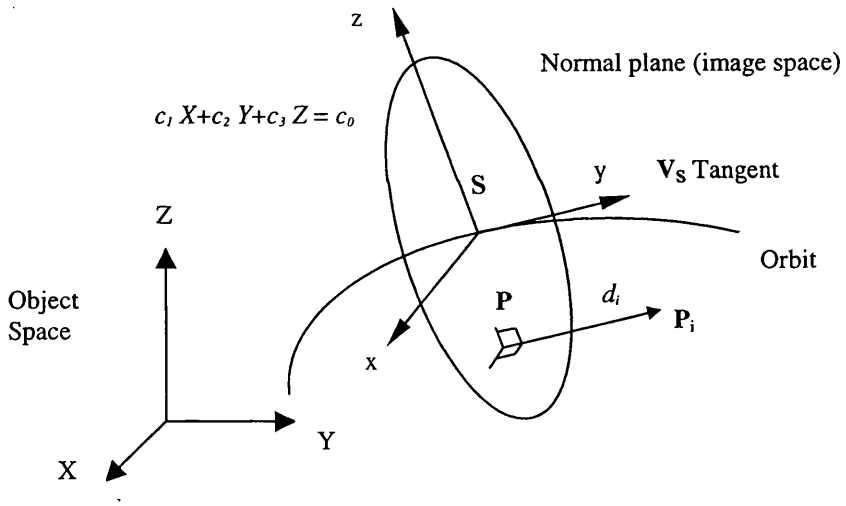

Figure 5.1 A sensor's track in 3-D space.

The concept of the proposed SAR simulation method is based on the zero-Doppler imagery and on the scanning process from the first azimuth line to the last one through the entire simulated area where each normal plane derived resembles the corresponding azimuth line. There remain unknown parameters to be solved, such as the range and azimuth timing offsets, which define the extent of the simulated area, and the incidence angle for each pixel, which constitutes the image structure. These parameters will be derived in the next section based on the consideration of the structure of a real SAR image.

5.2.2 The Structure of the Simulated Image

The structure of a simulated SAR image can be defined by the size of the range pixels and azimuth lines and by the extent of the simulated image. On the one hand, the azimuth timing difference between two neighbouring lines of a real satellite SAR image is generally consistent, due to a relative stable sensor speed, CSA [1995], hence that timing difference can be treated as the 'sampling width' of a simulated image. On the other hand, the range sampling rate provided by header data, CSA [1995], gives the slant range timing data of a real SAR image, so, the physical range sampling width can be restored for a simulated image. The corresponding ground-range image can be reconstructed based on the consideration of the incidence-angle in respect to the ellipsoid. Having derived the 'sampling width' of both components of the real SAR image, the extent of the corresponding simulated image can be decided gradually using the relationship between the DEM chip being sensed and the real SAR imaging geometry. The details needed to restore the SAR image structure are given in the following sections.

5.2.2.1 The sampling width of azimuth lines

The reflected power back from each sampled element of the scanned terrain surface within half distance of the azimuth sampling width d_w, or the azimuth spacing, is calculated and projected to the corresponding azimuth line of the simulated image. It is assumed that the sampling width of each azimuth line or the speed of the sensor is consistent within the simulated area. In respect to a near-circular orbit of the platform and a relative short journey of the sensor within a SAR scene, say 15 sec for the RADARSAT platform, the sensor speed is literally stable. However, the velocity vectors of the changing azimuth time of a SAR scene have to be considered as shown in equation (5.1). The sampling width of a real image d_w is calculated, using the total flying time between the azimuth time of the first azimuth line A_f (sec) and that of the last azimuth line A_l (sec) and the total number of azimuth lines N_a of a real SAR image, by

$$d_w = \frac{|A_f - A_l|}{N_a - 1} \cdot |\mathbf{V}_s| \,, \qquad \text{if} \quad |\mathbf{V}_s| \approx const. \tag{5.2}$$

The number N_a and the sensor speed $|\mathbf{V}_S|$ (m/sec) can be collected from the orbit/header data provided, CSA [1995].

As the input for simulation, a DEM has to be transformed from a local co-ordinate system into a geocentric system (Earth-fixed or Earth-rotation one depending on the definition of a real SAR image given), as in Section 2.6, producing a set of points in 3-D space. Falling within half of the sampling width, the DEM points are detected for each azimuth line by calculating the distance d_i (m) between each DEM point $\mathbf{P}_i(X_i, Y_i, Z_i)$ and the normal plane, as shown in Figure 5.1. Thus, the criterion for detecting a DEM point is given, according to analytic geometry, as

$$d_i \le \frac{1}{2}|d_w| \;;$$

where

$$d_i = \frac{(V_{Sx}-V_{Px})\cdot X_i + (V_{Sy}-V_{Py})\cdot Y_i + (V_{Sz}-V_{Pz})\cdot Z_i}{\sqrt{(V_{Sx}-V_{Px})^2+(V_{Sy}-V_{Py})^2+(V_{Sz}-V_{Pz})^2}} - \frac{(V_{Sx}-V_{Px})\cdot S_x + (V_{Sy}-V_{Py})\cdot S_y + (V_{Sz}-V_{Pz})\cdot S_z}{\sqrt{(V_{Sx}-V_{Px})^2+(V_{Sy}-V_{Py})^2+(V_{Sz}-V_{Pz})^2}} \tag{5.3}$$

5.2.2.2 The extent of azimuth lines

It has been assumed that the orbit data is known and covers the simulated area. The first and the last data point of the selected orbital path provided by the SAR header file can be used as the initial points for specifying the extent of the DEM at the simulated area, given the azimuth time of the first and the last data point of the orbital path as $A_f^{(0)}$ (sec) and $A_l^{(0)}$ (sec), respectively. The corresponding azimuth time of the first and the last azimuth line of the simulated image, given as A_f' (sec) and A_l' (sec), respectively, can be derived by the following progressive approach.

Let the minimal linear distance from the DEM point $\mathbf{P}_f$ to the normal plane at the first orbit position $\mathbf{S}_f^{(0)}$ be $|d_f|^{(0)}$ and the minimal distance from the DEM point $\mathbf{P}_l$ to the normal plane at the last orbit position $\mathbf{S}_l^{(0)}$ be $|d_l|^{(0)}$, respectively. Consider the sensor position moving from $\mathbf{S}_f^{(0)}$ to $\mathbf{S}_f$ where the minimal distance between the normal plane passing through $\mathbf{S}_f$ and the point $\mathbf{P}_f$ is less than half the sampling width, the sensor position $\mathbf{S}_f$ is obviously corresponding to that of the first azimuth line of the simulated image. The orbital track is a continuous curve in space, then, the flying distance from $\mathbf{S}_f^{(0)}$

to S_f is obviously greater than $|d_f|^{(0)}$, as shown in Figure 5.2. An iterative procedure is then applied to integrate the total azimuth time offset until the sensor approaches the DEM points and makes $|d_f|^{(i)}$ less than $0.5d_w$ and gives the azimuth time A_f' of the first azimuth line of the simulated image. The azimuth time offset of the azimuth lines $|\Delta A_f|^{(0)}$ counted from $S_f^{(0)}$ to S_f is given as

$$
\begin{aligned}
&|\Delta A_f|^{(0)} \cdot |\mathbf{V}_f|^{(0)} > |d_f|^{(0)} && \Rightarrow |\Delta A_f|^{(0)} = \frac{|d_f|^{(0)}}{|\mathbf{V}_f|^{(0)}} + |\Delta A_f|^{(1)};\\
&|\Delta A_f|^{(1)} \cdot |\mathbf{V}_f|^{(1)} > |d_f|^{(1)} && \Rightarrow |\Delta A_f|^{(1)} = \frac{|d_f|^{(1)}}{|\mathbf{V}_f|^{(1)}} + |\Delta A_f|^{(2)};\\
&\cdots\\
&|\Delta A_f|^{(i)} \cdot |\mathbf{V}_f|^{(i)} > |d_f|^{(i)} && \Rightarrow |\Delta A_f|^{(i)} = \frac{|d_f|^{(i)}}{|\mathbf{V}_f|^{(i)}} + |\Delta A_f|^{(i+1)};\\
&\cdots\\
&|\Delta A_f|^{(n-1)} \cdot |\mathbf{V}_f|^{(n-1)} > |d_f|^{(n-1)} && \Rightarrow |\Delta A_f|^{(n-1)} = \frac{|d_f|^{(n-1)}}{|\mathbf{V}_f|^{(n-1)}} + |\Delta A_f|^{(n)};\\
&|d_f|^{(n)} \le \frac{d_w}{2}, && \Rightarrow |\Delta A_f|^{(n)} = \frac{|d_f|^{(n)}}{|\mathbf{V}_f|^{(n)}} \approx 0
\end{aligned}
\qquad (5.4)
$$

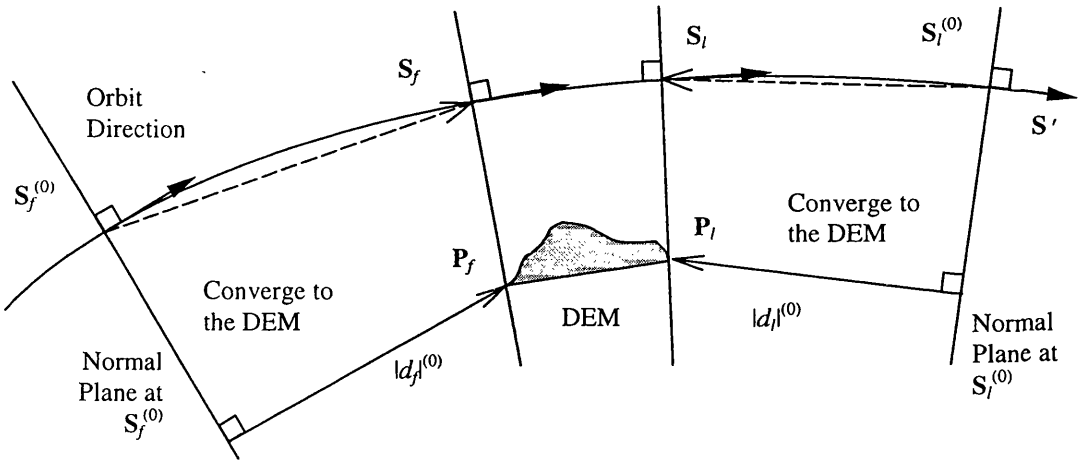

Figure 5.2. Along-track orbit profile in space.

$|\mathbf{V}_f|^{(0)}$ is the sensor speed at $\mathbf{S}_f^{(0)}$; $|\mathbf{V}_f|^{(i)}$ the sensor speed at $\mathbf{S}_f^{(i)}$; $|\Delta A_f|^{(i)}$ the azimuth time offset counted from $\mathbf{S}_f^{(i)}$ to $\mathbf{S}_f$; $|d_f|^{(i)}$ the minimal distance between the nearest DEM point and the normal plane at the new sensor position $\mathbf{S}_f^{(i)}$, i=1, 2, ..., n. Thus,

$$\begin{aligned} &\textbf{if} \quad |\mathbf{V}_f|^{(0)} \approx |\mathbf{V}_f|^{(1)} \approx \ldots \approx |\mathbf{V}_f|^{(i)} \approx \ldots \approx |\mathbf{V}_f|^{(n-1)} \\ &\textbf{then} \quad |\Delta A_f|^{(0)} = \sum_{i=0}^{n-1} \frac{|d_f|^{(i)}}{|\mathbf{V}_f|^{(i)}} + |\Delta A_f|^{(n)} \approx \sum_{i=0}^{n-1} \frac{|d_f|^{(i)}}{|\mathbf{V}_f|^{(0)}} \\ &\Rightarrow A_f' = A_f^{(0)} + |\Delta A_f|^{(0)} \approx A_f^{(0)} + \sum_{i=0}^{n-1} \frac{|d_f|^{(i)}}{|\mathbf{V}_f|^{(0)}} \end{aligned} \quad . \tag{5.5}$$

The same principle can be applied to the other direction to approach the DEM from $A_l^{(0)}$ to the corresponding azimuth time A_l' of the last azimuth line of the simulated image and gives

$$|d_l|^{(n)} \le \frac{d_w}{2} \qquad \Rightarrow A_l' \approx A_l^{(0)} + \sum_{i=0}^{n-1} \frac{|d_l|^{(i)}}{|\mathbf{V}_l|^{(0)}} \tag{5.6}$$

$|\mathbf{V}_l|^{(0)}$ is the sensor speed at $\mathbf{S}_l^{(0)}$; $|d_l|^{(i)}$ the minimal distance between the nearest DEM point and the normal plane at the new sensor position $\mathbf{S}_l^{(i)}$, i=1, 2, ..., n. The total number N_a' of the azimuth lines of the simulated image can be determined by

$$N_a' = \text{int}\left[\frac{N_a - 1}{|A_f - A_l|} \cdot |A_f' - A_l'|\right] + 1 \tag{5.7}$$

int[] denotes an integer number.

5.2.2.3 The sampling width of range pixels

Within each azimuth line, the sampling rate in range R_r (pixel/sec) of the slant-range pixels of a real image given by header information is used to derive the slant-range sampling width R_s as

$$R_s = \frac{c}{2 \cdot R_r} \tag{5.8}$$

c (m/sec) denotes the speed of an electromagnetic wave, [Curlander and McDonough, 1991] and [CSA, 1995]. In order to simulate a ground-range image, the length of each slant-range pixel R_s, or the range bin, must be transformed into that of a ground-range one R_g as

$$R_g = \frac{R_s}{\sin\Omega} \tag{5.9}$$

The incidence angle Ω of an electromagnetic wave considered with respect to the surface of the ellipsoid is based on the relation between a ground point and the corresponding orbit position provided by SAR image header files. Notice that the incidence angle for each ground point from near to far range can change significantly through the entire scene of a space-borne SAR image. The incidence angle Ω is determined by the angle between the range vector $\mathbf{R}$ and the outward normal vector $\mathbf{N}_e$ with respect to the surface of the ellipsoid and given as

$$\cos\Omega = \frac{\mathbf{R}\bullet\mathbf{N}_e}{|\mathbf{R}|\cdot|\mathbf{N}_e|} = \frac{\mathbf{R}\bullet\mathbf{n}_e}{|\mathbf{R}|} \qquad \mathbf{R} = \mathbf{S}-\mathbf{P} = (X-S_x)\cdot\mathbf{i}+(Y-S_y)\cdot\mathbf{j}+(Z-S_z)\cdot\mathbf{k} \tag{5.10}$$

$\mathbf{R}$ is given by equation (3.2); $\mathbf{n}_e$ denotes the unit vector of $\mathbf{N}_e$ that can be derived using the concept of the gradient in vector analysis and ($\mathbf{i}$ + $\mathbf{j}$ + $\mathbf{k}$) the unit vector. The surface function Φ (X, Y, Z) of the earth model, which is continuous and differentiable in a geocentric co-ordinate system, is defined as

$$\Phi(X,Y,Z) = \frac{X^2+Y^2}{a^2} + \frac{Z^2}{b^2} - 1 \equiv 0, \tag{5.11}$$

a and b denote the ellipsoidal parameters provided by SAR image header data, [CSA, 1995]. Thus, there exists a normal vector $\mathbf{N}_e$ passing through an arbitrary ground point $\mathbf{P}$ located on the mathematical surface of the ellipsoid. The gradient of the surface function Φ (X, Y, Z) is denoted as **grad**Φ or $\nabla\Phi$, [Paul and Nasar, 1987]. Then, the unit vector $\mathbf{n}_e$ of the normal vector $\mathbf{N}_e$ can be given by

$$\nabla\Phi = \frac{\partial\Phi}{\partial x}\mathbf{i} + \frac{\partial\Phi}{\partial y}\mathbf{j} + \frac{\partial\Phi}{\partial z}\mathbf{k} = \frac{2X}{a^2}\mathbf{i} + \frac{2Y}{a^2}\mathbf{j} + \frac{2Z}{b^2}\mathbf{k}$$
$$\Rightarrow \mathbf{n}_e = \frac{\mathbf{N}_e}{|\mathbf{N}_e|} = \frac{\nabla\Phi}{|\nabla\Phi|} = \frac{b^2X\cdot\mathbf{i} + b^2Y\cdot\mathbf{j} + a^2Z\cdot\mathbf{k}}{\sqrt{b^4\left(X^2+Y^2\right)+a^4Z^2}} \tag{5.12}$$

Therefore, equation (5.10) and (5.12) gives

$$\Omega = \cos^{-1}\left(\frac{b^2X\cdot(X-S_x) + b^2Y\cdot(Y-S_y) + a^2Z\cdot(Z-S_z)}{\sqrt{(X-S_x)^2+(Y-S_y)^2+(Z-S_z)^2}\cdot\sqrt{b^4\left(X^2+Y^2\right)+a^4Z^2}}\right) \tag{5.13}$$

5.2.2.4 The extent of range pixels

Consider the tangent or the velocity vector of the sensor $\mathbf{V_S}$ (V_{Sx}, V_{Sy}, V_{Sz}) on the orbit track at $\mathbf{S}(S_x, S_y, S_z)$ corresponding to the central azimuth line of the simulated image. The magnitude of the vector $\mathbf{R}_0$ with direction from $\mathbf{S}$ to an arbitrary DEM point $\mathbf{P}_0$ (X_0, Y_0, Z_0) is greater than that of the projected vector $\mathbf{R}_{near}$ in the direction perpendicular to $\mathbf{S}'$ within the simulated area as shown in Figure 5.3.

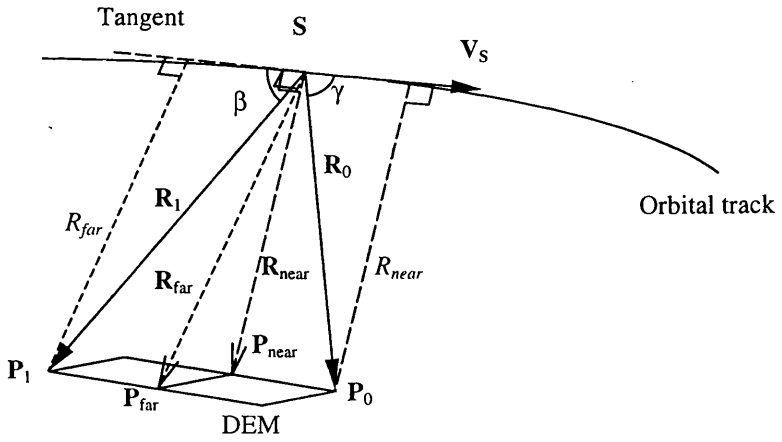

Figure 5.3. The minimal/maximal distance derived at the near/far range pixel.

Assuming that the speed of the sensor is a constant within the extent of the simulated SAR image, the azimuth time of the central azimuth line can be calculated by

averaging the first and the last azimuth time that can be solved using equation (5.5) and (5.6). The velocity vector of the sensor at the central azimuth line of the simulated image is equivalent to the tangent of the orbital track at the corresponding sensor position. When the nearest DEM point $\mathbf{P}_{near}$ is scanned by the sensor and stored in the near range pixel (bin) of a simulated image, the distance between $\mathbf{P}_{near}$ and the orbit position $\mathbf{S}$ must have the minimal value R_{near} and is given by

$$
\begin{aligned}
&|\mathbf{R}_0| \geq |\mathbf{R}_{near}| = R_{near} \\
&\mathbf{v} = v_x \cdot \mathbf{i} + v_y \cdot \mathbf{j} + v_z \cdot \mathbf{k} = \frac{V_{Sx}}{|\mathbf{V}_S|} \cdot \mathbf{i} + \frac{V_{Sy}}{|\mathbf{V}_S|} \cdot \mathbf{j} + \frac{V_{Sz}}{|\mathbf{V}_S|} \cdot \mathbf{k} \qquad (5.14) \\
&\Rightarrow R_{near} = |\mathbf{R}_0| \sin\gamma = |\mathbf{R}_0| \cdot |\mathbf{v}| \sin\gamma = |\mathbf{R}_0 \times \mathbf{v}| = \begin{vmatrix} \mathbf{i} & \mathbf{j} & \mathbf{k} \\ X_0 - S_x & Y_0 - S_y & Z_0 - S_z \\ v_x & v_y & v_z \end{vmatrix}
\end{aligned}
$$

γ is the angle between $\mathbf{R}_0$ and $\mathbf{V}_S$, and $\mathbf{v}(v_x, v_y, v_z)$ the unit velocity vector of the sensor. The distance R_{near} between the tangent of the orbit track and the DEM point can be used as the initial position of the near range pixel.

The same principle is also applied to detect the position of the far range pixel. The magnitude of the vector $\mathbf{R}_1$ with direction from $\mathbf{S}$ to an arbitrary DEM point $\mathbf{P}_1$ (X_1, Y_1, Z_1) is certainly greater than, or approximately equal to, that of the projected vector $\mathbf{R}_{far}$ in the direction perpendicular to $\mathbf{V}_S$ at $\mathbf{S}$ within the simulated area as shown in Figure 5.3. If the DEM point $\mathbf{P}_{far}$ is located on the far range pixel scanned by the sensor, the distance between $\mathbf{P}_{far}$ and the corresponding orbit position $\mathbf{S}$ must have the minimal value R_{far} from orbit track to the DEM points giving

$$
\begin{aligned}
&|\mathbf{R}_1| \geq |\mathbf{R}_{far}| = R_{far} \\
&\Rightarrow R_{far} = |\mathbf{R}_1| \sin\beta = |\mathbf{R}_1| \cdot |\mathbf{v}| \sin\beta = |\mathbf{R}_1 \times \mathbf{v}| = \begin{vmatrix} \mathbf{i} & \mathbf{j} & \mathbf{k} \\ X_1 - S_x & Y_1 - S_y & Z_1 - S_z \\ v_x & v_y & v_z \end{vmatrix}, \qquad (5.15)
\end{aligned}
$$

β is the angle between $\mathbf{R}_1$ and $\mathbf{V}_S$. Similarly, the distance R_{far} calculated between the tangent of the orbit track and the DEM point can be used as the initial location of the far range pixel.

The central point of the DEM can be easily collected and the minimal distance from that point to the orbital track is also recorded. Therefore, the exact incidence angle of the corresponding DEM point at the near, the central and the far range pixel can be decided using equation (5.13), and then the relationship between each slant-range pixel and the corresponding incidence angle is established using a curve-fitting routine. The incidence angle Ω_i of each slant-range pixel can then be interpolated subsequently. Therefore, the total number N_r' of the ground-range pixels of each azimuth line of the simulated image can be obtained by integrating the extent of every ground-range pixel as

$$N_r' = \mathrm{int}\left[\frac{1}{r_g}\cdot\sum_{i=1}^{N_s}\frac{R_s}{\sin\Omega_i}\right]+1 \;\; ; \quad N_s = \mathrm{int}\left[\frac{R_{far}-R_{near}}{R_s}\right]+1 \tag{5.16}$$

r_g denotes the assigned spacing of each ground range pixel of the simulated image; R_s is given by Equation (5.8) and N_s the total number of the slant-range pixels of the corresponding azimuth line of the simulated image.

5.2.3 Radiometric Considerations

A reflectivity model of the area being sensed is required to consider the radiometric characteristic of a simulated SAR image, [Holtzman *et al.*, 1978]. It has been mentioned that the proposed simulator is designed to deal with providing control in hilly areas with no regard to the characters of true ground cover hence the simulator cannot be used to restore the actual radiometric characteristic of a real SAR image for the simulated counterpart. Therefore, the reflectivity model employed for generating the simulated images is a simple cosine function, as mentioned in Section 2.5, which gives a relative intensity reflected in respect to a surface normal defined by a DEM cell. The relative intensity has to be normalized and stretched to meet the requirement of the density number (*DN*) of each simulated image pixel.

5.2.3.1 A Reflectivity model

According to the assumptions made before, each element of the area being sensed has the same reflection character, which is decided only by the orientation of the terrain surface element in respect to the sensor and is relatively rough. In computer graphics and

animations for a shading model in 3-D space, the orientation of a surface element is usually represented by unit normal vector. This is due to the Lambert's law, which states that the energy falling on a surface varies as the cosine of the angle of incidence of that energy, [Newman and Sproull, 1979]. The angle of incidence is related to the surface normal vector. The surface of the shaded object is always composed of many polygons, such as triangles, which gives an exact equation for a plane, and a surface normal can be uniquely determined. In order to improve the computing efficiency in animation, which demands many more polygons to be computed, the calculation of the angle of incidence (or the surface normal) is always carried out using approximate methods, such as interpolation [Watt and Watt, 1996].

Consider a reflectivity model employed for the SAR image simulation using a DEM with a grid structure. The accumulated relative intensity of each pixel I_r of a SAR image, representing the sum of the return power of each DEM cell in the area being sensed within the extent of a specific range pixel (bin), is given by

$$I_r = \sum_{i=1}^{n} \mathbf{n}_i \bullet \mathbf{R}; \qquad \mathbf{n}_i \bullet \mathbf{R} \geq 0 \tag{5.17}$$

$\mathbf{R}$ the range vector and $\mathbf{n}_i$ the unit normal vector of the surface of each DEM cell that can be derived from each DEM point and its neighbouring points. In order to derive the surface normal vector, or the local incidence angle, some approximations are always made, since there is no exact mathematical formula for describing terrain surface.

The traditional definition of a DEM cell for SAR image simulation is given as a 2-D patch surrounded by four DEM points at the corners, [Leberl, 1990]. This is based on the assumption that the 2-D patch is a plane giving a surface normal. It is even simplified further as the gradient of height between two neighbouring DEM points in 1-D space giving an approximate normal vector, [Domik *et al.*, 1986] and [Arai, 1991]. Also, Holecz *et al.* [1993] gives a surface normal vector based on the DEM cell defined by four DEM points of that cell and based on the averaged slope in easting and northing. However, it must be noticed that such a DEM cell surrounded by four DEM points, such as $\mathbf{P}_{i,j}$, $\mathbf{P}_{i+1,j}$, $\mathbf{P}_{i,j+1}$, and $\mathbf{P}_{i+1,j+1}$ in Figure 5.4 (a), always shows an irregularly undulated surface in the real world, instead of a plane. Namely, four points in three-dimensional space cannot uniquely determine a plane. Even in a simplified case, it is difficult to give the normal vector of an actual DEM cell. For example, there are four different aspects of

the slope for each side of the simplified DEM cell, as demonstrated in Figure 5.4 (b) in three-dimensional space. Apparently, the traditional definition of a DEM cell given as simply a 2-D patch or 1-D gradient does not reflect the physical world. Also, ambiguities of the definition for the normal vector may arise in the simplified cases. Hence a new definition for a DEM cell is proposed to obtain a realistic normal vector for the DEM point of interest considering the neighbouring DEM points.

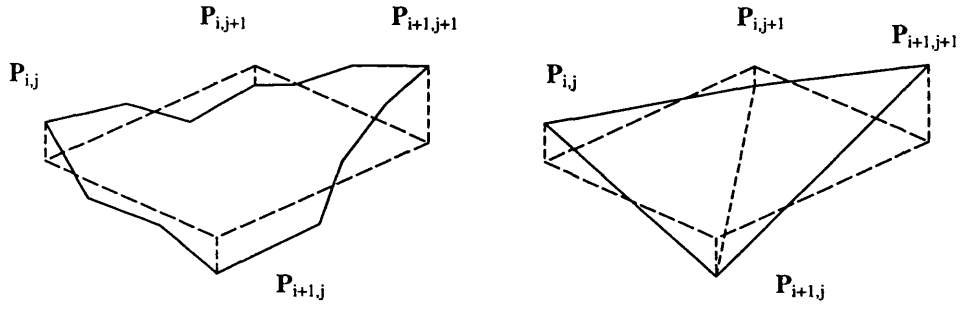

Figure 5.4 Traditional definition of a DEM cell: (a): The actual surface of the DEM cell defined by four corner points; (b): the four different aspects of the slope derived from each side of the DEM cell defined.

Define a DEM point $\mathbf{P}_{i,j}$ with height $Z_{i,j}$ as the centre of the DEM cell surrounded by four consecutive points $\mathbf{P}_{i-1,j}$, $\mathbf{P}_{i+1,j}$, $\mathbf{P}_{i,j-1}$, $\mathbf{P}_{i,j+1}$ with height $Z_{i-1,j}$, $Z_{i+1,j}$, $Z_{i,j-1}$, $Z_{i,j+1}$, respectively, as in Figure 5.5(a). The surface normal is given by the tangent plane passing through $\mathbf{P}_{i,j}$ on a surface, which is the outward vector of the cross-product of two tangent vectors in easting and northing direction. Each tangent vector must hold the same gradient to either side with respect to the kernel point $\mathbf{P}_{i,j}$, and can be derived from the neighbouring DEM points. Let a vector $\mathbf{P}_e'$ be defined from $\mathbf{P}_{i,j}$ to a new point $\mathbf{P}'_{i+1,j}$, along eastern direction of the vector $\mathbf{P}_e$ from $\mathbf{P}_{i,j}$ to $\mathbf{P}_{i+1,j}$, forming an isosceles triangle with $\mathbf{P}_{i-1,j}$ as $\Delta\mathbf{P}_{i,j}\mathbf{P}_{i-1,j}\mathbf{P}'_{i+1,j}$. The subscript *e*, *w*, *n* and *s* denotes eastern, western, northern and southern direction with respect to the central point $\mathbf{P}_{i,j}$. Thus, the new vector from $\mathbf{P}_e'$ has the same magnitude as the vector $\mathbf{P}_w$ from $\mathbf{P}_{i,j}$ to $\mathbf{P}_{i-1,j}$.

The tangent $\mathbf{T}_x$, passing through $\mathbf{P}_{i,j}$ in the X-Z plane, is equivalent to the resultant vector of $\mathbf{P}_w$ and $\mathbf{P}_e'$, holding the same relative slope from $\mathbf{P}_{i,j}$ to $\mathbf{P}_{i+1,j}$ and to $\mathbf{P}_{i-1,j}$, as in Figure 5.5(c) and giving

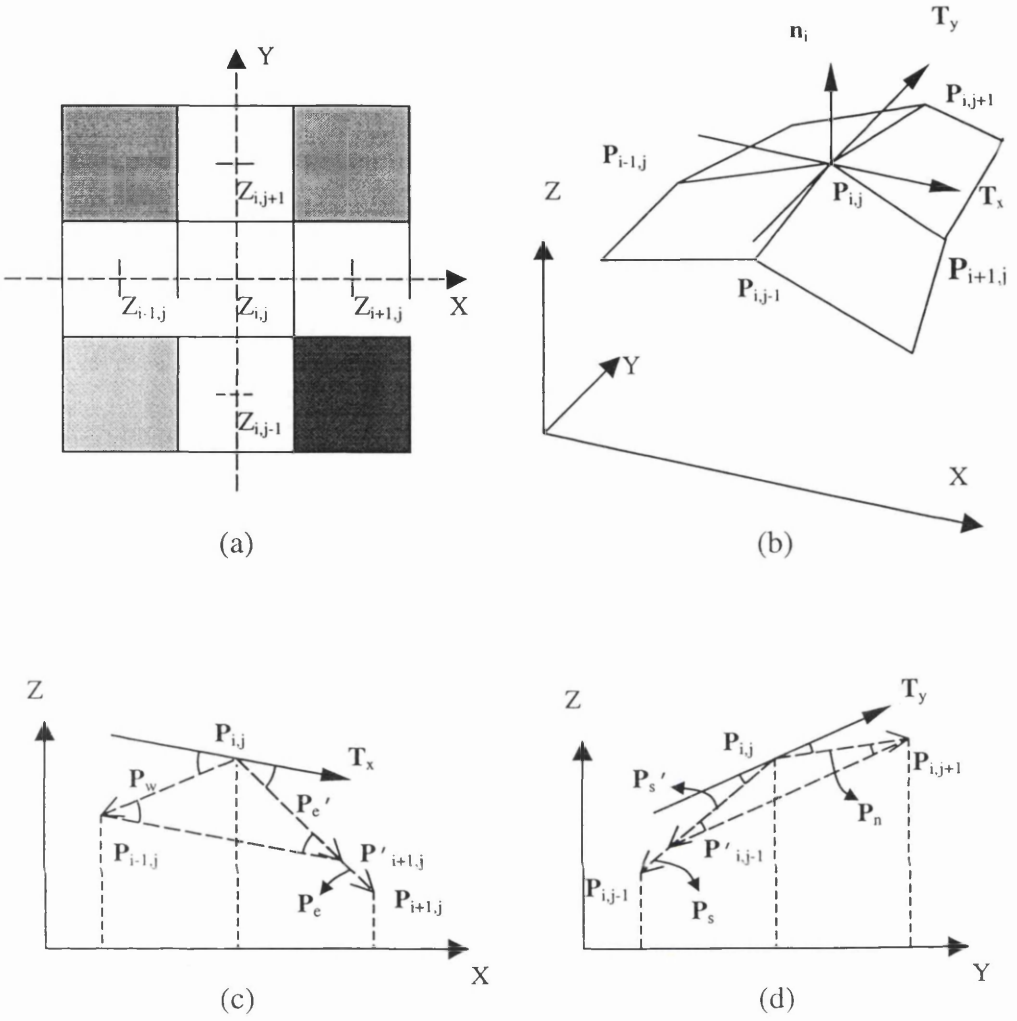

Figure 5.5 The proposed definition of a DEM cell. (a) A DEM point and four neighbouring points. (b) The unit normal vector uniquely defined at the central point in a 3×3 patch. (c) The vector derived from the three consecutive DEM points holding the same relative slope to either side in the X-Z plane. (d) The vector derived from the three consecutive DEM points holding the same relative slope to either side in the Y-Z plane.

$$\mathbf{P}_w = \mathbf{P}_{i-1,j} - \mathbf{P}_{i,j}\ ; \qquad \mathbf{P}_e = \mathbf{P}_{i+1,j} - \mathbf{P}_{i,j}$$
$$\mathbf{P}'_e = |\mathbf{P}_w| \cdot \frac{\mathbf{P}_e}{|\mathbf{P}_e|} = \mathbf{P}_w + \mathbf{T}_x \quad \Rightarrow \quad \mathbf{T}_x = \mathbf{P}'_e - \mathbf{P}_w \tag{5.18}$$

The same principle can also be applied to the Y-Z plane giving another isosceles triangle $\Delta \mathbf{P}_{i,j}\mathbf{P}'_{i,j-1}\mathbf{P}_{i,j+1}$ as shown in Figure 5.5 (d) and the tangent $\mathbf{T}_y$ is given by

$$\mathbf{P}_n = \mathbf{P}_{i,j+1} - \mathbf{P}_{i,j}; \qquad \mathbf{P}_s = \mathbf{P}_{i,j-1} - \mathbf{P}_{i,j}$$
$$\mathbf{P}'_s = |\mathbf{P}_n| \cdot \frac{\mathbf{P}_s}{|\mathbf{P}_s|} = \mathbf{P}_n - \mathbf{T}_y \quad \Rightarrow \mathbf{T}_y = \mathbf{P}_n - \mathbf{P}'_s \tag{5.19}$$

Therefore, there exists an uniquely determined tangent plane composed by two vectors $\mathbf{T}_x$ and $\mathbf{T}_y$ holding the same relative slope in either aspect of each axis passing through $\mathbf{P}_{i,j}$ and generating unit normal $\mathbf{n}_i$ of the tangent plane, as in Figure 5.5 (b), given by

$$\mathbf{n}_i = \frac{\mathbf{T}_x \times \mathbf{T}_y}{|\mathbf{T}_x \times \mathbf{T}_y|} \tag{5.20}$$

5.2.3.2 Density number of image pixel

The accumulated relative intensity of the return power I_r within the extent of each pixel bin of a simulated image can be normalized by the maximal intensity I_{max} as

$$0 \le \frac{I_r}{I_{\max}} \le 1 \quad , \quad I_{\max} \neq 0 \tag{5.21}$$

The positive real number of the simulated intensity can be stretched and converted to the range of the density number (*DN*, integer) of a real SAR image. In general, a SAR intensity image product is provided in a 16-bit (two-byte binary) format giving the range of the density number of each pixel from 0 to 2^{16}-1, however, that is not convenient for displaying on the computer screen and some other applications. Instead, an amplitude image, whose *DN* of each pixel is the square root of the intensity one, taking the advantage of the convenience for image segmentation, [Lee and Jurkevich, 1989], and visual interpretation, is used to present the simulated image for the following study. Thus, the *DN* of each pixel of the simulated image is converted and stretched, ranging from 0 to 2^8-1, as

$$DN = 255 \cdot \sqrt{\frac{I_r}{I_{\max}}}; \qquad 0 \le DN \le 2^8 - 1 \tag{5.22}$$

5.3 Real-Simulated Image Correlation for Providing Control

The aims of using the simulator are not only providing a simulated image for the real-simulated image correlation to find out the relationship between the real-simulated image pair, but also generating reliable and precise GCPs. Since the proposed simulation method mentioned above utilizes a set of real orbital data and relevant parameters from the header file of a real SAR image, the simulated image which is obtained has the same image geometry as the real one. If there is any difference of the structure between a real and a simulated image, the automatically derived GCPs may introduce errors into the radargrammetric results. On the contrary, if there is no significant error shown in the results derived from space intersection after systematic correction, it could be concluded that the simulator is accurate and so is the real-simulated image correlation.

The scanning (simulation) process of the simulator starts from the azimuth time of the first azimuth line of the simulated image derived in equation (5.5) and ends at that of the last azimuth line of the simulated image obtained in equation (5.6). In the course of simulation, the four corner elements of the sensed DEM that are treated as GCPs are detected in turn, when the range plane scans these DEM elements according to the revised plane equation (5.1). The detection criterion for the assigned GCPs is the same as in equation (5.3). If the GCPs are detected, the corresponding (simulated) range and azimuth time data will be recorded together with the relative co-ordinates in the simulated image as well as the ground co-ordinates. The relative image co-ordinates can be correlated with the real counterparts giving the absolute co-ordinates with respect to the real image using a real-simulated image correlation routine. After deriving the actual image co-ordinates of the GCPs, the nominal range and azimuth time data (observations on SAR images) are collected which can be compared with the simulated ones recorded, hence providing control (for the range and azimuth time corrections) is possible.

5.3.1 Real-Simulated Image Correlation

The pyramidal matching scheme, proposed by Denos [1992], has been optimized to a higher level of automation and used for the RADARSAT SAR image correlation of conjugate pairs to generate DEMs as described in Chapter 4. But, this area-based least-squares image correlation method with a region growing approach, [Gruen, 1985] and [Otto and Chau, 1989], requires a good approximation of the coverage of the image pair

and, in particular, each image must have the same size. It is expected that there is no significant parallax existing in the real-simulated image pair, and the simulated image is relatively smaller than the real one on which the simulated image has to be located. Namely, a search window, whose size is the same as that of the simulated image chip, must be used to move around the real image for locating the position of the simulated image within the real image using a correlation measure. Hence the problem of the real-simulated image correlation should be solved using an alternative method without the need of any good initial value other than the least squares approach.

Guindon [1995] argued that there does not necessarily exist any linear relationship between the grey values of the simulated image and those of the real counterpart, and then used a rank correlation measure as the criterion for the real-simulated correlation, instead of the well-known normalized cross-correlation measure. According to James *et al.* [1992], rank correlation is used to measure the degree of association between two rankings of the same objects, such as the rankings of school pupils according to (body) weight and according to height. Thus, one of the conditions of using the rank correlation method is that the objects correlated must be the same. Thus, a good approximation of the location of the correlated area is essential to guarantee the same objects being correlated. Hence using a rank correlation measure faces a dilemma, i.e., the exact location of the simulated image is actually unknown, and there is no way to ensure the same objects are being correlated.

The application of the normalized cross-correlation measure to the real-simulated image correlation, however, can be justified, if a good simulator is employed. An adequate simulator is expected to give an exact geometry for the simulated image without scaling or rotation problems and to set the density numbers of the real-simulated image pair to be as linearly related as possible. In fact, the cross-correlation coefficient is a measure of the distortion of the linear relationship between two data sets, [James *et al.*, 1992]. Since the same orbital data and the same image structure as the real image have been used to simulate a SAR image, the geometric distortions can be minimized. Stretching the *DN*s of the simulated images, as given in equation (5.22), reduces the relative radiometric differences between the simulated image and the real one.

The real-simulated image correlation is carried out by searching for the location of the entire simulated image ($m \times n$ pixels) in the real image ($p \times q$ pixels), including every non-zero *DN* pixel, to give the exact shift (line u, pixel v) between both images, as in

Figure 5.6. The entire simulated image is used for the real-simulated image correlation. Notice that the extent covered by the DEM chip in the simulated image is not necessarily a regular shape due to varied SAR image orientations (see Section 5.5.2), the fringe areas with no DEM samples in the simulated image are filled with zero DN pixel. Thus, the zero *DN* pixels in the fringe areas of the simulated image must be excluded in the real-simulated image correlation to avoid bias of a correlation measure. Therefore, the criterion for the best real-simulated image correlation measure is defined as the maximal correlation coefficient $r_{u,v}$ and given by

$$\max_{\substack{0\le u\le p-m\\ 0\le v\le q-n}} r_{u,v} = \frac{\sum_{i=0}^{m-1}\sum_{j=0}^{n-1}\left(DN_{i,j}-DN_M\right)\cdot\left(DN'_{u+i,v+j}-DN'_M\right)}{\sqrt{\sum_{i=0}^{m-1}\sum_{j=0}^{n-1}\left(DN_{i,j}-DN_M\right)^2}\cdot\sqrt{\sum_{i=0}^{m-1}\sum_{j=0}^{n-1}\left(DN'_{u+i,v+j}-DN'_M\right)^2}}; \quad DN_{i,j}\neq 0 \qquad (5.23)$$

$DN_{i,j}$ denotes the non-zero gray value at the location (i, j), in (row, column), of the simulated image with the size of $m \times n$ pixels; DN_M the mean of non-zero *DN*s of the simulated image; $DN'_{u+i,v+j}$ the gray value within the search window in the real image and DN'_M the mean of *DN*s within the search window in the real image. The cross-correlation measure can be carried out using the programme `ncc`, coded in C by the author, as described in Appendix B.3.

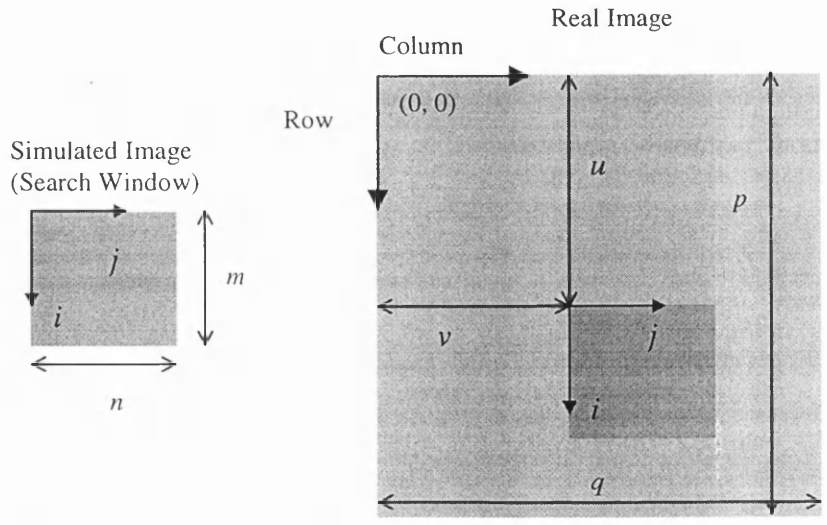

Figure 5.6 A cross-correlation measure for searching the corresponding location of the simulated image in a real image.

5.3.2 Providing Control for Radargrammetry

The simulator records the azimuth time and range data when the candidate GCP is detected, as mentioned above, giving A_{GCP} and R_{GCP}, respectively. The co-ordinates (n_a, n_r), in (row, column), of the GCPs generated in the simulated image are given by

$$n_a = \text{int}\left[\frac{N_a - 1}{|A_f - A_l|} \cdot |A_{GCP} - A_f'|\right] + 1$$
$$n_r = \text{int}\left[\frac{1}{r_g} \cdot \sum_{i=1}^{n_s} \frac{R_s}{\sin \Omega_i}\right] + 1 \; ; \quad n_s = \text{int}\left[\frac{R_{GCP} - R_{near}}{R_s}\right] + 1 \tag{5.24}$$

N_a, A_f and A_l are defined in equation (5.2); A_f' given by equation (5.5); n_s the simulated slant-range pixel number where the candidate GCP is located; R_s given by equation (5.8), Ω_i given by equation (5.13); R_{near} given by equation (5.14) and r_g is defined in equation (5.16). The structure of the simulated image is the same as that of the real image hence there is no rotation or scaling problems. Given a translation, the co-ordinates of the candidate GCP (col_{GCP}, row_{GCP}) in the real image co-ordinate system is derived as

$$col_{GCP} = n_r + u \quad ; \quad row_{GCP} = n_a + v \tag{5.25}$$

The ground co-ordinates of the corner elements of a DEM in object space are already known, and the actual SAR image co-ordinates can be derived using equation (5.25), which give the range and the azimuth time observations. This makes the provision of ground control for radargrammetry using the proposed simulator with a known DEM chip in an area of undulated relief possible.

5.4 Procedures of Providing Control

Figure 5.7 describes the procedures of SAR image simulation for generating GCPs from a known DEM chip. The simulator records the co-ordinates of the four GCPs in a local co-ordinate system and those in the simulated image co-ordinate system that must be correlated with the real SAR image co-ordinate system as illustrated in Figure 5.6. All of the image co-ordinates of the derived GCPs form a disparity file as input for space intersection as explained in Chapter 3. The co-ordinates of the GCPs generated using the

weighted space intersection or the non-weighted solution may be different from those recorded from the known DEM showing shifts between the map co-ordinates and the derived ones. Such shifts can be used as the systematic corrections for other ground points solved, as shown in Figure 5.8. The processes marked by dashed lines in Figure 5.7 and 5.8 show the procedures for providing control in geocoding that require corrections for range and azimuth time shifts. More details about geocoding are given in Chapter 7.

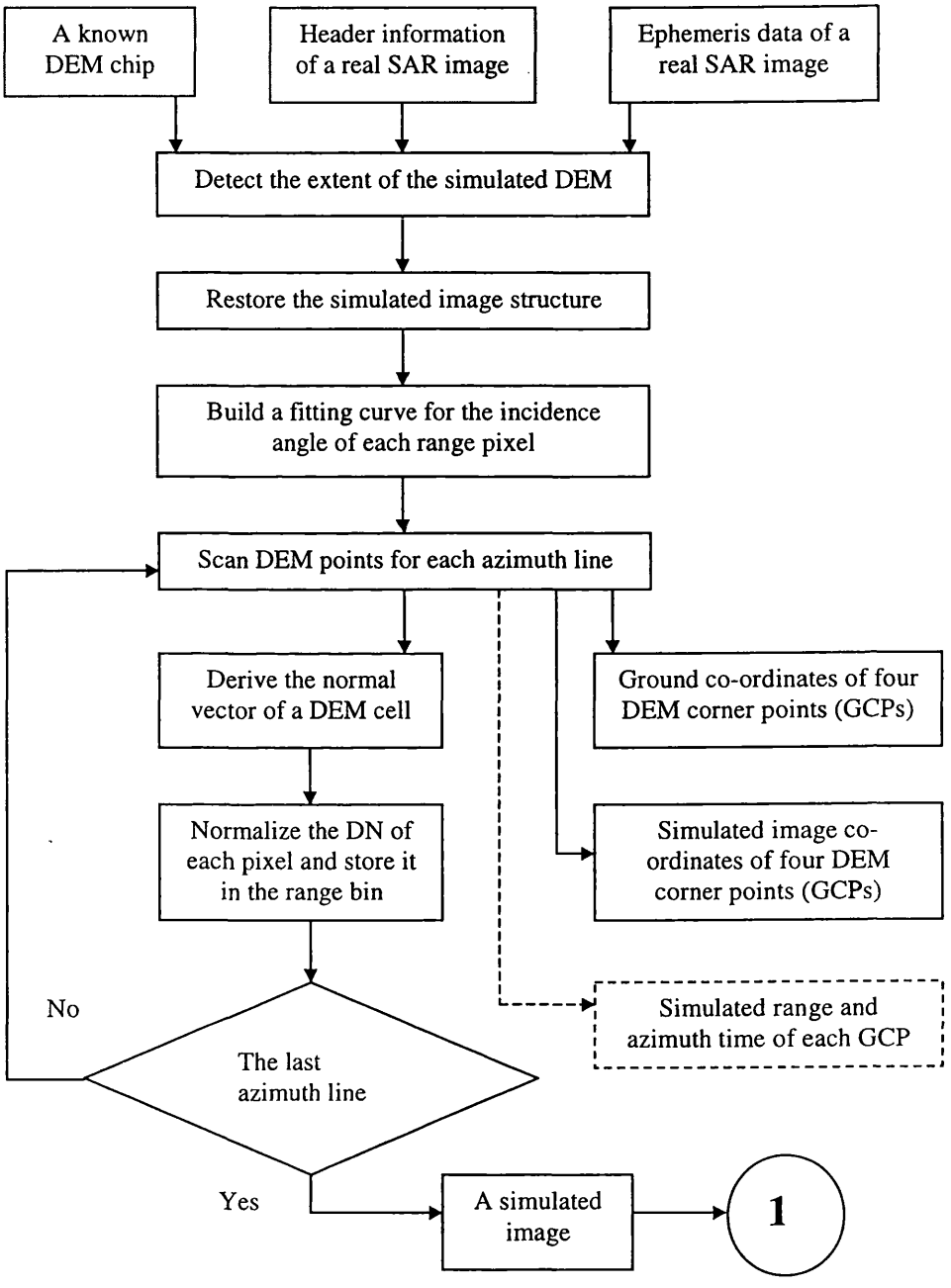

Figure 5.7 Flowchart of the proposed SAR image simulator.

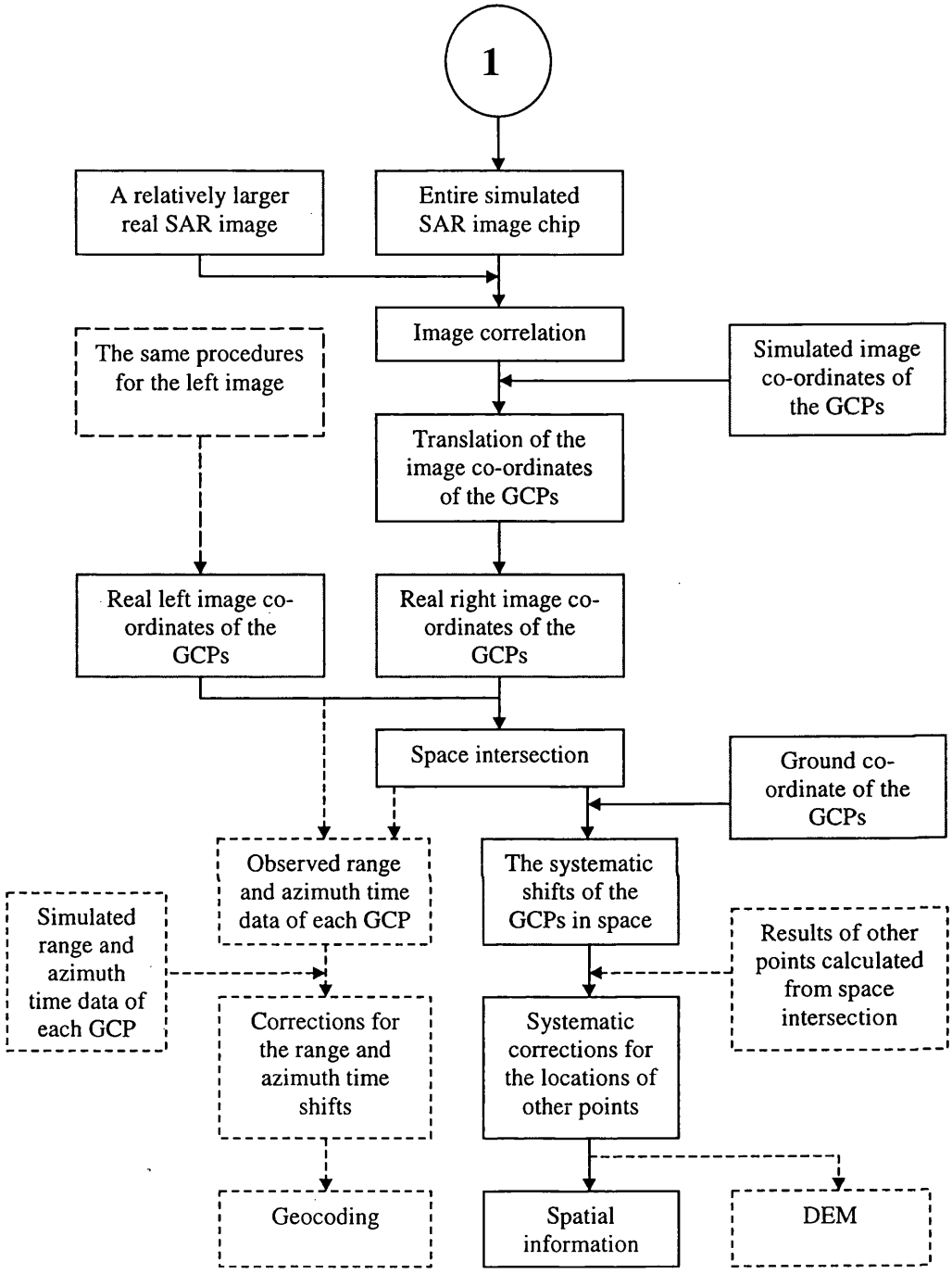

Figure 5.8 Providing control for radargrammetry.

5.5 Test Results

The proposed simulator is performed by a programme `sarsimul`, coded by the author in FORTRAN, reads in a file of specific parameters, which gives the information required for the real SAR image geometry and ephemeris data, `sarsimul.dat`, and a DEM file, `sarsimul.dem`. The input parameter file and the DEM format are shown in

Table 5.1 (a) and (b), respectively. The header information is provided with the RADARSAT SAR data, [CSA, 1995]. The input parameters can be extracted from the header files as in Table 5.1 (a). The co-ordinates of each DEM element to be used for simulation have to be transformed in advance from the map co-ordinate system to a geocentric co-ordinate system using the conventional projection transformation procedures (as in Section 2.6) and giving co-ordinates in the standard format as (x, y, z) or (E, N, H).

Contents	Unit	Descriptions	Source
1997 8 22 5 54 50.76	date-time	Given time of the first data point	Platform Position Data Record -
6	-	Number of the given data points	
4.0	s	Sampling interval of the data points	
1878434.23 4878054.87 4901508.03	m	Sensor position of the first point	
3220956.05 4118837.03 –5319652.26	mm/s	Sensor velocity of the first point	
... ...	m mm/s	Repeat the state vectors for other points until the image scene is fully covered	
6378140.0 6356755.0	m	Earth semi-major/semi-minor axes	Data Set Summary Record
0.001874683	s	Azimuth line spacing = (Azimuth time interval) ÷ [(number of azimuth line)-1]	
12.581	degree	Scene centre heading angle	
18466900.0	pixel/s	Range sampling rate	
6	- •	Number of the polynomial coefficient For the ground-range-to-slant-range (GRSR) transformation	Detailed Processing Parameters Record
8.3931088E+05	m	Constant of the GRSR polynomial	
3.3013824E-01	m	Coefficient of the 1st power term	
...	m	Repeat until the the 5th power term	
12.5	m	Range pixel spacing	
1081 1081	row /col	Size of the DEM to be used for simulation	Defined by users

Table 5.1 (a) Format of the parameter file `sarsimul.dat` for `sarsimul`.

Contents	Unit	Descriptions
4625570.37 433896.05 4355430.34	m	DEM element, x, y and z in the Earth-fixed geo-centric system, of the 1st column of the 1st row of the DEM
...	m	Repeat until the last column of the 1st row, and then repeat until the last column of the last row

Table 5.1 (b) Format of the DEM file `sarsimul.dem` for `sarsimul`.

5.5.1 Validation of the Simulated Image

The quality of the simulated image is a critical factor in the real-simulated image correlation for providing control, as in Section 5.3.1. In order to assure the quality of the simulated image, it will be helpful to validate the performance of the image simulator by evaluating the distortions of the terrain features being simulated. This can be carried out using a least-squares correlation method to detect the parallaxes existing in the real-simulated image pair of the same size.

The real images at the Aix-Marseilles test site are the same as those described in Table 3.4. The sub-scenes of the size 1024 × 1024 pixels of the real images corresponding to the coverage of the simulated ones were selected manually from each descending SAR image (left image: DS1 and right image: DS7b), as shown in the upper row of Figure 5.9. The simulated images, as shown in the bottom row of Figure 5.9, have been correlated with the corresponding real images to find any difference between real-simulated images in terms of parallax of both images. Theoretically, there must be no parallax between a perfectly simulated image and a real counterpart.

The simulated images were generated using the IGN DEM in a 50m grid with the original size of 271 × 271 pixel as shown in Figure 4.9. The DEM has to be interpolated into a 12.5m grid in order to be compatible with the pixel spacing of the simulated image. In terms of visual comparison, most of the terrain features, say layover effects, appearing in the moderate-to-hilly areas in the real image can also be seen in the simulated one. However, in the urban areas of Marseilles, where man-made objects strongly affect the reflected energy, natural features and artificial ones mixed together as demonstrated by the real image that may not be simulated correctly without ground truth data. Since the objective of the simulator is only dealing with terrain relief to derive useful ground control, those artificial features and ground cover are of no concern in this thesis.

To evaluate the results of simulation, the pyramidal correlation scheme (see Chapter 4) was applied to measure the similarity between the real-simulated images. The least squares correlation approach is applicable in the case for similarity comparison with sub-pixel accuracy, because the real-simulated image pair has the same size and the exact location has been selected manually. The relative parallax derived from the least squares correlation of a real-simulated image pair is defined as the relative position of the best-matched conjugate points of right image in respect to the left image co-ordinates. An accurate simulation leads to a high correlation for the real-simulated image pair that

means low parallaxes could be derived. Due to the effects of speckle and artificial objects, the quality of the results derived from image correlation may be somewhat degraded. Since the nominal resolution cell of a RADARSAT SAR image is equivalent to two pixels due to multi-look (4 looks) processing (see Section 2.2.2), the distortions between the real-simulated image pair are expected to be within ±2 pixels.

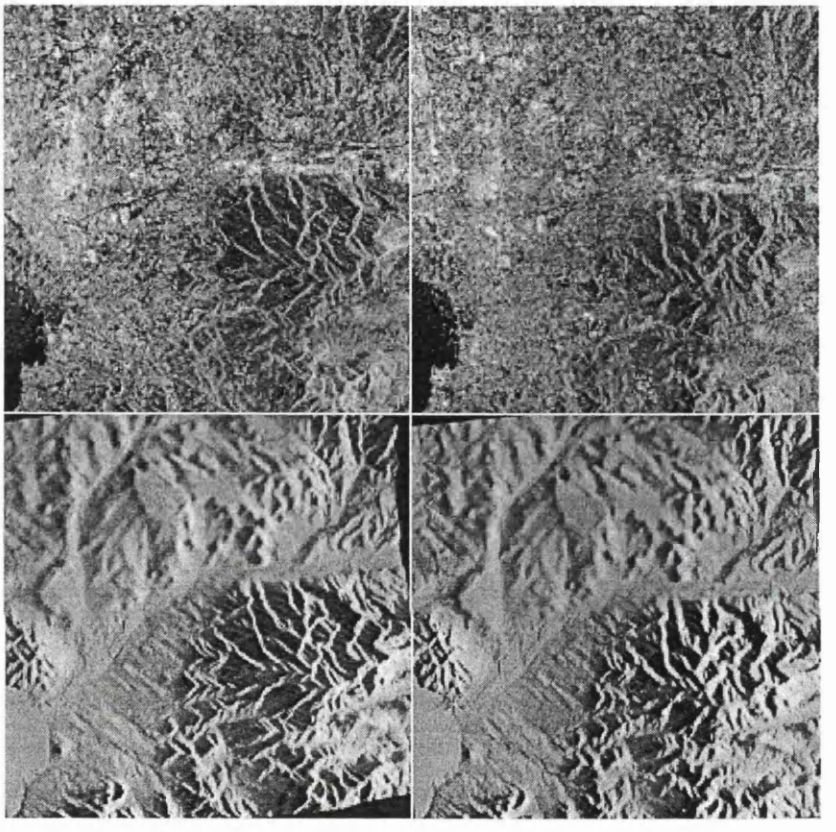

Figure 5.9 Enhanced real image pair and simulated ones. Top row: the real image pair. Bottom row: simulated image pair based on the reference DEM. Left column: a sub-scene of the real-simulated image pair (DS1). Right column: a sub-scene of the real-simulated image pair (DS7b). Size: 1024 × 1024 pixels.

However, according to the statistics shown in Table 5.2, both cases of the real-simulated image correlation demonstrate that the accuracy of the simulated image is better than ±1 pixel in terms of the standard deviation of the parallaxes derived. Figure 5.10 (a) shows the histograms of the parallaxes derived from the real-simulated image correlation of the left image and the right one, respectively, of the descending orbits. Because of the assumptions made in Section 5.2, the simulator only considers terrain relief. Thus, the real-simulated correlation is not expected to succeed in flat areas, as shown by the dark areas in Figure 5.10 (b) for the coverage of the correlated points in the

real-simulated images of the descending pair (DS1 and DS7). The primitive validation of the simulated image proves that the simulator works well in hilly areas.

Orbit	Image Pair	Samples	Coverage	S. D. (p)	Min.(p)	Max.(p)
Descending	Real+Simulated (DS1)	50379	20.0%	0.47	-3.22	+2.77
Descending	Real+Simulated (DS7b)	14781	5.6%	0.55	-3.15	+3.54

(Unit: p = pixel)

Table 5.2 Statistics of the parallaxes of the real-simulated pair of SAR images.

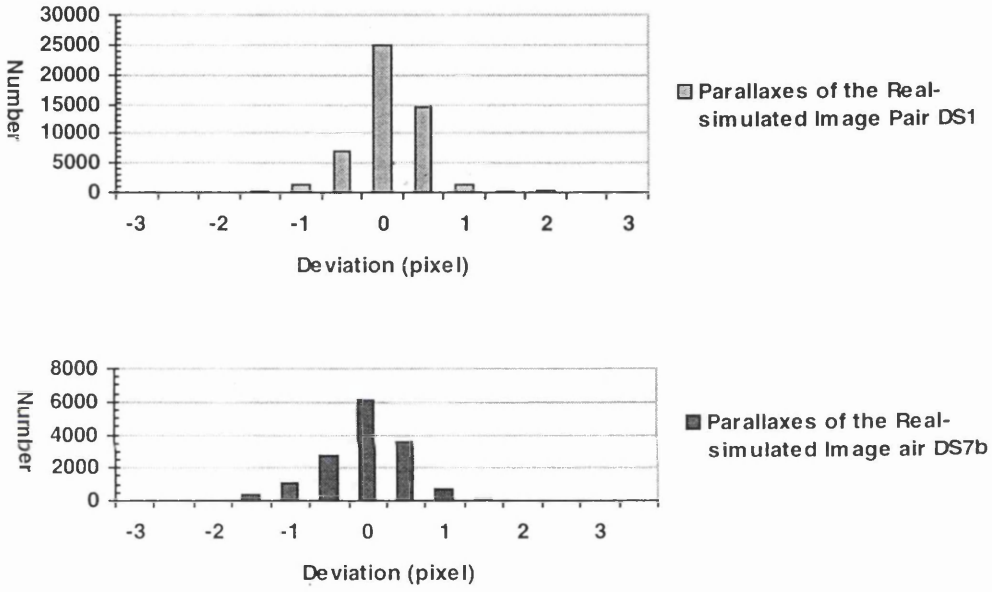

Figure 5.10 (a) Histograms of the parallaxes of the real-simulated image pairs (above: DS1; below: DS7b).

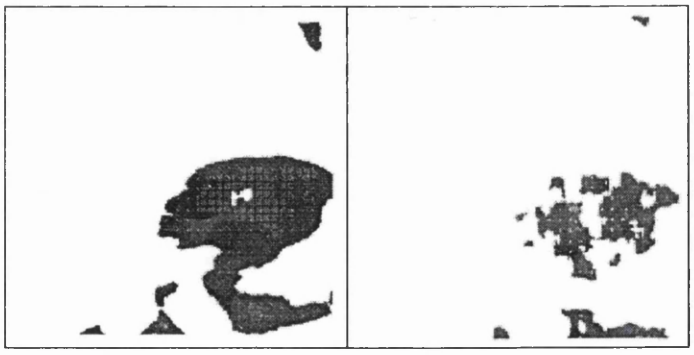

Figure 5.10 (b) Correlated image pixels (dark areas) of the real-simulated image pairs. Left: DS1. Right DS7b. Size: 1024 × 1024 pixels.

5.5.2 Verification of the Automatically Generated GCPs

Having verified the accuracy of the simulated image, the simulator can be used to provide GCPs automatically whose precision has to be validated and to be compared with the manually collected counterpart. A small chip of the reference DEM in 50m grid of 21 × 21 pixels size has been used for SAR simulation as shown in Figure 5.11. The DEM has to be interpolated into a 12.5m grid (81 × 81 pixels) to meet the need of the simulator covering an area of 1km × 1km. There are four real test images being simulated, and the characteristic of each image is listed in Table 5.3 (a), which are located on the same Aix-Marseilles test-site (see Chapter 3). The size of the simulated image based on the same DEM varies, according to different geometric aspects described by the header data of the real images being simulated, as listed in Table 5.3 (b).

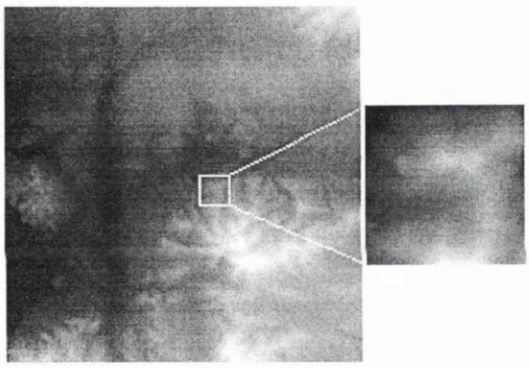

Figure 5.11 Reference DEM and the extracted DEM chip to be used for simulation. Left: the reference DEM in a 50m grid (13.5km × 13.5km). Right: the extracted DEM chip of size 21 × 21 pixels (1km × 1km) interpolated into a 12.5m grid (81 × 81 pixels).

Orbit Direction	RADARSAT Beam Mode	Year-Month-Date	Full-scene size (Row/column)	Alias Name
Descending	Standard-1	1997-08-22	7901 / 9075	DS1
	Standard-7	1998-03-13	7875 / 8937	DS7b
Ascending	Standard-1	1998-03-01	7876 / 8961	AS7
	Standard-7	1997-08-08	7901 / 9139	AS1

Table 5.3 (a) Four test images being simulated.

Alias name	DS1	DS7b	AS1	AS7
Size (row/column)	93/121	89/100	95/96	98/101

Table 5.3 (b) Size of each simulated image based on the same DEM.

These simulated images, as shown in Figure 5.12 (a)~(d) together with the real counterpart, were employed to correlate with the real image (1024 × 1024 pixels) to find the location of the simulated image in the real image co-ordinate system using equation (5.25). Assign every corner element of the DEM as a GCP, there are four GCPs available as in Figure 5.12 (e).

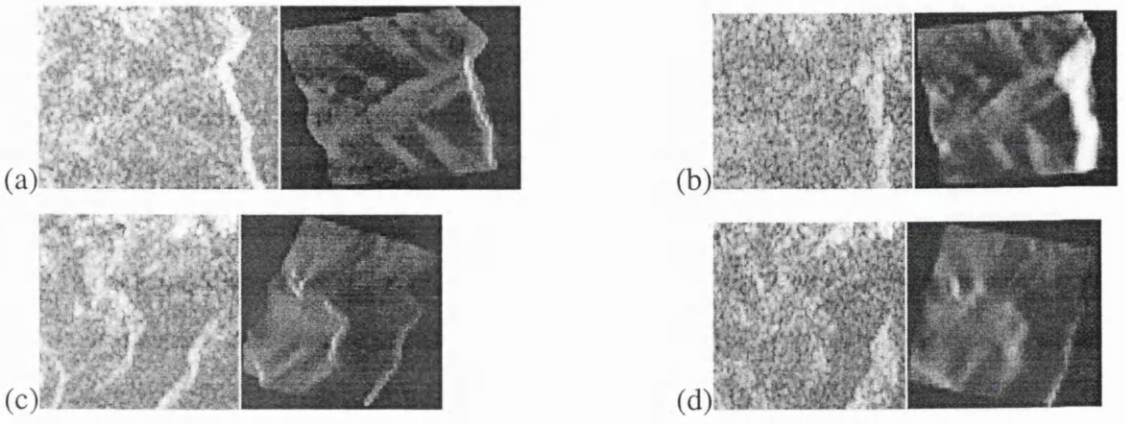

Figure 5.12 Real (left)-simulated (right) image chips. (a) DS1 (93 × 121 pixels). (b) DS7b (89 × 100 pixels). (c) AS1 (95 × 96 pixels). (d) AS7 (98 × 101 pixels)

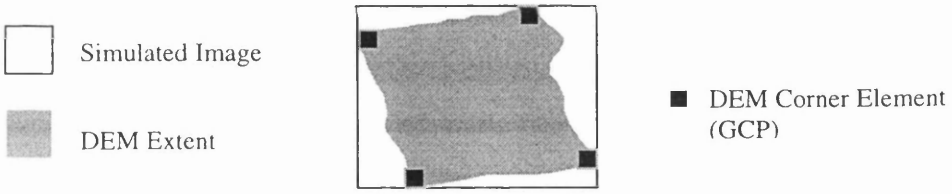

Figure 5.12 (e) A sketch of the simulated image (DS1) and the GCPs.

Following the procedures as described in Figure 5.7 and 5.8, the differences of the ground co-ordinates generated and the real ones of each GCP can be obtained giving the systematic corrections required. The ground co-ordinates of the GCPs in the real world were extracted from the DEM and kept as a record to be compared.

In order to check the consistency of all the GCPs, the residuals of each automatically generated GCP in respect to the mean of the positioning errors is calculated using the non-weighted space intersection as shown in Table 5.4 for the same-side descending image pair. For comparison and contrast, the residual error of each GCP selected manually on 1:25,000 maps using the non-weighted space intersection (see Chapter 3) is also demonstrated in Table 5.4.

The resultant co-ordinate measuring error of images and 1:25,000 maps is estimated as 36.7m in 3-D space, in case of 25m accuracy in plan and 10m in height (see Table 2.6 in Section 2.5). The RMS error calculated in 3D of the two manually selected GCPs is 32.5m, as presented in Table 5.4, which is reasonable comparing with the predicated error. But, the RMS error of the four automatically generated GCPs is only 10.6m showing a much higher quality of ground control than the manual counterpart.

In case of the weighted space intersection, the RMS errors of the automatically generated GCPs and the manually derived ones are compared again and listed as in Table 5.4. The effects from the poor quality GCPs can be improved using the weighted space intersection algorithm, as expected in Chapter 3. On the contrary, the precision of the automatically derived GCPs cannot be improved further, and even slightly worse (-0.8m). This is because the quality of the automatically derived GCPs is good, and the observations made automatically in range and in azimuth direction for a simulated image have no prior knowledge to support different weights applicable to the range and the azimuth time observations in the least squares solution. It confirms that the weight should be given to an observation according to the actual need, but not given arbitrarily, (recall Chapter 3 and Gauss [1823]). In general, giving an inadequate weight is liable to distort the results of a least squares solution.

A pair of the same-side ascending images is also tested using the same procedures as described above. The comparisons of the results derived from the ascending pair as shown in Table 5.5 for both cases of the non-weighted space intersection and the weighted solution, respectively, showing similar trends as seen in Table 5.4. The resultant residual error of the two manually selected GCPs of the ascending pair is 40.6m, which is slightly greater than the predicated error due to relatively poor image quality. As mentioned before, the quality of the GCPs generated using the manual map-and-image correlation method cannot be assured. In addition, the resultant residual error of the four automatically generated GCPs is merely 8.8m, which is much better than that of the manually selected ones. The effects from the poor quality GCPs can be improved using the weighted space intersection algorithm, but that is of no use for the high quality GCPs derived automatically using the simulation method, since there is no significant observation error applicable.

Notice that the automatically generated GCPs are derived using the terrain features simulated using the known (accurate) DEM chip, whose quality can be reflected into that of the automatically generated GCPs with high fidelity without degradation. This

is opposed to the manually collected GCPs using the traditional map-image correlation process, whose quality has been limited by the image quality and the performance of a human operator, as shown in Section 2.5.

Type of GCP	No. of GCPs		R.M.S.E.	Mean*	Min	Max.
Manually Selected GCPs	2	E	16.8	-260.1	-17	+17
		N	**25.0**	-49.4	**-25**	**+25**
		H	12.1	+220.5	-12	+12
		3D	**32.5**	**Non-weighted solution**		
Automatically Generated GCPs	4	E	7.9	-259.1	-12	+10
		N	2.7	-52.0	-3	+3
		H	6.5	+219.6	-9	+9
		3D	**10.6**	**Non-weighted solution**		
Manually Selected GCPs	2	E	17.2	-262.7	-17	+17
		N	**18.8**	-108.2	**-19**	**+19**
		H	12.5	+216.0	-12	+12
		3D	**28.4**	**Weighted solution**		
Automatically Generated GCPs	4	E	7.9	-23.0	-9	+9
		N	5.0	-110.1	-3	+3
		H	6.5	+216.1	-3	+5
		3D	**11.4**	**Weighted solution**		

*Mean: The systematic shift used for corrections. (unit: metre)

Table 5.4 Residuals of the GCPs derived manually and those generated automatically from the descending pair (left: DS1, right: DS7b) using the non-weighted space intersection (above) and the weighted solution (below).

Type of GCP	No. of GCPs		R.M.S.E.	Mean*	Min	Max.
Manually Selected GCPs	2	E	7.7	-230.5	-8	+8
		N	**38.6**	-124.2	**-39**	**+39**
		H	10.6	-109.9	-11	+11
		3D	**40.6**	**Non-weighted solution**		
Automatically Generated GCPs	4	E	7.2	-221.5	-8	+10
		N	3.4	-116.7	-4	+4
		H	3.7	-101.8	-3	+6
		3D	**8.8**	**Non-weighted solution**		
Manually Selected GCPs	2	E	8.5	-233.7	-9	+9
		N	**32.4**	-107.0	**-32**	**+32**
		H	10.3	-109.3	-11	+11
		3D	**35.0**	**Weighted solution**		
Automatically Generated GCPs	4	E	7.3	-224.0	-9	+10
		N	4.1	-103.4	-6	+5
		H	3.7	-101.4	-3	+6
		3D	**9.2**	**Weighted solution**		

*Mean: The systematic shift used for corrections. (unit: metre)

Table 5.5 Residuals of the GCPs derived manually and those generated automatically from the ascending pair (AS1(left)+AS7(right)) using the non-weighted space intersection (above) and the weighted solution (below).

5.5.3 Applications of the Automatically Generated GCPs

In order to evaluate the performance of the automatically derived control for space intersection, a total number of 32 ground check points have been selected manually from two images of the descending-pass images, including DS1 (left) and DS7b (right), as already described in Chapter 3. The image co-ordinates of each manually identified and matched check points were used as input for space intersection following the rigorous method proposed in Chapter 3. The two manually selected GCPs and the four automatically generated ones are used for systematic corrections of the results derived using the non-weighted space intersection, individually. The results derived were compared with the co-ordinates measured from the maps of a 1:25,000/50,000 scale, [IGN, 1989] and [IGN, 1992], as shown in Table 5.6. The same procedures are applied to the check points which are corrected by the manually selected GCPs and the automatically derived ones using the weighted solution as shown in Table 5.6.

Type of GCPs		R.M.S.E. (m)	Mean (m)	Min.(m)	Max.(m)
Manually Selected GCPs	X	25.3	+10.2	-43	+71
	Y	**20.0**	0.6	**-53**	**+72**
	Z	19.7	-4.7	-43	+26
	3D	**37.9**	**Non-weighted solution**		
Automatically Generated GCPs	X	25.4	+10.5	-42	+71
	Y	20.2	+3.0	**-51**	**+74**
	Z	19.7	-4.7	-43	+26
	3D	**38.0**	**Non-weighted solution**		
Manually Selected GCPs	X	25.6	+10.6	-45	+71
	Y	**17.0**	+5.7	**-42**	**+36**
	Z	19.4	-4.3	-43	+25
	3D	**36.3**	**Weighted solution**		
Automatically Generated GCPs	X	25.7	+10.9	-45	+72
	Y	17.7	+7.6	**-40**	**+38**
	Z	19.4	-4.4	-44	+25
	3D	**36.7**	**Weighted solution**		

Table 5.6 Statistics of the 32 check points calculated using the non-weighted space intersection (above) and the weighted solution (below) with the manually selected GCPs and the automatically generated ones for the descending pair (DS1+DS7b).

The RMS errors of the check points calculated using the automatically generated GCPs for systematic corrections are similar to those using the manually selected GCPs. This is comparable with the estimated measuring error of ground points (GCPs or check points) at a 1:25,000 scale (26m, see Table 2.6) and the predicted observation error from space intersection (28m, see Table 3.2). There is no enormous difference between the results derived using either the manually selected GCPs or the automatic ones, because

the results calculated are compared with the manually measured co-ordinates on maps whose resultant error may be as large as 38m ($=\sqrt{(26^2+28^2)}$), as has been calculated in Section 3.6.2. It can be seen that the measuring errors of the co-ordinates of the check points on maps/images dominate the deviations, no matter what kind of GCPs used. Notice that the extent of the deviations (precision) of the check points calculated using the weighted space intersection is relatively smaller than that using the non-weighted solution. The same trend can be seen again from the DEM obtained using the descending image pair as shown in Table 5.7. Thanks to the better image quality of the descending pair, the difference of shifts in height is not significant either using the manually collected GCPs or using the automatically derived ones for the descending image pair. The manually collected GCPs provide reasonably good quality control for generating DEMs in this case (recall Table 5.4). The DEM generated from the descending pair has been shown as in Figure 4.10.

However, this is not the case for generating a DEM from the ascending pair that shows an evident difference between the results calculated using the manually selected GCPs and those using the automatically generated ones as shown in Table 5.7. The generated DEM from the ascending pair corrected using the automatically generated GCPs is shown as in Figure 5.13. The difference of shifts in height between the DEM corrected using the manually selected GCPs and that using the automatically generated ones is about 8m for the ascending image pair. It is probably due to the poor image quality of the ascending image pair that leads to the significant errors of the measurements made for the manually selected GCPs (recall Table 5.5). The histogram of the deviations in height for the DEM generated from the ascending pair using the manually selected GCPs is shown in Figure 5.14 (above) that has been improved significantly using the automatically generated GCPs, as demonstrated in Figure 5.14 (below), in terms of systematic corrections.

Type of GCPs	Configuration	Coverage	Mean (m)	S. D. (m)	Min.(m)	Max.(m)
Manual	DS1+DS7b	81.0 %	1.4	23.9	-189	223
Automatic	DS1+DS7b	81.0 %	1.4	23.9	-189	223
Manual	AS1+AS7	76.4 %	**10.2**	23.4	-209	233
Automatic	AS1+AS7	76.4 %	**2.3**	23.6	-217	219

Table 5.7 Accuracy statistics of the DEMs derived from the descending pair and the ascending one using the manually selected GCPs and the automatically generated ones.

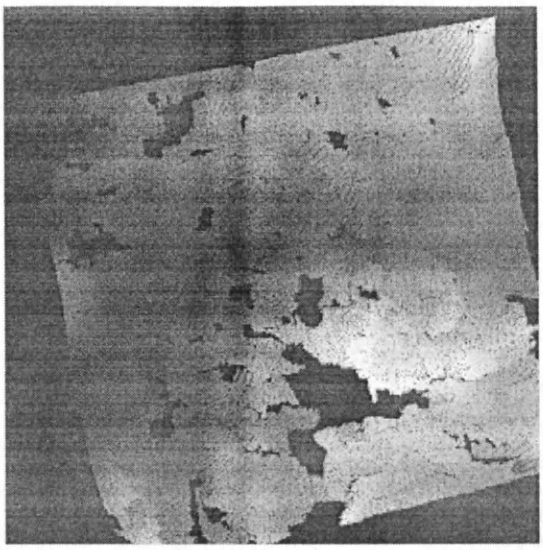

Figure 5.13 A Raw DEM generated from the ascending same-side image pair (using four automatically generated GCPs. Size :13.5 km × 13.5 km in a 25m grid).

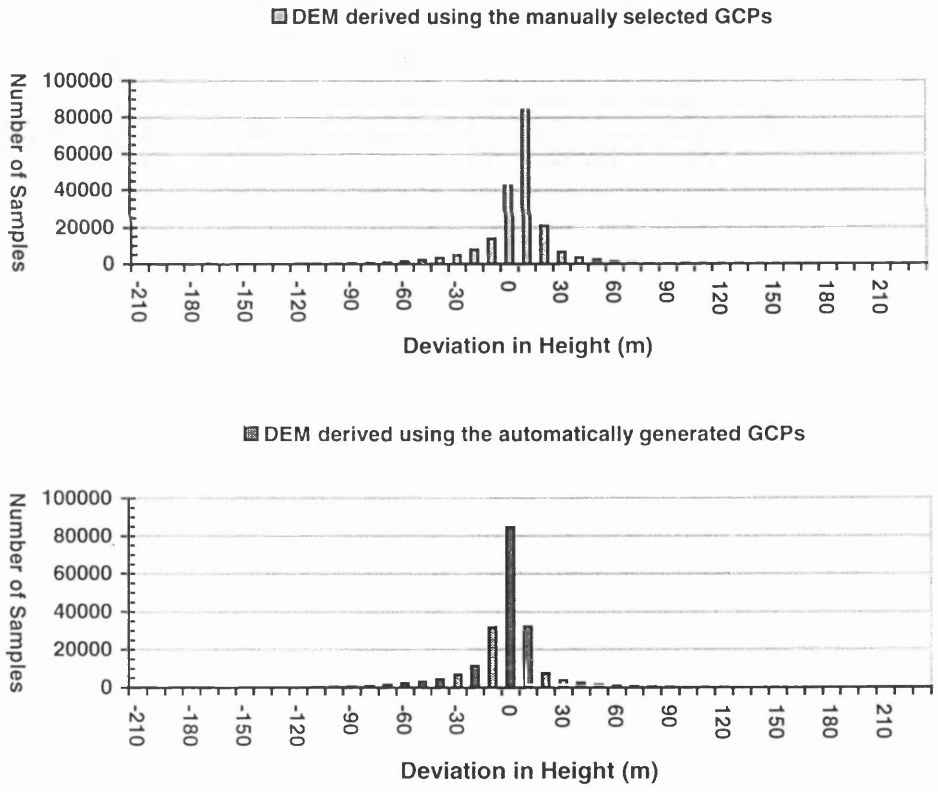

Figure 5.14 Histograms of the deviations in height of the DEM generated from the ascending image pair using different sources of GCPs (above: using two manually selected GCPs; below: using four automatically derived GCPs).

5.5.4 Discussion

Validation of the simulated images indicates that there are no significant distortions shown in terms of the parallaxes between the simulated-real image pair measured using the pyramidal least squares correlation routines with a region-growing approach. Sub-pixel accuracy for the simulated images has been achieved. The maximal extent of the parallaxes ranges from –3.2 ~ +3.5 pixels. It has been verified that the SAR image simulator is not sensitive to the absolute accuracy of the orbit data as shown by different orbit passes, however, a well-defined geometry of the SAR image is essential for achieving an automatic simulation. The perpendicular relationship between the resultant range vector and the resultant velocity vector is assumed for the simulator that is reasonable for the case of the RADARSAT SAR data as shown above.

The real-simulated image correlation is carried out using a cross-correlation measure that gives the exact location of the simulated image chip of interest in respect to the real SAR image co-ordinate system when the maximal cross-correlation coefficient is detected. The correlated image co-ordinates are measured, in terms of accuracy, with deviation about ±1 pixel. Thanks to the sub-pixel accuracy of the proposed simulator applicable, the quality of the automatically derived GCPs affected by the SAR image simulator and the real-simulated image correlator is expected to be within ±2 pixels.

In terms of providing control, the accuracy of the simulated image considered is placed on the top priority with no regard to computational load. The computing factor is of no importance in the case of simulating an image chip of small size as about 100×100 pixels. The ground co-ordinates of the automatically derived GCPs can be obtained from the known DEM chip used for simulation hence the accuracy of the GCPs is kept on the same order of the accuracy of that DEM when it was produced (±5m in height as mentioned in Section 4.4.1). The quality of the automatically generated GCPs is obviously better than that of the GCPs collected manually from maps/images as shown by the accuracy statistics. The use of the weighted space intersection is justified in the case of using the manually collected (relatively poor quality) GCPs for systematic corrections so that the effects of observation errors of azimuth lines can be reduced. Nonetheless, the use of the non-weighted space intersection still works when there are smaller observation errors, such as the case of the automatically derived GCPs.

The advantage of the automatically generated GCPs can be seen from the systematic correction being made for the DEM derived from the ascending image pair

whose image quality is relatively poor leading to an incomplete ground control provided by a manual method. It has been shown that all of the co-ordinates measured manually suffer more or less from the limitations of the mapping scale and the ambiguities of the locations of GCPs measured from maps and images. Hence it can be concluded that the automatically generated GCPs are able to replace the role of the manual ones under the condition of a known DEM chip of a small area with terrain of varied relief available.

The known DEM chip can be derived from maps of a 1:25,000 scale or commercially available DEM products provided that the quality of the DEM is reasonable, say accuracy in height of ±5m at least. It is not very difficult to obtain a 1:25,000 scale map in developed areas nowadays. Some countries even produce maps of a larger scale, such as the ortho-rectified image-maps of a 1:10,000 or a 1:5,000 scale. However, the coverage of larger scale maps in the world is still far from complete. Thus, the proposed method can only be employed in the areas where adequate local maps or a portion of DEM data is available. It means that this method of providing control is suitable for improving the positioning accuracy in a mapped area. At least a small portion of mapped area is required, but not the entire area.

The provision of such a known DEM chip in an unknown area may be difficult. When there is no known DEM applicable for providing control, the manually selected GCPs have to be derived using the weighted space intersection routines to obtain reasonable systematic corrections as demonstrated by the experimental results (recall Chapter 3). After correcting systematic shifts, further analysis and refinement for the stereo-generated DEM can be done as shown in Chapter 6 that is a preparatory stage for geocoding a SAR image using the stereo-generated DEM, which will be discussed in Chapter 7.

5.6 Summary

The quality of the manually selected GCPs cannot be assured due to the limitations of a mapping scale, the scattering characteristics of a SAR image and the uncertainties arising from manual measurements. A SAR image simulation technique with a higher level of automation and an image correlation routine have been proposed and employed to generate GCPs in this chapter. In general, the SAR image simulator is not sensitive to the accuracy of the orbit data, provided that the real SAR image geometry is well-defined in range and azimuth time data. The extent of the simulated area can be

detected automatically if the orbit data covering the simulated area is available. The geometric considerations for the simulated image follow the image structure of a real SAR image based on the assumption of the perpendicular relationship between the resultant range vector and the resultant velocity vector.

A known DEM chip with varied terrain surface available, say 1km × 1km, is essential for simulation. A cross-correlation measure is adopted for locating the simulated image chip in the real SAR image co-ordinate system. The quality of the automatically generated GCPs has been shown better than that of the manually selected ones from the experimental results. Since the co-ordinates of each point of a DEM are already known and the corresponding image co-ordinates can be derived using the proposed simulation technique, providing GCPs automatically, instead of manually collected GCPs, is possible. The use of a non-weighted space intersection can effectively suppress the effects from the observation errors of azimuth lines when a known DEM is unavailable and manually selected GCPs are required.

Chapter 6

Refinement of the Generated DEMs

6.1 Introduction

Using the rigorous algorithm of space intersection and the pyramidal image correlation scheme with a region-growing technique directed by an optimized parameter selection strategy, as described in Chapter 3 and 4, a raw DEM composed of irregularly distributed ground points can be derived. Further effort for the automatic provision of ground control, which improves the accuracy of the GCPs used, ensures the quality of the radargrammetric results derived, as shown in Chapter 5. The DEM obtained is, however, incomplete in terms of practical applications, which demand spatial data without gaps or blunders. This chapter focuses on refining the DEMs generated, in conjunction with further analysis that may clarify the full potential and limitations of the DEM obtained for further applications, such as geocoding.

Refinement of the DEM generated has to be carried out carefully. This is because there is no 'true' DEM to be compared. In this chapter, the reference DEM with accuracy quoted as ±5m, [Alias, 1994, private communication], will be used to validate the quality of the DEM derived. Each step of refinement for the DEM derived is followed by a quality check in respect to the reference DEM.

There are typical terrain induced effects appearing in a SAR image pair, for example, layover, leading to the formation of gaps in a raw DEM generated. These effects, besides the errors predicted by the error model of observation errors for space intersection as mentioned in Chapter 3, decrease the quantity, and deteriorate the quality, of the results derived from image correlation routines, as discussed in Section 6.2. A primitive refinement of the DEMs generated can be made to improve the DEM coverage without degrading the overall accuracy, for example, filling the major gaps using the DEMs generated from different orbit directions, as demonstrated in Section 6.3. Since the

original elevation data is not changed, there is no effect on the quality of the DEM derived, but the coverage of that DEM can be improved efficiently.

Further improvements can be made using an interpolation method to fill minor gaps. This makes a 'complete' DEM without gaps or voids, but the DEM quality might be affected at this stage. In addition, a filtering technique is employed to suppress noise and to derive a practical DEM, as demonstrated in Section 6.4. Filtering DEMs can make significant effects on the final results. Again, a quality check for the DEM derived is essential. Two data sets of different orbit passes, including the ascending and descending orbits, will be tested to validate the algorithms used.

6.2 Characteristics of the Generated DEM

In Chapter 3, the error model of space intersection has been established to predict the theoretical deviations caused by the observation errors of image co-ordinates. But it is not enough for a complete understanding of the error behaviour shown in the DEM generated from a SAR image pair, particularly the intrinsic limitations of the SAR image geometry. Consider a hilly area sensed by a SAR sensor, there are three kinds of terrain distortions known as layover, shadowing and foreshortening effects due to the SAR imaging geometry. Their impacts on derivation of spatial information, such as generating a DEM, can be significant.

6.2.1 Layover effects

When the terrain slope, in terms of angle, is greater than the incidence angle, layover effects appear in the radar data of high incidence angles, where the near/higher ground points are placed on top of the far/lower ones. This causes ambiguity between different ground points having the same nominal distance to the SAR sensor, and spatial information is lost as shown in Figure 6.1. Let A, B, C and D the ground points in the layover area of the left image and ground point B and C in the layover area of the right image. Within a layover belt, at least two, or more, distinct ground points are projected onto a single image pixel. For instance, ground point A and C are exactly the same point in left image, and point C is projected nearer than B either in the left or right image. Hence the range information conveyed by the slant range pixels from point A to D in the left image or point B and C in the right image is indistinguishable.

The width of a layover belt of one SAR image can be narrow and be different from another image with varied incidence angles. Consider image correlation for generation of a DEM in layover areas. The image correlation routine employing a region-growing technique tends to carry out image correlation towards or from both sides of the layover belt whose edges can be treated as the image features that dominate the image texture in hilly areas. Firstly, the exact location of these features in one image may be displaced slightly from the expected location in the other image due to varied incidence angles hence introducing errors. Secondly, the region-growing procedures towards or away from a layover edge may also generate different results due to the ill-defined layover edges. The outcome of image correlation in hilly areas, then, can be less reliable and be incomplete due to information loss.

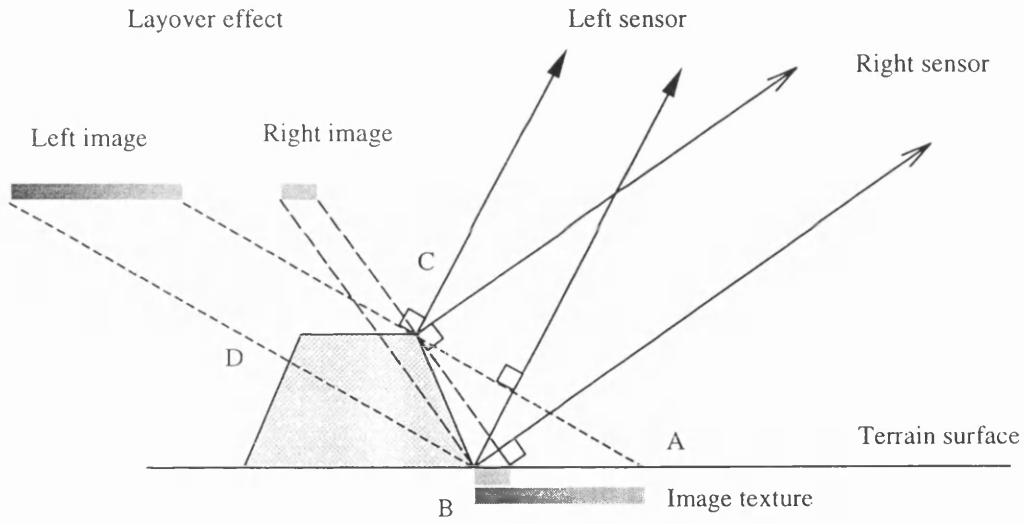

Figure 6.1 Layover effects

The layover maps simulated from the ascending and descending images, as described in Table 5.3(a), can be produced from the SAR image simulator, as proposed in Chapter 5. These layover maps are shown in Figure 6.2 (a) and (b). Figure 6.2 (a) demonstrates the grey images of the descending image pair in the top row (left: DS1, right: DS7b) and those of the ascending image pair in the bottom row (left: AS7, right: AS1). The original size of each image is 1024 × 1024 pixels. Obviously, the layover areas of the lower incidence angles (AS7 or DS7) are smaller than, and included in, those of the higher incidence angles (AS1 or DS1) as shown in Figure 6.2 (a). The overlapping

layover maps give ideas about the level of information loss may occur when the space intersection and image correlation methods are applied to different geometric configurations of SAR image pairs. Figure 6.2 (b) shows the overlapping layover map of the descending image pair (top-left: DS1+DS7), that of the ascending image pair (top-right: AS1+AS7), that of the high-incidence-angle images (bottom-left: AS1+DS1) and that of the four images (bottom-right: AS1+AS7+DS1+DS7).

Generally, extraction of spatial information is difficult and is less reliable in the dark-grey/black areas where both images of a conjugate pair are affected by layover effects. In terms of terrain mapping, although an image pair given as (DS1+DS7) or (AS1+AS7) can only generate an incomplete elevation data set, those elevation data without layover effects provide the basis for refinement and make digital elevation modeling possible. This will be discussed further in Section 6.3.

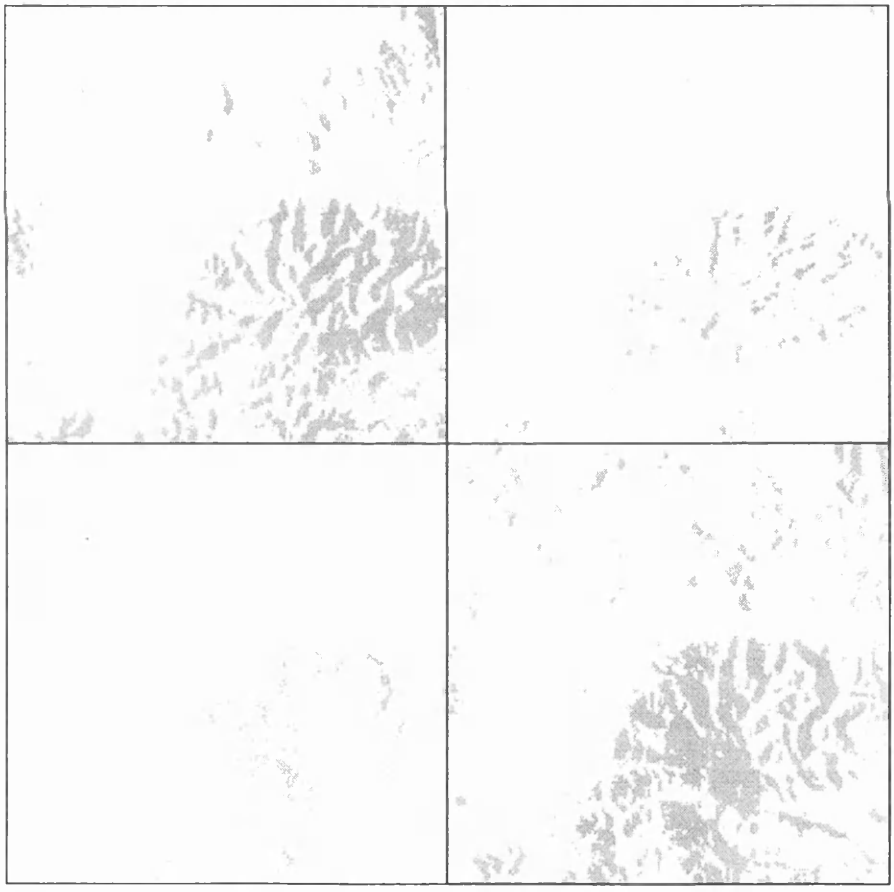

Figure 6.2 (a) Layover maps of the four test images (Top-left: DS1. Top-right: AS1. Bottom-left: AS7. Bottom-right: AS1. Size: 1024 × 1024 pixels)

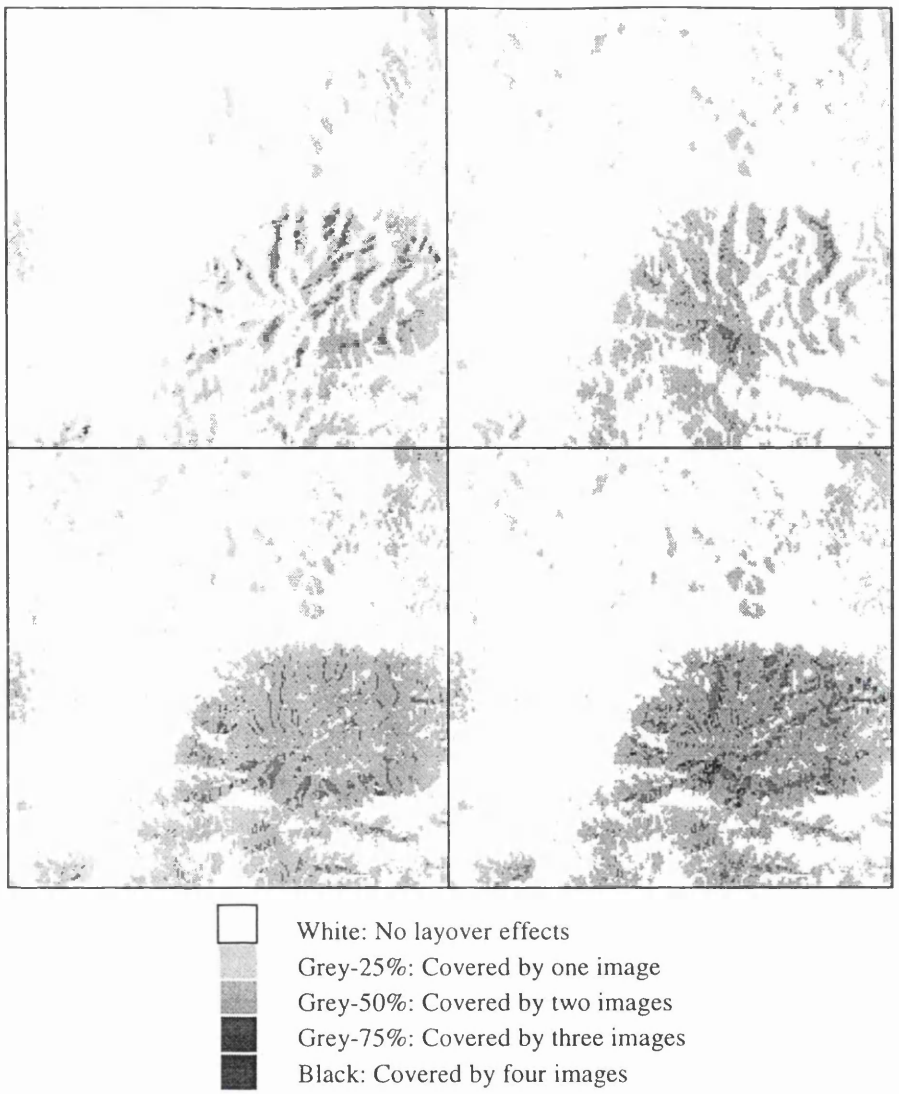

Figure 6.2 (b) Overlapping layover maps from image pairs of different orbit direction (Top-left: DS1+DS7b. Top-right: AS1+AS7. Bottom-left: AS1+DS1. Bottom-right: AS1+AS7+DS1+DS7b. Size: 11km × 11km.)

6.2.2 Shadowing effects

When the terrain slope, in terms of angle, plus the incidence angle is greater than 90°, shadowing effect occurs as dark areas. Theoretically, there are no features available within the shadowing area to allow image correlation to be applied. This causes gaps in a generated DEM. But, speckle and noise appearing in SAR images gives the shadowing areas a low density number (DN), instead of zero value. Consider the relationship between the actual terrain relief and the shadowing effect. Given an incidence angle of 23°, the shadowing effect will appear in the areas where the terrain slope is greater than 67°. However, such effects are relatively less significant than those of layover, because

terrain slope exceeding 40° is seldom seen in flat-to-moderate relief areas. In hilly areas, the layover effects dominate the image features and the shadowing effects are still less significant.

6.2.3 Foreshortening effects

The foreshortening effect provides a more positive reason for producing a DEM from SAR data. The foreshortening effect pushes ground points of higher elevation towards the SAR sensor, without superimposition, preserving terrain information to be retrieved for generating a DEM. The steeper the incidence angle of the direction of microwave propagation, the greater the foreshortening effect on SAR imagery. In some areas where the slope of terrain surface approaches to the incidence angles of an image, those ground points may be compressed so seriously that spatial information loss can be possible. For instance, the extent of a feature of one image may be not equivalent to that of the other image. In this case, the foreshortening portion of the high-incidence-angle image may be under-sampled compared with its counterpart in right image. Hence some pixels of the low-incidence-angle image may miss their counterparts, leading to some kinds of narrow and interlaced gaps appearing in a raw DEM, as shown in Figure 6.3.

Figure 6.3 shows that various terrain effects can cause information loss, such as gaps, blank dots and holes in a derived DEM. The left image in Figure 6.3 was extracted from the reference DEM (see Figure 4.9) in a hilly area, and the right image from the DEM (see Figure 4.10) generated using the descending image pair (DS1+DS7b). The gaps remaining in the DEM generated match the prediction made from the layover map shown in Figure 6.2 and must be refined with appropriate methods in order to provide further applications. For more details of DEM refinement see next section.

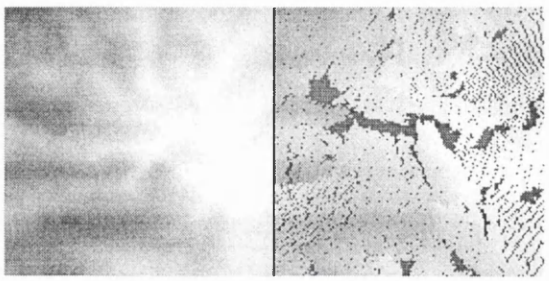

Figure 6.3 Gaps in the generated raw DEM (right) caused by various terrain effects (compared with the reference DEM (left), size 3.2km × 3.2km.)

6.3 Data Fusion of the Raw DEMs

The same-side RADARSAT SAR images of the descending orbits (DS1+DS7b) and those of the ascending orbits (AS1+AS7) form stereoscopic SAR image pairs, respectively, to be correlated together to produce parallax files using the optimized pyramidal correlation scheme, as demonstrated in Chapter 4. The parallax files generated can then be used to generate DEMs according to the rigorous space intersection proposed in Chapter 3. As mentioned before, there are no GCPs to be used as input for the space intersection algorithm. A total number of four GCPs generated automatically, using the method proposed in Chapter 5, have been used to correct the systematic shifts caused by inferior orbit data.

The original generated DEMs have been shown in Figure 4.10 and Figure 5.13 for the descending pair and the ascending pair, respectively. Notice that the brighter the area, the higher the elevation is represented. Obviously, there are numerous gaps in the hilly areas as shown in both figures. The generated DEMs have to be compared with the corresponding data points of the reference DEM at the same location giving the accuracy statistics that have been shown in Table 5.7 in Chapter 5. Obviously, the results obtained are reasonable in terms of the DEM quality, but unsatisfactory in terms of the quantity of elevation samples, and there are many gaps and holes remaining in the derived DEM. In this section, a straightforward method is applied to the generated DEMs in order to increase the quantity of the DEM samples without degrading the DEM quality.

Radar illumination for ground objects can vary enormously due to different aspects and orbit directions, [Skolnik, 1981]. Similarly, terrain effects can be serious for SAR data on one side, but less significant on the other. Assuming two or more image pairs from different orbital directions are available, for example, the ascending and descending orbits, the layover and shadowing effects may be complemented using DEMs generated from different directions. In doing so, each DEM data set must be transformed into an elevation data file composed of the ground co-ordinates in the format of easting, northing and height (E, N, H) for each DEM element. Both DEM data files have the same format as (E, N, H) for each row of the files, therefore, merging both files together can be easily done. Hence, a new DEM can be generated by merging together two raw elevation files, which can be derived using space intersection for both descending and ascending orbits, into one DEM file. Note that the two data sets have to be corrected by good quality GCPs for systematic shifts in advance, as illustrated in Chapter 5. The new DEM

generated is shown in Figure 6.4 (right) for the DEM derived from the descending pair (shown in Figure 6.4 (left)) and that of the ascending pair (shown in Figure 6.4 (centre)). Therefore, most of the major gaps in raw DEMs can be filled. Appendix E.1 gives the DEM derived form data fusion of a larger scale. Error statistics of the new DEM generated comparing with the reference DEM are shown in Table 6.1.

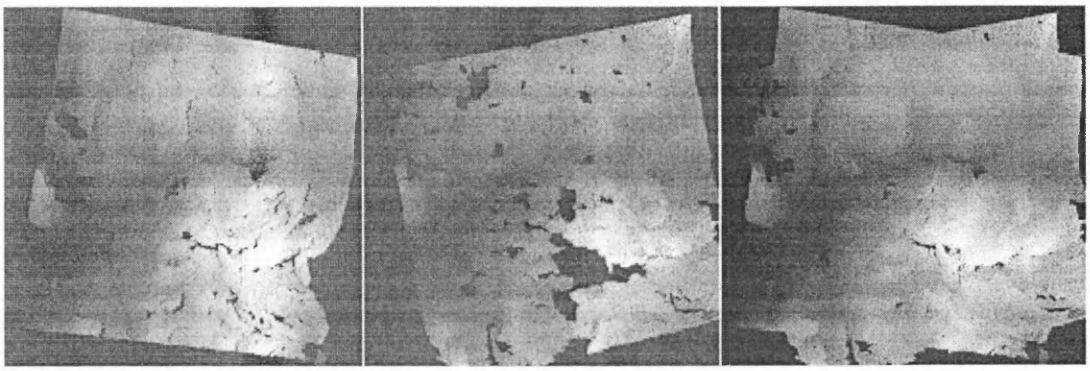

Figure 6.4 A new DEM (right) generated by merging descending (left) and ascending (centre) data sets. (Size: 13.5 km × 13.5 km in a 25m grid, approximately.)

Steep terrain surface, such as cliffs, and failures of image correlation due to different illumination of image features contribute to the formation of the remaining minor gaps and to the 'blunder'. The blunder is caused by the ambiguity of the range information in layover areas as stated in Section 6.2. Since the pyramidal least-squares correlation method with a region-growing approach was applied to derive parallax data, image correlation may fail, but false image correlation is unlikely to occur. The region-growing approach, according to Otto and Chau [1989] as mentioned in Section 2.4, searches for the best-matched point based on the analysis and comparison of the results derived from the least-squares adjustment and assures the matched region can grow only at the best correlated pixel.

All of the samples of the DEMs were categorized according to the height deviations giving a histogram as demonstrated in Figure 6.5 (a). The error distribution of the new DEM is comparable with the histogram of the DEM generated from the descending pair as shown in Figure 6.5 (b) and that from the ascending pair as have been seen in Figure 5.14 (b). In general, there is no significant bias remaining in the DEMs generated and most of the errors tend to concentrate within ±30m symmetrically with respect to zero value. As discussed before, information loss in layover areas and in shadowing areas due to terrain effects cannot be recovered completely. Also, the

problems of failed image correlation owing to speckle and varied image texture are also difficult to overcome. Using the results derived from image pairs of different orbits may fill major gaps, but not all. So, the new DEM generated still needs to be refined further.

Orbit	Type	Coverage	Mean (m)	S. D. (m)	Min.(m)	Max.(m)
Descending	S1+S7	81.0 %	+1.4	23.9	-189	+223
Ascending	S1+S7	76.1 %	+2.3	23.6	-217	+219
DEM derived from both data sets			+1.8	23.8	-217	+223

Table 6.1 Accuracy statistics of the new DEM generated (using four automatically generated GCPs for correcting systematic shifts in advance.)

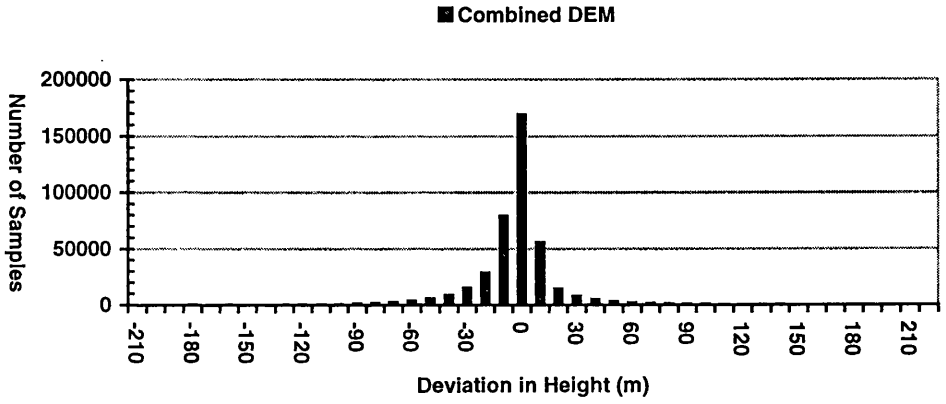

Figure 6.5 (a) Histogram of the deviations in height of the new DEM (generated by merging the ascending and descending data sets together.)

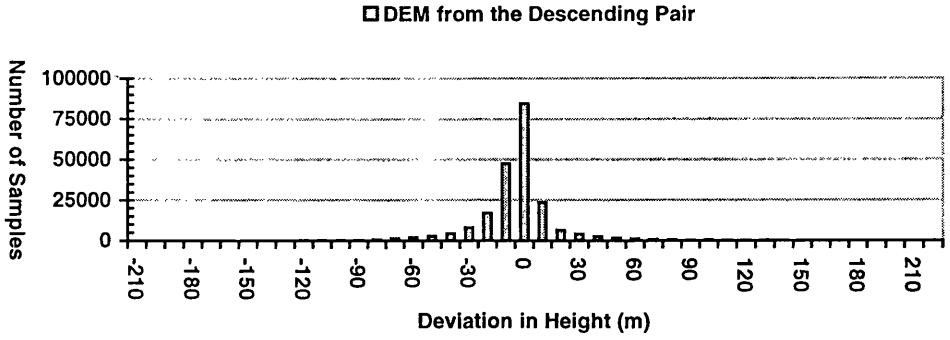

Figure 6.5 (b) Histogram of the deviations in height of the DEM generated from the descending image pair.

6.4 Further Refinement of the DEM Generated

In terms of digital elevation modeling, the specifications of the data model required must be given and then further refinement for that DEM can be possible. Generally, the DEM automatically generated using photogrammetric or radargrammetric methods have extensive coverage in the area of interest with high density of the order of the pixel spacing of the images used, and with the spatial distribution of nearly a regular grid. As there are abundant data available, the elevation model of a regular grid is relatively easy to retrieve and be processed for further applications, for example, in the raster-based Geographical Information System (GIS), [Burough and McDonnell, 1998], and in geocoding. The data model of a regular grid is then adopted for the DEM generated in this thesis.

Due to spatial information loss caused by layover and shadowing effects, it can be expected that the possibility of refinement for a raw DEM is quite limited in hilly areas. Filling gaps using some interpolation routines is possible for any kind of terrain surface, although the DEM quality varies depending on the terrain effects. In addition, filtering the noise existing in a derived DEM is also possible, however, over-done smoothing has to be avoided. All of the refinement methods employed are based on the considerations for automation, instead of the use of any manual editing method that degrades the level of automation in the whole digital radargrammetric system. Each step adopted for DEM interpolation or DEM filtering may introduce errors and affect the results derived, so, the detailed analysis of the refined DEM will be given step-by-step to verify the overall quality derived.

6.4.1 DEM Interpolation

Interpolation is given as the procedure of estimating the unknown values at specific locations within the extent covered by the measurements made in the same area. The need of interpolation for digital elevation modeling arises in various cases, [Burough and McDonnell, 1998], such as:

(1) The raw DEM has a different resolution or orientation from that required,
(2) A desired surface model has a different data model from the original one, and
(3) The resultant DEM does not cover the whole area of interest completely.

For instance, evaluating the quality of the results derived from the image correlation and space intersection routines needs a reference DEM for comparison. In doing so, the raw DEM generated has to be interpolated into the same resolution and orientation as the data model of the reference DEM, such as in a regular grid structure or a local map co-ordinate system. There are many algorithms available for interpolation, ranging from the simplest linear interpolator and the moving averages with inverse-distance weighting method to the most sophisticated kriging in geo-statistics. The grid-based interpolation routines, used in photogrammetry and surveying, include point-wise searching techniques and patch-wise polynomial fitting methods, [Petrie, 1990a]. The polynomial equations used for densification (interpolation) of a coarse grid-based DEM vary with the number of the regular grids included, ranging from one grid (2×2 points) to 9 grids (4×4 points). The classic moving averages with inverse-distance weighting method is straightforward for a random-to-grid interpolation and easy to implement. There are many options available for searching the neighbouring reference points (random elevation samples), including the search radius, the number of sectored search directions and the total number of reference points searched *etc.*

Initially, kriging was developed by the French geo-mathematician Georges Matheron and the South African mining engineer D.G. Krige [Burrough and McDonnell, 1998] as an optimal method of interpolation for use in mining industry, in the sense that weights are chosen so as to optimize the interpolation function. A given variogram model is essential to determine the optimal weights for interpolation. Unfortunately, this is always unavailable for generation of a DEM where spatial data is exactly required, according to O'Neill [1991]. In addition, it has been said that when there is no variogram available, kriging has similar performance to that of the moving averages with inverse-distance weighting method, [Isaaks and Strivastava, 1989].

A full analysis of these interpolation algorithms is beyond the scope of the thesis. In this thesis, the kriging procedure without giving variogram is adopted due to its potential flexibility for dealing with interpolation of spatial data (recall that the result derived will be similar to that of the moving averages with inverse-distance weighting method, according to Isaaks and Strivastava [1989]). In order to fill any gaps within the area of interest, the DEM generated, as in Figure 6.6 (left), has been interpolated into a complete DEM in a 50m grid, as shown together with the reference DEM in Figure 6.6 (right). The interpolation of the generated DEM was carried out in the same co-ordinate

system as the reference DEM (French Conformal Conic Zone III). Appendix E.2 shows the interpolated DEM of a larger scale.

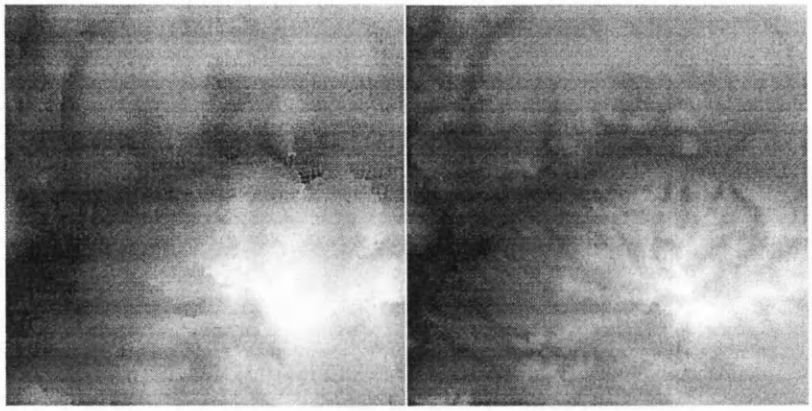

Figure 6.6 Interpolated DEM (left) and reference DEM (right). The height increases with increasing brightness. Size: 10km × 10km.

In general, gaps in the test area have been filled, except a small area off shore in the Mediterranean Sea where elevation data is of no concern whatsoever. The surrounding blank area of the test-site has to be cut to derive an effective area of DEM that can be compared with the reference DEM without interference from zero values. A sectioned area of a difference DEM of 10km by 10km is then derived. Figure 6.7 shows the absolute difference in height between the reference DEM and the interpolated DEM obtained in a 50m grid. The darker the gray value, the larger the deviation is represented.

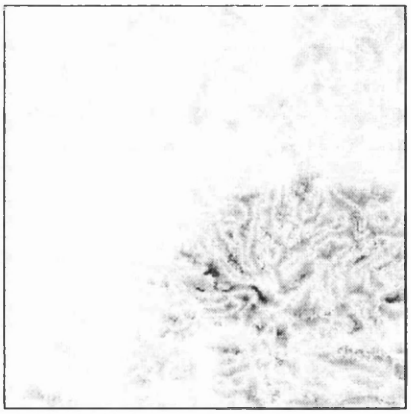

Figure 6.7 Absolute difference DEM image (between the interpolated DEM and the reference one, the error magnitude increases with increasing darkness.)

Note that the absolute difference DEM shows a similar pattern to the layover map demonstrated in Figure 6.2 (b) that indicates the deviations in height of the DEM

generated are related to the layover effects. The artifacts appearing in the absolute difference DEM image demonstrate a contour-like pattern. This is due to incomplete information extraction in the areas of hilltop. Hence it shows continuous and greater deviations in height in that area of the interpolated DEM. Namely, the detailed terrain features of the generated (interpolated) DEM suffer from the layover effects and cannot be completely restored in hilly areas. These deviations cause the blunder as shown statistically in Table 6.2, which gives the accuracy statistics in height in the effective (interpolated) DEM area. Further analysis in the following section will show that the DEM generated is rather smoother than the actual terrain surface. The histogram of the height deviations of that interpolated DEM is shown in Figure 6.8.

It can be seen that the RMS error has been reduced, comparing with the raw DEM as shown in Table 6.2. The deviations of 84.8% samples in the population are less than ±21.63m and 88.12% samples less than ±30m. Blunder percentage is defined as the ratio of the number of samples whose deviation in height is larger than three times of the standard deviation (S.D. or σ) derived in respect to entire population that is equivalent to 2.6% samples. The 'blunder' of the interpolated DEM is caused by the layover effects as shown in Figure 6.7, instead of false image correlation, so, it is not quite possible to be removed from the DEM.

DEM Samples	Mean (m)	S.D. (σ) (m)	RMS (m)	Min. (m)	Max. (m)	Error (%) ≥ ± 1 σ	Blunder (%) ≥ ± 3 σ
40401	-1.595	21.58	21.63	-192	+138	15.21	2.6

Table 6.2 Statistics of the interpolated DEM (compared with the reference DEM in a 50m grid)

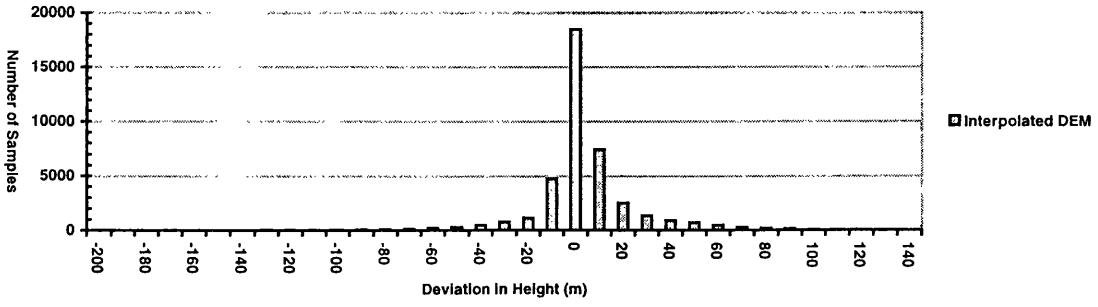

Figure 6.8 Histogram of deviations in height of the interpolated DEM

6.4.2 Detailed Analysis for the Interpolated DEM

A detailed analysis for the DEM derived is made in this section to give a full understanding of it, leading to further refinement. Two profiles in northing of the interpolated DEM in a hilly terrain area (E = 854.4km) and a flat-moderate area (E = 849.5km) have been selected to demonstrate the differences between the derived DEM and the reference one, as listed in Table 6.3 and sketched in Figure 6.9. The local co-ordinate system is referred to the French Lambert Conformal Conic Zone III map projection system.

DEM Profile	Terrain Type	Mean (m)	S. D. (m)	RMSE (m)	Min. (m)	Max. (m)
E=849.5km	**Moderate**	-5.1	5.0	**7.1**	-19.1	+14.9
E=854.4km	**Hilly**	-11.5	29.8	**32.0**	-153.1	+47.2

Table 6.3 Statistics of the differences in height between profiles in northing of the interpolated DEM compared with the reference one.

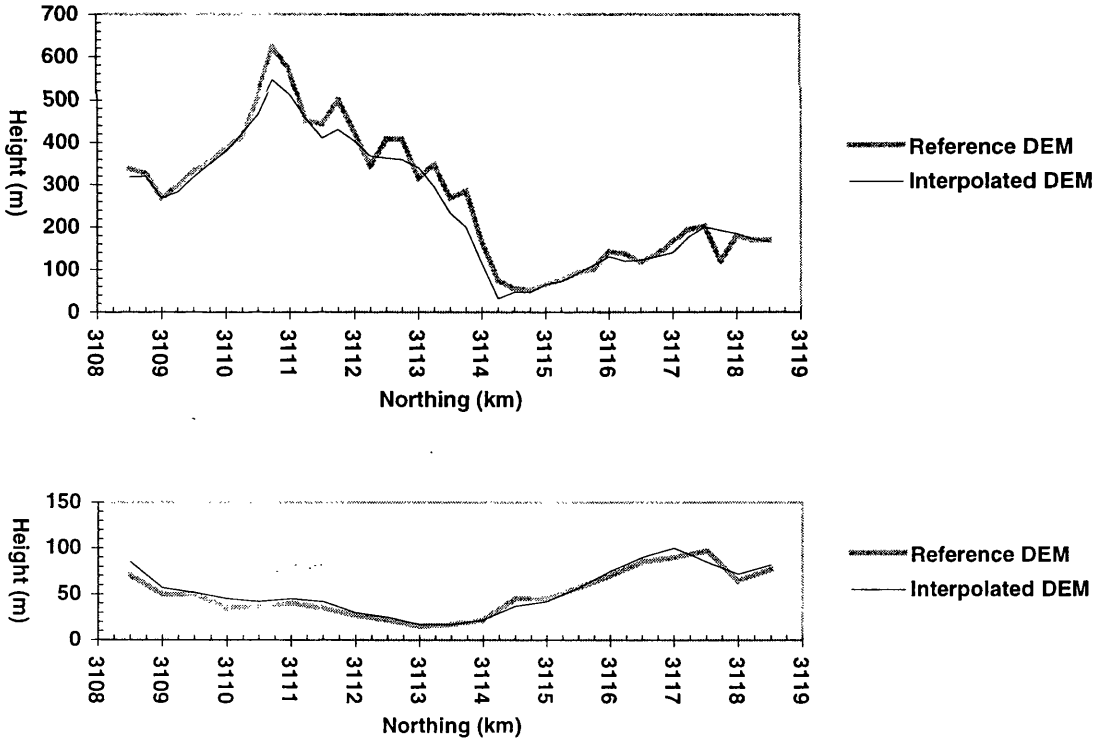

Figure 6.9 Terrain profiles in a hilly area (above, E = 854.4km) and in a moderate-flat area (below, E = 849.5km) of the interpolated DEM compared with the reference DEM.

It can be seen from these examples that the DEM quality in flat-moderate areas is relatively stable compared with that in hilly areas. Although the terrain trends can be roughly determined as seen in the interpolated DEM derived, some of the major terrain features have been smoothed out, due to information loss in layover areas. Besides individual profiles, more detailed comparisons were made between the interpolated DEM and the reference one in terms of profiles in northing and easting direction. The statistics of the terrain relief in terms of each profile of the reference DEM in northing is given in Figure 6.10 and shows a relatively moderate surface at the western part of the test area and a hilly terrain at the eastern part. Figure 6.11 illustrates the accuracy statistics of the elevation samples in terms of each profile of the interpolated DEM in northing compared with the reference one. Apparently, the accuracy in height of the derived DEM at the western part of the test-site is better than 14m, while that of the eastern part goes up to 34m. It shows a general tendency that the accuracy of the interpolated DEM is better in the moderate areas than in the hilly areas. Also, the deviations in height as shown in Figure 6.11 are somewhat related to the statistical characters of terrain surface (Figure 6.10).

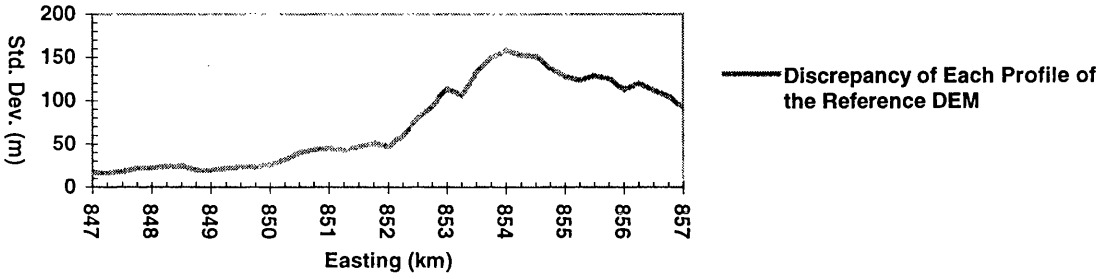

Figure 6.10 Standard deviation of each profile in northing of the reference DEM

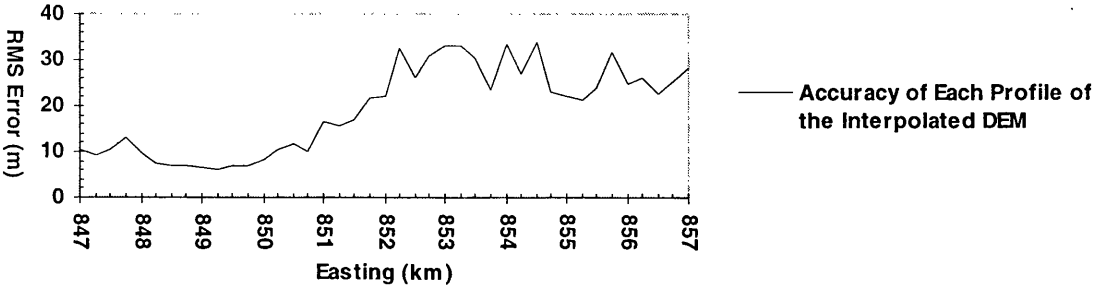

Figure 6.11 RMS errors of each profile in northing of the interpolated DEM (compared with the reference DEM.)

Two selected profiles in easting of the interpolated DEM, fixing N-values, in a hilly area and a flat-moderate area, have also been compared with the reference one as listed in Table 6.4 and shown in Figure 6.12. In addition, the discrepancy in height of each profile in easting of the reference DEM and the accuracy of the interpolated DEM compared with the reference one is shown in Figure 6.13 (a) and (b), respectively. The statistics of the terrain relief in terms of each profile in easting of the reference DEM is given in Figure 6.13 (a) and shows a relatively moderate surface at the northern part and a hilly terrain at the south of the test-site. Figure 6.13 (b) gives the accuracy statistics of the elevation samples in terms of each profile in easting of the interpolated DEM compared with the reference one. Again, the deviations in height as shown in Figure 6.13 (b) are related to the statistical characters of terrain surface (Figure 6.13 (a)).

DEM Profile	Terrain Type	Mean (m)	S. D. (m)	RMSE (m)	Min. (m)	Max. (m)
N=3,110.8km	**Moderate**	-4.0	7.9	**8.8**	-41.3	+21.6
N=3,116.0km	**Hilly**	+4.1	30.8	**31.0**	-81.0	+98.4

Table 6.4 Statistics of the differences in height between profiles in easting of the interpolated DEM compared with the reference one.

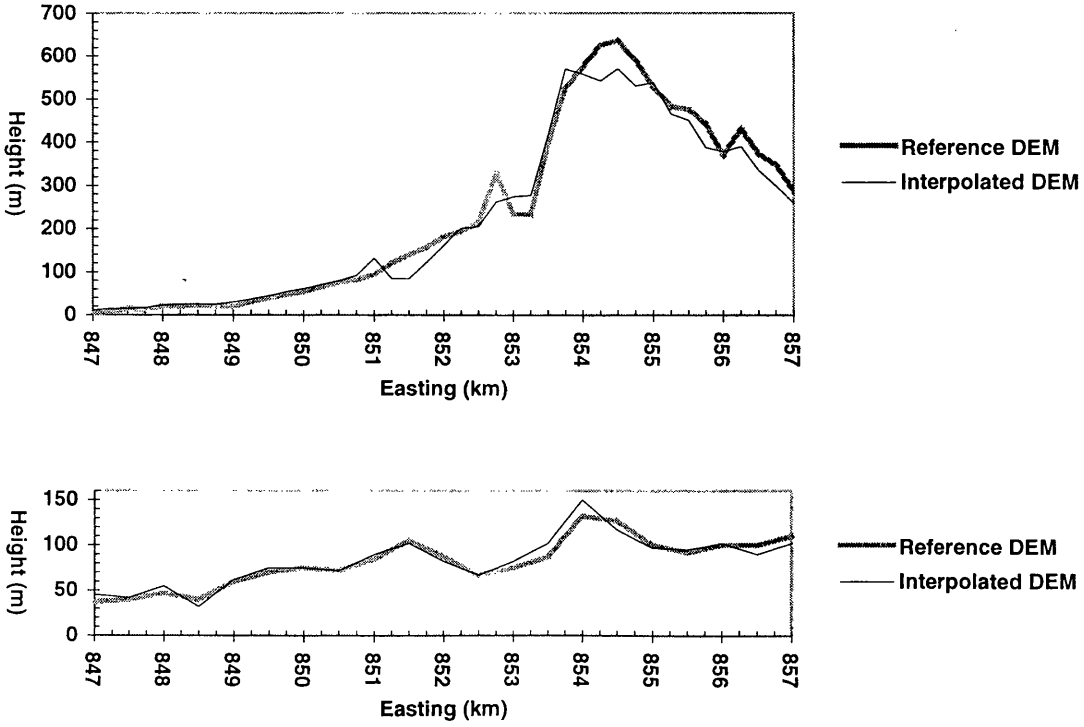

Figure 6.12 Terrain profiles in a hilly area (above, N=3110.8km) and a flat-moderate area (below, N=3116km) of the interpolated DEM compared with the reference DEM.

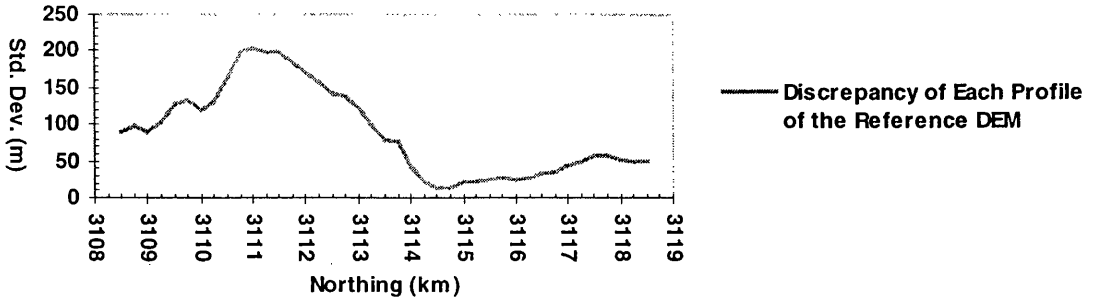

Figure 6.13 (a) Standard deviation of each profile in easting of the reference DEM

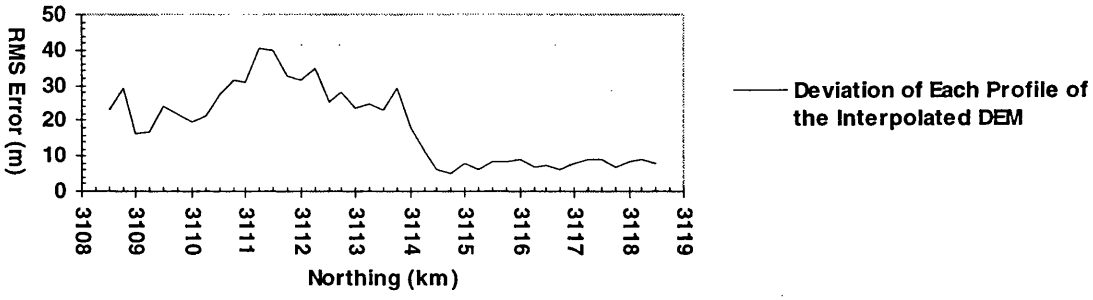

Figure 6.13 (b) RMS error of each profile in easting of the interpolated DEM (compared with the reference DEM.)

Figure 6.14 gives a sketch of the deviations in height of the generated DEM samples against the reference elevation. Firstly, the DEM samples generated and the corresponding deviations are classified according to the reference elevation data, such as [0m~5m), [5m~10m) and so on. Secondly, the deviations of the DEM samples collected in each group of the same (similar) elevation interval are averaged giving a mean deviation to be plotted. It seems that the deviations in height of the generated DEM increase with increasing true elevation. This is not consistent with the relationship curve of the errors in height against the elevation data as shown in Figure 3.18, because layover in SAR imagery has significant effects on the results derived leading to information loss (ambiguity) in the hilly areas.

Generally, the quality of the DEM derived is much better in low-altitude areas than in high-altitude areas, and the elevation data within the layover or shadowing areas cannot be reconstructed perfectly. Information loss in hilly areas is evident. Also, the interpolation procedure applied to the DEM derived does not introduce any significant errors into the resultant DEM in flat-moderate areas. This conclusion for the interpolated

DEM has been validated by the above statistical and graphical analysis. Further refinement will be tested in the next section.

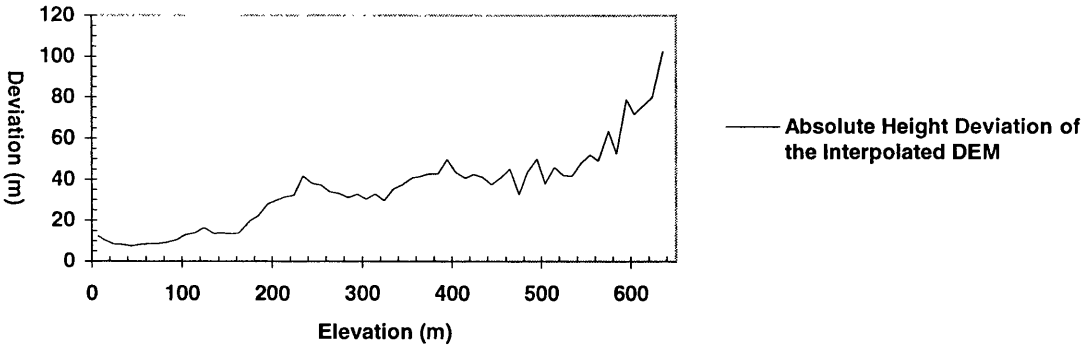

Figure 6.14 Relationship curve of the deviations in height of the DEM samples generated against the reference elevation data.

6.4.3 DEM Filtering

The accuracy statistics shown above give only an overall evaluation of the quality of the resultant DEM. Due to information loss caused by layover effects, it seems that there is little that can be improved for the DEM derived in hilly areas. However, the quality of the resultant DEM in flat-to-moderate areas is relatively stable, it may be useful to observe it closely to see any possibility of improvement for it. For instance, Figure 6.15 illustrates a sectioned DEM profile of 2km long depicted from Figure 6.12 (a) showing a couple of 'spikes' with respect to the relatively moderate terrain surface of the reference DEM.

Such undulation of terrain relief regarded as 'noise' may be due to man-made objects, for example, factories or building blocks, or uncertainties of image correlation. This is also probably because the conjugate features of a SAR image pair may exhibit different density numbers between one image and the other due to random-like speckle hence adding to or subtracting from the expected parallax value. DEM noise can be caused due to the geometric model employed, mismatched points from image correlation and even terrain covers (vegetation, forests and buildings, *etc*). In Chapter 3, the error model indicates that errors may come from the image co-ordinate measurements and the geometric model employed. This section concentrates on these factors. There remain the factors of terrain cover or false image correlation that will be discussed in Chapter 7 after geocoding has been done.

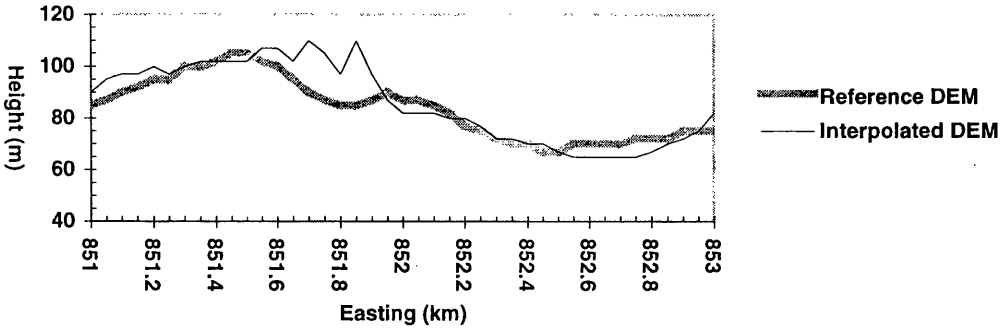

Figure 6.15 Comparison between the reference DEM and the interpolated one (a section of the DEM profile of 2 km, Y=3116km).

In photogrammetry, the quality control of the DEM data acquired by the automatic correlation method can be done using the reverse transformation from terrain co-ordinates (*E, N, H*) back to photographic image co-ordinates (x, y) and superimposing the 'simulated' ground point on the real image, as reported by Petrie [1990b]. This method demands a manual editing to check the bad DEM points, and a DEM without information ambiguity (or a one-ground-point-to-one-image-point transformation) is required. Since information loss and range ambiguity are quite common in a DEM generated from SAR data due to layover effects, this approach suitable for optic data may not be applicable for SAR data. Also, the manual editing method is not considered here for achieving a higher level of automation. Twu [1996] proposed a geometric constraint condition for eliminating the gross errors in the DEM generated from ERS-1 SAR data based on the good quality orbit data provided. Apparently, the geometric constraint condition cannot be applied to RADARSAT SAR images because the good quality orbit data required is not always available as mentioned in Section 2.3.3.

The refinement or change for the interpolated DEM can only be justified if the outcome derived has noise. On the one hand, true terrain relief can never be known, therefore, any comparison between an interpolated DEM and a reference DEM is only a relative difference measure. On the other hand, if the method of refinement employed is not suitable or the correction of the DEM generated is over-done, it also runs a risk of degrading the original DEM quality. It means that further refinement has to be done carefully. Smoothing reduces possible random errors in the course of the DEM sampling

process and filters out small pits or peaks of the original DEM hence it is a general practice for the DEM users, not the DEM producers. This operation may help with hydrological applications, according to Vieux [1995], that are sensitive to any minor 'noise' in a DEM derived.

According to prior knowledge of the generation of DEM, as in Chapter 3 and 4, some mismatched samples can remain in the DEM derived. In addition, the DEM generated is going to be used for geocoding, therefore, it can be helpful to consider DEM filtering to improve the DEM generated. Consider an automatic filter without human editing for the interpolated DEM. There are two factors to be taken into account, including a suitable filter without any threshold required and a reasonable window size for filtering. Other filters which require a threshold will not be discussed further.

Firstly, filtering is a typical low-level operation in image processing for reducing noise and other spurious effects that may be present in an image as a result of sampling [Young and Fu, 1986], for example, averaging and median smoothing. Wiman [1998] employed both filters for eliminating the gross errors produced from the digital surface models using a normalized cross-correlation measure. A weighted average filter based on the weight given by the squared correlation coefficient is used to filter the elevation data. The window size is determined empirically. In addition, assuming that the gross error is isolated, the median filter is used to eliminate that gross error.

The median filter replaces the height of the pixel of interest, according to the statistical median of the height values of the neighbouring samples within a predefined window size. Generally, there is no specific model which can be established universally for the terrain elevation samples due to the random character of natural terrain, and the height of the pixel of interest is not necessarily equivalent to the central value in a set of ordered elevations. The median filter may perform quite well in signal processing, but it does not necessarily meet the physical reality of natural terrain.

The moving average filter is a straightforward and computationally efficient technique for image smoothing, but the main disadvantage of the moving average filter is that it blurs edges and other sharp details. However, sharp features, such as cliffs, in DEMs are not common in flat-moderate areas, therefore, there is nothing to lose for the DEM generated in case of using the averaging filter. Geometrically, a continuous terrain surface can be expected and the change of terrain relief is locally steady in flat-moderate areas. Hence the moving average filter that suppresses the DEM noise of the pixel of interest, based on the averaged height of the surrounding pixels, is adopted.

Secondly, as mentioned in Chapter 3, the error model for the image co-ordinate measurements of SAR data predicts a theoretical error magnitude |E| (as in equation (3.17)) that implicitly contains the errors coming from the image correlation or space intersection routines. The predicted error magnitude can be treated as the radius of an error sphere in which the errors of DEM samples behave randomly. The maximal extent of the filtered area is being set as the error sphere with radius of that predicted error magnitude. This is because there is no universal mathematical model to describe the terrain surface and to support the filtering of the 'noise' exceeding the suggested extent. Hence it avoids the risk of over-done smoothing for the generated DEM. In practice, the error sphere can be projected onto ground surface (represented by a DEM) and approximated by a window of the size of a 2|E| square as shown in Figure 6.16.

For example, if the theoretical error gives 28m and let the sampled grid spacing G_{DEM} of an interpolated DEM be 12.5m, the radius of the moving average filter cannot be greater than int[|E|/G_{DEM}]+1, or 3 pixels. On the contrary, if the interpolated DEM is sampled in a 50m, or greater, grid, smoothing that DEM cannot be justified. This is because the interpolation process of a relatively greater grid size has introduced more neighbouring (reference) elevation points than that of a small grid.

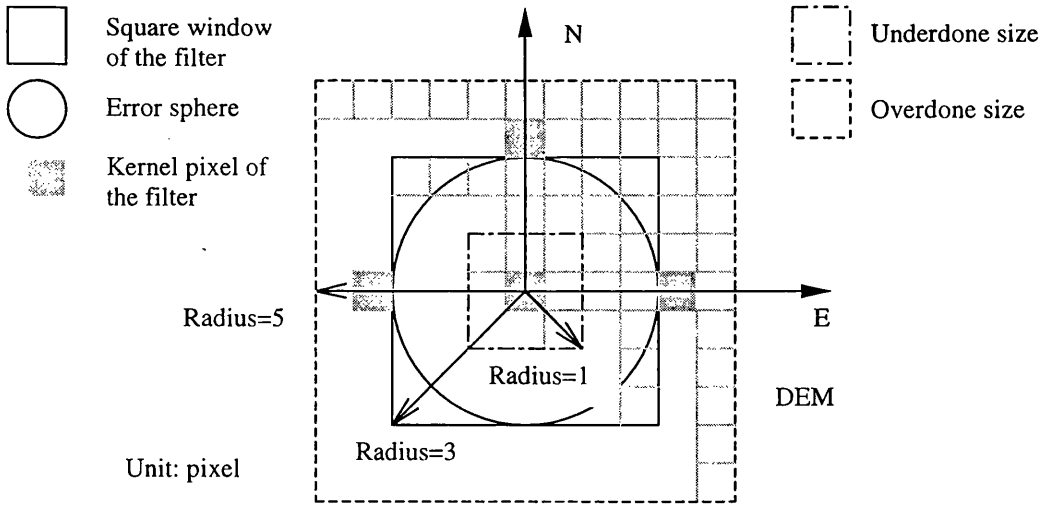

Figure 6.16 Window size of a moving average filter

The DEM generated and interpolated in a 12.5m grid has been tested to show the results derived from DEM filtering. Table 6.5 gives the accuracy statistics for the DEMs filtered using different window sizes of the moving average filter.

It can be seen in Table 6.5 that the overall accuracy of the DEM derived and filtered cannot be improved significantly, compared with the reference DEM in a 50m grid as mentioned before.

DEM Samples	DEM Filtering Radius (pixel)	Mean (m)	S.D. (σ) (m)	RMS (m)	Min. (m)	Max. (m)	Error (%) ≥ ± 1 σ	Blunder (%) ≥ ± 3 σ
40401	**0 (no filtering)**	**-1.595**	**21.58**	**21.63**	**-192**	**+138**	**15.2**	**2.6**
40401	1	-1.586	21.02	**21.08**	-174	+138	14.9	2.4
40401	2	-1.599	20.84	**21.90**	-172	+136	14.8	2.3
40401	**3**	**-1.596**	**20.68**	**20.74**	**-170**	**+132**	**14.7**	**2.2**
40401	4	-1.594	20.53	**20.59**	-163	+129	14.7	2.2
40401	5	-1.593	20.40	**20.46**	-152	+125	14.7	2.1

Table 6.5 Statistics of the DEM filtered using an averaging filter.

Figure 6.17 shows that the RMS errors of the interpolated DEM in flat-to-moderate areas have been reduced slightly about 1m. The RMS errors in flat-to-moderate areas remain stable when increasing the window size of the filter. Those RMS errors in hilly areas can also be improved on the order of several metres. For a close view of the change of the DEMs filtered, Figure 6.18 shows the results derived using different window sizes for a sectioned profile of the interpolated DEM of 2km long depicted from Figure 6.15. When the radius of the filter window exceeds 3 pixels, the results do not show any more improvements for the DEM while running the risk of over-done smoothing. Finally, the filtered DEM, particularly in the flat-to-moderate areas where the quality is good, is ready for other applications, such as geocoding, that will be demonstrated in Chapter 7.

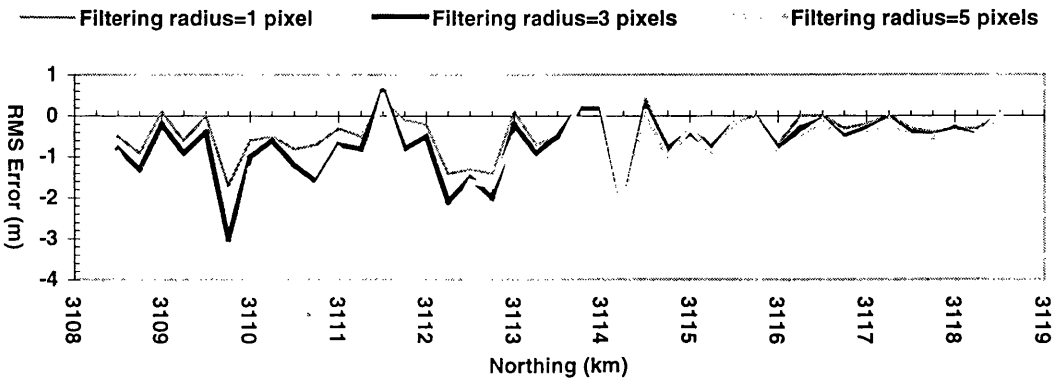

Figure 6.17 RMS errors of each profile in easting of the generated DEM using the moving average filter of different window sizes.

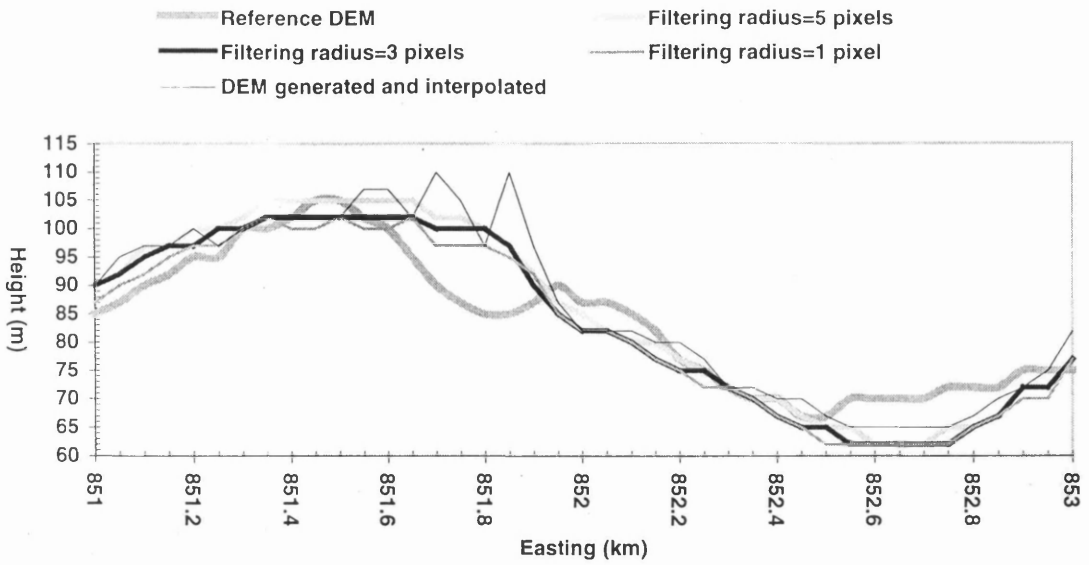

Figure 6.18 A sectioned profile (N=3116km) of 2km long of the generated DEM using a moving average filter: (a) radius=1 pixel; (b) radius=3 pixels; (c) radius=5 pixels.

A sequence of the refined DEMs of three-dimensional perspective view is demonstrated in Figure 6.19. It can be seen that the terrain features in the moderate relief areas have been restored reasonably, comparing the reference DEM (top image) with the interpolated DEM (middle image) and the smoothed DEM (bottom image). Also, the 'noise' of the interpolated DEM has been suppressed using the moving average filter, in terms of visual comparison with the reference DEM. Although the major terrestrial trends can be shown in the DEM derived at the last stage, the DEM quality decreases in the hilly areas where layover effects make digital elevation modelling difficult.

The terrain features in the central part of the hilly area cannot be reconstructed completely. For instance, valleys disappeared in the hilly areas showing a relatively smooth surface. So, further applications of the generated DEM for the specific needs of other areas may not be applicable, such as drainage network modelling or other hydrological applications. The application of the DEM derived for geocoding can be practical in moderate-flat areas, but it is not expected to be applicable in hilly areas. This problem is strongly related to layover effects and can only be avoided by selecting a suitable image pair with minimal level of layover. Further validation of the DEM derived will be tested for SAR image geocoding as presented in Chapter 7.

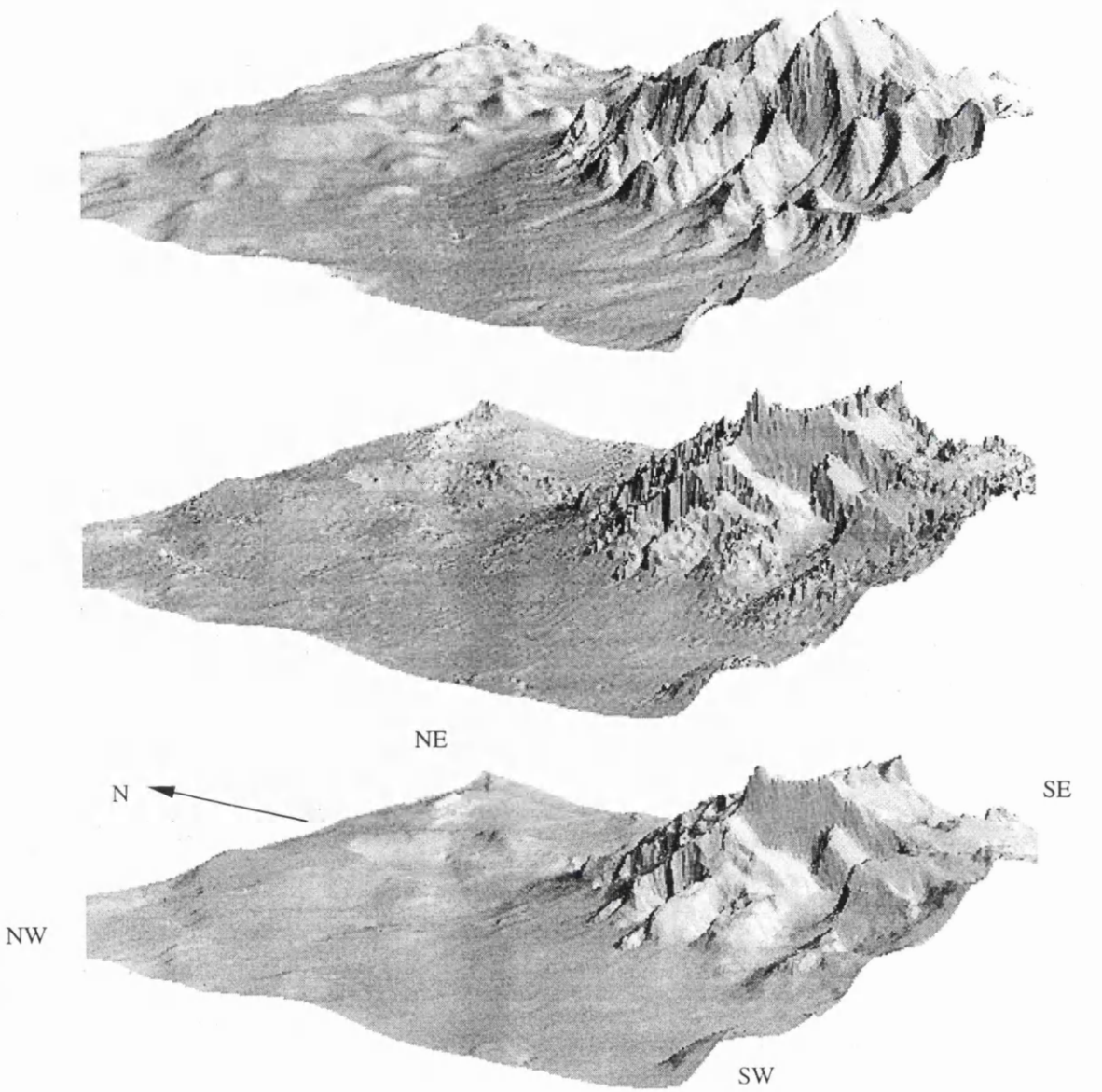

Figure 6.19 Perspective images of the DEMs. (Top: reference DEM; middle: interpolated DEM; bottom: the filtered DEM after suppressing noise. Size:10km×10km. Viewing direction: from southwest (SW) to northeast (NE). Vertical exaggeration factor: 5.)

6.4.4 Discussion

The new DEM derived from two different orbit directions is able to fill the major gaps of the raw DEMs and increase the DEM coverage with no degradation of the DEM quality. Practically, the satellite space-borne SAR data can revisit the same areas and make this approach workable. The second step of refinement is made for that DEM using a interpolation routine to fill minor gaps. This is based on the grid-based digital elevation modeling that is similar to the spatial distribution of the derived elevation data, and is convenient for further raster-based operations and applications. Although a DEM of a

fixed grid data structure is easy to retrieve and to store, the capacity for processing and storage space requested is greater than other data models.

Generally, the DEM derived shows better results in flat-to-moderate areas than in hilly areas. In the moderate-relief areas, the DEM quality ranges from 6m to 14m based on the comparison of profiles between the interpolated DEM and the reference one. These figures are better than the predicted observation errors made in Chapter 3, thanks to the optimized pyramidal image correlation scheme using the least-squares approach with a region-growing method, as mentioned in Chapter 4, which avoids blunder being generated. The use of the automatically generated GCPs ensures that the quality of the DEMs derived is stable and approaches sub-pixel accuracy in moderate terrain relief areas. Due to layover effects, the DEM quality in the hilly areas ranging from 22m to 40m in terms of DEM profiles is less reliable than that in the moderate relief areas.

Further refinement of the interpolated DEM focuses on filtering the minor noise remaining. This is based on the consideration of the possible observation errors, according to the proposed error model as in Chapter 3, and the requirement for automation. The moving average filter is an intuitive smoothing method that matches the random characters of natural terrain within a limited extent. The attempt at refinement made here only considers the local uncertainties remaining in the procedures of generating the DEM, such as those from the pyramidal image correlation routines that lead to ± 1 pixel observation errors of image co-ordinates. Thus, the window size of the filter is confined by the theoretical error magnitude predicted. Hence the possibility of over-done smoothing for the interpolated DEM is reduced. It can be concluded that the overall quality of the DEM derived using the filtering method cannot be improved significantly, however, the 'noise' of a DEM can be suppressed, according to visual comparison.

Generally, the layover effect is the main concern for the applications of radargrammetry that limits the use of SAR data in hilly areas. Radargrammetric configuration and layover must be considered together to make a compromise between a good geometric configuration and a minimal level of layover. Nonetheless, the results derived using the rigorous stereo SAR approach as shown here provide reasonable spatial information in flat-to-moderate areas with relatively higher quality and give approximate (coarse) three-dimensional data in hilly areas with lower reliability.

6.6 Summary

The raw DEMs derived from the automatic image correlation and space intersection procedures after using good quality GCPs still show numerous gaps. The intrinsic limitations of the SAR image geometry, particularly layover effects, cause spatial information loss in hilly areas that cannot be restored completely. This shortcoming can be overcome partly using the elevation data sets derived from two, or multiple, image pairs of different orbit directions. A 'complete' DEM can be derived employing adequate interpolation routines, according to a specific data model, such as a fixed grid structure. The quality of the DEMs derived is dependent upon the complexity of terrain relief. The DEM quality derived in a moderate relief area is much better than that in a hilly area. Further improvement for the quality of the DEM derived, such as a noise filtering method, is limited, because the DEM quality in the flat-moderate areas has approached sub-pixel accuracy in respect to the reference DEM. The three-dimensional data derived in the hilly areas under the circumstances of layover effects is relatively coarse.

Chapter 7

Geocoding Using the Derived DEM

7.1 Introduction

Geocoding is the method of geometric rectification for a space-borne remotely sensed image, particularly the SAR imagery, according to a specific map projection and a DEM in order that the terrain induced image distortions in that image can be eliminated. This provides further applications, such as image mosaic, multi-sensor data integration, geological analysis and change detection *etc.* An existing DEM in the area of interest is essential to correct the terrain induced distortions in SAR images, such as layover and foreshortening effects. Geocoding also requires an accurately described relationship established between the image and object space.

Traditional methods employing polynomial fit functions have been used in geocoding SEASAT and SIR-A/B SAR images, such as Naraghi *et al.* [1983], Domik *et al.* [1986] and Curlander *et al.* [1987]. Recent geocoding methods for ERS-1 data employ a map-to-image transformation based on the range-Doppler equations, for instance, Dowman *et al.* [1993] and Schreier *et al.* [1993]. The range-Doppler approach is performed only for an anchor point grid (or a super-grid structure) constructed by regularly distributed DEM elements to reduce computational load. All of the other DEM elements are then transformed into image co-ordinates by an efficient bilinear interpolation (or other polynomial fit functions), according to the anchor point grid established as mentioned in Section 2.6.

Precise terrain corrected geocoding is a standard operation for SAR data. Unfortunately, the DEM required is not always available. This chapter focuses on SAR image geocoding to be used as an example of application of the DEM derived in Chapter 6 to validate the proposed algorithms in the thesis. Thus, an algorithm of SAR image geocoding with the minimal degradation of accuracy must be considered. Absolute ground control in geocoding is usually provided using the manually collected GCPs whose quality is not always stable. In order to guarantee good quality geocoded products

derived, reliable ground control has to be used to compensate range and azimuth time errors in header/orbit data.

The proposed method for geometric rectification, as described in Section 7.2, imports the same orbit data and imaging geometry as used by the proposed simulator in Chapter 5. A direct approach to relate the image to object space is developed that ensures the minimal accuracy degradation in geocoding. Since there are no polynomial fit functions used, the risks of possible errors caused by the polynomial fit functions can be completely avoided. Automatic provision of ground control is carried out using a known DEM chip and a simulation approach, as in Chapter 5, to compensate orbit drifts and range shifts. Recall that the simulator proposed gives the corner elements of the known DEM chip as GCPs that provide control with accuracy better than a resolution cell of a real SAR image. An error model for geocoding considering the across-track orbit error is also proposed.

The proposed algorithm of geocoding, as demonstrated in Section 7.3, is not necessarily superior to the standard methods in terms of computational efficiency, because there is neither a polynomial fit function nor a super-grid (or an anchor grid) structure employed for reducing computational load. The main concern is the geometric accuracy of the geocoded images in order that the demonstration of using the generated DEMs and of the automatic provision of GCPs in geocoding is not misleading. The validation of the geocoding algorithm using a reference DEM is given in Section 7.4. Also, further analysis for the SAR image geometry in respect to the use of the automatically derived GCPs is given together with the evaluation of orbit drifts. Finally, the resultant geocoded images using the generated and refined DEM are evaluated to validate the previously proposed algorithms for generating DEMs from stereo SAR data, as presented in the preceding chapters, leading to the conclusions of the Ph.D. project as presented in Chapter 8.

7.2 Geocoding for SAR images

7.2.1 Geometric and Radiometric Considerations

The standard map-to-image (or backward transformation) methods of geocoding, such as Dowman *et al.* [1993] and Schreier *et al.* [1993], project the specific DEM elements, which are selected using an anchor grid structure, onto the SAR image to

establish the relationship between the image and object space. This is carried out using the range-Doppler equations (see equation (3.1) and (3.2)). Polynomial fit functions are commonly used in the standard methods for reducing computational load, i.e., an interpolation routine has to be introduced to carry out geocoding. Although the errors caused by the interpolation operations employed for geocoding may be less important for the general use of the geocoded images, however, it still runs a potential risk of accumulating errors. As mentioned before, the geocoding method used here is to evaluate the DEM generated in previous Chapters. In order to demonstrate the accuracy of the DEM derived in the form of a geocoded image with high fidelity, all possible errors have to be considered and to be avoided. It leads to an unusual algorithm of geocoding developed in this section, which is based on the zero-Doppler assumption.

Considering a SAR imaging geometry, the Doppler equation in equation (3.1) gives

$$(\mathbf{V_S}-\mathbf{V_P})\bullet(\mathbf{S}-\mathbf{P})=0\ ,\quad \textbf{if}\quad f_{DC}=\frac{2(\mathbf{V_S}-\mathbf{V_P})\bullet(\mathbf{S}-\mathbf{P})}{\lambda|\mathbf{S}-\mathbf{P}|}=0 \qquad (7.1)$$
$$\Rightarrow (\mathbf{V_S}-\mathbf{V_P})\perp(\mathbf{S}-\mathbf{P})$$

In the case of the zero-Doppler image geometry, the resultant range vector is always perpendicular to the resultant velocity vector at that azimuth time as demonstrated in Chapter 3 and 5. The Doppler cone then evolves to a zero-Doppler range circle (plane), which is equivalent to the normal plane perpendicular to the resultant velocity vector of the sensor (recall Chapter 3). The normal plane is formulated and given as in equation (5.1). The resultant velocity vector has to be corrected using the velocity vector of the ground point, or the Earth rotation (recall Chapter 5).

The concept of the proposed method of SAR image geometric rectification is based on a direct approach relating the SAR image to DEM elements (object space) and on the known orbit data set and the SAR image header files. Certainly, the DEM used in geocoding must be transformed into the same geo-centric (inertial) co-ordinate system as that used by the orbit data before geocoding, as stated in Section 2.6. According to the azimuth time sequence, the resultant position vector and the resultant velocity vector of the sensor are changing along the orbit as described in Chapter 5. When the azimuth time accumulates from the first azimuth line to the last azimuth line, the normal plane (range beam) scans the sensed area and detects a DEM element $\mathbf{P}_i$ within a defined extent d_i,

given by equation (5.3), to form a geocoded image line by line. The extent d_i is equivalent to the resolution of an azimuth line. The normal plane has been illustrated in Figure 5.1. Figure 7.1 provides an across-track view of the scanning process in the normal plane.

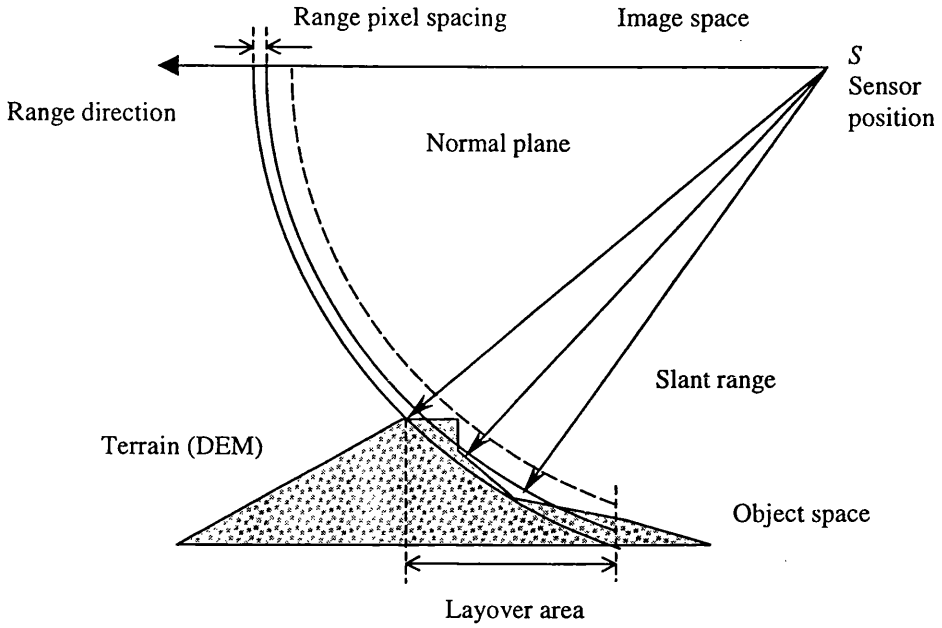

Figure 7.1 A cross-section of the SAR imaging geometry.

Namely, all of the DEM elements have to be scanned by each azimuth line, which is represented by a normal plane. Equation (5.4) and (5.5) is used to automatically decide the extent of the DEM and the corresponding azimuth time of the first azimuth line and that of the last azimuth line of a real image to be geocoded. Beyond the extent of the DEM, other image lines are ignored. In doing so, systematic shifts in range and in azimuth time are not allowed, therefore, ground control has to be supplied in advance, as discussed in next section. Within each azimuth line, all of the detected DEM elements have to be classified according to the distance between the DEM element and the sensor position using equation (3.2), and be related to each corresponding 'range-bin'. The range-bin is given by each range pixel of each azimuth line of a real SAR image to be geocoded. This can be done using the relationship between the ground-range and the slant-range defined by SAR image header data, or the ground-range-to-slant-range transformation parameters, according to CSA [1995], as

$$R_s^{(col)} = \sum_{i=0}^{5} a_i \cdot (col)_{GCP}^i \tag{7.3}$$

$R_s^{(col)}$ the calculated slant-range of the $(col)^{th}$ range pixel of a real image (or the $(col)^{th}$ range bin) and $\{a_i \mid i=0,1,\ldots,5\}$ the transformation parameters for RADARSAT SAR data.

Hence the normal plane derived scans terrain the surface (represented by a DEM) in along-track direction to detect any encountered DEM element and to assign the appropriate density number (*DN*) of the corresponding image pixel to that detected DEM element directly, according to the corresponding range bin. In this case, it is quite possible to give the same *DN* of an image pixel to several DEM elements apart from each other within the layover area as shown in Figure 7.1. Because, as emphasized before, geometric accuracy has been placed as the top priority in order to allow precise measurements of check points for validation of the generated DEM, the *DN* of the nearest pixel with no re-sampling is assigned to the appropriate pixel of the geocoded image. Also, there is no radiometric correction applied to the geocoded image, since the geometric accuracy of a geocoded image can be evaluated by measuring man-made objects with no regard to terrain relief.

7.2.2 Providing Control for Geocoding

The way to provide ground control automatically in radargrammetry has been described in Chapter 5 and is based on the assumption of the availability of a zero-Doppler processed SAR image and of known orbit/header data. The zero-Doppler assumption has been justified in Chapter 3 and 5, and can also be verified from the geocoding results derived as shown later in this chapter. The same principle of the automatic provision of ground control can be applied to geocoding. The main concern here is the use of ground control to compensate orbit drifts or range shifts before geocoding. The provision of control is carried out in SAR image space (recall Figure 5.7 and 5.8). Notice that the proposed geocoding algorithm is used to relate a SAR image to object space directly, and the *DN* values will be assigned directly to the detected DEM elements in the course of scanning process. So, the orbit data must be correct in the first place before starting the scanning process to assure that a *DN* value can be assigned directly to the correct DEM element. Thus, the correction for the timing shifts in range

and in azimuth direction must be imported to the geocoding routine together with image header data. Figure 7.2 demonstrates the idea of the provision of ground control using the proposed simulation technique and a known DEM with significant terrain relief, and the concept of the scanning process of the proposed geocoding method is presented.

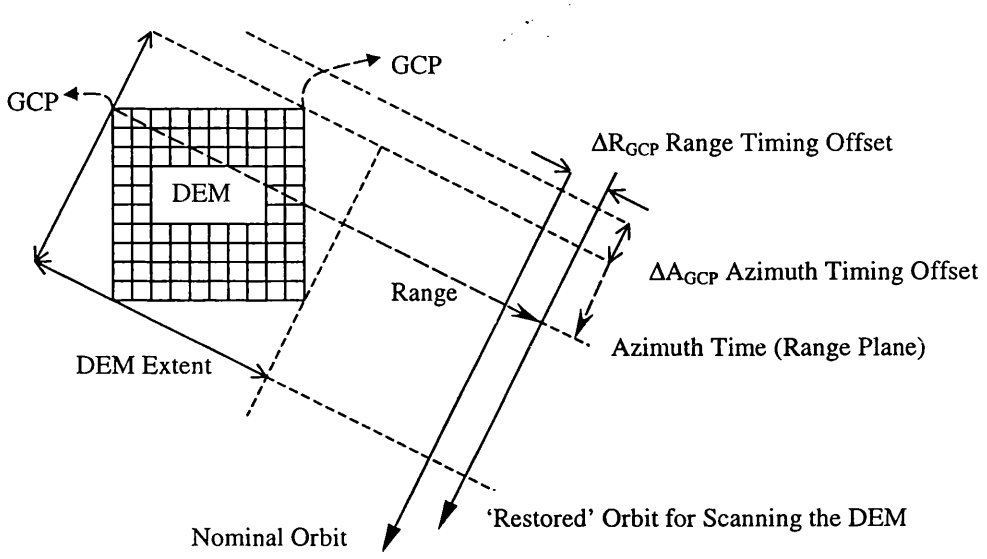

Figure 7.2. Top-view of the SAR imaging geometry.

Firstly, a known DEM chip is used to generate a simulated image, which is to be correlated with the real counterpart. The simulator and the real-simulated image correlator have been described in Chapter 5. Figure 7.3 shows the azimuth time sequence relating the azimuth time of a simulated image to that of the real one. The simulator scans the DEM and detects its four corner elements to be used as GCPs. The azimuth time of each GCP, A_{GCP} (sec), recorded in the scanning process is counted from the nominal azimuth time of the first data point $A_f^{(0)}$ (sec) provided in the header file with the real image. The precision of the simulator for calculating azimuth time is given as dA_{GCP} (sec) hence the simulated azimuth time of each GCP is given as $A_{GCP} \pm dA_{GCP}$. The corresponding azimuth line of each GCP within a real image can be derived from the results of the real-simulated image correlation. The header information of RADARSAT SAR data, [CSA, 1995], provides the nominal azimuth time for that azimuth line as $A^{(0)}{}_{GCP}$ (sec). The error of the nominal azimuth time provided is given as $dA_f^{(0)}$. Thus, there may exist the azimuth time offset ΔA_{GCP}, or the along-track orbit error, between the provided azimuth time and the simulated one of each GCP giving

$$\begin{aligned} \Delta A_{GCP} &= \left(A_f^{(0)} + dA_f^{(0)}\right) + \left(A_{GCP} \pm dA_{GCP}\right) - \left(A_{GCP}^{(0)} + dA_f^{(0)}\right) \\ &\Rightarrow \Delta A_{GCP} \mp dA_{GCP} = A_f^{(0)} + A_{GCP} - A_{GCP}^{(0)} \end{aligned} \tag{7.3}$$

Since the basis of the azimuth time system is the same for both values, the azimuth timing offset is obtained with no regard to the error of $dA_f^{(0)}$. The simulator's error dA_{GCP} in azimuth line can be obtained from the precision analysis of the GCPs as discussed later in this chapter.

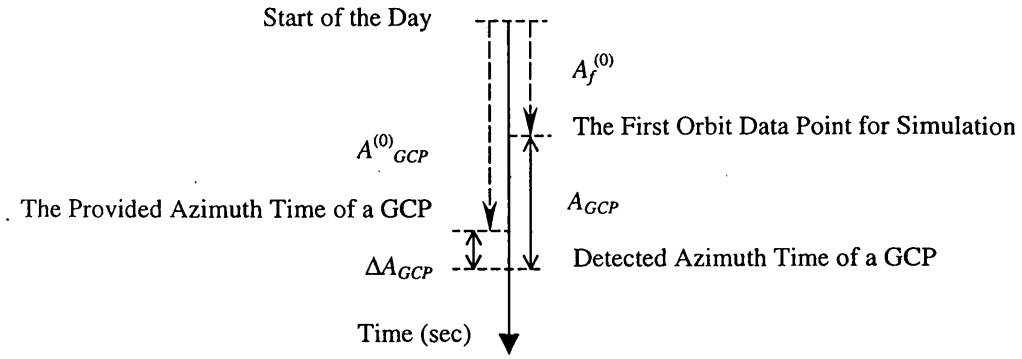

Figure 7.3 The azimuth time sequence of the SAR image.

In the simulation process, the distance between the sensor and a GCP is detected and recorded as R_{GCP} which is based on the nominal orbit position. The simulator's error for detecting the range is given as dR_{GCP} in the scanning process that can be obtained from the precision analysis of the GCPs as discussed later. Therefore, the simulated range of the detected GCP is given as $R_{GCP} \pm dR_{GCP}$. The nominal range observation of the GCP, $R^{(o)}{}_{GCP}$, can be derived from the ground-range-to-slant-range transformation, based on the nominal orbit position and the transformation parameters given by image header file, as given in equation (7.2). The deviation of the nominal range compared with the detected range is given as ΔR_{GCP}. Let $\Delta\mathbf{R}$ and $\Delta\mathbf{S}$ be the error vector of the range vector and that of the sensor position vector, respectively, equation (3.2) gives

$$\begin{aligned}
&\mathbf{R}+\Delta\mathbf{R}=\mathbf{S}+\Delta\mathbf{S}-\mathbf{P}\\
&R_{GCP}^{(o)}+\Delta R_{GCP}=|\mathbf{S}+\Delta\mathbf{S}-\mathbf{P}|;\qquad R_{GCP}\pm dR_{GCP}=|\mathbf{S}+\Delta\mathbf{S}-\mathbf{P}|\\
&\Rightarrow \Delta R_{GCP}\mp dR_{GCP}=R_{GCP}-R_{GCP}^{(o)}
\end{aligned} \tag{7.4}$$

Equation (7.4) gives only the error magnitude of the range vector based on the nominal orbit position and the range observation. Since there is no way to know what the magnitude of each component of the deviation vector $\Delta\mathbf{S}$ is, it is not quite possible to know the exact position of the sensor. In fact, the 'actual' orbit position may be any point of the across-track arc having the same range counted from the GCP in the normal plane of the corresponding azimuth time. In this sense, the 'restored' orbit position, which is corrected by the magnitude of a range shift, is not necessarily coincident with that of the 'actual' orbit as demonstrated in Figure 7.4 (a). Therefore, the across-track orbit error may cause a deviation of the incidence angle Ω as shown in Figure 7.4 (b). Consider the error magnitude of the orbit position projected onto the across-track component as dS, the error of the incidence angle $d\Omega$ is determined by

$$d\Omega=\tan^{-1}\left(\frac{dS}{|\mathbf{R}+\Delta\mathbf{R}|}\right)\approx\tan^{-1}\left(\frac{dS}{R}\right),\qquad \text{if}\ \ |\mathbf{R}|>>|\Delta\mathbf{R}| \tag{7.5}$$

The incidence angle error then affects the results of the ground-range-to-slant-range transformation and accumulates the error of each projected range pixel size, ΔR_g, from one end of an azimuth line to the other. The total magnitude of the ground-range errors accumulated from the nearest range pixel to the $(col)^{th}$ range pixel is given as

$$\sum_{i=1}^{(col)}\Delta R_g^{(i)}\approx R_s\cdot\sum_{i=1}^{(col)}\left(\frac{1}{\sin\Omega_i}-\frac{1}{\sin(\Omega_i+d\Omega)}\right),\qquad \text{if}\ \ \Omega_i>>d\Omega \tag{7.6}$$

i denotes the range pixel number in a real SAR image; Ω_i the incidence angle of the i^{th} range pixel and R_s the slant-range pixel size. For instance, let the across-track orbit error be 100m and the range 880km, equation (7.5) gives $d\Omega$ approximately as 0.006511°. Let the incidence angle be approximately 23° , the slant range resolution 4.5m and the total number of the range pixels (col) = 8000 pixels for each azimuth line, the total error magnitude accumulated on the far ground-range is then given as 24.7m, according to

equation (7.6). Such a ground-range error, with respect to a full-scene SAR image size, is approximately equal to the size of one range resolution cell in the case of RADARSAT SAR standard mode data.

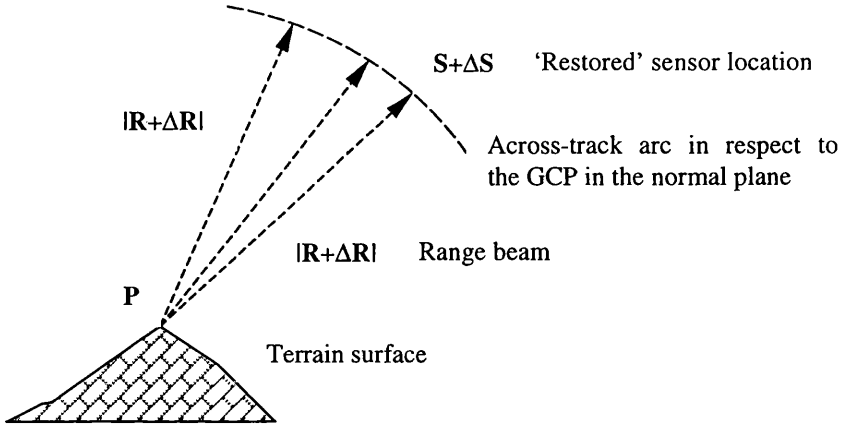

Figure 7.4 (a) Uncertainty of the actual orbit position in the normal (across-track) plane.

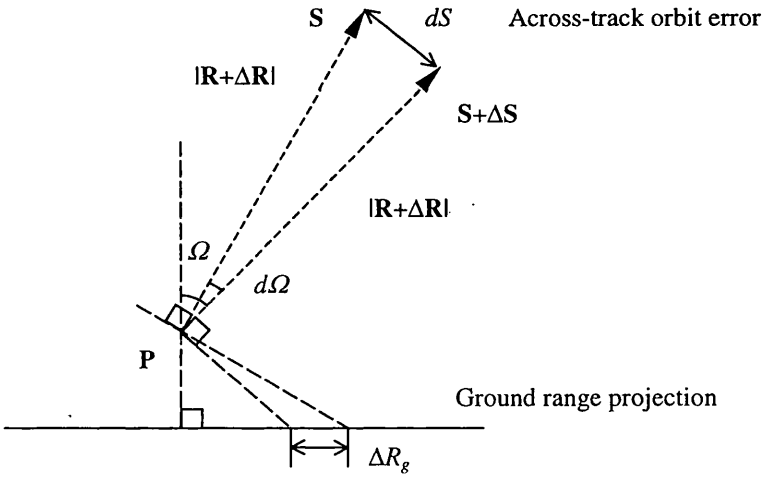

Figure 7.4 (b) Effects of incidence angle error on each ground-range pixel caused by the across-track orbit error.

7.3 Procedures of SAR Image Geocoding

Figure 7.5 describes the procedures of SAR image geocoding. The SAR image simulator produces a simulated image based upon a known DEM chip with significant terrain relief as described in Chapter 5. Before geocoding, the simulator is used to derive the corresponding azimuth time and range data of the four GCPs based on the nominal orbit information provided. The simulated image must be correlated with the real image

to provide the exact co-ordinates of the four GCPs in the real image that give the observations of the azimuth time and range of each GCP. The differences between the range/azimuth time data calculated and those observed show shifts in range and in azimuth direction that may provide control for geometric rectification as shown in Figure 5.7 and 5.8.

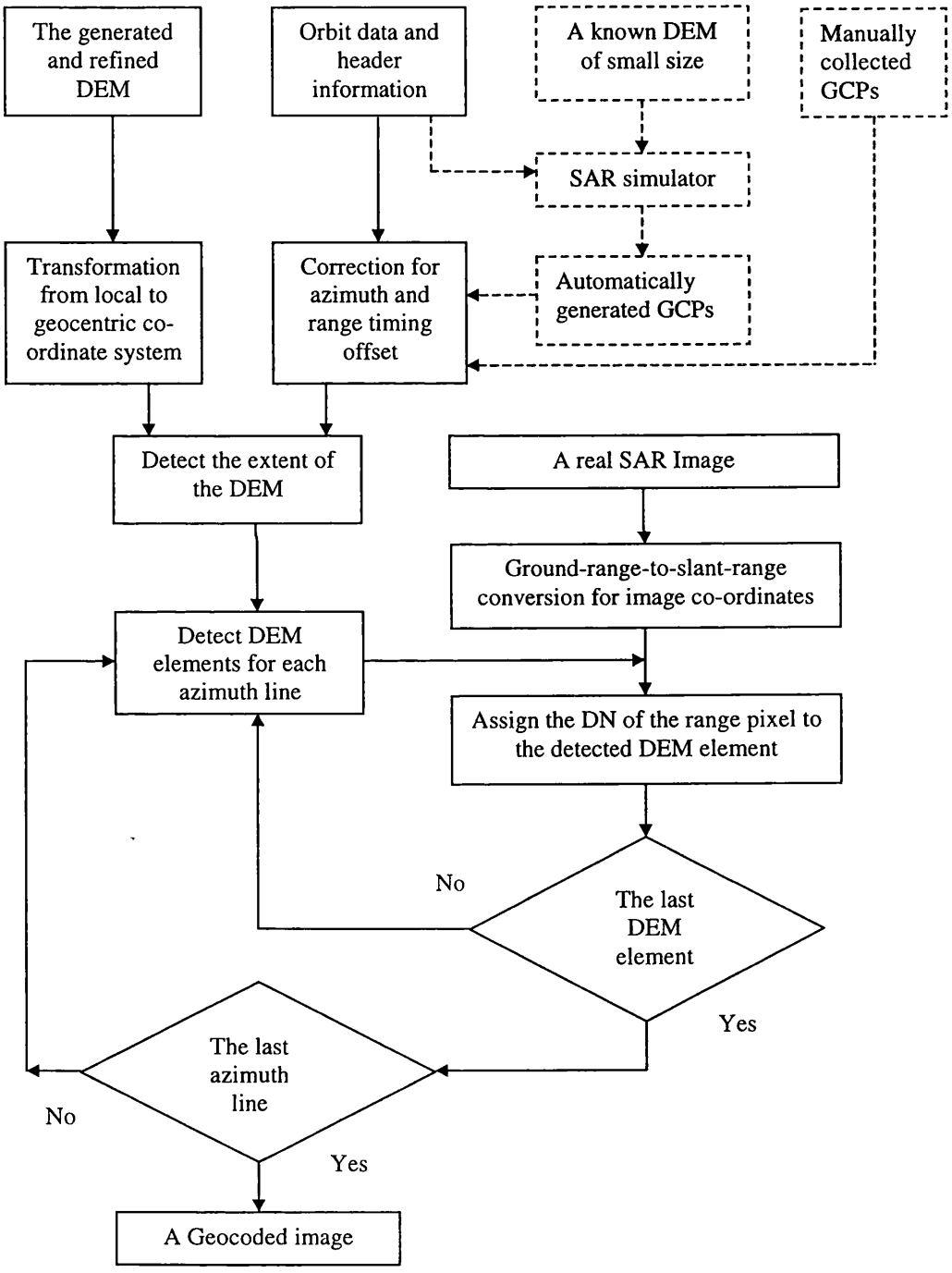

Figure 7.5 Procedures of the proposed SAR image geocoding algorithm.

The SAR image geocoding is carried out using a scanning process to search for every DEM element encountered within the defined extent of the range pixel of each azimuth line. The *DN* of each range pixel is then given to that DEM element, whenever it is detected, without any interpolation or re-sampling. However, the proposed geocoding algorithm is only used to demonstrate the use of the generated DEM and the automatically derived GCPs. It does not necessarily superior to the current methods in terms of computational efficiency. Nevertheless, the geometric accuracy of the geocoded image is guaranteed that may lead to a correct conclusion for validating the proposed algorithms in previous chapters.

7.4 Test Data and Results

The proposed SAR image geocoding routine `sargeoco`, coded in FORTRAN by the author, reads in the file containing specific parameters and ephemeris data, `sargeoco.dat`, a DEM file, `sargeoco.dem`, an azimuth time data file `sargeoco.azi` and a real SAR image file `sargeoco.img`. The parameter file `sargeoco.dat` is shown as in Table 7.1 (a).

Contents	Unit	Descriptions	Source
1997 8 22 5 54 50.76	date-time	Given time of the first data point	Platform Position Data Record
6	-	Number of the given data points	
4.0	s	Sampling interval of data points	
1878434.23 4878054.87 4901508.03	m	Sensor position of the first point	
3220956.05 4118837.03 –5319652.26	mm/s	Sensor velocity of the first point	
... ...	m mm/s	Repeat the state vectors for other points until the image scene is fully covered	
7901 9074	line/pixel	Full-scene SAR image size	Data Set Summary Record
18466900.0	pixel/s	Range sampling rate	
6	-	No. of the polynomial coefficient for ground-range-to-slant-range (GRSR) transformation	Detailed Processing Parameters Record
8.3931088E+05	m	GRSR polynomial constant term	
3.3013824E-01	m	Coefficient of the 1st power term	
...	m	Repeat until the 5th power term	
12.5	m	Range pixel spacing	
81 81	row/col	DEM size	Given by users
-0.006172508	sec	Azimuth time offset	
94.15	m	Range offset	
93 121	line/pixel	Geocoded SAR image size	

Table 7.1 (a) Format of the parameter file `sargeoco.dat` for `sargeoco`.

All of the header and orbit data files are provided with the SAR image, [CSA, 1995], as listed in the column 'source' of each table. The format of the DEM file is exactly the same as shown in Table 5.1 (b). Table 7.1 (b) shows the azimuth time of each azimuth line of the entire SAR image that can be extracted directly from the header files. Table 7.1 (c) shows the image co-ordinates together with the corresponding *DN* of each pixel of the SAR image being geocoded.

Contents	Unit	Descriptions	Source
21292606	msec	Azimuth time of the 1st azimuth line of the real SAR image	Processed Data Record
...	msec	Repeat until the last azimuth line of the SAR image	

Table 7.1 (b) Format of the azimuth timing data file `sargeoco.azi`

Contents	Unit	Descriptions	Source
3001 4001 255	pixel/line/*DN*	Co-ordinates and *DN* of the 1st pixel of the 1st azimuth line of the SAR image	Processed Data Record
...	pixel/line/*DN*	Repeat until the last pixel of the last azimuth line of the SAR image	

Table 7.1 (c) Format of the SAR image file `sargeoco.img`

7.4.1 Verification of the Automatically Generated GCPs

A small chip of the reference DEM in a 50m grid with the size of 21 × 21 pixels was used for simulation in order to provide control, as described in Chapter 5 (see Figure 5.11). This DEM chip has to be interpolated into a 12.5m grid (81 × 81 pixels) to meet the need of SAR image simulation. One SAR image chip of each tested image DS1, DS7b, AS1 and AS7 at the Aix-Marseilles test site in south France, as described in Table 5.3 (a), has been simulated. This is a preparatory stage for providing control based on the same DEM chip. These simulated images, as shown in Figure 5.12, were employed to correlate with the real SAR image (1024 × 1024 pixels) to determine the relative location of the simulated image chip.

Assign every corner of the DEM as a GCP, there are four GCPs available for each case. As mentioned in Chapter 5, the simulator gives the detected range and azimuth time data of each GCP. Also, the simulated-real image correlation results provide the observations of the real image co-ordinates of each GCP in range and in azimuth

direction. The averaged differences in range and in azimuth timing data of the four GCPs in respect to each real image are shown in Table 7.2.

Alias name		DS1	DS7b	AS1	AS7
Range Difference	Mean (m)	+94.2	-41.4	+8.3	+110.0
	RMSE (m)	**2.6**	**2.2**	**1.6**	**3.4**
Azimuth Timing Difference	Mean (sec) (m)	-0.00617 (-46.0)	-0.02023 (-150.7)	+0.01412 (+105.2)	+0.00825 (+61.5)
	RMSE (sec) (m)	0.00027 (**2.0**)	0.00008 (**0.6**)	0.00062 (**4.6**)	0.00017 (**1.3**)

Table 7.2 Statistics of the precision of the four automatically generated GCPs.

Obviously, orbit shifts are relatively significant and must be corrected. The differences of the azimuth timing data have been converted to those of the physical distance, assuming the averaged sensor speed as 7500m/sec. In respect to the mean of the differences, the RMS errors of the four GCPs of each image are consistently better than 4m in range and 5m in azimuth direction. These RMS errors can be considered as the precision of the simulator, dR_{GCP} and dA_{GCP}, as described in equation (7.2) and (7.4), respectively. These errors are well below half of the pixel spacing of a RADARSAT SAR standard mode image (6.25m). In terms of providing control for geocoding, the averaged differences in range and in azimuth time are treated as orbit shifts, and are imported to the geocoding routine together with the header information as shown in Table 7.1 (a).

7.4.2 Validation of the Geocoding Algorithm

The geocoding algorithm is validated using a French reference DEM that is initially in a 50m grid with the original size of 271 × 271 pixels as the same DEM used in previous chapters. The DEM has to be interpolated into a 12.5m grid to cope with the pixel spacing of the real SAR image. A sub-scene of the size 1024 × 1024 pixels sectioned from each SAR image at the test-site has been imported to the geocoding routine together with the ground control data provided automatically as described in Section 7.4.1. Four sub-scene geocoded images, including DS1, DS7b, AS1 and AS7, have been produced using the reference DEM according to different geometric conditions as shown in Figure 7.6. Appendix F.1 shows the geocoded image (DS1) at a larger scale.

Figure 7.6 Geocoded images using the reference DEM. (Top-left: DS1. Top-right: DS7. Bottom-left: AS7. Bottom-right: AS1. Size: 11km × 11km.)

In order to evaluate the geocoded images derived, a total number of seven ground check points were selected to show the relative deviations in plan compared with the corresponding co-ordinates measured from a 1:25,000 scale map. All of the check points were selected in flat-moderate areas, as in Figure 7.7, because it is very difficult to identify evident objects in hilly areas due to layover effects. The accuracy of the measurements made for the check points on the maps of a 1:25,000 scale is estimated as 25m in easting or northing, as shown in Table 2.6. Table 7.3 shows that the geocoding algorithm can give positioning accuracy of 25m, or a resolution cell of the RADARSAT SAR standard mode image, without using any manually selected GCPs. Most of the check points are selected from the corners of buildings that can be identified in all of the four images, so that their actual elevation data are not necessarily equivalent to the ground elevation. Therefore, the co-ordinates of each check point in the geocoded image may exhibit shifts in range direction from the expected ones as demonstrated by the mean values in Table 7.3 and 7.4.

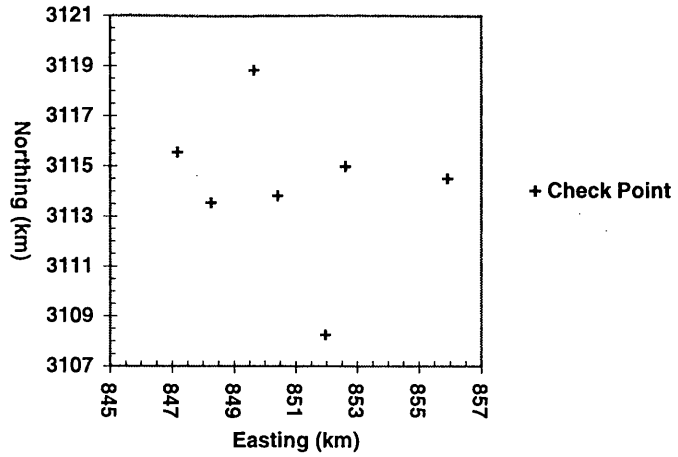

Figure 7.7 Locations of the check points of the geocoded images.

Alias Name	DS1		DS7b		AS1		AS7		Mean (m)	
Component	E	N	E	N	E	N	E	N	E	N
Mean (m)	-32	+1	+15	+3	-19	+9	+2	+2	-8	+3
RMSE (m)	21	16	13	21	21	18	18	19		
2-D (m)	26		25		28		26			

Table 7.3 Positioning accuracy of the check points measured in respect to each geocoded image derived using the reference DEM.

Check Point No.	Mean (m)		RMSE (m)		2D (m)
	E	N	E	N	
1	-13	-5	5	9	10
2	-8	9	26	6	27
3	11	-4	11	5	12
4	-26	-16	32	22	39
5	5	28	23	5	24
6	-22	11	24	10	26
7	-8	-3	23	22	32
Mean (m)	-8	+3			

Table 7.4 Positioning accuracy of each check point measured from the four geocoded images derived using the reference DEM.

Figure 7.8 demonstrates the averaged deviation of each individual GCP in plan measured from the four geocoded images derived using the reference DEM. Figure 7.9 illustrates the deviations of the check points in easting and in northing averaged from the four geocoded images. The co-ordinates of the check points measured show no enormous bias.

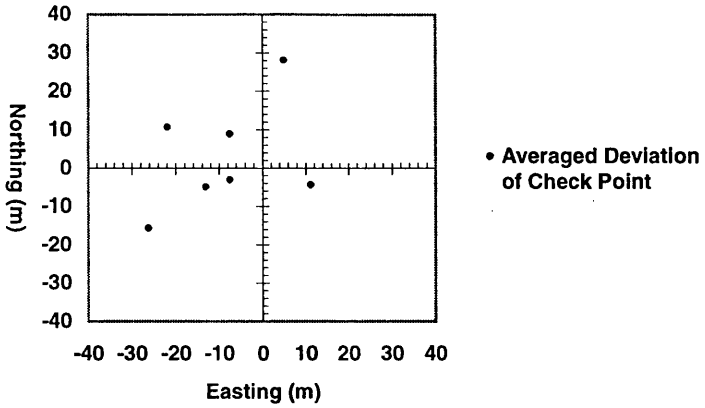

Figure 7.8 Deviations in plan of the check points measured and averaged from the four geocoded images derived using the reference DEM.

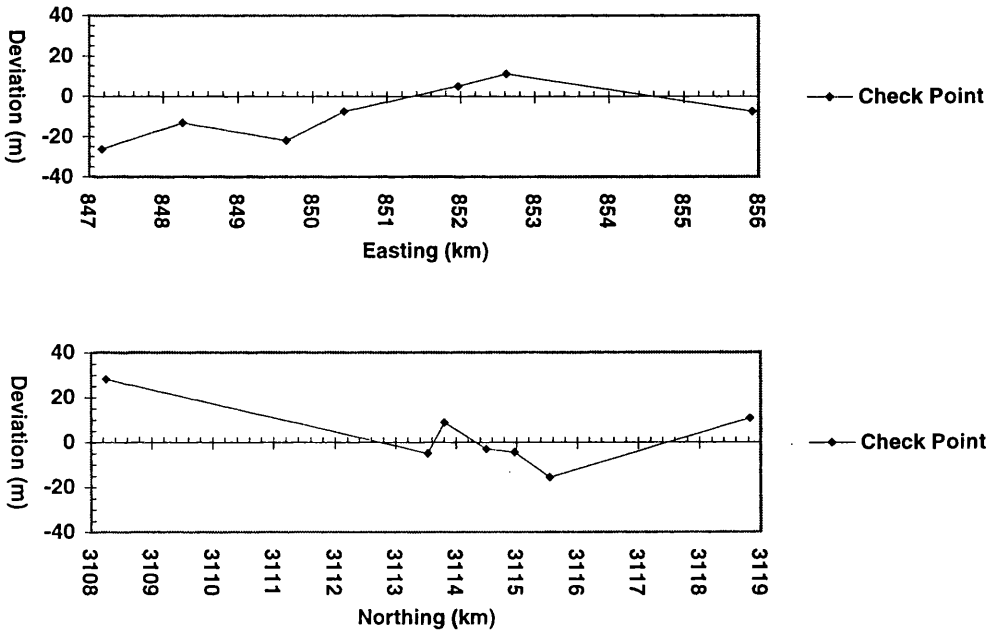

Figure 7.9 Deviations of the check points (in easting, above, and in northing, below) measured and averaged from the four geocoded images derived using the reference DEM.

7.4.3 Geocoding Using the Derived and Refined DEM

After validation, the geocoding algorithm can be used to produce geocoded images using the generated and refined DEM derived in the preceding chapters. Notice that the raw DEM is generated automatically using the pyramidal image correlation strategy with a region-growing approach (in Chapter 4) and using the rigorous space

intersection algorithm (in Chapter 3). Further improvement of the DEM quality is possible using automatically derived GCPs which give high quality ground control and minimize the systematic shifts based on a simulation method (in Chapter 5), if a known DEM chip with significant terrain relief available. The generated elevation data that is initially a set of scattered points distributed irregularly with numerous gaps and holes has been filled and interpolated into a fixed grid to cope with the resolution of a real SAR image. More detailed description about the refinement and analysis of the generated DEM is given in Chapter 6.

Information loss in layover areas is expected as discussed in Chapter 6 and the quality of a geocoded image is liable to decrease with increasing layover coverage. Figure 7.10 shows the comparison and contrast between the overlapping layover map (right) simulated for the real images based on a reference DEM and the absolute difference DEM (left) obtained from the generated DEM and the reference one.

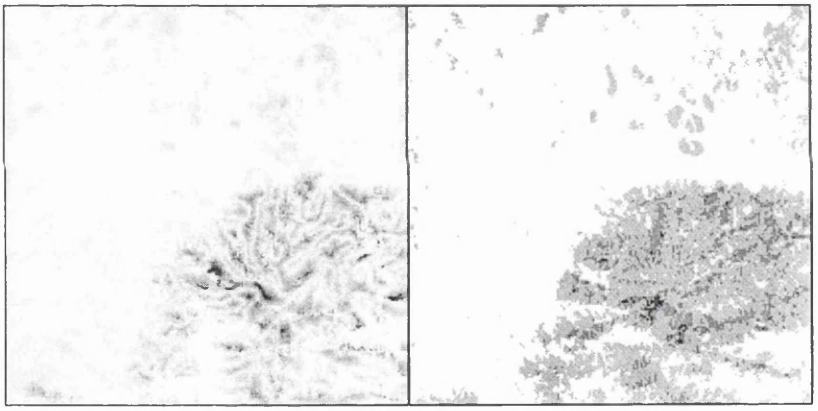

Figure 7.10 Elevation error map and overlapping layover map. (Left: The absolute difference in height increases with decreasing brightness, depicted from Figure 6.7. Right: The overlapping layover map of the two SAR image pairs of different orbits, extracted from Figure 6.2 (b). The overlapping times increase with decreasing brightness. Size: 10km × 10km.)

The overlapping layover map was derived from two image pairs of different orbit directions. The quality of the elevation data derived in the flat-moderate areas is expected to be better than that derived in the hilly areas. After refinement of the generated DEM, a sub-scene of size 1024 × 1024 pixels of each SAR image at the same test-site has been imported to the geocoding routine together with ground control provided in Section 7.4.1 to generate geocoded images. The same seven ground check points were measured within the test site to show the relative deviations of the co-ordinates of the geocoded images in

plan compared with the counterparts measured on a 1:25,000 scale map as shown in Table 7.5. In general, the quoted figures show that the generated DEM can give a similar positioning accuracy as shown in Table 7.3. The deviations of the individual check points of the geocoded image using the generated DEM range from 12m to 21m, as demonstrated in Table 7.6. That is comparable with their counterparts derived using the reference DEM, giving deviations from 10m to 39m, as shown in Table 7.4.

Alias Name	DS1		DS7b		AS1		AS7		Mean (m)	
Component	E	N	E	N	E	N	E	N	E	N
Mean (m)	-16	+7	0	+5	-10	+7	-7	-4	-8	+4
RMSE (m)	15	10	14	24	20	13	20	20		
2D (m)	18		28		24		28			

Table 7.5 Positioning accuracy of the check points measured in respect to each geocoded image derived using the generated DEM.

Check Point No.	Mean (m)		RMSE (m)		2D (m)
	E	N	E	N	
1	-14	-11	14	14	20
2	-8	12	9	5	10
3	+24	+2	6	10	12
4	-20	-12	9	14	17
5	+2	+25	14	9	17
6	-28	+4	14	16	21
7	-14	-6	11	14	18
Mean (m)	-8	+4			

Table 7.6 Positioning accuracy of each check point measured from the four geocoded images derived using the generated DEM.

Figure 7.11 shows the averaged deviation of each GCP in plan measured from the four geocoded images. Figure 7.12 demonstrates the deviations of the check points averaged from the four geocoded images using the generated and refined DEM in easting and in northing, individually. It is interesting to notice that Figure 7.9 and Figure 7.12 show similar error curves of the check points, arranged according to easting and to northing. Firstly, it proves that there is no big difference between the generated (refined) DEM and the reference DEM in the flat-moderate areas, so the errors behave in the same way. Secondly, these errors are probably caused by the unknown height of the objects being measured. In fact, all of these objects measured are buildings in the urban areas and in the rural areas of Marseilles, [IGN, 1992]. A small building may produce a significant layover feature, which is the actual 'object' being measured (recall the layover effects

described in Section 6.2.1), provided that the aspect of the radar illumination is appropriate. Thirdly, it may be due to the measuring errors of map/image co-ordinates caused by the human operator (the author). Also, it may be owing to the minor uncertainty in the SAR image geometry. Recall that the relative location accuracy of the RADARSAT SAR image pixel is reported as 30m, according to Denyer *et al.* [1993].

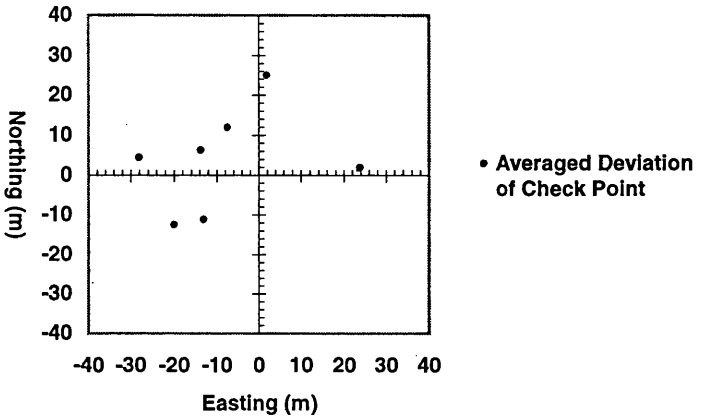

Figure 7.11 Deviations in plan of each check point measured and averaged from the four geocoded images derived using the generated DEM.

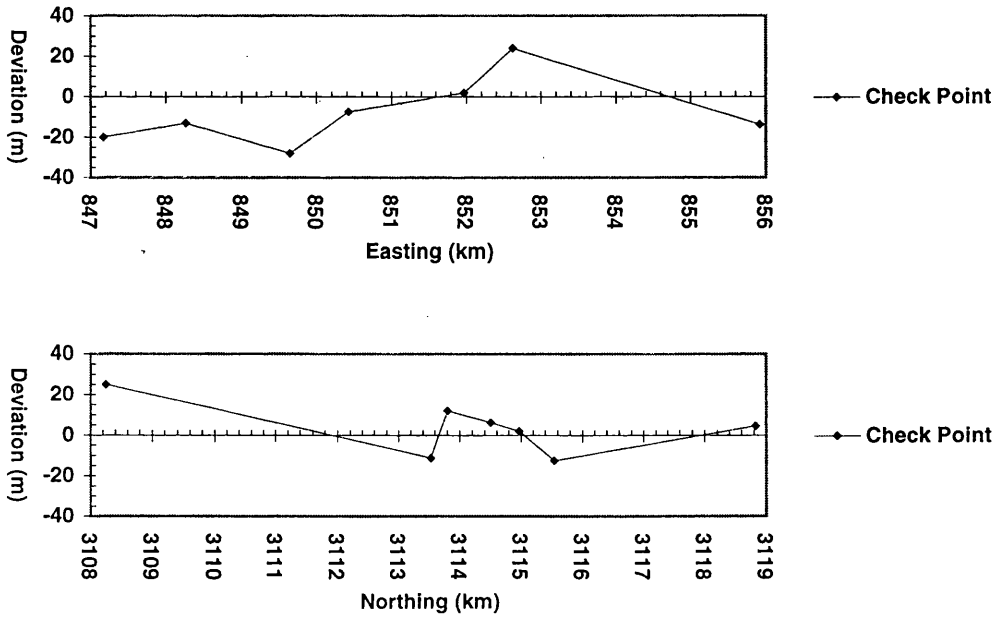

Figure 7.12 Deviations of the check points (in easting, above, and in northing, below) measured and averaged from the four geocoded images derived using the generated DEM.

Figure 7.13 shows the geocoded descending image pair (DS1 and DS7b at top-left and top-right, respectively) and the ascending pair (AS7 and AS1 at bottom-left and bottom-right, respectively) derived using the generated DEM. The geocoded images show distortions remaining in the hilly areas, where the DEM generated is not accurate enough to restore the distortions caused by terrain relief, compared with the geocoded images shown in Figure 7.6. Appendix F.2 shows the geocoded image (DS1) of a large scale.

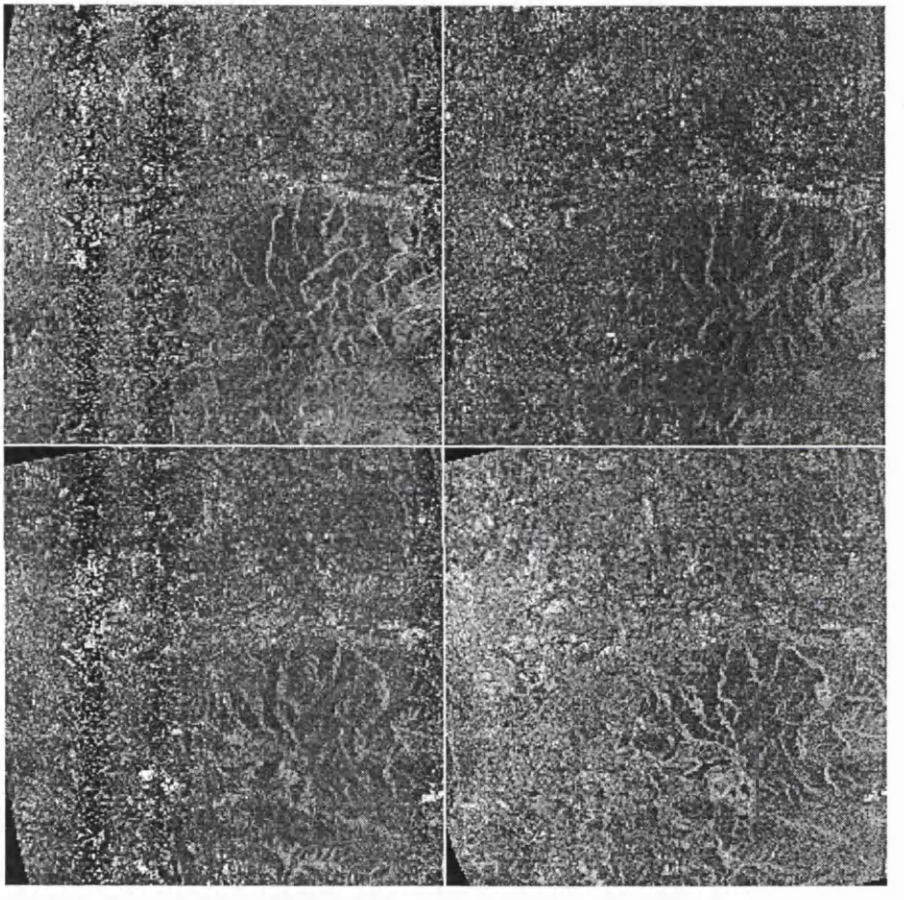

Figure 7.13 Geocoded images derived using the generated and refined DEM. (Top-left: DS1. Top-right: DS7b. Bottom-left: AS7. Bottom-right: AS1. Size: 11km × 11km.)

Figure 7.14 shows the image chips extracted from the geocoded images (DS1) derived using the DEM generated (left), those derived using the reference DEM (central) and the absolute difference images (right) of the left images and the central ones, giving a close look at the geocoded images. The size of each image chip in Figure 7.14 is 2.5km × 2.5km. The geocoded images in the top row were sectioned within a hilly area. The geocoded images in the bottom row were extracted from a flat-moderate area.

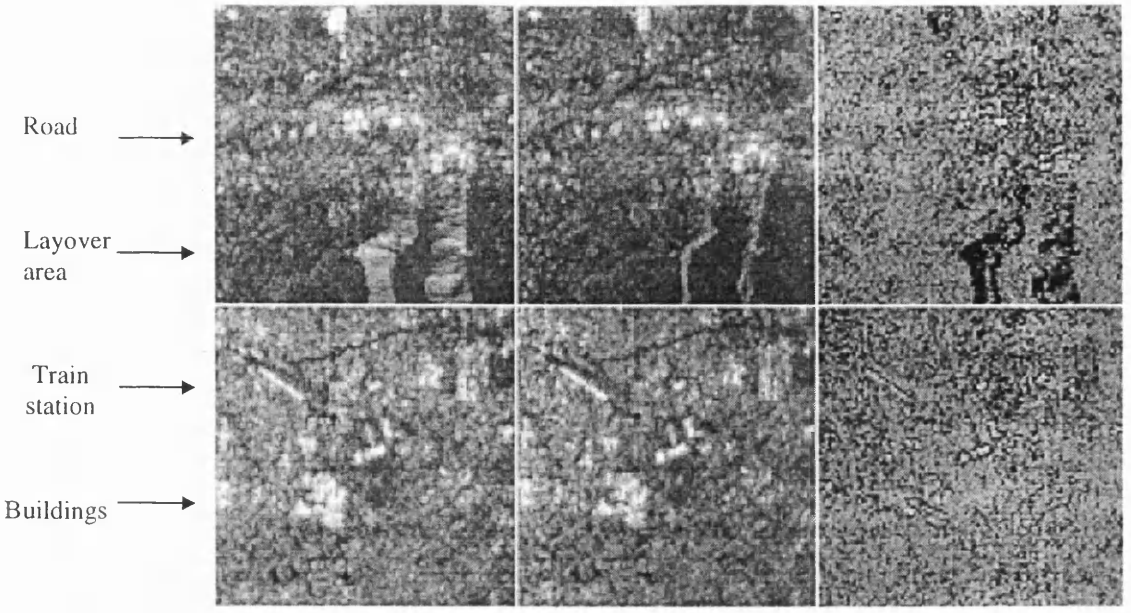

Figure 7.14 Examples of the geocoded image chips (DS1) in a hilly area (top row) and in a moderate-flat area (bottom row). (Left: the geocoded image using the reference DEM. Central: the geocoded image using the DEM derived. Right: the difference image of the left and the central images. Size: 2.5km ×2.5km. The darker the right image, the greater the difference in grey value).

The absolute difference images show that image distortions in the hilly areas are evident (images in the upper row), but not in the moderate-flat areas. The absolute differences between the geocoded images increase with increasing darkness in Figure 7.14. Notice that the roads (the dark lines) of the left geocoded images and the middle ones in Figure 7.14 cannot be identified in the absolute difference images, i.e., the geocoded positions of the roads in both images are overlapping each other (see the right images). Most of the bright objects (buildings) in the geocoded images are also overlapping each other, which causes bright spots, showing correct geocoding. Particularly, the position of train station in the images in the bottom row has been geocoded correctly giving a bright linear feature. It proves that the quality of the DEM generated is suitable for geocoding in flat-moderate areas. However, the layover areas as shown in the bottom part of the geocoded images in the upper row cannot be rectified completely giving the dark areas. Appendix F.3 gives the absolute difference image of a larger extent.

Figure 7.15 gives a perspective view of the geocoded image DS1 derived using the reference DEM (above) and that of the geocoded image DS1 draped on the DEM generated (below). Obviously, in terms of visual comparisons, the differences between both images are insignificant in the moderate areas, but both images differ in the hilly

areas. The geocoded image in layover areas cannot be rectified completely due to information loss caused by SAR imaging geometry.

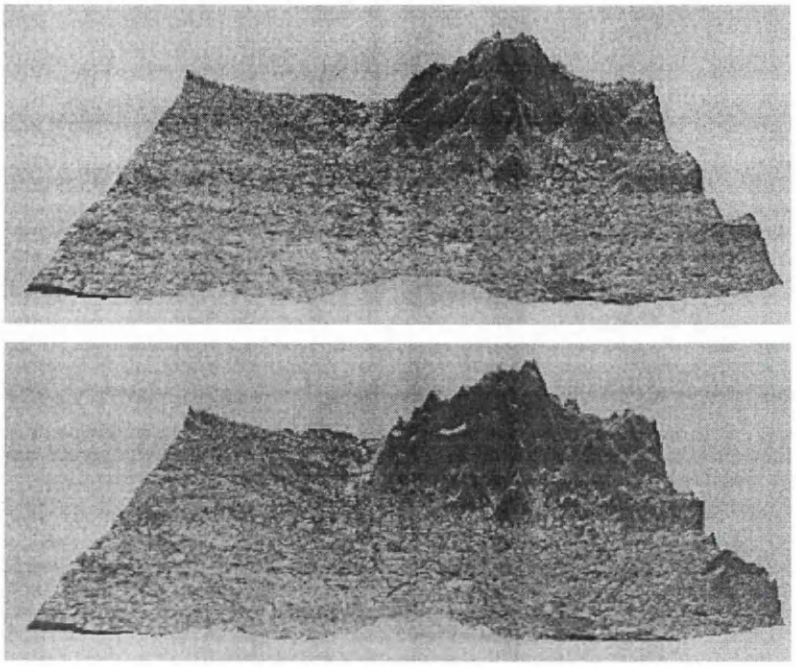

Figure 7.15 Perspective viewing of the geocoded image (DS1) derived using the reference DEM (above) and the DEM generated (below). Size: 11km × 11km. Viewing from west to east direction. Vertical exaggeration factor: 6.

7.4.4 Discussion

Verification results of the automatically generated GCPs show that the along-track orbit shifts vary from 46m to 151m and the resultant radial orbit drifts including the range shifts differ from 8m to 110m hence using GCPs for geocoding is essential. The automatically generated GCPs give high quality ground control with RMS errors ranging from 1.6m to 3.4m in range and from 0.6m to 4.6m in azimuth time (converted by the sensor speed of 7500m/sec). This ensures that the geocoded images may reflect the actual positional errors caused by the generated and refined DEM. In addition, the high quality GCPs generated using the simulator based on the zero-Doppler assumption show that the errors coming from the zero-Doppler assumption are limited and tolerable in this case. It should be noticed that the known DEM required for simulation must convey varied terrain relief to provide enough significant features for the real-simulated image correlation.

The geocoding algorithm employed in this chapter has generated reasonable geocoded SAR images from different orbit directions and incidence angles. The geocoding algorithm is developed for quick implementation and for showing the use of the derived DEM and the automatically generated GCPs with relatively good geometric accuracy. The geocoding algorithm has been validated using a reference DEM and seven independent check points. It shows that the positional errors in plan range from 25m to 28m in terms of individual images, with no corrections for the height data of check points. In terms of individual check points, the positional errors vary from 10m to 39m. Positional deviations may vary for individual check points, due to speckle, varied illumination of man-made objects, unknown relative elevation data of the objects being measured and human factors in observations. Nevertheless, the overall accuracy of the check points calculated is comparable with the measuring errors on maps/images (recall Table 2.6) showing that human factors (measurement errors) are more critical than the proposed geocoding algorithm itself. The systematic shifts remaining are about 8m in easting and 3m in northing showing no large bias.

The DEM generated from space intersection, with further refinement, has been shown to be practical for the production of geocoded images in various geometric conditions in flat-moderate areas. The positional errors in plan of the geocoded products using the generated DEM range from 18m to 28m and the positional deviations calculated vary from 10m to 21m in terms of individual check points. The geocoding results obtained using the derived DEM are better than those produced using the reference DEM. Also, Figure 7.9 and 7.12 show similar error curves, which validate that using the generated and refined DEM can produce geocoded images of the same order of accuracy as those produced by using the reference DEM. The experimental results of geocoding using the generated and refined DEM justify the use of the proposed algorithms described in the preceding chapters. It has been shown that a higher level of automation is achieved for most of the key steps for extracting spatial information from SAR image pairs. It leads to the conclusions made in the final chapter of the thesis.

7.5 Summary

The proposed geocoding algorithm employing a direct image-to-map approach makes full use of the simulation technique with a known DEM chip allowing the automatic provision of GCPs for SAR image geocoding based on the assumption of a

consistent sensor speed within the sensed area and of a zero-Doppler imaging geometry. The quality of the automatically generated GCPs has been shown to be better than 5m either in range or in azimuth direction. This is better than other traditional methods for providing control. The geometric accuracy is placed as the top priority for geocoding to reveal the errors coming from the generated and refined DEM. The generated and refined DEM has been used to produce the geocoded SAR images in flat-moderate areas, which are comparable with the results derived using the reference DEM. The quality of the generated DEM in layover areas limits the geocoding applications in hilly areas because of information loss under such circumstances. The procedures and algorithms proposed for digital radragrammetry have shown that a higher level of automation with minimized human errors involved has been achieved.

Chapter 8
Conclusions

In terms of full digital radargrammetry for extracting spatial information from stereoscopic Synthetic Aperture Radar (SAR) data, work carried out in this thesis is incomplete. However, the results derived in the course of this Ph.D. project can be useful for understanding radargrammetry and may give a rough guide for further research. In this final chapter, a review of the Ph.D. work will be given in section 8.1 to show what has been done. Future work regarding digital radargrammetry is suggested in Section 8.2.

8.1 Review of the Ph.D. Project

In terms of extraction of spatial information from stereoscopic SAR data, a DEM is surely not the only type of spatial information that can be derived. However, generation of a DEM from stereo SAR images may be used to show the use of stereo radargrammetry as well as the level of automation achieved. Generation of a DEM requires an accurate geometric model to solve the space intersection problem and an optimized image correlation method to carry out the parallax measurements automatically. Particularly, the SAR image geometry is not as straightforward as that of the optical counterpart described by the well-known projective geometry. Many assumptions have to be made to make the space intersection problem solvable. This leads to a question on the sensitivity (stability) of the radargrammetric model when observation errors and some assumptions cannot be avoided. This question has been answered partly, if not completely, by proposing a refined geometric model as well as an error model (in Chapter 3). The positioning accuracy of 32 independent check points derived ranges from 36.3m to 38.8m in 3-D which is comparable with the predicted error of 28m based on the measuring error of one pixel.

The problem of SAR image correlation is much more complicated than that of optical data. This is due to speckle and the alien image geometry to human eyes. Previous

work on this topic has achieved reasonable results. However, many human operations are required in the previously available methods, such as the pyramidal correlation scheme employing the least squares correlation method with a region-growing approach, in particular selection of the parameters commanding the structure of an image pyramid. Manual operations, such as a trial-and-error method employed by previous authors, hamper automation. An attempt to avoid the trial-and-error approach at the beginning stage of the pyramidal image correlation has been made to provide a rule for selecting parameters (in Chapter 4). The accuracy of the DEMs generated is stable ranging from 20.7m to 25m in height.

"To see is to believe." as the old saying is. It may be true in photogrammetry, but it is not necessarily correct in radargrammetry. What a human operator sees in a SAR image does not necessarily correspond to the same object being measured on a map, due to different aspects of radar illumination and speckle. This causes problems of providing Ground Control Points (GCPs) in radargrammetry. There are two ways to solve these problems. On the one hand, the radargrammetric model has to be insensitive to poor quality GCPs, or to get rid of GCPs (as refined in Chapter 3). On the other hand, when GCPs are desperately needed, generation of GCPs has to be made automatically. The automatic provision of GCPs has been made possible using the corner elements of a known DEM chip in an area of varied terrain relief (see Chapter 5). In fact, the automatically generated GCPs are invisible to human eyes. The RMS errors of the GCPs generated automatically range from 8.8m to 11.4m in 3-D that are better than the manually collected counterparts, whose RMS errors range from 28.4m to 40.6m.

The Ph.D. project is concluded by assessments of the geocoded images generated using the DEM generated and refined. Hence a 'complete' generated DEM is required with no gaps, holes and noise. The DEM interpolation and filtering methods have been applied cautiously to preserve the quality of the DEM derived using the image correlation and space intersection routines. The quality of the DEM derived has been verified using a reference DEM of ±5m accuracy. That was done step-by-step following the refinement procedures set out in Chapter 6. The DEM derived from interpolation and filtering processes gives an overall accuracy in height of 21.6m. The accuracy of the DEM derived in the moderate-flat area ranges from 6m to 14m in terms of each profile, which is much better than that in the hilly area.

It is also important to select a suitable geocoding algorithm which preserves the quality of the DEM used for geocoding, in order to avoid any misleading evaluation of the algorithms proposed in the thesis. Owing to considerations of computational efficiency, the currently available geocoding methods tend to employ some polynomial fit functions to relate the original SAR image pixel to the geocoded one in image space, according to a defined anchor grid structure derived using a map-to-image transformation approach. Thus, there are two steps of transformation in the standard geocoding approach. In order to reduce any risk arising from the polynomial fit functions, a direct image-to-object method is employed to relate the original SAR image pixel to the corresponding DEM elements being sensed (in Chapter 7). The positional accuracy of the geocoded images in terms of independent check points ranges from 10m to 21m in plan.

All of the above-mentioned results have been validated numerically by means of using independent check points or a reference DEM, as illustrated in the appropriate chapters. In terms of the aims set out in Chapter 1 and considerations of a digital ragrammetric system, the Ph.D. work can be reviewed as follows:

(1) A refined stereo space intersection algorithm without the need for GCPs and accurate orbit information has been developed, which is based on the assumption of zero-Doppler imagery and of stationary image geometry. The proposed weighted space intersection solution helps with improving the precision of the results derived and allowing for the effects from the zero-Doppler assumption. The systematic correction is carried out independently after the space intersection routine, and the minimal requirement of the number of GCPs is two. The algorithm has proved practical and generates reasonable results from space-borne SAR data. However, other kinds of SAR data, such as the air-borne SAR and the extra-terrestrial (planetary) SAR images, have not been tested.

(2) An error model is proposed to describe the error behaviour of the measurements of the SAR image co-ordinates, either in azimuth lines or in range pixels. The predicted errors are comparable with the actually derived errors. The error model has to be compatible with the geometric model, if that geometric model is to be refined for other kinds of SAR data.

(3) The proposed optimized strategy of selecting parameters for commanding the pyramidal correlation scheme has been proved reasonable, which improves the level of automation for the generation of a DEM from stereo SAR data. But, the least

squares image correlation routine with a region-growing approach consumes enormous computational resources. In addition, the currently available methods can only deal with the same-side SAR image configuration, but not with the opposite-side configuration.

(4) A SAR image product simulator is proposed, and the automatic provision of GCPs using the simulation method with a known DEM chip helps with the systematic corrections required in radargrammetry. The quality of the automatically derived GCPs is better than, or at least similar to, that of the manually selected GCPs. The simulation method is applicable for producing a small image chip, but it is not suitable for simulating a full-scene SAR image. Providing control in flat areas or unknown areas, where a known DEM chip with significant terrain relief is not available, can be difficult.

(5) A direct image-to-object geocoding method is proposed to relate the SAR image pixels to object space. The comparisons made between the geocoded images using the reference DEM and those using the DEM generated and refined show the overall DEM quality is reliable in moderate-to-flat areas. However, information loss in hilly areas cannot be restored. Also, the proposed geocoding algorithm is not efficient to carry out a full-scene SAR image geocoding in terms of computing.

In general, the potential and the limitations of the stereo radargrammetric techniques have been revealed. Computational efficiency of the algorithms and the geometric accuracy required for applications need to achieve a balance. Also, the effects of the radar illumination of different aspects on measuring specific objects, such as the identification of buildings in urban areas, are still not well understood, and this contributes to the uncertainties in extracting spatial information and to the processes of evaluating the results derived. The success of a digital radargrammetric system depends on more effort to solve, at least, the problems listed in next section.

8.2 Future Work

This Ph.D. project did not aim to achieve a full automation of digital radargrammetry. Many more items of work have to be done to make the full use of SAR data and of digital radargrammetry. The following list for future work in digital radargrammetry is still far from complete, and can only provide a rough guide:

(1) Refining the radargrammetric model to be suitable for other remotely sensed SAR data, such as air-borne and planetary SAR images. Refine the error model according to the appropriate geometric model.

(2) Improving the least squares correlation algorithm with a region-growing approach to be efficient in computing, without degrading the robustness and the accuracy of the current method.

(3) Considering the SAR image correlation strategy for opposite-side image pairs. The problem of the automatic elimination of the dissimilarity in the opposite-side image pair has to be overcome.

(4) Solving the problem of the automatic provision of GCPs in flat-to-moderate areas using any available ground truth information, such as the method of automatic image-map feature correlation.

(5) Investigating the effects of the radar illumination of different aspects on measuring objects. For instance, the shape and the orientation in 3-D of the object illuminated have to be considered.

(6) Improving the level of automation for segmentation and extraction of the features of interest in SAR images giving automatic object detection, linear, area and volume measures.

To sum up, the extraction of spatial information from stereo SAR data has shown practical, and digital radargrammetry is promising, but many items of work need to be done, such as automatic feature extraction from a SAR image. Particularly, the ambiguity between the 'true' feature and speckle remains a big problem. The work carried out in the thesis has shown that the number of the problems in making maps from SAR data which have been solved is rather limited at this stage, and there are many more problems in digital radargrammetry waiting to be tackled.

References

[Ackermann, 1984] Ackermann, F., 1984. Digital image correlation: performance and potential applications in photogrammetry. *Photogrammetric Record*, 11(64):429-439.

[Ackermann and Hahn, 1991] Ackermann, F. and Hahn M., 1991. Image pyramids for digital photogrammetry. In *Digital Photogrammetric Systems*. Edited by H. Ebner, D. Fritsch and C. Heipke. Wichmann Verlag, Heidelberg, pp:43-58.

[Albertz and Kreiling, 1980] Albertz, J. and Kreiling, W., 1980. *Photogrammetric Guide*. Wichmann Verlag, Heidelberg. 280 pages.

[Arai, 1991] Arai, K., 1991. GCP acquisition using simulated SAR and evaluation of GCP matching accuracy with texture features. *International Journal of Remote Sensing*, 12(10): 2389-2397.

[Barber, 1985] Barber, B.C., 1985. Theory of digital imaging from orbital synthetic-aperture radar. *International Journal of Remote Sensing*, 6(7): 1009-1057.

[Bayer *et.al.*, 1991] Bayer T., Winter R. and Schreier, G., 1991. Terrain influences in SAR back-scatter and attempts to their correction. *IEEE Transaction on Geo-science and Remote Sensing*, GE-29 (3):451-462.

[Burrough and McDonnell, 1998] Burrough, P. A. and McDonnell, R. A., 1998. *Principles of Geographical Information Systems*. Oxford University Press. 333 pages.

[CSA, 1995] Canadian Space Agency, 1995. *RADARSAT Canadian Data Processing Facility Product Specification*. CDRL No.IS-3, MacDonald-Dettwiler, Canada.

[Chen and Dowman, 1996] Chen, P.-H. and Dowman, I. J., 1996. Space intersection from ERS-1 synthetic aperture radar images. *Photogrammetric Record*, 15 (88):561-573.

[Chen, 1997] Chen, P.-H., 1997. *Providing Control for Generating a DEM from SAR Data*. Mphil/PhD Transfer Report, University College London. 84 pages.

[Clark, 1991] Clark, C., 1991. *Geocoding and Stereoscopy of Synthetic Aperture Radar Images*. Ph.D. Thesis, University of London. 223 pages.

[Cooper and Robson, 1996] Cooper, M.A.R. and Robson, S., 1996. Theory of close range photogrammetry. In *Close Range Photogrammetry and Machine Vision.* Edited by Atkinson, K.B. Whittles Publishing, U.K. pp:9-51.

[Curlander, 1982] Curlander, J.C., 1982. Location of spaceborne SAR imagery. *IEEE Transaction on Geo-science and Remote Sensing*, GE-20 (3):359-364.

[Curlander, 1984] Curlander, J.C., 1984. Utilisation of spaceborne SAR data for mapping. *IEEE Transaction on Geo-science and Remote Sensing*, GE-22 (2):106-112.

[Curlander *et al.*, 1987] Curlander, J.C., Kowk, R. and Pang, S.S., 1987. A post-processing system for automated rectification and registration of space-borne SAR imagery. *International Journal of Remote Sensing*, 8(4):621-638.

[Curlander and McDonough, 1991] Curlander, J.C. and McDonough, R.N., 1991. *Synthetic Aperture Radar.* John Wiley and Sons Inc., New York. 647 pages.

[Day and Muller, 1989] Day, T. and Muller, J.P., 1989. Digital elevation model production by stereo-matching SPOT image-pairs: a comparison of algorithms. *Image Vision Computing*, 7(2):95-101.

[Denos, 1992] Denos, M., 1992. A pyramidal scheme for stereo matching SIR-B imagery. *International Journal of Remote Sensing*, 13(2):387-392.

[Denyer *et al.* , 1993] Denye, N., Raney, R.A. and Shepherd N., 1993. The RADARSAT data processing facility. *Canadian Journal of Remote Sensing*, 19(4): 311-316.

[Domik *et al.*, 1986] Domik, G., Leberl, F.W. and Cimino, G., 1986. Multiple incidence angle SIR-B Experiment over Argentina: generation of secondary image products. *IEEE Transaction on Geo-science and Remote Sensing*, GE-24 (4):492-497.

[Dowman, 1981] Dowman, I.J., 1981. *A Photogrammetric Plotting Instrument for Automatic Image Correlation and Height Determination.* Ph.D. Thesis, University of London. 313 pages.

[Dowman, 1992] Dowman, I.J., 1992. The geometry of SAR images for geocoding and stereo application. *International Journal of Remote Sensing*, 13(9):1609-1617.

[Dowman *et al.*, 1992] Dowman, I.J., Clark, C. and Denos, M., 1992. Three dimensional data from SAR images. *International Archives of Photogrammetry and Remote Sensing*, 29(4):425-427.

[Dowman *et al.*, 1993] Dowman, I.J, Laycock, J. and Whalley, J., 1993. Geocoding in the UK. In *SAR Geocoding: Data and Systems*. Edited by Schreier, G. Wichmann Verlag, Heidelberg, pp:373-387.

[Dowman *et al.*, 1994] Dowman, I.J., Chen, P.-H., Clochez, O. and Saundercock, G., 1993. Heighting from stereoscopic ERS-1 data. *Proceedings of the Second ERS-1 Symposium*, ESA SP-361, 1:609-614.

[Dowman *et al.*, 1997] Dowman, I.J., Twu, Z.-G. and Chen, P.-H., 1997. DEM generation from stereoscopic SAR data. *International Symposium: Geomatics in the Era of RADARSAT 1997*, Ottawa. CD-ROM.

[Dowman and Chen, 1998] Dowman, I. J. and Chen, P.-H., 1998. A rigorous stereo method for RADARSAT data. *RADARSAT ADRO Final Symposium*, Montreal. CD-ROM.

[Elachi, 1988] Elachi, C., 1988. *Space-borne Radar Remote Sensing: Application and Techniques*. IEEE Press, U.S.A.

[Elhassen and Ali, 1995] Elhassen, I.M. and Ali, A.E., 1995. Radargrammetry with Almaz SAR imagery. *Geometics Research Australasia*, No.62:63-92.

[ESA, 2000] European Space Agency, 2000. *ERS Missions*. URL: http://earth1.esrin.esa.it/ERS.

[Fernandes, 1993] Fernandes, M.J., 1993. *Precise Satellite Orbit Determination with Particular Application to ERS-1*. Ph.D. Thesis, University of London. 301 pages.

[Ferretti *et al.*, 1999] Ferretti A., Prati, C. and Rocca, F., 1999. Multibaseline InSAR DEM reconstruction: the wavelet approach. *IEEE Transaction on Geo-science and Remote Sensing*, GE-37(2):705-715.

[Fonseca and Manjunath, 1996] Fonseca, L.M.G. and Manjunath, B.S., 1996. Registration techniques for multi-sensor remotely sensed imagery. *Photogrammetric Engineering & Remote Sensing*, 62(9):1049-1056.

[Fritsch. and Hobbie (Ed.), 1995] Fritsch, D. and Hobbie, D. (Ed.), 1995. *Photogrammetric Week'95.*, Wichmann Verlag, Heidelberg, 353 pages.

[Gauss, 1823] Gauss, C.F., 1823. *Theoria combinationis observationum erroribus minimis obnoxiae: Pars Prior. Commentatines societaties regiae scientarium Gottingensis recentiores, 5.* In *Theory of the Combination of Observations Least Subject to Errors, Part One, Part Two, Supplement.* Translated to German by Borsch, A. and Simon, P., 1887, and translated to English by Stewart, G.W., 1995. SIAM, Philadelphia, U.S.A. 241 pages.

[Gelautz *et al.*,1998] Gelautz, M., Frick, H., Raggam J., Burgstaller, J. and Leberl, F., 1998. SAR image simulation and analysis of alpine terrain. *ISPRS Journal of Photogrammetry and Remote Sensing*, 53(1): 17-38.

[Ghiglia and Pritt, 1998] Ghiglia, D.C. and Pritt, M.D., 1998. *Two-Dimensional Phase Unwrapping-Theory, algorithms, and Software.* Artech House Inc., Norwood, U.S.A. 493 pages.

[Goller *et al.*, 1999] Goller A., Gelautz, M. and Leberl, F., 1999. Parallel image processing applied to radar shape-from-shading. *Photogrammetric Engineering & Remote Sensing*, 65(3):259-267.

[Green, 1985] Green, R.M., 1985. *Spherical Astronomy.* Cambridge University Press, Cambridge. 520 pages.

[Gruen, 1987] Gruen, A.W., 1987. Adaptive least squares correlation: a powerful image matching technique. *South African Journal of Photogrammetry, Remote Sensing and Cartography,* 14(3):175-187.

[Gruen, 1996] Gruen, A.W., 1996. Least squares matching: a fundamental measurement algorithm. In *Close Range Photogrammetry and Machine Vision.* Edited by Atkinson, K.B. Whittles Publishing, U.K. pp:217-255.

[Guindon and Maruyama, 1986] Guindon, B. and Maruyama, H., 1986. Automated matching of real and simulated SAR imagery matching as a tool for ground control. *Canadian Journal of Remote Sensing*, 50(1): 2-11.

[Guindon, 1993] Guindon, B., 1993. Development of a SAR data acquisition planning tool (SARPLAN) based on image simulation. *International Journal of Remote Sensing*, 14(2): 333-344.

[Guindon, 1995] Guindon, B., 1995. Performance evaluation of real-simulated image matching techniques in the acquisition of ground control for ERS-1 image geocoding. *ISPRS Journal of Photogrammetry and Remote Sensing*, 50(1): 2-11.

[Hartl and Thiel, 1993] Hartl, Ph. and Thiel, K.-H., 1993. Radar interferometry-basic concept and application. *Workshop and Conference on International Mapping from Space, Working Group IV/2 of ISPRS,* Hannover, pp:207-32.

[Hartl *et.al.*, 1995] Hartl, Ph. and Thiel, K.-H., Wu, X. and Xia, Y., 1995. Earth observation by means of SAR: present state and future possibilities. In *Photogrammetric Week'95*. Edited by D. Fritsch and D. Hobbie. Wichmann Verlag, Heidelberg, 353 pages.

[Ho, 1984] Ho, W.-H., 1984. *The Potential of Low Resolution Digital Camera in Close-range Photogrammetry.* PhD Dissertation, University of Illinois at Urbana Champaign, USA.

[Holecz *et al.*, 1993] Holecz, F., Meier, E. and Nuesch, D., 1993. Postprocessing of relief induced radiometric distorted spaceborne SAR imagery. In *SAR Geocoding: Data and Systems*. Edited by Schreier, G. Wichmann Verlag, Heidelberg, pp:299-352.

[Holtzman *et al.*, 1978] Holtzman, J.C., Frost, V.S., Abbott, J.L. and Kaupp, V.H., 1978. Radar image simulation. *IEEE Transaction on Geo-science and Remote Sensing,* GE-16 (4):296-303.

[Honikel, 1998] Honikel, M., 1998. Improvement of InSAR DEM accuracy using data and sensor fusion. *International Archives of Photogrammetry and Remote Sensing*, 32(2):127-130.

[Hsia and Newton, 1999] Hsia, J.-S. and Newton, I., 1999. A method for the automated production of digital terrain models using a combination of future points, grid points, and filling back points. *Photogrammetric Engineering & Remote Sensing*, 65(6):713-719.

[IGN, 1989] IGN, 1989. *Serie Bleue 1:25,000 Cartes.* Map edition 3 *Institut Geographique National*, Paris, France.

[IGN, 1992] IGN, 1992. *Serie Orange 1:50,000 Cartes.* Map edition 8. *Institut Geographique National*, Paris, France.

[IGN, 1993] IGN, 1993. *Serie Verte 1:100,000 Cartes.* Map edition 8. *Institut Geographique National*, Paris, France.

[IGN, 1994] IGN, 1994. *Catalogue IGN 94. Institut Geographique National*, Paris, France. 48 pages.

[Isaaks and Strivastava, 1989] Isaaks E.H. and Strivastava, R.M., 1998. *An Introduction to Applied Geostatistics*. Oxford University Press, New York.

[James *et al.*, 1992] James, R.C., Alchian, A.A., Beckenbach, E.F., Bell, C., Craig, James, G., Michal, A.D. and Sokolnikoff, I.S., 1992. *Mathematics Dictionary*. Fifth Edition. Van Nortrand Reinhold, U.S.A. 548 pages.

[JPL, 2000] Jet Propulsion Laboratory, 2000. *Shuttle Radar Topography Mission (SRTM).* URL: http://www.jpl.nasa.gov/srtm .

[Kaupp *et al.*, 1982] Kaupp, V.H., Waite, W.P. and MacDonald, H.C., 1982. Incidence angle considerations for Spacecraft imaging Radar. *IEEE Transaction on Geo-science and Remote Sensing,* GE-20(3):384-389.

[Kingsley and Quegan, 1992] Kingsley, S. and Quegan, S., 1992. *Understanding Radar Systems*. McGraw-Hill Int., U.K. 375 pages.

[Kowk *et al.*, 1987] Kowk, R., Curlander, J.C. and Pang, S.S., 1987. Rectification of terrain induced distortions in radar imagery. *Photogrammetric Engineering & Remote Sensing*, 53(5):507-513.

[Kowk *et al.*, 1990] Kowk, R., Curlander, J.C. and Pang, S.S., 1990. An automated system for mosaicking spaceborne SAR imagery. *International Journal of Remote Sensing*, 11(2):209-223.

[Laycock *et al.*, 1992] Laycock, J.E., Dowman, I.J., Whalley J. and Upton M., 1992. *Precision Geocoding Project: Final Report (Phase 2).* GEC-Marconi Research Centre GEO-MRC-TR-2004/1, U.K. 26 pages.

[Leberl *et al.*, 1985] Leberl, F.W. Domik, G. and Korbick, M., 1985. Mapping with aircraft and satellite radar. *Photogrammetric Record*, 11(66):647-665.

[Leberl *et al.*, 1986] Leberl, F.W. Domik, G., Raggam, J. and Korbick, M., 1986. Radar stereo mapping techniques and application to SIR-B images of Mt. Shasta. *IEEE Transaction on Geo-science and Remote Sensing*, GE-24(4):473-481.

[Leberl, 1990] Leberl, F.W., 1990. *Radargrammetric Image Processing.* Artech House Inc., Norwood, U.S.A. 595 pages.

[Leberl *et al.*, 1994] Leberl, F.W., Maurice, K., Thomas, J.K. and Michel, M., 1994. Automated radar image matching experiments. *ISPRS Journal of Photogrammetry and Remote Sensing*, 49(3): 19-33.

[Lee and Jurkevich, 1989] Lee, J.-S. and Jurkevich I., 1989. Segmentation of SAR images. *IEEE Transaction on Geo-science and Remote Sensing,* GE-27(6): 674-680.

[Linder and Meuser, 1993] Liner, W. and Meuser, H.-F., 1993. Automatic tiepointing in images. In *SAR Geocoding: Data and Systems.* Edited by Schreier, G. Wichmann Verlag, Heidelberg, pp:207-212.

[Luscombe *et al.* , 1993] Luscombe, A.P., Ferguson, I., Shepherd N., Zimcik, D.G. and Naraine, P., 1993. The RADARSAT synthetic aperture radar development. *Canadian Journal of Remote Sensing*, 19(4): 298-310.

[Marek and Schmidt, 1994] Marek, K.-H. and Schmidt, K., 1994. Preliminary results of the comparative analysis of ERS-1 and ALMAZ-1 SAR data. *ISPRS Journal of Photogrammetry and Remote Sensing*, 49(3): 12-18.

[Marr and Poggio, 1979] Marr, D. and Poggio, T., 1979. A computational theory of human stereo vision. *Proceedings of the Royal Society of London,* B.204:301-328.

[Marr and Hildreth, 1980] Marr, D. and Hildreth, E., 1980. Theory of edge detection. *Proceedings of the Royal Society of London,* B.207:187-217.

[Massmann *et al.*, 1993] Massmann, F.H., Reigber, C., Konig, R., Raimondo, J.C. and Rajasenan, C., 1993. ERS-1 Orbit information provided by D-PAF. *Proceedings of the Second ERS-1 Symposium*, ESA SP-361, 2:765-770.

[Mercer, 1995] Mercer, J.B., 1995. SAR technologies for topographic mapping. In *Photogrammetric Week'95.* Edited by D. Fritsch and D. Hobbie. Wichmann Verlag, Heidelberg, 353 pages.

[Meier *et al.*, 1993] Meier, E., Frei, U. and Nuesh, D., 1993. Precise terrain corrected geocoded images. In *SAR Geocoding: Data and Systems.* Edited by Schreier, G. Wichmann Verlag, Heidelberg, pp:173-185.

[Mikhail, 1976] Mikhail, E.M., 1976. *Observations and Least Squares.* IEP, New York. 497 pages.

[Moreira *et al.*, 1995] Moreira, J., Schwäbisch, M., Fornaro, G., Lanari, R., Bamler, R., Just, D., Steinbrecher, U., Breit, H., Eineder, M., Franceschetti, G., Geudtner A. and Rinkel H., 1995. X-SAR interferometry: first results. *IEEE Transaction on Geo-science and Remote Sensing,* GE-33(4):950-956.

[Naraghi *et al.*, 1983] Naraghi, M., Stromberg, W. and Daily, M., 1983. Geometric rectification of radar imagery using digital elevation models. *Photogrammetric Engineering and Remote Sensing*, 49(2): 195-199.

[Newman and Sproull, 1979] Newman, W.M. and Sproull, R.F., 1979. *Principles of Interactive Computer Graphics.* McGraw-Hill Inc., U.S.A. 541 pages.

[O'Neill, 1991] O'Neill, M.A., 1991. *A Dynamic Numerical Camera Model for the SPOT-1 Sensor.* Ph.D. Thesis, University of London. 475 pages.

[Otto and Chau, 1989] Otto, G.P. and Chau, T.K.W., 1989. Region-growing algorithm for matching of terrain images. *Image Vision Computing*, 7(2):83-94.

[Paillou and Gelautz, 1999] Paillou P. and Gelautz, M, 1999. Relief construction from SAR stereo pairs: the "optimal gradient" matching method. *IEEE Transaction on Geo-science and Remote Sensing,* GE-37(4):2099-2107.

[Paul and Nasar, 1987] Paul, C.R. and Nasar, S.A., 1987. *Introduction to Electromagnetic Fields.* McGRaw-Hill Book Co., New York. 742 pages.

[Petrie, 1990a] Petrie, G., 1990a. Modelling, interpolation and contouring procedures. In *Terrain Modelling in Surveying and Civil Engineering.* Edited by Petrie, G. and Kennie, T.J.M. Whittles Publishing, U.K. pp:112-127.

[Petrie, 1990b] Petrie, G., 1990b. The impact of analytical photogrammetric instrumentation on DTM data acquisition and processing, in *Terrain Modelling in Surveying and Civil Engineering.* Edited by Petrie, G. and Kennie, T.J.M. Whittles Publishing, U.K. pp:50~72.

[Quam, 1984] Quam, L.H., 1984, Hierarchical warp stereo. *Proceedings Image Understanding Workshop.* DARPA, New Orleans, pp:149-155.

[Raggam and Gutjahr, 1998] Raggam, H. and Gutjahr, K., 1998. DEM generation using RADARSAT stereo data. *RADARSAT ADRO Final Symposium*, Montreal. CD-ROM.

[Ramapriyan *et al.*, 1986] Ramapriyan, H.K., Strong, J.P., Huang, Y. and Murray, C.W., 1986. Automated matching of pairs of SIR-B images for elevation mapping. *IEEE Transaction on Geo-science and Remote Sensing,* GE-24(4):462-472.

[Rantakokko and Rosenholm, 1999] Rantakokko, H. and Rosenholm, D., 1999. Rectification of slant range imagery through a direct image to ground relationship. *Photogrammetric Record*, 16(94):685-694.

[Renouard and Perlant, 1993] Renouard, L. and Perlant, F., 1993. Geocoding SPOT products with ERS-1 SAR geometry. *Proceedings of the Second ERS-1 Symposium*, ESA SP-361, 1:653-658.

[Rignot *et al.*, 1991] Rignot, E.J.M., Kwok, R., Curlander, J.C. and Pang, S.S., 1991. Automated multi-sensor registration: requirements and techniques. *Photogrammetric Engineering & Remote Sensing*, 57(8):1029-1038.

[Roth *et al.*, 1998] Roth, A., Knöpfle, W., Gebhardt, S., Rabus, B and Scales D., 1998. Evaluation of interferometric digital elevation models derived from ERS tandem data. *International Archives of Photogrammetry and Remote Sensing*, 32(2):242-247.

[Saundercock, 1995] Saundercock, G.P., 1995, The geocoding of synthetic aperture radar imagery and an application to nautical charting. *Photogrammetric record,* 15(85):57-64.

[Schreier (Ed.), 1993] Schreier, G. (Ed.), 1993. *SAR Geocoding: Data and Systems.* Wichmann Verlag, Heidelberg, 435 pages.

[Schreier *et al.*, 1993] Schreier, G., Kosmann, D. and Roth, A., 1993. The D-PAF ERS-1 SAR geocoding system GEOS. geocoded images. In *SAR Geocoding: Data and Systems.* Edited by Schreier, G. Wichmann Verlag, Heidelberg, pp:135-158.

[Singh *et al.*, 1998] Singh, K., Lim, O. K., Kwoh, L. K. and Lim, H., 1998. An accuracy evaluation of DEM generated using RADARSAT stereo images. *Proceedings IGRASS '98*, Seattle, USA. CD-ROM.

[Skolnik, 1981] Skolnik, K.I., 1981. *Introduction to Radar Systems.* Second Ed. McGraw-Hill, Inc., Singapore. 581 pages.

[Slama *et al.*, 1980] Slama, C.C., Theuer, C. and Henriksen, S.W., 1980. *Manual of Photogrammetry.* Fourth Ed. ASPRS, Falls Church, Virginia. 1056 pages.

[Smith *et al.*, 1984] Smith, D.J. , Veck, N.J., Macklin J.T. and Luscombe, A.P., 1984. *SAR Simulation Concept and Tools: Final Report.* GEC-Marconi Research Centre, Essex, U.K. 109 pages.

[Sonka *et al.*, 1993] Sonka, M., Hlavac V. and Boyle, R., 1993. *Image Processing, Analysis and Machine Vision*. Chapman & Hall, London. 555 pages.

[Sowter, 1998] Sowter, A., 1998. The automatic extraction of DEM data from stereo RADARSAT pairs over the tropics. *International Archives of Photogrammetry and Remote Sensing*, 32(2):291-298.

[Sylvander *et al.*, 1998] Sylvander, S., Petitcolas, B. Cousson, D. and Souyris, J.-C., 1998. Evaluation of the potential of RADARSAT images for the production of digital terrain model by radargrammetry. *RADARSAT ADRO Final Symposium*, Montreal. CD-ROM.

[Tanimoto and Pavalidis, 1975] Tanimoto, S. and Pavlidis, T., 1975. A hierarchical data structure for picture processing. *Computer Graphics and Image Processing*, 4:104-119.

[*The Economist*, 1999] *The Economist*, 1999. Paradise misplaced. In *The Economist* (Millennium special edition). 353(8151):51.

[Toutin, 1996] Toutin, T., 1996. Opposite side ERS-1 SAR stereo mapping over rolling topography. *IEEE Transaction on Geo-science and Remote Sensing,* GE-34(2):543-549.

[Toutin, 1999] Toutin, T., 1999. Error tracking of radargrammetric DEM from RADARSAT images. *IEEE Transaction on Geo-science and Remote Sensing,* GE-37(5):2227-2238.

[Twu, 1996] Twu, Z.-G., 1996. *Automatic Height Extraction from Stereoscopic SAR Imagery*. Ph.D. Thesis, University of London. 222 pages.

[Twu and Dowman, 1996] Twu, Z.-G. and Dowman, I.J., 1996. Automatic height extraction from stereoscopic ERS-1 SAR imagery. *International Archives of Photogrammetry and Remote Sensing*, 31(B2):380-383.

[Vieux, 1995] Vieux, B.E., 1995. DEM aggregation and smoothing effects on surface runoff modeling. In *Wetland and Environmental Applications of GIS.* Edited by Lyon, J.G. and McCarthy, J. CRC Press, USA, pp:205-269.

[Watt and Watt, 1996] Watt, A. and Watt, M., 1996. *Advanced Animation and Rendering Techniques Theory and Practice*. ACM Press, New York. 455 pages.

[Welch and Papacharalampos, 1990] Welch, R. and Papacharalampos, D., 1990. 3-D computation and display of terrain models from stereo imaging radar data. *IGRASS'90,* Washington D.C., pp:1967-1969.

[Wildey, 1986] Wildey, R.L., 1986. Radarclinometry for the Venus radar mapper. *Photogrammetric Engineering & Remote Sensing*, 52(1):41-50.

[Wiman, 1998] Wiman, H., 1998. Automatic generation of digital surface models through matching in object space. *Photogrammetric Record*, 16(91):83-91.

[Wivell *et al.*, 1992] Wivell C.E., Steinwand, D.R., Kelly, G.G. and Meyer, D.J., 1992. Evaluation of Terrain Models for the geocoding and terrain correction of Synthetic Aperture Radar (SAR) images. *IEEE Transaction on Geo-science and Remote Sensing*, GE-30(6):1137-1144.

[Wong and Ho, 1986] Wong, K.-W. and Ho, W.-H., 1986. Close-range mapping with a solid state camera.. *Photogrammetric Engineering & Remote Sensing*, 52(1):67-74.

[Young and Fu, 1986] Young, T.Y. and Fu, K.-S., 1986. *Handbook of Pattern Recognition and Image Processing*. Academic Press Inc., London. 705 pages.

[Zebker and Goldstein, 1986] Zebker, H.A. and Goldstein, R.M., 1986. Topographic mapping from interferometric synthetic aperture radar observations. *Journal of Geophysical Research*, 91(B5):4993-4999.

[Zebker *et al.*, 1994] Zebker, H.A., Werner, C.L., Rosen, P.A. and Hensly, S., 1994. Accuracy of topographic maps derived from ERS-1 Interferometric Radar. *IEEE Transaction on Geo-science and Remote Sensing*, GE-32(4):823-836.

Appendices

A. Lists of Software Used in the Thesis

A.1 Kernel Programmes

Kernel Programme	Description	Source	Author
`rsatsar1`	Space intersection for deriving the co-ordinates of unknown ground points from a pair of homologous image point (see Appendix B for more details)	/ps/research/beta /phchen/sar/	Pu-Huai Chen
`sarsimul`	SAR image product simulator using a set of orbit data and a known Digital Elevation Model (DEM) (see Appendix B for more details)	/ps/research/beta /phchen/sar/	Pu-Huai Chen
`ncc`	Normalized cross correlation for a target and a reference image (see Appendix B for more details)	/ps/research/beta /phchen/sar/	Pu-Huai Chen
`sargeoco`	Geocoding a real SAR image using a set of header data and a known DEM (see Appendix B for more details)	/ps/research/beta /phchen/sar/	Pu-Huai Chen
`gruen`	Stereo matching using Gruen [1985] adaptive least-squares correlation (see Twu [1996] for more details)	ps/research /wizard/mia /bin-sun4	G. P. Otto and T. K. W. Chau
`gruens`	Stereo matching using Gruen's least-squares correlation method with a sheet-growing approach (see Twu [1996] for more details).	ps/research /wizard/mia /bin-sun4	G. P. Otto and T. K. W. Chau

A.2 Auxiliary Script Files

Auxiliary script file	Description	Source	Author
`cheops`	Providing a harness for the pyramidal stereo correlation harness to execute `gruen` and `gruens` (see Twu [1996] for more details).	ps/research /wizard/mia /bin-sun4/	M. I. Denos and M. A. O'Nell
`cascade`	Commanding the generation of seed points and giving parameters for `cheops` to carry out stereo-matching (see Twu [1996] for more details)	ps/research /wizard/mia /bin-sun4/	M. I. Denos and M. A. O'Nell
`flz3togem6`	Co-ordinate transformation routines: from the French Lambert Conformal Conic Zone III (map) system to a global geocentric co-ordinate system	/ps/research/beta /phchen/sar/	Mark Upton
`gem6toflz3`	Co-ordinate transformation routines: from a global geocentric co-ordinate system to the French Lambert Zone III (map) system	/ps/research/beta /phchen/sar/	Mark Upton

A.3 Other Routines

Other Routines	Description	Source	Author
readbyte	Extract specific records of known size and field offset from a data file	/ps/research/beta /phchen/sar/	Pu-Huai Chen
readword	Extract a specific word of know location and field offset from a data file	/ps/research/beta /phchen/sar/	Pu-Huai Chen
pixel	Numerical presentation of an area of arbitrary size of interest from a binary image file	/ps/research/beta /phchen/sar/	Pu-Huai Chen
xx	Accuracy statistics calculator for the ground co-ordinates derived from space intersection	/ps/research/beta /phchen/sar/	Pu-Huai Chen
xyz_to_dem	Convert scattered elevation points to a DEM of a grid (HIPS) format.	/usr/hipl/	T. Day
DEM_to_nxyz	Convert a grid-format (HIPS) DEM to co-ordinates list.	/usr/hipl/	T. Day
krige_some	Generate an interpolated DEM using selected input points	/usr/hipl/	T. Day
comparek	Compare the input DEM data with a reference DEM using a kriging method	/ps/data/deimos /alpha/tin/bin /sun4/	T. Day
DEM_diff	Find statistics of a float format DEM	/usr/hipl/	T. Day
mav	Generate a square-patch moving average of a (HIPS) float image	/usr/hipl/	T. Day
imagine™	Displaying and generation of 3D perspective viewing of DEMs draped with a geometrically rectified image. This is a sophisticated product with many more functions.	/usr/local/bin	ERDAS® Inc.
rsatqp	RADARSAT orbit quick propagator. Propagate state vectors through gravity potential.	/ps/research/beta /phchen/sar/	Calvin Harr

B. Guide of the Software Developed in the Thesis

B.1 Programme `rsatsar1`

Programme	Guide of Usage
Name: `rsatsar1` *Environment:* SunOS R4.1 *Language:* FORTRAN	*Synopsis*: `rsatsar1` *Description:* The programme `rsatsar1` reads the header files of RADARSAT SAR images, `rsat.1` and `rsat.2`, and a parallax data file, `rsat.ddm`, as shown in Table 3.3, to find the co-ordinates of ground points from a pair of stereoscopic SAR images. The Doppler data is assumed as zero for RADARSAT SAR data. The image co-ordinates of conjugate point pairs are firstly transformed from the screen system into image co-ordinate system. The sampled state vectors of the sensor are then interpolated according to the corresponding azimuth time (line). The sidereal time of the corresponding azimuth line is calculated giving the conversion between the inertial/geocentric co-ordinate systems. The range (pixel) is restored using the ground-range-to-slant-range transformation parameters. The image scene centre location is treated as the initial position of the first unknown ground point, which is the first homologous point pair in the parallax data file. Space intersection is carried out by an iterative least-squares adjustment of indirect observations in an inertial co-ordinate system. The Gauss-Jordan elimination method is used to solve the normal equation. The solved location of the first ground point is used as the approximation for the next homologous point pair in the parallax data file. Repeat the least-squares solution for every homologous point pair until the end of the parallax file is reached. The solved ground co-ordinates are transformed back to a geocentric system as output. The throughput is in a format of (X, Y, Z) in a geocentric co-ordinate system. Since there is no GCPs required in the algorithm, the output data file must be compared with the co-ordinates derived using GCPs in a local map co-ordinate system giving systematic corrections, if necessary. *Author:* Pu-Huai Chen

B.2 Programme `sarsimul`

Programme	Guide of Usage
Name: `sarsimul` *Environment:* SunOS R4.1 *Language:* FORTRAN	*Synopsis*: `sarsimul` *Description:* The programme `sarsimul` reads in the header file of a SAR image, `sarsimul.dat` and a DEM file, `sarsimul.dem`, as shown in Table 5.1, to simulate a ground-range SAR intensity image. The Doppler data is assumed as zero for RADARSAT SAR data. The input DEM is a co-ordinate list in the format of (E, N, H) in a geocentric co-ordinate system. The sampled state vectors of the sensor are interpolated according to the corresponding azimuth time (line). The sidereal time of the corresponding azimuth line is calculated giving the conversion between the inertial/geocentric co-ordinate systems for the DEM points to be simulated. The extent of the simulated area in azimuth direction is detected using a progressive approach based on the first and the last data points of the state vectors. The extent of the simulated area in range direction is detected using a progressive approach based on the central azimuth line within the simulated area together with the corresponding state vectors. The real SAR image structure is then determined using the header data provided, which will be applied to the simulated image. The relationships of ground-range pixels are restored using a curve-fitting function, according to the angle of incidence of the near, the centre and the far range pixel calculated in respect to an ellipsoid. Scan the DEM points for each azimuth line and detect the corner points of that DEM. Intensity of each image pixel (real type) is given by a reflectivity model that is the dot product of the unit surface normal vector of the defined DEM cell and the range vector. The real numbers are firstly normalized within the interval [0.0, 1.0]. Then, the density numbers (integers) of image pixels are derived by stretching and transforming the real numbers into integers from 0 to 255, which is stored in the corresponding range bin. Repeat the scanning process until the end of azimuth line is reached. The throughput is an intensity (binary) image together with the size of the image generated and the co-ordinates of the four corner points of the DEM. *Author:* Pu-Huai Chen

B.3 Programme ncc

Programme	Guide of Usage
Name: ncc *Environment:* SunOS R4.1 *Language:* C	*Synopsis*: `ncc -t Target_img -a TL TS -r Refer_img -e RL RS -p Out_f` *Description*: The programme `ncc` finds the relative location of the target image `Target_img` in respect to the reference image `Refer_img`. The normalized cross-correlation coefficient, also known as the product moment correlation coefficient or the Pearson's coefficient, is being used as the measure of the best matching between `Target_img` and `Refer_img`. The image pixel of zero density number in `Target_img` is not taken into account in the correlation measure. Both images being correlated must be in a raw binary format without header offset. The output file `Out_f` gives the relative location of the best matching measured for `Target_img` in respect to `Refer_img`. *Options*: `-t Target_img` specifies the name of the target image file. `-a TL TS` specifies the size of the target image as `tl` lines by `ts` samples. `-r Refer_img` specifies the name of the reference image file. `-e RL RS` specifies the size of the reference image as `rl` lines by `rs` samples `-p Out_f` specifies the name of the output file. *Author:* Pu-Huai Chen

B.4 Programme `sargeoco`

Programme	Guide of Usage
Name: `sargeoco` *Environment:* SunOS R4.1 *Language:* FORTRAN	*Synopsis:* `sargeoco` *Description:* The programme `sargeoco` reads the header file of a SAR image, `sargeoco.dat`, a DEM file, `sargeoco.dem`, an azimuth timing data file, `sargeoco.azi`, and an image file, `sargeoco.img`, as shown in Table 7.1, to geocode a ground-range SAR intensity image according to the map (DEM) co-ordinate system. The Doppler data is assumed as zero for the RADARSAT SAR data. The header file specifies the structure of the real ground-range SAR image. The orbit and range shifts can be corrected by giving appropriate values. The size of DEM and the image to be geocoded is given in `sargeoco.dat`. The input DEM is a co-ordinates list in the format of (*E*, *N*, *H*) in a geocentric co-ordinate system. The azimuth timing data required is a timing value list of the entire real SAR image. The image file to be geocoded is a co-ordinate list of the image pixel location and the density number. The sampled state vectors of the sensor are interpolated according to the corresponding azimuth time (line). The sidereal time of the corresponding azimuth line is calculated giving the conversion between the inertial/geocentric co-ordinate systems for each DEM cell, which will be filled in an appropriate density number. The extent of the DEM (geocoded area) in azimuth direction is detected using a progressive approach based on the first and the last data points of the state vectors. The extent of the geocoded area in range direction is detected using a progressive approach based on the central azimuth line within the simulated area together with the corresponding state vectors derived. The SAR image structure defined by the header data is used to guide the scanning process for detecting the DEM provided. The relationships of the ground-range pixels are restored using the slant-range-to-ground-range transformation parameters. Scan the DEM points for each azimuth line of the SAR image. The density number of each image pixel is assigned to the DEM cell being detected in respect to the appropriate range bin defined and calculated using the distance between the sensor and the DEM cell. Repeat the scanning process until the end of azimuth line is reached. The throughput is an intensity (binary) image together with the size of the geocoded image generated. *Author:* Pu-Huai Chen

C. Index-Map and the Location of Each Ground Point

C.1 Index-Map of the Aix-Marseilles Test Site

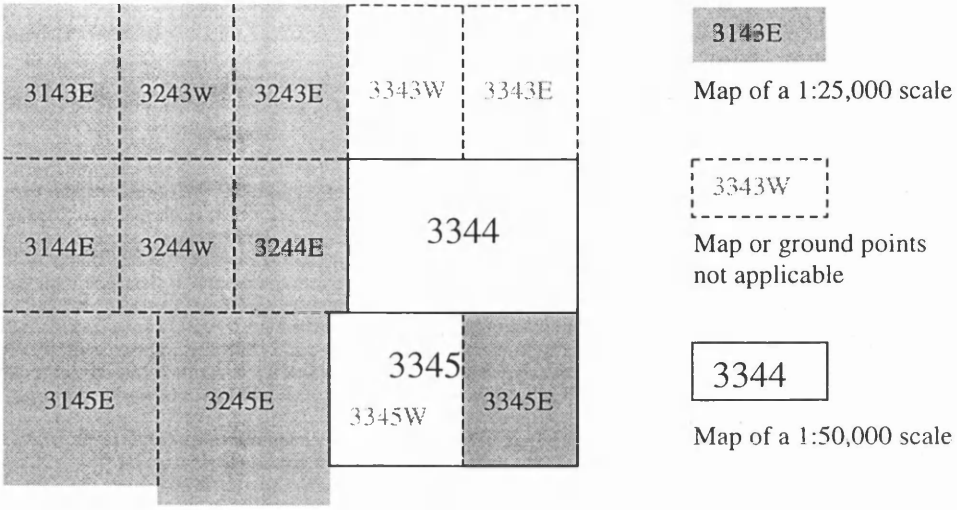

Index-Map in the French Lambert Zone III system (After IGN [1994]).

C.2 Locations of Ground Points in French Lambert Zone III System

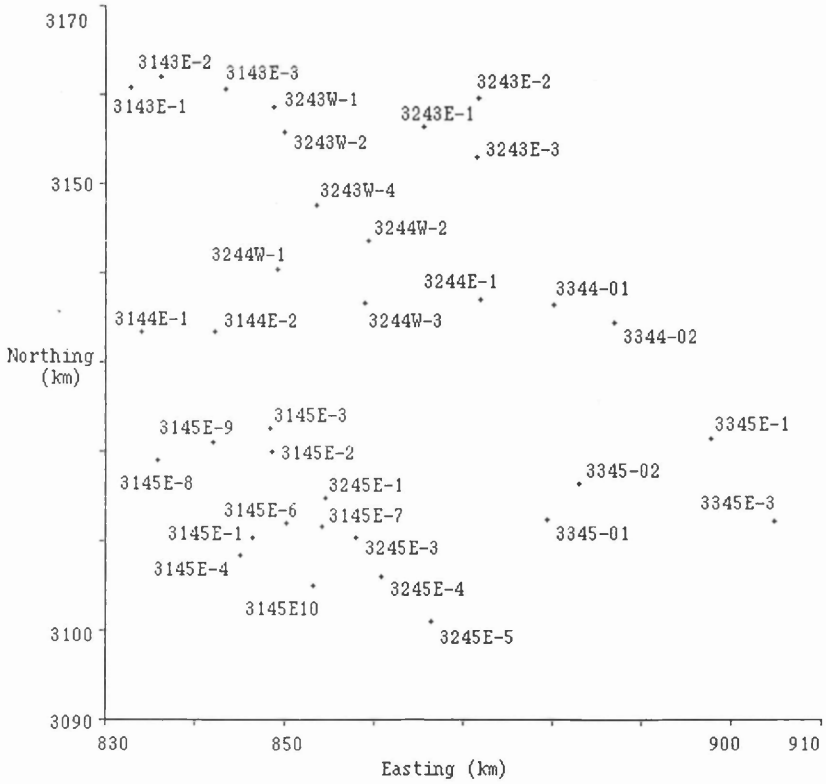

D. Test Images and the Reference DEM

D.1 Full-Scene RADARSAT SAR Image (DS1)

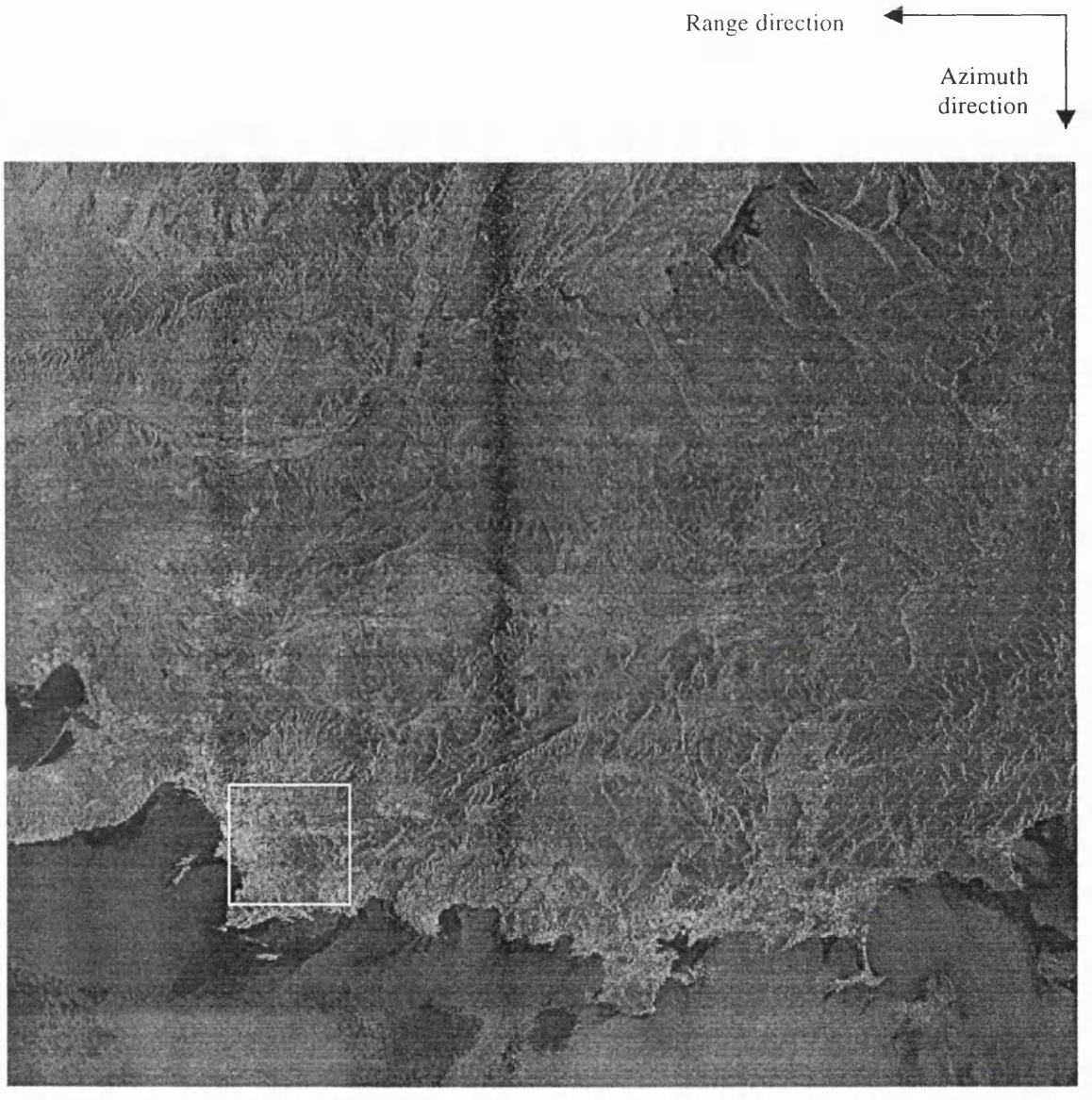

Full-scene RADARSAT SGF DS1 (Descending Standard Beam-1) image

Size: 7901 × 9074 pixels.

Date: 1997-08-22.

The extracted sub-scene is marked as shown above.

Size: 1024 × 1024.

Top-left corner: line:1885, pixel:5299.

D.2 Sub-Scene of DS1 Image for Image Correlation

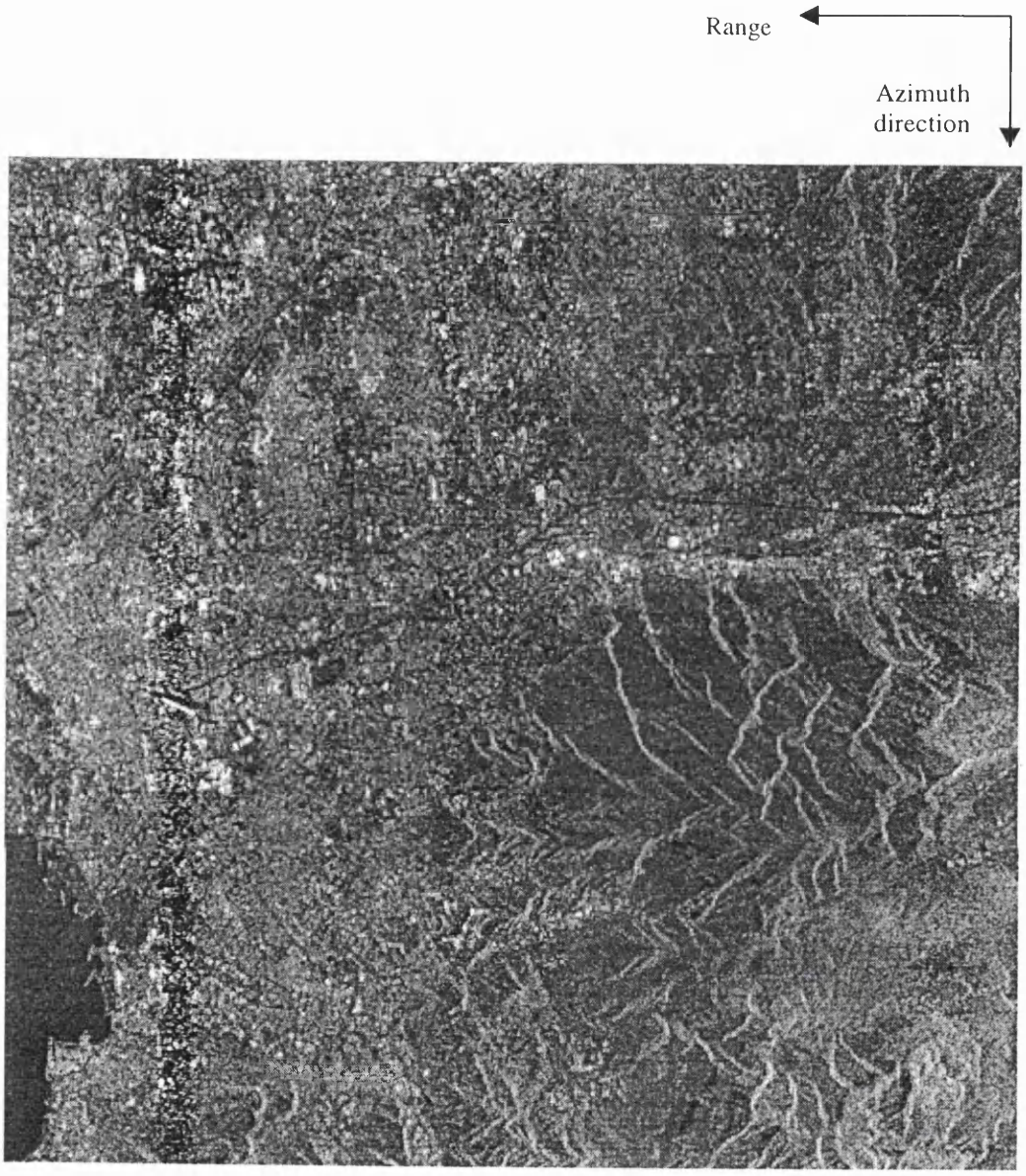

Left image (a sub-scene of DS1) for image correlation.

Size: 1024 × 1024 pixels.

D.3 IGN Reference DEM at the Aix-Marseilles Test Site

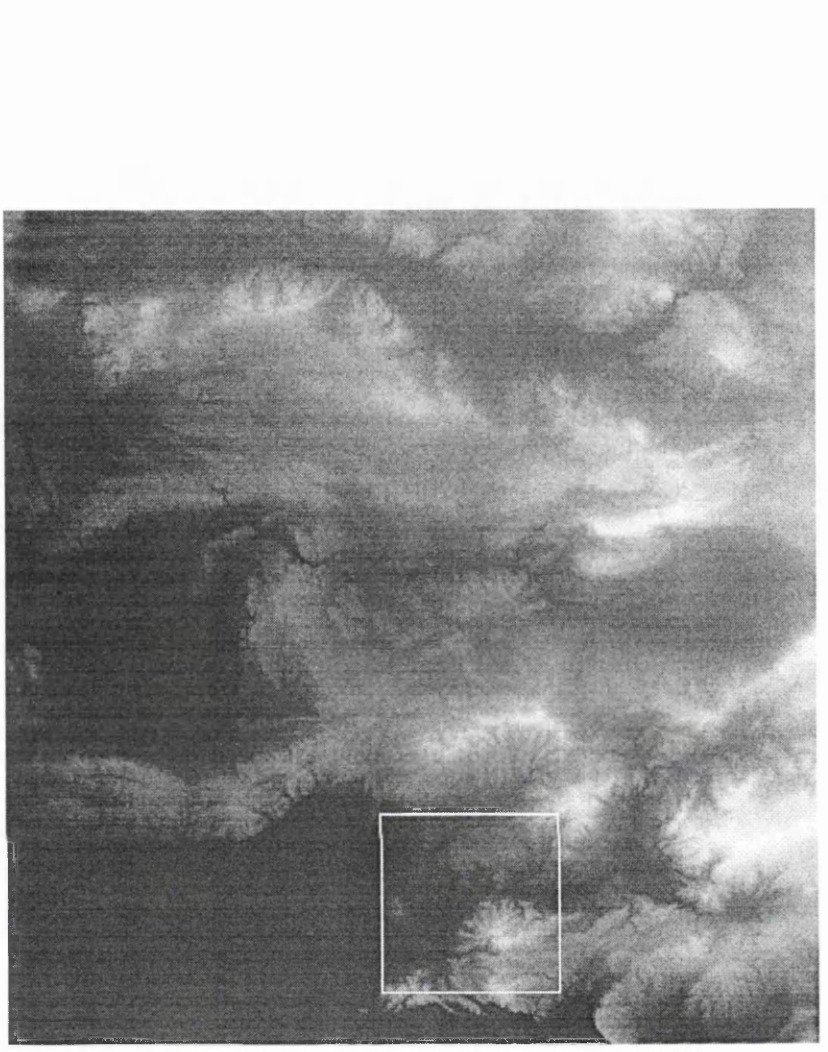

IGN reference DEM.

Size: 61km × 63km (E × N) in a 50m grid.

Bottom-left corner: E = 817km, N = 3103km in French Lambert Zone III system.

The height of DEM point increases proportionally with the brightness.

The extracted reference DEM for comparison is marked as shown above.

Size: 13.5km × 13.5km in a 50m grid.

Bottom-left corner: E = 845km, N = 3107km.

D.4 The Extracted Reference DEM for Comparison

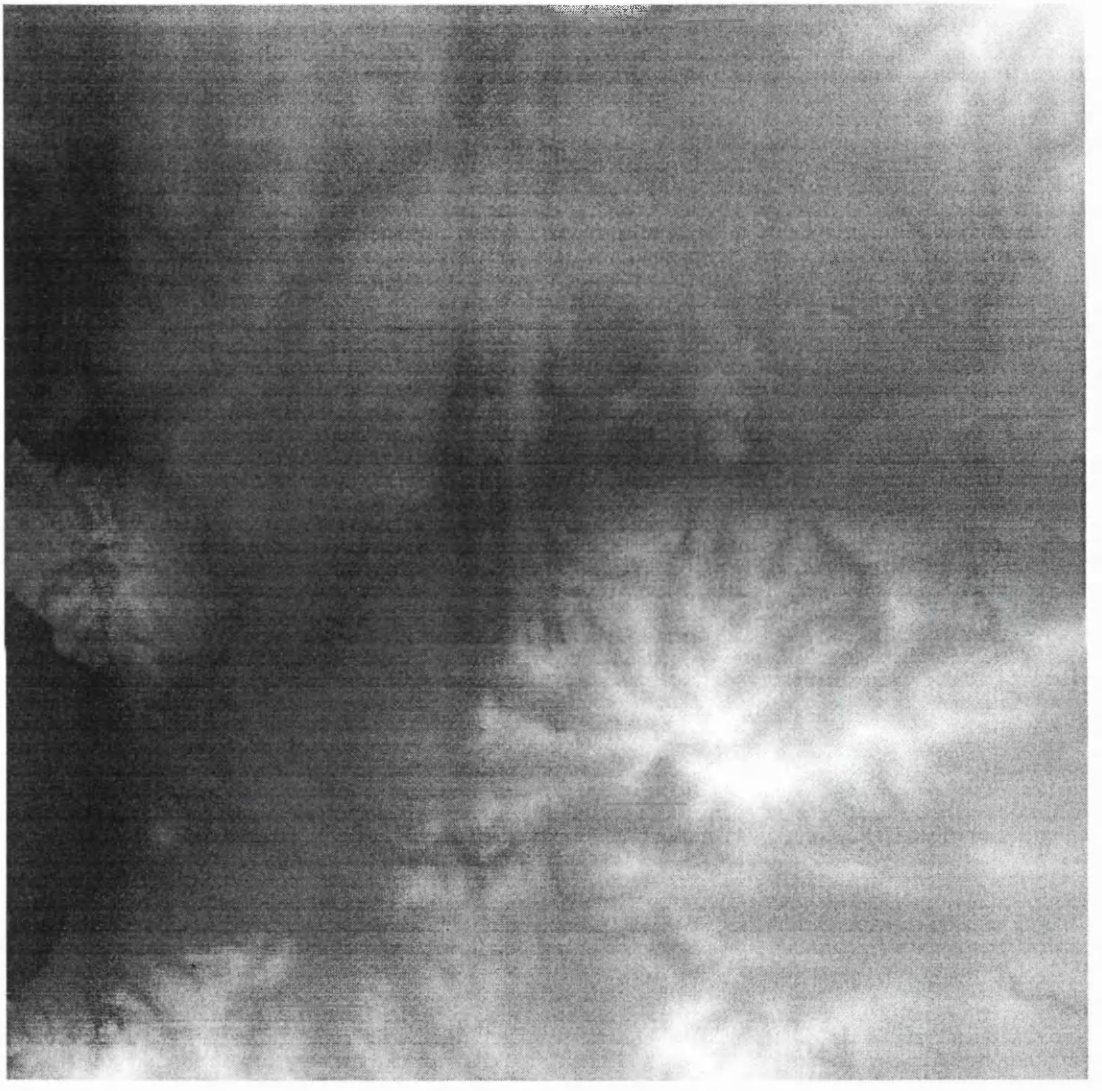

Size: 13.5km × 13.5km in a 12.5m grid.

Bottom-left corner: E = 845km, N = 3107km.

E Refined DEMs

E.1 DEM Derived Using Data Fusion of Different Orbits

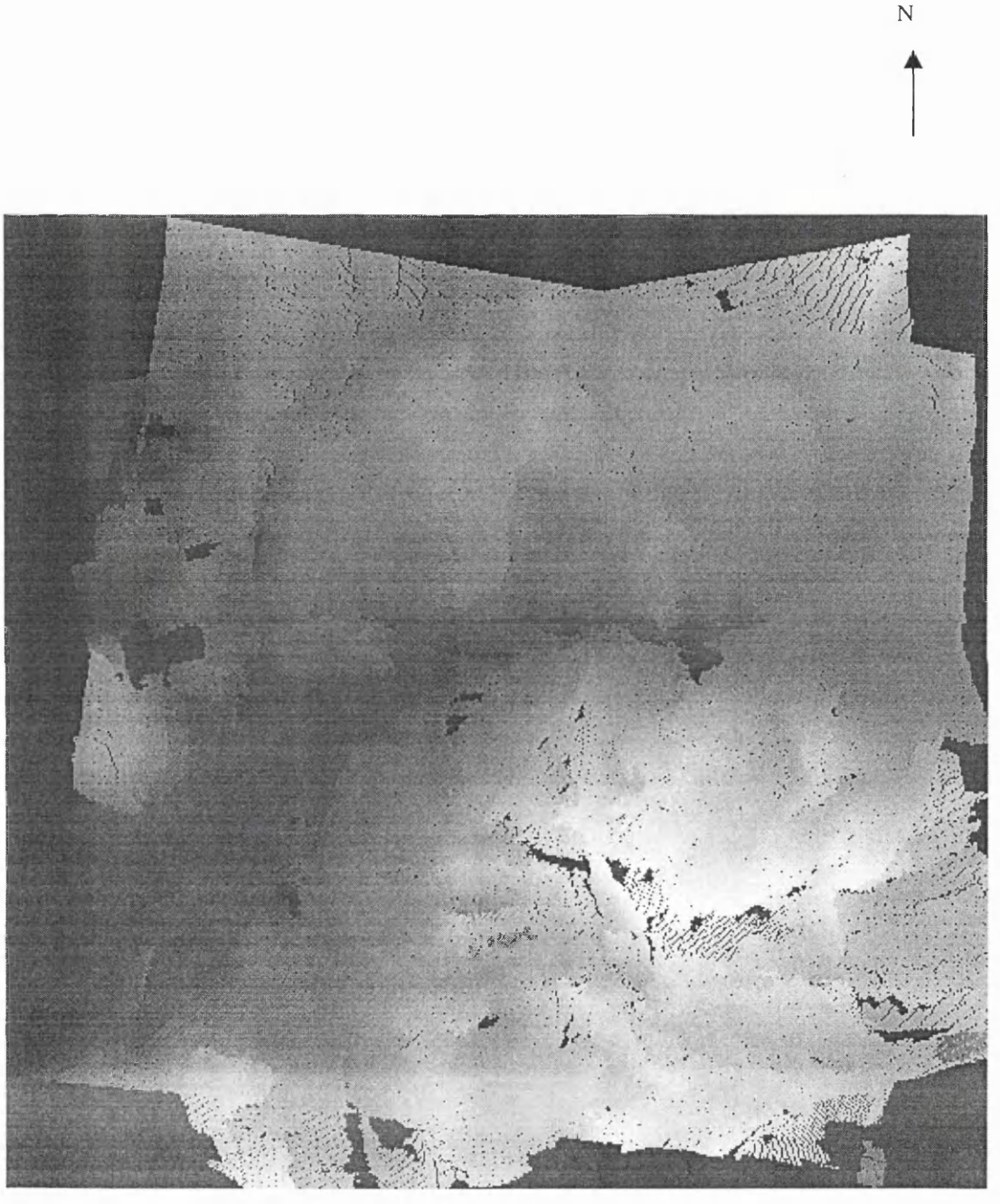

Size: 13.5km × 13.5km in a 25m grid approximately.

Bottom-left corner: E = 845km, N = 3107km.

E.2 Interpolated DEM

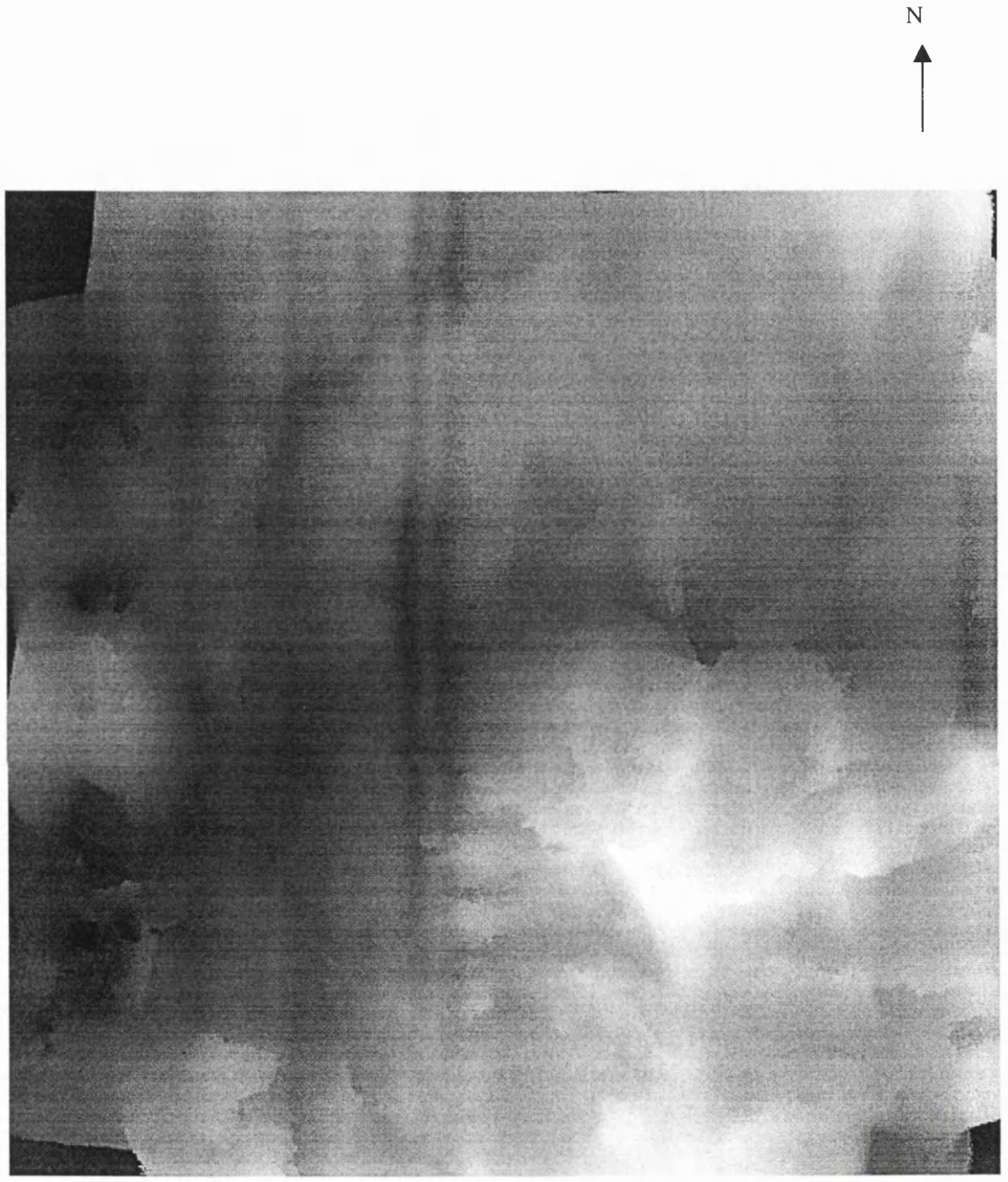

Size: 13.5km × 13.5km in a 25m grid approximately.

Bottom-left corner: E = 845km, N = 3107km.

Search radius for interpolation: 1000m.

Sectioned search directions: 64

F Geocoded SAR Images

F.1 The Geocoded SAR Image (DS1) Derived Using the Reference DEM

Size: 11km × 11km in a 12.5m grid approximately.

Bottom-left corner: E = 846.5km, N = 3108km.

F.2 The Geocoded Image Derived (DS1) Using the DEM Generated and Refined

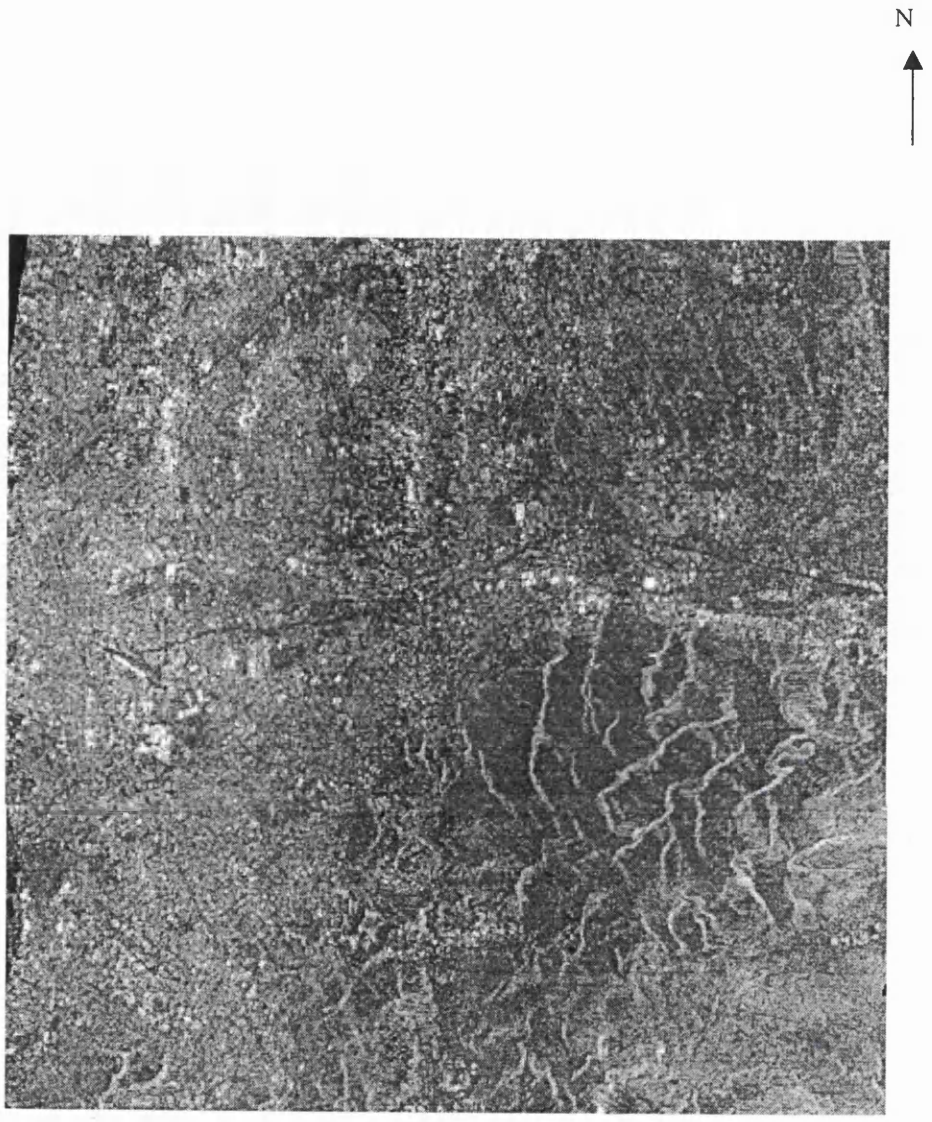

Size: 11km × 11km in a 12.5m grid approximately.

Bottom-left corner: E = 846.5km, N = 3108km.

F.3 Difference Image between the Geocoded Images (DS1) in F.1 and F.2

N

Size: 11km × 11km in a 12.5m grid approximately.

Bottom-left corner: E = 846.5km, N = 3108km.

The absolute difference between the geocoded images derived using the reference DEM and the DEM generated and refined increase with decreasing brightness.